

Classical Rydberg Electron Interactions with Half Cycle Pulses

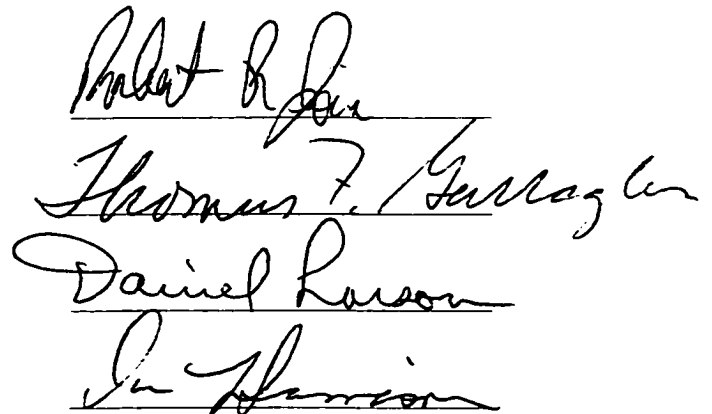
Thomas Joseph Bensky
Los Angeles, CA

B.S. California State University, Northridge, 1993

A Dissertation presented to the Graduate Faculty of the University
of Virginia in Candidacy for the Degree of Doctor of Philosophy

Department of Physics

University of Virginia
August 1998


Robert R. Jones
Thomas F. Gallagher
Daniel Larson
J. Harrison

UMI Number: 9916263

**UMI Microform 9916263
Copyright 1999, by UMI Company. All rights reserved.**

**This microform edition is protected against unauthorized
copying under Title 17, United States Code.**

UMI
300 North Zeeb Road
Ann Arbor, MI 48103

Abstract

We report on classical interactions between sub-picosecond half-cycle pulse (HCP) fields and Rydberg states in atoms. Two experiments are reported. The first uses a HCP pair to create a unique field whose polarization executes a circular rotation for only 1/4 of a field cycle. This field contrasts sharply to more conventional circularly polarized fields that continually circulate about their propagation axis. The ionization response of Sodium Rydberg states due to this field is studied in regimes where the 1/4-cycle field behaves like a rapid, impulsive field or as a slowly varying ramped field, depending on the initial Rydberg state excited. In a surprising result, the ionization response due to the impulsive field shows a remarkable independence of the rapidly varying polarization of the field, in contrast to that from more conventional, circularly polarized fields. The second experiment presented uses a single HCP field to radiatively assist in ion-electron recombination in Calcium. A continuum state is induced in Rydberg atoms using a strong static field, and as much as 10%-15% of the continuum population is recombined. The continuum state exhibits a wildly dynamic behavior over many tens of picoseconds after excitation, depending on the initial Rydberg state and static field strength. There is strong dependence on the orientation of the HCP relative to the static field. Throughout this work, a classical mechanics based numerical analysis has provided valuable insight into the heart of both experiments. Prospects for future work are discussed.

Contents

0.1	Acknowledgements	11
1	Introduction and Background	13
1.1	Atomic Physics	14
1.2	Alkali Rydberg Atoms	17
1.3	Ultrafast Lasers	22
1.3.1	Broad Bandwidth and Coherent Excitation	23
1.4	Half Cycle Pulse Fields	25
1.4.1	Unipolarity	26
1.4.2	Time Scales	29
1.4.3	Field Strengths	30
1.5	Conclusions	30
2	Experimental Apparatus	34
2.1	Laser Systems	34
2.1.1	Nd:Yag Laser	35
2.1.2	Argon-Ion Laser	36
2.1.3	Ultrafast Laser System	38
2.1.4	Dye Lasers	47
2.2	Rydberg Atom Production	51
2.3	Half Cycle Pulse (HCP) Generation	54
2.4	Vacuum System, etc.	57
2.5	Data Acquisition	64
3	The interaction between a Half-cycle pulse and a Rydberg electron	67
3.1	Introduction	68
3.2	The HCP/Rydberg Atom Interaction	69
3.2.1	The Interaction in the Impulsive Regime	69
3.2.2	The Interaction in the Non-Impulsive Regime	76
3.3	Conclusions	79
4	The Interaction of a Rydberg Atom with Two Time Separated Half-Cycle Pulses	82
4.1	Introduction	83

4.1.1	Interactions with two parallel time separated HCPs	83
4.1.2	Interactions with two cross polarized time separated HCPs	86
4.2	Experiment	90
4.2.1	Rydberg Atom Production	90
4.2.2	HCP Generating Apparatus	92
4.2.3	Data Acquisition and Experiment Prerequisites	95
4.3	Ionization due to a 1/4-cycle circularly polarized field ¹	103
4.3.1	Results and Discussion: Impulsive Regime	103
4.3.2	Results and Discussion: Non-Impulsive Regime	108
4.4	Classical Numerical Analysis	112
4.4.1	Numerical Integration of the Equations of Motion	112
4.4.2	Classical Insight: Impulsive Regime	116
4.4.3	Classical Insight: Non-Impulsive Regime	121
4.5	A Systemic Investigation	123
4.6	Conclusions	126
5	Electron-Ion Recombination Using Half-Cycle Pulses	129
5.1	Introduction	129
5.2	HCP Assisted Electron-Ion Recombination	131
5.3	HCP Assisted Recombination with a Static Field Induced Continuum	137
5.4	Experiment	141
5.5	Data Analysis and Discussion	148
5.5.1	Data Presentation and Discussion	148
5.5.2	Data Calibration	151
5.5.3	Systematic Study	155
5.6	Classical Numerical Analysis	161
5.6.1	Introduction	161
5.6.2	Results	165
5.7	Electron-ion recombination or Wavepacket Dynamics?	172
5.8	Wrap-Up	176
5.9	Quantum Numerical Analysis	177
5.10	Orienting the HCP perpendicular to the static field	184
5.11	Conclusions	185
6	Conclusions	188
6.1	Ionization due to 1/4 Cycle Circularly Polarized Radiation	188
6.2	HCP Assisted Electron-Ion Recombination	189
6.3	Future Directions	190
6.3.1	1/4 Cycle Circularly Polarized Fields	190
6.3.2	HCP Assisted Recombination	191

A	$\vec{F} = m\vec{a}$: Classical Numerical Analysis of Rydberg Atom/HCP Interactions	194
A.1	Introduction	194
A.2	Numerical Integration	196
A.3	A Classical Rydberg State	198
A.3.1	The Differential Equation of Motion	200
A.3.2	Preparing it for the Computer	201
A.3.3	Initial Conditions	202
A.3.4	Performing the Integration	209
A.3.5	Programming Examples	211
A.3.6	After the Integration	216
A.4	Orientation Considerations	216
A.4.1	Results	218
A.5	Applying External Fields	222
A.5.1	Adding an External HCP field	222
A.5.2	Adding External HCP and Static Fields	224
A.5.3	Adding Two Cross-Polarized HCPs	224
A.6	Conclusions	225
B	Publication: Effects of unipolarity on the ionization of Rydberg atoms by subpicosecond half-cycle pulses	228
C	Publication: Single-shot detection of wavepacket evolution	233
D	Publication: Probing electronic radial wave packets using impulsive momentum retrieval	240

List of Tables

1.1	Some physical properties of Rydberg atoms and their dependencies on n	19
1.2	Quantum defects for s, p, and d states of Na of K.	21
1.3	Classical Kepler orbit periods for different Rydberg states.	29
A.1	Initial conditions of a numerical $n = 25d$ classical Rydberg state, and how they compare to quantum mechanical expectation values. These values are computed for an ensemble of 10,000 initial orbits.	221

List of Figures

1.1	Left: The classical orbit for a highly excited, low angular momentum Hydrogen atom orbit with a point-like core. Right: The same orbit for an alkali atom, with a finite sized core.	20
1.2	Example of coherent excitation: a Rydberg series and a 15cm^{-1} laser pulse frequency centered on $n = 42$	24
1.3	A HCP field function which closely resembles an actual HCP, as produced in the lab. Note the dominant unipolar portion of the total field. This functional form was taken from Ref. [13]	27
2.1	A sketch of a Ti:Sapphire based mode locker, adapted from reference [6]	41
2.2	A schematic of the regenerative amplifier.	44
2.3	The basic design and components of a Hansch-style dye laser.	48
2.4	Generating a THz HCP of radiation.	56
2.5	Experimental components, as assembled inside of the vacuum system.	58
3.1	The shift in a classical $n = 25d$ electron's momentum distribution due to a HCP polarized along the x-axis, incident at $t = 1$ ps. The HCP impulse \vec{A} was set to 0.015 (a.u.)	72
3.2	A $-1/r$ attractive Coulomb potential. The arrows represent different ways in which energy can be imparted to a Rydberg electron by a HCP.	73
3.3	Experimental data of the ion signal collected from an $n = 25d$ Rydberg electron as a function of incident HCP amplitude. The circles are predicted by a classical mechanics based analysis. Note the dashed step function passes through the 50% ionization level. There is an experimental uncertainty in the actual HCP amplitude by a factor of ~ 2.5	75
3.4	The alteration of the Coulomb binding potential due to a HCP electric field, $\vec{F} = F_0(t)\hat{z}$. The dashed line is the unperturbed Coulomb potential. Various levels along a HCP envelope with a peak field of 10 kV/cm are plotted. Curve (A) 0%, (B) 10% (C) 30%, (D) 70%, (E) 100% of maximum HCP amplitude. A bound $n = 25$ Rydberg electron is shown by the horizontal line inside of the potential well.	78

4.1	Ionization versus δ , the time delay between two HCPs with parallel orientations, for the $n = 18$ Rydberg state of Na. Note the increased in ionization near $t=0$, where the two HCP fields are overlapped. Time delays different from $t=0$ map out the overall HCP envelope seen. . .	85
4.2	The net field produced by two counterpropagating, cross polarized HCP fields. The first HCP is polarized along the \hat{x} -axis, and the second along the \hat{y} -axis. The top inset shows the linear polarized net field produced when $\delta = 0$. The middle inset shows the net field for $\delta = 0.25$ ps. The bottom inset shows the net field for $\delta = 0.5$ ps. Note how in the latter two cases, the net field (the arrows) executes circular motion for only 1/4 of a cycle.	89
4.3	The excitation scheme to create Rydberg atoms from ground state Na atoms.	91
4.4	The ion signal produced by pulsed field ionization of Na atoms excited via two photon excitation to ns or nd Rydberg states, as a function of the grating angle on the 2nd dye laser (see text).	93
4.5	The experimental apparatus for irradiating Rydberg atoms with 1/4-cycle circularly polarized THz radiation. Shown in the figure are two GaAs wafers whose bias fields are oriented at 90 degrees with respect to each other. The positions of the atomic beams and dye laser beams are also shown. The dye laser beams are polarized in a direction that maximizes the symmetry of the problem.	94
4.6	The timing of all fields involved in the cross-polarized HCP experiment.	96
4.7	Scan (a) is the ion signal level versus bias field for two parallel, simultaneous HCPs at the “ $t=0$ ” position. Scan (b) is the same signal for a single HCP. There is a factor of 1.8 in field between the two scans. . .	101
4.8	Scan (a) is the ion signal level versus bias field for two perpendicular, simultaneous HCPs at the “ $t=0$ ” position. Scan (b) is the same signal for a single HCP. There is a factor of $\approx \sqrt{2}$ in bias fields between the two scans.	102
4.9	The mechanism behind the time delay for light that irradiates one of the two GaAs wafers used in this experiment. Two mirrors mutually oriented at 90 degrees are mounted on a movable translation stage. Note that changing the stage position by an amount d changes the optical path of the light by an amount $2d$. This time delay leg is what is represented by the broken line labeled “Variable Delay” in Fig. 4.5.	104
4.10	The ionization of the $n = 23d$ state in Na as a function of field amplitude in each of two cross polarized HCPs with a relative time delay of (a) 0 ps, (b) 0.25 ps, and (c) 0.5 ps. The scans are identical, and artificially offset for illustration. The HCP amplitude determination was aided by the classical calculation.	105

- 4.11 The ratio of the field required to produce a certain percentage of ionization between the linear case produced by two simultaneous cross polarized HCPs and a single HCP as a function of n , the principal quantum number. 108
- 4.12 The ionization of an $n = 18d$, $m = 0$ Rydberg state as a function of the delay time between two cross-polarized HCPs. The amplitude of each HCP is held fixed during the scan. The normal pitch curve is data for two HCPs polarized parallel to each other. The bold pitch curve is for two cross polarized HCPs. The bias voltage on the HCP pair used each scan is identical. 111
- 4.13 Classical numerical predictions of the ionization of the $n = 23d$ state in Na as a function of HCP field, F_0 (see text) for two cross polarized HCPs with a relative time delay of (a) 0 ps, (b) 0.25 ps, and (c) 0.5 ps between them. The scans are identical, and artificially offset for illustration. This figure is the calculated analogy of Fig. 4.10. 115
- 4.14 Classical momentum distributions of an $n = 25d$, $m = 0$ electron ensemble irradiated with a Gaussian HCP, polarized along the \hat{x} -axis. Note the abrupt shift in the p_x momentum distribution. p_y and p_z remain unchanged. 117
- 4.15 Classical momentum distributions of an $n = 25d$, $m = 0$ electron ensemble irradiated with two cross polarized, Gaussian HCPs with a 0.5 ps relative delay. The first HCP is polarized along the \hat{x} -axis, and the second along the \hat{y} -axis. 119
- 4.16 A HCP with ≈ 1.0 THz (30 cm^{-1}) of bandwidth plotted against an atomic Rydberg series. The HCP is frequency centered at the $n = 25$ and $n = 35$ resonance energies for comparison. Note how many states lie under the HCP envelope. 120
- 4.17 Calculated ionization of an $n = 14d$, $m = 0$ Rydberg state as a function of the delay time between two parallel (normal pitch curve) and cross-polarized (bold pitch curve) HCPs. The field amplitude of each HCP is 20kV/cm 122
- 4.18 The ratio of the field required to produce any percentage of ionization between the 1/4-cycle circularly polarized case and the linear case created by two simultaneous cross-polarized HCPs versus n , the principal quantum number. The triangles are predicted by the classical calculation, the circles are data, and the solid line helps to guide the eye. The insets serve as reminders to the net 1/4 cycle field produced, as viewing it along the propagation axis. Inset A is for the 0.25 ps delay case, and inset B is for the 0.5 ps delay case. 125

5.1	A one dimensional Coulomb potential. Bound, state population with energy E_1 is excited into the continuum, at (a), with positive energy E_2 , and begins to expand outwards, at (b). The charge expands with momentum p_0	132
5.2	A one dimensional potential with an unbound, outgoing charge. The momentum, p_0 , of the outgoing charge is shown. The direction of the impulse, \vec{A} , delivered by the HCP is shown by the large arrow. Initially, the charge portions are all at energy E_2 . After interacting with the HCP, the charges are placed at energy E_b and E_c	133
5.3	Three snapshots of a classical continuum wavepacket evolving in time (left column), and their associated momentum distributions (right column). Note the gradual narrowing of the momentum distribution as a function of time. The dotted line represents a boundary in the momentum distribution, below which population cannot be recombined.	138
5.4	Potential energy vs. z . A one-dimensional Coulomb potential immersed in a static field of strength $F_s = 212$ V/cm along the $+\hat{z}$ -axis. The energy level shown (the arrow) is the energy level of a bound $n = 42$ Rydberg state. The $z > 0$ side of the potential is called the "uphill" side, while the $z < 0$ side is called the "downhill" side, for obvious reasons.	139
5.5	The experimental setup used in the HCP assisted recombination experiment.	142
5.6	Time of ionization scans for different excitation methods near $n = 42$. The bold line is coherent excitation of the wavepacket by a 10 cm^{-1} wide laser pulse centered on $n = 42$. The normal pitch lines are the wavepacket's component states found by scanning a narrow band (1 cm^{-1}) dye laser through the same frequency range covered by the broadband laser. Both the laser bandwidth and wavepacket composition can be inferred from this scan using a Rydberg series as a backdrop.	145
5.7	A sample data set for an $n = 42$ wavepacket in a static field with strength 212 V/cm. Top: the HCP field is polarized antiparallel to the static field, meaning the HCP's impulse, \vec{A} , is parallel to the static field. Bottom: the HCP field is polarized parallel to the static field, meaning the HCP's impulse, \vec{A} , is oriented antiparallel to the static field. The plots illustrate the absolute bound fraction versus wavepacket evolution time before interacting with the HCP.	150
5.8	Bound fraction versus time at 25 different static field values, for $n = 42$. The static field was ramped between 90 V/cm (static field count 0) to 340 V/cm (static field count 25) in steps of 10 V/cm. The HCP impulse is antiparallel to the static field.	157

5.9	Bound fraction versus time at 25 different static field values, for $n = 42$. The static field was ramped between 90 V/cm (static field count 0) to 340 V/cm (static field count 25) in steps of 10 V/cm. The HCP impulse is parallel to the static field.	158
5.10	Frequency domain representations of the acquired recombination data at 110 V/cm. The Stark structure is evident by the large peak towards the left. The radial structure is evident by the bold group of peaks. .	159
5.11	Stark splitting versus static field strength for recombination when the HCP impulse oriented antiparallel to the static field. Bottom: The line is the Stark energy splitting, $3nF$, and the points (+) are data. . . .	160
5.12	Dotted line: Pure Coulomb potential. Solid line: Combined Coulomb and static field potential. The static field magnitude is 212 V/cm. The horizontal line is the bound energy level for $n = 42$. Note the inwards shift of the outer turning point on the uphill ($z > 0$) side.	162
5.13	Absolute bound fraction versus time for classical calculation (bold line) and data (normal line). This plot is for an $n = 42$ wavepacket involving approximately 5 n -states. The static field and HCP impulse are oriented antiparallel to each other. The figures at the top and bottom of the plot are the $z - x$ coordinates of the classical electron ensemble launched by the calculation. The bold curve is artificially offset by 0.05.	166
5.14	Absolute bound fraction versus time for classical calculation (bold line) and data (normal line). The static field and HCP impulse are oriented parallel to each other. This plot is for an $n = 42$ wavepacket involving approximately 5 n -states. The figures at the top and bottom of the plot are the $z - x$ coordinates of the classical electron ensemble launched by the calculation. The bold curve is artificially offset by 0.05.	167
5.15	Various time snapshots of the calculated momentum fraction that are recombined. Left Column: HCP impulse polarized antiparallel to the static field. Right Column: HCP impulse polarized parallel to the static field.	174
5.16	Upper: Sum of $n = 42$, $F = 212$ V/cm between recombination spectra obtained for the HCP impulse oriented parallel and antiparallel to the static field. Lower: Difference between the same recombination spectra.	175
5.17	Quantum mechanical stark map of d -character for H. The difference in field between each horizontal trace is 10 V/cm. The solid line is the classical field ionization limit, $1/16n^4$	182
5.18	Quantum mechanical stark map of d -character for Ca, which includes quantum defects (core effects). The difference in field between each horizontal trace is 10 V/cm. The solid line is the classical ionization limit, $1/16n^4$	183

- 6.1 A two dimensional plot of the charge distribution of a continuum wavepacket recombined to its parent ion by a HCP 10 ps after excitation. Its spatial distribution is shown after A) 10 ps, B) 15 ps, C) 47 ps, and D) 72 ps. The HCP is polarized along the $+\hat{z}$ -axis. There is no static field present in this problem. Note the highly localized charge distribution that develops in inset D. All plots are identically scaled, with the x and z axes running between ± 20000 a.u. 192
- A.1 An $n = 25, l = 2$ classical orbit (solid line). The x and y axes have the same scale. Note how highly elongated the low- l orbit appears (solid line) compared to the high- l , more circular orbit (dashed line). The nucleus is the dark dot at the focus near $(0, 0)$ 199
- A.2 The classical probability density of finding an electron at any given point along a Rydberg orbit (bold curve). The nucleus is the point on the right part of the plot. The classical trajectory is the shown in the bottom plane of the plot (normal pitch line). Notice the highly peaked density towards the left, at the outer turning point. The height scale is chosen so that the peak at the outer turning point does not completely dominate the plot, at the expense of “cropping” it as shown. 205
- A.3 Inset A: Orbit in a fictitious integration space coordinate system. Inset B: Orbit oriented with respect to a real lab coordinate system such that $m = 0$ 219
- A.4 A numerical Rydberg state. The plot shows the numerically integrated values of r_x vs. r_y for one Kepler period. 220

0.1 Acknowledgements

As a matter of life and love, I dedicate this thesis to my parents, “mom and dad.” Throughout my life, they have provided me with nothing but unconditional love and support in my endeavors, and I am deeply thankful to them for that. My father has been, as always will be the smartest man I know, for me to look up to, admire, ask questions to, and emulate as my role model. He has definitely served as my inspiration to pursue technical and scientific fields, which has given me so much to grasp onto in life. My mother is the most beautiful and caring woman. Her constant concern and love for her children is always apparent, and this love is always with me in whatever I do. She continues to give me strength and confidence. Thanks a lot mom and dad, here’s to you.

As a matter of Physics goes, I dedicate this thesis to Professor Duane Doty at California State University, in Northridge, California. From the second week of his Physics 220B class, Electricity and Magnetism, I was always dumbfounded by how much this man knows about Physics. How can one person know so much? In those early college days, I was just learning Calculus for the first time as was really fascinated with all of the new concepts I was learning. Then I walked into his E+M class, and was further amazed how he actually *used* Calculus for something! It was at this point I learned that Physics was actually a major one could choose, and I’ve been hooked ever since. I remember thinking how I wanted to be smart, just like him, and use Calculus, not just plug into formulas the way Engineering majors did (my first major choice back then). I don’t know why using Calculus played such a big role back then, maybe it was the ease in which Prof. Doty handled those “trig. substitution integrals.” In either case, thank you Prof. Doty. To me, you are that special professor every student hopes to meet in school, and you continue to serve as a inspiration to me in research, teaching, and further pursuing academics.

Working for Bob Jones over the past 3 1/2 years has been quite an lifetime experience for me. The work I did in this thesis was the most difficult I’ve ever encountered. But he motivated me to work through problems and difficulties, I think because I so enjoyed having any new results to show him (even though they were usually wrong!). I am also very grateful for the time he took to discuss things with me. Without his guidance, this thesis would simply not have been possible. Any student would be lucky to receive the personal attention I did from him during this thesis. He is truly a professional and brings the word “style” to the business of research, and I thank him for all of his teachings. I just wish he’d tell me the secret to getting such a short, perfectly Gaussian pulse out of the laser, every time! Thanks Bob.

Although many of my original graduate school classmates are gone, some off to other endeavors or labs, others “just gone,” the first two years were hard, but tolerable thanks to you. Thanks to Major Steve Bruch, for convincing me that jogging, by just throwing on some shoes and going, was an “ok” thing to do, and to his wife, Kimmie, for all of those free and delicious dinners. Thanks also to Alina “I don’t care” Cichocki for homework help, and Brian Kolo who always had the one-line answer worked out in his head to any physics problem, and was always ready to talk about homework, even (especially) at 3am!

To my best friend in Charlottesville, Fred(rik) Fatemi. I didn’t know him much during the first two years, but later in the research years, we became friends by complaining about everything and everybody to each other in sort of the same strange way that we both understood. Hope you find some good stuff at the next Y.S. (get me a TRS-80 if it’s less than \$10). Although your flannel trend definitely caught on, I don’t think your “old man retired style” (socks with sandals) ever will, although

you've been trying now for 2 years (p.s. go out and buy some tennis shoes!). In short, thanks a lot for putting up with me, and my standard "Nahh, I can't, I better to work on this." response. Best of luck at NIST and beyond.

Thanks to Nathan Tielking for helping me acclimate to the lab during my first two summers. He had a lot to do with getting me interested in lasers and atomic physics, and getting started out would have been much more difficult without his help. I have good memories of working with him in the lab. If only he didn't answer so many of my questions with the words "Well, in principle..." Thanks Nathan, and best wishes at your new job at NRL.

Thanks to Gunnar Haeffler, our visiting graduate student from Sweden. He helped out a lot during the initial stages of my first experiment, and I really enjoyed having him here in the lab. Please come back to Charlottesville, so we can enjoy a large bowl of watery pasta at the Castle snack bar. How do you spell the name of your school again? Chalmers or Chalmers?

Thanks also to Matt (my fellow lab mate), Warren (likes Windows NT for some reason), Drew, Jay, Elena, Mike N., Robert, Michael B., Lung, Matt G., and Greg (Mr. "the South" turned Mr. New England).

Finally, I thank my loving, beautiful wife Sonia. She picked her life up and moved out here when we got married, and life has been the best for me ever since. How nice it is to meet her at home each day after work, or to sneak out to 7-11 in the middle of the night for junk food with no cash, and having to charge \$1.34. Thanks for tolerating all of those weird topics and used books all over the place. Say "hi" to L.B., S.K., and L.G. for me. You're 1 in 1.0×10^6 sweetie.

Chapter 1

Introduction and Background

I find that modern atomic physics seems to exist at a convergence point between pure curiosity and high technology. It is a field driven by the pursuit of the answers to questions about very fundamental physics that perhaps may only be found using the most state-of-the-art devices in laser and optical science technology. Atomic physics lies where these two worlds meet. On the one hand it exists as a field full of traditional and fundamental research. On the other, it is strongly influenced and driven by high technology. The field itself is a good mix of the two worlds, with endless possibilities.

In this chapter, a general consensus of atomic physics, as experienced by me over the last 3-4 years of study, is given. It contains descriptions of experimental and physical systems that this thesis has been based around, and those that I enjoy discussing and learning about the most. These systems include excited-state atoms known as Rydberg atoms, ultrafast lasers and optical systems, and half-cycle pulses of radiation. It is a combination of these which have made the work and results in this thesis possible. Throughout later chapters, the properties, terms and general ideas associated with these systems are frequently and loosely used, so beginning this thesis with a discussion devoted only to them seems appropriate.

1.1 Atomic Physics

Atomic physics is a branch of physics focusing primarily on studying the interaction between an atom and an electromagnetic field. The atom itself can be almost any atom on the Periodic table. For whatever reason, some may be more convenient, or desirable than others (especially from an experimental standpoint). Others may be less convenient, but more suitable to the goal of the study. The electromagnetic field can come from a variety of sources. It may be an externally applied electromagnetic field, like that from a laser, pulse generator, spark gap, semiconductor antenna, or even blackbody radiation. It might also be a more subtle, “natural” field, like that from a passing ion, another atom nearby, or even from within the atom itself.

The interaction of an applied electromagnetic field with an atom is of fundamental importance, due to the electromagnetic structure of the atom itself. The dominant force in most atomic systems is the familiar inverse square Coulomb force, $\vec{F} = -1/r^2\hat{r}$, between a positively charged nucleus and negatively charged electron. This is the most fundamental force that “holds” atoms together. External fields enter the picture as perturbations to the naturally occurring internal fields, and we may begin to ask a very basic question: How will our atom respond to a...

...strong field, weak field, static field, changing field, high frequency field,
low frequency field, mixed frequency field, narrow bandwidth field,
high bandwidth field, etc.

The list goes on and on, but even these fields form the basis for a great amount of atomic physics research, even sub-divisions within the field. Generally speaking, the more capabilities available in creating an electromagnetic field, the more interesting and “new” atomic response might be expected. In this regard, the search for new and

unusual sources of radiation continues. So, armed with a suitable radiation source and atomic system, a study can begin. What is there to study?

The oldest type of atomic physics, and still the most fundamentally important is spectroscopy. This is a study that, at its most fundamental level, answers the question “Will this atom absorb a photon of a given frequency?” It requires irradiating atoms with photons whose frequency is known and controllable in a very precise manner. If, by a variety of means, one can ascertain that a photon of given frequency has been absorbed by the atom, immediate knowledge of the structure of the irradiated atom can be obtained. In particular, one can immediately conclude that there must be resonant structure in this atom, somehow related to the incident photon frequency. Spectroscopic information like this is typically cataloged, and forms “roadmaps” to atoms that might very well be used by other researchers in their own work, for years and years to come[4]. Some spectroscopic work like this was performed in the course of this thesis, in the initial setup of an experiment. In this case, not to reveal any energy levels of some new, unknown atom, but to calibrate and ensure that the lasers in use were working properly and predictably.

Another type of study is in the characterization of radiation sources. Atoms are systems with strong structure, and form the ideal backdrop in characterizing a radiation source whose properties are not fully understood. Relatively new, “half cycle” pulses of radiation were used in this thesis. Although previously characterized by other devices, much was learned about the fields themselves by monitoring the atomic response to them, including pulse length, amplitude, shape, and degree of polarization.

In some of the most exciting work being done today, the time-dependent response of atoms to electromagnetic fields is being studied. In general, this involves irradiating an atomic sample with a field, then monitoring the atom’s response from that point

onward in time. Radiation upsets the natural stationary state of the atom, and it will enter a non-stationary state after irradiation; this is its response. Obviously, the atom's response is strongly dependent on the applied field itself. One example includes exciting many electronic atomic states at once with a burst of radiation containing many simultaneous photons. The electronic character of the atom will now take on a non-stationary, time dependent character. In some experiments, one can watch a superposition of excited states, or wavepacket, "bounce" back and forth between the nucleus and some maximum spatial coordinate. Another example is pushing electrons around with a field that behaves like booster rockets on a satellite[1]. Time-dependent studies such as this are rich in quantum mechanics, leaving plenty of room for new thought and analysis. The experiment in Chapter 5 is based around a time dependent atomic state excited in this manner.

A push to use atoms for something other than basic research is an underlying goal in this field as well. In characterizing fields, atoms can actually be used as receivers or detectors for radiation bands currently undetectable in any efficient manner[5]. By pushing, "kicking," or exciting charge distributions in new ways, perhaps new and exotic versions of atoms can be "made" that can be used in creating new materials or in forcing different by-products of industrial chemical reactions. Indeed atomic physics remains an exciting field with much work yet to be done. After my exposure to atomic physics during this thesis, I believe that new and unique radiation sources will continue to form the cornerstone of atomic physics, and will dictate just what we will learn about atoms, and what we won't. The search for these new fields should at least in part, be a goal of atomic physics research.

1.2 Alkali Rydberg Atoms

In choosing an atomic system to study, one might ask “Why not study Hydrogen?” It is the simplest of all atoms, exactly solvable, and is typically what one would picture an atom to be: an electron with a single charge of -1 , orbiting a point-like nucleus with a charge of $+1$. In practice however, Hydrogen is not the most convenient choice. Why? Well, consider a few practical experimental issues.

First, consider the fundamental atomic process of photoexcitation, whereby an atomic electron moves from one (bound) energy state to another by the absorption of a photon. Exciting an atom in this manner is a very basic starting point in many types of experiments. The exact quantum mechanical solution predicts the energy levels of an electron in a Hydrogen atom can be found from the equation $E_n = 13.6\text{eV}/n^2$, where n is the principal quantum number of the n^{th} energy level. This means to excite the electron from its ground state ($n = 1$) to the first excited state ($n = 2$) takes a 10.2 eV photon. This is a strong photon, far in the U.V., which is generally difficult to generate in the lab, presenting a rather immediate experimental barrier.

Second, consider another fundamental process of “field ionizing” an electron, whereby an applied external field is strong enough to cause electrons to jump right off of their host atoms. This is commonly used to calibrate or probe atomic systems during a study. For an $n = 1$ state in Hydrogen, the strength of this field would be in excess of 300 Megavolts/cm. The ground state of a Hydrogen atom is very tightly bound, and a rather specialized field is a required prerequisite to *using* Hydrogen for some atomic physics study.

Third, a source of Hydrogen atoms will be needed. Typically, studying Hydrogen in the lab requires the use of fast proton beams[2]. A collision between such a beam and an atomic or molecular target will produce excited states of neutral Hydrogen

atoms, whose single electron has some final state distribution in n . A substantial amount of sophistication is needed just to generate the Hydrogen atoms, which has nothing to do with studying atomic physics itself.

These points alone make Hydrogen somewhat prohibitive for *easy* and *convenient* study. Over the course of this work, the most appealing quality of our lab environment has been that, although complicated, the apparatus always provided a pretty direct route between simply walking through the door of the lab and actually performing an atomic physics experiment. In other words, *all* of the lab time was not spent designing, testing, and maintaining, sophisticated atomic sources and containment chambers for exotic species of study. As described in Chapter 2, the apparatus is simple, yet very effective in its purpose to allow for the convenient study of atomic systems. As shown by the few points above, a lab that studies Hydrogen may not have this same practical appeal.

All is not lost, however. Looking at the periodic chart, under Hydrogen and in the same column, we find the “alkali metals.” All of these atoms are in the same column because in structure, they are very similar. The inner core of these atoms consists of k protons and neutrons, followed by $k - 1$ electrons in the filled innermost energy levels. This leads to a net core charge of $+1$. Outside of this core, they all have one outer valence electron. So they *look* a lot like Hydrogen. As for actual sources, the alkali metals are readily available in stock form from chemical supply houses, just a phone call away.

For the photoexcitation process, consider Na, an atom used in Chapter 4 of this thesis. Na has a ground state electron in a $3s$ state. Exciting this electron to the first possible excited state (the $3p_{1/2}$ level) requires a yellow, 590 nm photon, which is very easy to generate from a conventional dye laser, and is very similar in frequency to the color of Sodium street lamps (no 10.2 eV photon is needed here).

In our lab, the outer valence electron of an alkali atom is typically photoexcited to a Rydberg state, or atomic state with high principal quantum number n ($n \geq 15$ or so). These so called highly excited “Rydberg atoms”[3] are very hydrogen-like (practically the best alternative), and form a desirable atomic system to study: an outer electron of charge -1 bound to a core with net charge is $+1$.

Perhaps the most attractive feature of Rydberg atoms is their exaggerated properties, intimately tied to their large value of principal quantum number, n . Some of the more important properties exploited in this work are summarized in Table 1.1. Most of these quantities are linked to a classical picture of an atom: a classical electron in a planetary-like orbit around the nucleus. For Rydberg atoms, this classical, kinematics-based picture usually serves as a surprisingly accurate picture, considering atoms are inherently quantum mechanical.

Property	n-dependence
Binding Energy	$1/n^2$
Energy between adjacent n -states	$1/n^3$
Orbital Radius	n^2
Orbital Period	n^3
Field ionization Limit	$1/n^4$
Radiative Lifetime	n^3

Table 1.1: Some physical properties of Rydberg atoms and their dependencies on n .

Demonstrating the exaggerated properties of a Rydberg atoms, consider this comparison of an $n = 25$ Rydberg atom to an $n = 1$ Hydrogen atom:

- The Rydberg atom diameter is 625 times as large,
- it can be field ionized with an electric field 390,000 times weaker,
- and can be photoexcited to neighboring n -state with photon frequency 7,000 times smaller.

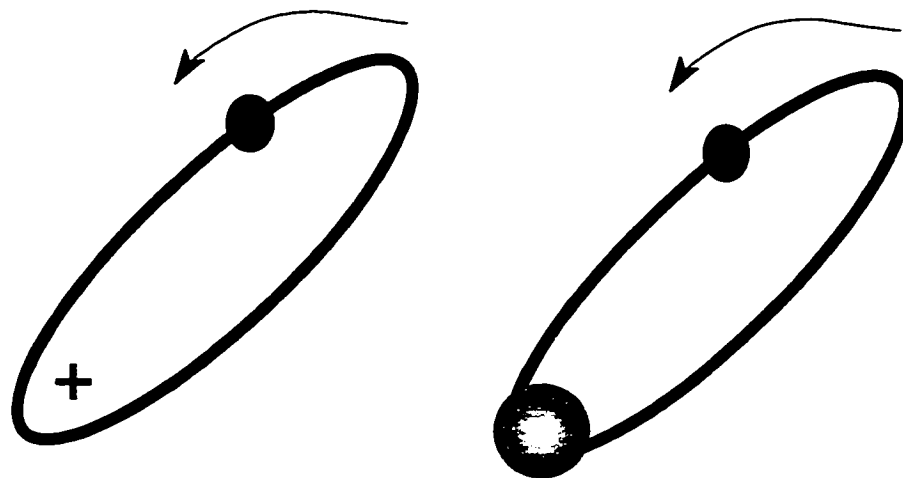


Figure 1.1: Left: The classical orbit for a highly excited, low angular momentum Hydrogen atom orbit with a point-like core. Right: The same orbit for an alkali atom, with a finite sized core.

The finite sized core of an alkali Rydberg atom, however, gives it more complicated properties, not found in Hydrogen, which has a single “point-like” proton at the nucleus. When the Rydberg electron is far from the core, it is sensitive only to the core’s net charge (+1). However, when the electron comes near the core, the finite size and structure of the core now plays a role. In particular, the core can be polarized and penetrated by the electron. For linear (s-states) or highly elongated states (p, d) the electron’s classical orbit takes it through the core, where it experiences an additional short range potential due to the excessive positive charge present. The difference between a Hydrogen and alkali atom is illustrated in Fig. 1.1, which shows identical orbits with a ideal point-like core and finite sized core.

This excess positive charge tends to increase the electron’s binding energy, or equivalently, shifts the energy levels of the electron down, compared to the equivalent state in Hydrogen. This shift in energy times n^3 is called the “quantum defect.” The

quantum defect can be thought of as a factor whose relative magnitude describes the “amount” of electron-core interaction. Table 1.2 lists

Atom	Quantum Defect, δ_l
Na	$\delta_s = 1.348$
Na	$\delta_p = 0.855$
Na	$\delta_d = 0.12$
K	$\delta_s = 2.181$
K	$\delta_p = 1.712$
K	$\delta_d = 0.27$

Table 1.2: Quantum defects for s, p, and d states of Na of K.

some quantum defects for Na and K. Note the larger quantum defects present for the lower-angular momentum states (s and p), where core interaction is more likely.

Quantum mechanically, the quantum defect manifests itself as a phase shift of the wavefunction, relative to the same wavefunction in Hydrogen. This shift is in the amount of $\pi\delta_l$, where δ_l is the quantum defect. The familiar Rydberg formula for calculating energy levels, given by $E = -1/2n^2$ is now given by $E = -1/2(n - \delta_l)^2$.

The most exciting experiments are those that take advantage of a Rydberg atom’s exaggerated properties, exploring effects otherwise impossible in lower lying, or ground state atoms. The most attractive properties are certainly their low electromagnetic transition frequencies, relatively long lifetimes, and binding fields that are conveniently approached and exceeded with common lab equipment. The “low” transition frequencies can typically be accommodated in the optical (visible) portion of the electromagnetic spectrum, making laser beam alignment and placement convenient (e.g. because you can see the beams). Long lifetimes mean Rydberg atoms are a species that will “live” long enough to be used in an experiment, in fact, they are practically eigenstates as far as most experiments are concerned. Lab accessible fields means a common lab power supplies and cheap transformers can produce fields to probe, cali-

brate, ionize and otherwise perturb a Rydberg system, to any desired degree, with the turn of a knob. For reasons like these, Rydberg atoms continue to serve as attractive systems in atomic physics research, and are used exclusively in this work.

1.3 Ultrafast Lasers

As mentioned, of fundamental importance in atomic physics is the interaction of atoms with electromagnetic fields. As one might expect, more sophisticated fields, lend to more sophisticated atomic interactions, potentially full of new and interesting physics. Currently, however, one many not simply generate any desired field. The type of field it is possible to generate depends strongly on the technology available. One can easily produce “a field” by wiring the terminals of a battery across capacitor plates, or by running a nail down the length of a metal file. But unique, interesting, controllable, reproducible, and classifiable fields are harder to generate. Further, each of these desirable field properties is usually achievable only through increased monetary investment and apparatus complexity. Nevertheless, the externally applied field, serving as the investigator’s probe into an atomic system, remains of central importance which cannot be overstated.

The work in this thesis would not have been possible without the fields produced by an “ultrafast laser system,” the fundamental laser system about which our lab operates. Ultrafast lasers are laser systems capable of producing the shortest bursts of coherent electromagnetic radiation known to man. At the time of this writing, pulses lasting 5 - 200 femtoseconds (5×10^{-15} – 200×10^{-15} seconds) are routinely generated. Our lab is routinely capable of pulses in the 120-150 fs range. To put a femtosecond pulse width in perspective, one minute is the logarithmic average between the length of one of these short laser pulses and the age of the universe[6]. There are

many characteristics of ultrafast laser pulses that make them a novel field for use in atomic physics, including high peak (Terawatt) power, small optical coherence length, and large coherent bandwidth. These are all interesting properties that deserve more discussion, however, the large coherent bandwidth supplied by an ultrafast laser pulse is the only such property used in this thesis, so it is discussed further below.

1.3.1 Broad Bandwidth and Coherent Excitation

Fourier's theorem says something short in time has a conversely broad spectrum in the frequency domain. This is manifested in the familiar expression associated with waves, that $\Delta t \Delta \nu \sim 1$. So, a short laser pulse (Δt small) must have a large spread of frequencies ($\Delta \nu$ large)[7]. The narrow, neatly shaped ultrafast Gaussian pulse, described above, is a consequence of the fact that the enormous number of frequency components in this pulse have a very specific and "locked" relationship between all of their relative phases. After all, adding a bunch of sine-waves together with no particular phase relation (e.g. incoherent light) can be achieved with a 99 cent light bulb, and is done everyday by the sun, but these sources do not produce ultrafast pulses of light. Making something meaningful in the time domain by the superposition of electromagnetic waves requires *organization* among the relative phases. The important point here is each short pulse delivered by an ultrafast laser contains an enormous spread (bandwidth) of photons frequencies, or wavelengths, in some cases as high as $\Delta \lambda = 400$ nm[8], in 100,000 different frequencies[9].

As atomic physics goes, recall the structure of a Rydberg atom discussed above. An infinite number of bound energy levels exist, the n^{th} with energy $E = -1/2n^2$. Consider a frequency doubled pulse with a bandwidth of 15 cm^{-1} and central frequency tuned near an $n = 42$ Rydberg level. The large pulse bandwidth means that a spread of electromagnetic frequencies exist about the central $n = 42$ line. In

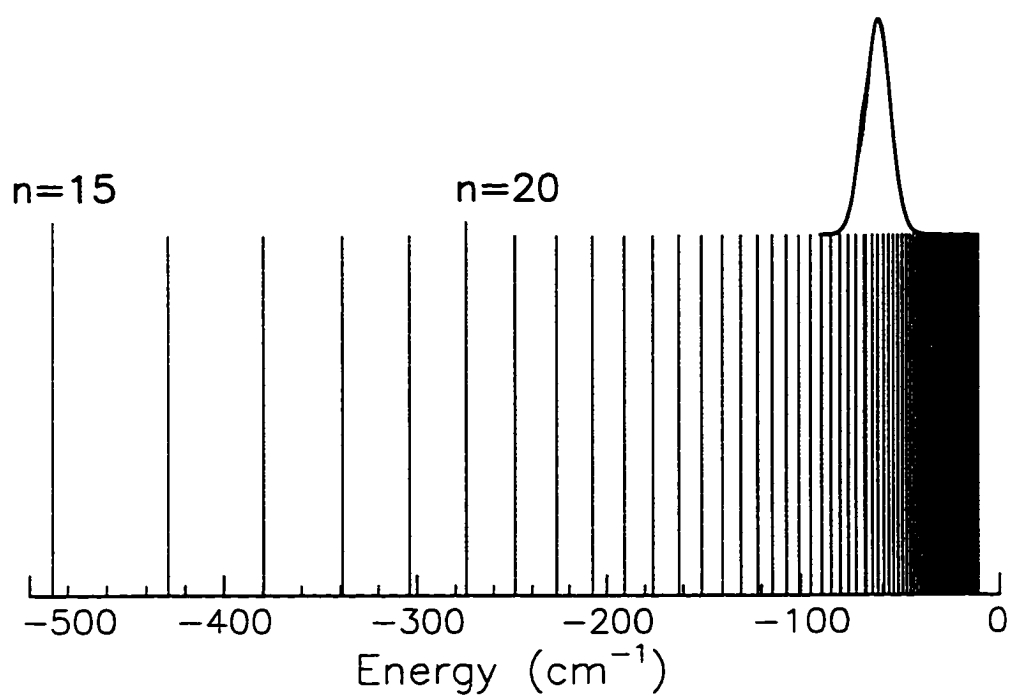


Figure 1.2: Example of coherent excitation: a Rydberg series and a 15cm^{-1} laser pulse frequency centered on $n = 42$.

fact, the author has experimentally determined that the electromagnetic frequencies in such a pulse overlaps not only the $n = 42$ resonance, but $n = 40, 41, 43,$ and 44 resonances as well. This means with each laser pulse, 5 different n -states are simultaneously excited. Because the laser field is coherent, the excited wavefunctions will be coherent as well. A schematic of this excitation process is shown in Fig. 1.2, in which a laser pulse frequency centered at $n = 42$ with 15 cm^{-1} of bandwidth is plotted against a Rydberg series. All Rydberg levels within the pulse envelope will be coherently excited.

This is a truly unique excitation process. The usual picture of electron photoexcitation is that *one* photon excites *one* electron from *one* energy level to *one* other energy level. In the case of broadband laser pulses, *many* frequencies are present, distributing the electron population from the initial energy level to *many* others, coherently. This resultant excited charge distribution is called a wavepacket, and is the motivating factor behind many studies today. The experiment described in Chapter 5 of this thesis involves an experiment with just such a wavepacket.

1.4 Half Cycle Pulse Fields

As discussed, ultrafast laser pulses are very short. But at the central frequency of the laser used in our lab, there are still tens of optical cycles of the electric field during the 100 - 150 fs envelope of the laser pulse (57 or so for a 780 nm laser pulse with a flat amplitude envelope). Technological developments over the past five years have enabled the creation of freely propagating, unipolar, "half cycle" pulses of radiation, using ultrafast laser pulses as a catalyst. The electric field for such a pulse, as a function of time, starts at zero, rises to a maximum amplitude, then returns to zero, and the pulse is done; 1/2 of a cycle. An example of a HCP field function is shown

in Fig. 1.3. Note the large dominant unipolar lobe (the HCP). The long negative tail is a field artifact of the generating process, to be described later.

The HCPs used here have a full-width half-maximum (FWHM) of approximately 500 fs (0.5 ps), are observed to be highly unipolar, and can have large field amplitudes relative to the binding fields of Rydberg states. The central frequency and bandwidth of the HCP are both approximately 0.5 THz ($\sim 15 \text{ cm}^{-1}$). Since the beginning of HCP use in studying Rydberg systems[12], a large number of experimental and theoretical studies have been stimulated. This is largely due to the unique HCP/Rydberg atom interactions. These properties are discussed below.

1.4.1 Unipolarity

Consider how a multi-cycle electric field interacts with a (nearly) free electron. The electric field, $E(t)$, exerts a time dependent force, $F(t)$, on the electron of charge q , via the familiar law $\vec{F}(t) = q\vec{E}(t)$, where in this case, $\vec{E}(t) = E_0 \cos \omega t$. As the field oscillates “up” the electron is forced up. As the field oscillates “down,” the electron is forced down. When the field leaves, the electron is left with the same momentum as it had before the field arrived. The electron simply “wiggles” with the field, with frequency ω , and returns to its initial state after the field has passed. For a nearly free electron, as is the case of a Rydberg electron at its outer turning point[14], a multicycle, optical field such as this has little or no effect. There is no net change in the momentum of the electron.

As mentioned in Section 1.2 though, Rydberg electrons with low angular momentum (d and p) states, have non-negligible interactions with the core, meaning at times, the electron is near or inside the spatial volume occupied by the core. When interacting with a multicycle field near the core, the field will now dramatically alter the initial conditions of the electron. This is due to the near proximity of the core,

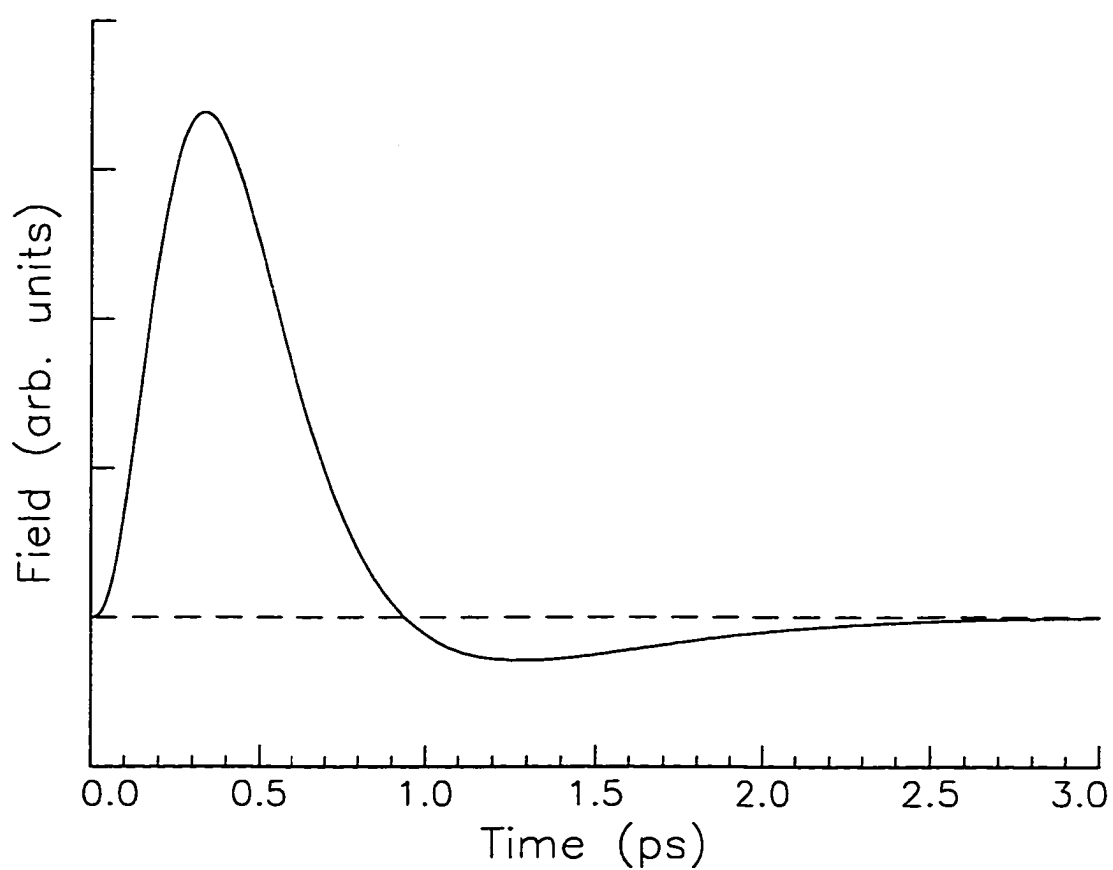


Figure 1.3: A HCP field function which closely resembles an actual HCP, as produced in the lab. Note the dominant unipolar portion of the total field. This functional form was taken from Ref. [13]

as a “third body” to and from which momentum may be transferred. Hence, in Rydberg atom studies, optical fields only interact with Rydberg electrons in the small spatial volume (≈ 1 a.u.) around the core. This is a somewhat limiting interaction, considering the large volume that an excited Rydberg electron can traverse (size $\sim n^2$ see Ref. [3], p. 5, Fig. 1.2). This is a general limiting factor for any field whose time integrated field is zero.

As mentioned, the functional form of a HCP electric field sweeps through only a half of a cycle. This means the field amplitude has the same sign over the course of the pulse’s lifetime; it is a unipolar pulse. Its time integrated field is *not* zero. Since its field amplitude has the same sign, the force it exerts on a charged particle will be in only one direction. There will be no “wiggle” up and down as in the case of an optical field. There will only be a “kick” in one direction. In effect, HCPs can transfer momentum to a Rydberg electron regardless of its location in its orbit, and herein lies their most attractive feature in studying Rydberg systems: altering the momentum distribution of a Rydberg electron, anywhere along its orbital path. This is of fundamental importance, as \vec{p} (momentum) is a very fundamental quantum mechanical quantity. There is as much physical information about a quantum system in its momentum-space wavefunction, as there is in its coordinate-space wavefunction (no information is lost in a Fourier transform); and HCPs allow us to externally alter this at will.

In practice, this momentum “kick” can even give the electron enough momentum for it to escape from the atom entirely, leading to ionization. This ionization process is very different from any seen before, and is discussed in Ref. [12]. The momentum transfer can be controlled by varying the amplitude of the HCP. Large amplitudes may certainly force the electron from the atom, leading to prompt ionization, while smaller amplitudes will result in an alteration of a electron’s momentum, leaving it

bound, but speeding it up, slowing it down, or even causing it to reverse direction. HCPs are truly marvelous fields for Rydberg atom studies.

1.4.2 Time Scales

As generated, a HCP field has a Gaussian or 1/2-sine lobe appearance, with a FWHM of approximately 0.5 ps. This time scale fits well into the interaction picture of Rydberg atoms. Time scales normally dominating Rydberg atom studies are the classical Kepler orbital period of the electron, $\tau_K = 2\pi n^3$. Some of these orbital times are list in Table 1.3.

n	Orbital Period
15	0.51 ps
20	1.2 ps
25	2.4 ps
30	4.1 ps
35	6.5 ps
40	9.7 ps

Table 1.3: Classical Kepler orbit periods for different Rydberg states.

This means for an n -state of 15 or greater, the HCP field duration is less than the orbital time of a Rydberg electron. For higher n -states, like 25, 30, and above, the HCP time scale becomes *much less* than the orbital period. In this regime, a HCP becomes an impulsive force, much like the force a swinging bat exerts an baseball. A HCP exerts an impulsive force when “hitting” a highly excited Rydberg electron.

This impulsive nature of HCP interactions has proven to be important from a resolution standpoint. Consider the quick interaction between a bat hitting a baseball. The trajectory of the ball after the interaction is almost entirely a function of the ball’s initial momentum and direction relative to the bat when struck. During the brief ball/bat interaction, the position of the ball or bat does not change appreciably.

In an impulsive HCP/electron interaction, the electron doesn't move very much either. The final state electron depends almost entirely on its initial state at the onset of the HCP, and the strength of the HCP itself. This is precisely the power of HCPs in these studies. They can serve as a probe into the momentum distribution of Rydberg electrons at the time of the interaction[15]. This is the "resolution" issue. The HCP interaction is impulsive, and information on its pre-HCP state can be seen in the results of the interaction. HCP interactions have also been examined in the non-impulsive regime ($n \leq 14$)[16], in which cases the initial state information is lost, or at least blurred.

1.4.3 Field Strengths

Finally, HCP field strengths can be laboratory controlled from zero, up to 30 kV/cm, limited only in preserving the HCP generation apparatus. With a range like this, HCPs have been used to "tear" atoms apart, kicking Rydberg electrons right off of atoms. Conversely, HCPs can gently "tickle" Rydberg charge distributions, leaving them bound, but gently displacing them, causing them to oscillate about the core, much like a mass on a spring. They have also been used to redistribute bound population about an atom[17], and probe a variety of different wavepackets[18].

1.5 Conclusions

Rydberg atoms, ultrafast lasers, and half-cycle pulses form remarkably powerful arsenal of experimental tools in the field of atomic physics, each contributing its own, unique property. In the following thesis, two experiments are presented that exclusively use these systems. The first, discussed in Chapter 4, combines two half-cycles pulses with mutually perpendicular polarizations, to produce a novel THz field that executes a 1/4-cycle of circular polarization. The ionization of Na Rydberg atoms

as a result is studied. The second experiment, discussed in Chapter 5, uses HCPs to “push” escaping electrons back onto the parent ions, from which they came. In effect, putting atoms back together with HCPs. Along the course of this thesis, extensive classical computer modeling has been performed to support and explain the data acquired in the two experiments. Appendix A will contain a detailed discussion of the techniques and implementation of these models. The next chapter, Chapter 2, will discuss the details of the lab and experimental apparatus used in this thesis.

Bibliography

- [1] Bart Noordam, *Physics World*, December 1997, p. 22 - 23.
- [2] R. F. Stebbings and F. B. Dunning, *Rydberg states of atoms and molecules*, Cambridge University Press, Cambridge, 1983, Chapter 13.
- [3] T. F. Gallagher, *Rydberg Atoms*, Cambridge University Press, 1994.
- [4] C.E. Moore, *Atomic Energy Levels*, NSRDS, 1952.
- [5] G.M. Lankhuijzen, et. al., *Phys. Rev. A.* **57**, 440 (1998); T.W. Ducas, et. al., *Appl. Phys. Lett* **35**, 382 (1979); H. Figger, et. al., *Opt. Commun.* **33**, 37 (1980); D. Kleppner and T.W. Ducas, *Bull. Am. Phys. Soc.* **21**, 600 (1976).
- [6] M. Murnane, Invited Session, American Physical Society meeting of D.A.M.O.P., Washington D.C., 1997.
- [7] Note however, that the converse *is not* true; a large electromagnetic frequency distribution does not “automatically” imply a short pulse in time.
- [8] A. Laubereau and A. Seilmeier, Ed., *Proceedings of the 7th International Symposium on Ultrafast Processes in Spectroscopy*, IOP Publishing Ltd., 1992, p. 51.
- [9] J.C. Diels, W. Rudolph, *Ultrashort Laser Pulse Phenomena*, Academic Press, 1996, p. 209.

- [10] C. C. Davis, *Lasers and Electro-Optics*, Cambridge University Press, 1996, Chapter 20.
- [11] B. Bederson and H. Walther, Ed., *Advances in ATOMIC, MOLECULAR, and OPTICAL PHYSICS*, Academic Press, 1998, Volume 38, Section II.A.2, p. 7.
- [12] R. R. Jones, D. You, P. H. Bucksbaum, *Phys. Rev. Lett.*, **70**, 1236 (1993).
- [13] A. Bugacov, et. al., *Phys. Rev. A*, **51**, 1490 (1995).
- [14] The probability of finding a Rydberg electron at some point along its classical orbit is inversely proportional to its velocity (e.g. the faster it moves through a point in space, the less probable it is to find the electron there). The outer turning point of a classical orbit is the slowest point along the orbit. Hence, a Rydberg electron is most likely to be found at its outer turning point, where any nucleus/core effects are at an absolute minimum. The electron approximately behaves as if it was free.
- [15] R. R. Jones, *Phys. Rev. Lett.*, **76**, 3927, 1996.
- [16] R. R. Jones, et. al., *Phys. Rev. A*, **51**, R2687, 1995.
- [17] N. E. Tielking and R. R. Jones, *Phys. Rev. A*, **52**, 1371, 1995.
- [18] See Ref. [15], M.B. Campbell, T.J Bensity, and R.R. Jones, *Phys. Rev. A*, in press; F. Robicheaux, *Phys. Rev. A* **56**, 4032 (1997); G.M. Lankhuijzen, F. Robicheaux, and L.D. Noordam, *Phys. Rev. Lett.* **79**, 2427 (1997); B. Broers, et. al., *Phys. Rev. A* **49**, 2498 (1994); C. Raman, et. al., *Phys. Rev. A* **55** R3995 (1997); M.T. Frey, et. al., *Phys. Rev. A* **55**, R865 (1997).

Chapter 2

Experimental Apparatus

In this chapter, the experimental apparatus and general experimental techniques used in this thesis are discussed. This chapter is written from a very practical standpoint, serving almost as a “manual” for anyone wanting to also use the equipment discussed. Some theoretical and operational background on the equipment (particularly the lasers) is given, as understanding something about how the lasers work is helpful in using them on a day to day basis. The three general topics of discussion in this chapter echo the topics introduced in Chapter 1, except here they will be presented with much more technical detail from an “in the lab” point of view. In particular,

- the operational principles of our ultrafast laser,
- the production of Rydberg atoms,
- and half-cycle pulse generation and use

are discussed.

2.1 Laser Systems

The two different laser systems used directly in this study were an ultrafast laser system and Hansch-style organic dye lasers. The ultrafast laser system itself consists

of four laser subsystems, the Ti:Sapphire-based mode locker, Argon laser, Nd:YAG laser, regenerative amplifier, and multipass amplifier. This laser system is enormously complex, and will be presented in some detail. The organic dye lasers are homemade, and contain several important design and operation techniques that will be discussed.

2.1.1 Nd:Yag Laser

Neodymium-doped yttrium aluminum garnet (Nd:YAG) serves as the active medium in this laser. In operation, two flash lamps, whose output matches the principle absorption band of neodymium, creates a population inversion in the Nd:YAG material (e.g. the "YAG rod"). The most probable lasing transition in the rod emits light at 1064 nm, the fundamental, and well known frequency of this laser. After being pumped by the flashlamps, if laser oscillation can be prevented, this inversion can build, effectively storing energy in the laser rod, much as a capacitor stores electrical charge. By design, the oscillation in the laser cavity is prevented until maximum energy build-up, or maximum population inversion is accomplished. This is by the use of a Q-switch placed near the highly reflecting mirror at the back of the laser cavity (away from the output coupler).

The Q in Q-switch stands for "quality," and is a number describing the quality or efficiency in which a (laser) cavity stores energy. A Q-switch is basically an electronically triggered switch which can change the Q-factor of a laser cavity from high to low, on demand. In this model YAG laser, when the Q-switch is open, optics in the laser cavity do not allow light to make a single round trip through the cavity; the Q-factor of the cavity is low, and it has a high losses. When the Q-switch is closed, light may begin oscillation in the laser cavity, stimulating the 1064 nm transition with each pass through the YAG rod; the Q of the cavity is relatively high. The population inversion is quickly depleted and the laser ejects a short pulse of light with high peak

power, approaching tens of megawatts, in a < 5 ns pulse. This short pulse, with high peak power permits harmonic generation in non-linear crystals situated just outside of the laser cavity, in front of the output coupler.

The 1064 nm output is invisible and is usually blocked in operation, to prevent scattering of harmful IR light throughout the lab. Frequency doubled light at 532 nm (green) and tripled light at 355 nm (blue) are output and directed towards experiments. Typically, the YAG beams are not directly used in our experiments, instead, their beams are directed into other lasers as pump sources. Any excess light is dumped.

The YAG lasers are typically used by simply turning them on, waiting for the “simmer” light to come on, then turning the “lamp energy” knob up to the maximum level. YAG laser beams deposit quite a bit of energy at objects they strike. Care should be taken when turning on the laser to be sure that unwanted beams are blocked and that the beams are not pumping dye lasers whose pumps have not been turned on yet. The “lamp energy” knob should be turned up *slowly*, while watching for the beam and any undesirable effects.

2.1.2 Argon-Ion Laser

The Argon-Ion laser is a laser which uses an ionized form of the rare gas Argon as its active medium. An Argon ion has strong emission lines in the blue-green portion of the visible spectrum. The prime attraction of Argon lasers is that they can deliver tens of watts of a continuous wave (CW) laser beam, at 514 or 488 nm. All ion lasers contain an expensive “laser tube” filled with Argon gas.

The laser is excited by a high-current discharge that passes along the length of the laser tube, and is concentrated in a small diameter hole bored in the center of the tube, creating a relatively high current density. An initial spike of a few thousand

volts[3] breaks down the gas. This drops the voltage to between 100 and 400 V, with a discharge current of 10 - 60 A. These are the numbers normally read from the black control panel set near the laser on the optics bench. These high current densities ionize the gas and provide an excitation mechanism for the ions to promote population to upper energy states, creating a population inversion. There is no Q-switching mechanism in this CW laser, and lasing begins immediately, as evident by the visible output beam present as soon as the laser is turned on. The output coupler of the laser has a Brewster cut window, preventing any light polarized parallel to the optics bench from executing laser oscillation. Hence, the Argon laser outputs a beam highly polarized perpendicular to the optics bench.

When using the laser, it should be turned on and current increased to the desired output power, typically 8 Watts, for its purpose of pumping the mode-locker. The laser should then be allowed to sit and warm up for about one-half of an hour. After that time, the power output, as reported on the command module, will have dropped significantly, and the "tune" button on the module should be pressed. Then, the two mirror alignment knobs at the rear of the laser should be turned *carefully and slowly*, while monitoring the reported output power. Adjustments in these knobs should be made until the module again reports the desired output power. Normally, a few such adjustments are needed throughout the day. The argon laser has been known to shut off abruptly in the presence of severe electrical noise from half-cycle pulse generation elsewhere in the lab, or from abrupt cooling water pressure drops. No normal, reliable operation should be expected near the end of the ion-tube's lifetime (after ≈ 3000 hours). Check the tube's lifetime periodically from the command module menus. Be careful to keep your hands out of the Argon laser beam; *it hurts*.

2.1.3 Ultrafast Laser System

The ultrashort pulses produced by this laser, and fascinating optical science that goes into the production and amplification of these pulses, remains a topic of constant interest and curiosity. They are truly remarkable lasers, rapidly evolving in the laser industry.

Ti:Sapphire Mode Locked Laser

A Titanium doped Sapphire mode locked laser, with its mysterious and bizarre principles of operation lies at the heart of ultrafast pulse generation. When in the “mode-locked” state, this laser will output a 100 fs/78 MHz train of pulses. Thinking of this laser nothing but a “black box:”

send in a power stabilized Argon pump beam in at ≈ 8 Watts, and get out a 100 fs/78 MHz pulse train.

Technology has advanced to such a level that with a mode-locked laser built and ready for use, it is *this simple* to produce such phenomenally short laser pulses. The pulse train can be easily seen in the lab by examining the output of the photodiode situated near the output coupler of the laser using an oscilloscope. A pulse train will be evident, whose pulse widths appear to be ≈ 1 ns on the oscilloscope, limited by the response time of the photodiode itself (ultrafast pulses are *fast*; much faster than response time of the Si or Ge photodiode material, and to a newcomer in the lab, this is a first observable indication of this). The 78 MHz repetition rate is the round-trip frequency of a pulse in the laser cavity, dependent on the cavity’s physical length.

A Ti:Sapphire crystal is a small, expensive crystal with remarkable properties, which serves as the active element in this laser. It is produced by introducing Ti_2O_3 into a melt of Al_2O_3 . The crystals grown from this melt have a small percentage of

the Al^{3+} ion replaced with the Ti^{3+} ion. The Ti^{3+} ion is responsible for the laser action[4]. Absorption bands in this crystal are between 400 and 600 nm, peaked near ≈ 500 nm, convenient for pumping by the Argon laser. The Argon laser pumping creates gain or a population inversion in the Ti:Sapphire crystal. The emission lines are very broad, extending from near 600 nm to above 1 μm . The lifetime of these excited states is strongly dependent on the temperature of the crystal. For stable mode locking, the crystal must be maintained at or below room temperature (so remember to turn on the cooling water before trying to run this laser). This broad emission spectrum is of fundamental importance in generating a short pulse from this laser.

Recall from Section 1.3, that a broad frequency spectrum is required to generate a pulse that is short in time. In fact, 10 fs pulses will have a bandwidth of ≈ 80 nm with a central frequency of 800 nm[9]. This is where the short pulse generation begins: the Ti:Sapphire crystal is pumped by the Argon laser, and emits a broad spectrum of light between 600 and 1000 nm. Now what about lasing action? The emitted light may now begins to traverse the laser cavity. The mode of operation of this laser is the one that finds itself the most *energy advantageous*, given the configuration of the laser[5]. This laser is configured so that the ultrafast pulses are generated via a passively mode-locked mechanism.

Since the emission of the Ti:Sapphire crystal is fairly broad in bandwidth, there are lot of frequency modes present in the cavity. Suppose an electromagnetic “spike” is introduced into the cavity by physically striking the laser, or more commonly, gently tapping the output coupler. This physical impact to the laser cavity abruptly “shakes up” the physical cavity configuration (dimensions), causing a noisy spike, in the otherwise smooth spectrum of noise present.

This spike, among a sea of flat electromagnetic noise, will appear as a pulse, with an appreciable amplitude above the noise. It will have some height and width; that is what a spike is. The properties of the spike are quickly welcomed by the laser cavity. It has a width in time, which now means its intensity is higher than anything in the cavity (intensity has an inverse time dependence). When the spike passes through the crystal, it will experience a little less absorption than components of the noise spectrum. Its basic shape is preserved by the crystal. As it continues to oscillate in the cavity, its intensity increases, and the index of the crystal begins to exhibit an intensity dependent index of refraction. This causes the crystal to behave like a positive lens, and the pulse “self-focuses” itself inside the crystal, further promoting its intensity. The pulse begins to exceed the oscillation threshold of the laser cavity, and it begins to sweep gain out of the crystal. This focused pulse is better mode matched to the cavity construction, and an ultrafast laser pulse is born.

The short, high intensity pulse is the most energy advantageous configuration for radiation in the cavity. The broadband gain of the crystal is able to amplify all (frequency) components of the short pulse through lasing action. The result is a 78 MHz pulse train of 100 fs pulses. Each pulse has an energy of about 1 nJ.

An intensity dependent index of refraction is not confined only to the crystal itself. At the pulse intensities involved, all materials demonstrate this effect at some level (lenses, mirrors, windows, etc.). Further, a broadband pulse is comprised of several, phase coherent frequency components. Each frequency component experiences a slightly different index in any material, a consequence of the general dependence of index on frequency. The temporal shape of the short pulse is highly dependent on the fixed and coherent phase relationship between its frequency components. As this pulse passes through the crystal, or even different optics, self-phase modulation, or group velocity dispersion (GVD) can occur, severely distorting the temporal profile

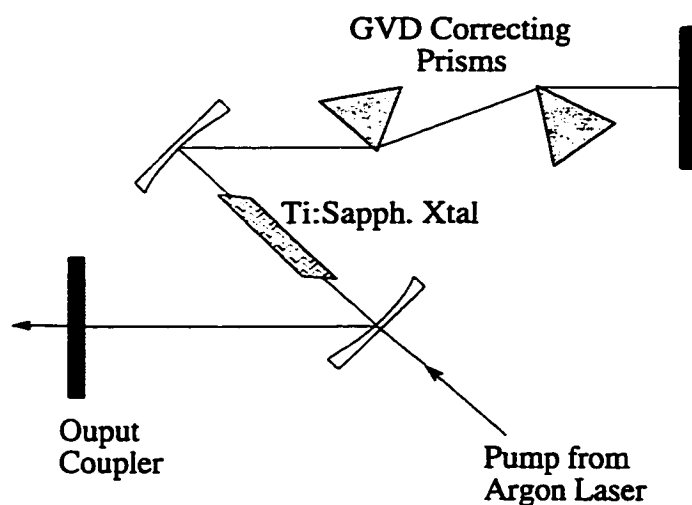


Figure 2.1: A sketch of a Ti:Sapphire based mode locker, adapted from reference [6]

of the pulse. The linear form of this effect is reversible and is the reason for the prism pair found in the cavity of the mode-locker: to correct for this dispersion or self-phase modulation, as the intense, broadband pulse traverses the crystal. A sketch illustrating these principles is shown in Fig. 2.1. It shows the Ti:Sapphire rod, pump beam, GVD correcting prisms, and cavity mirrors.

As mentioned, the raw pulse energy output from the mode-locker is small, about 1 nJ. At the 78 MHz rate of the pulse train, the power delivered is ≈ 100 mW. This is fine for some applications, but the YAG lasers run at only 15 Hz, so short pulses, synchronized to this rate, will be needed. For this, pulses are extracted from the 78 MHz train only at 15 Hz, as needed by the rest of the laser system; all other pulses are discarded. So, a 1 nJ pulse will be extracted from the pulse train every 15th of a second, which must be amplified before use. This optical amplification is the purpose of the pulse expander, compressor, regenerative and multi-pass amplifiers.

Pulse Expansion and Compression

Before pulse amplification can begin, two particular properties of these pulses must be emphasized:

- The pulses are short, and will reach very high intensities after amplification, and
- the intense pulses will be severely distorted through self-phase modulation as they interact with various materials and optics.

These properties are made worse by the fact that the Ti:Sapphire crystals are small; their polished faces through which pulses are passed, have an area of about 20 mm². The beams must be kept small to ensure clean passage without clipping or diffraction on the crystal edges. Should a pulse of this spot size and intensity be amplified, it would almost surely destroy the (expensive) optics it interacts with, and otherwise be completely destroyed by the effects of phase modulation. For this reason, the pulse is reversibly “stretched” in time by a factor of 2000 times its original width. After expansion, the pulse can be safely amplified, with the undesirable effects mentioned above minimized. After amplification, the pulse is then compressed back to its original temporal width. What exists now is the identical pulse output from the mode locker, carrying about 10⁷ times the energy.

The pulse expander exploits the fact that different frequencies will diffract from a grating at an angle related to their wavelength, λ . To first order, this angle, θ , is given by $2d\sin\theta = \lambda$, where d is the groove spacing. If a broadband laser pulse is incident upon a grating, its frequency components can be temporally “chirped” upon interacting with the grating. A chirped pulse is one that has a time-dependent frequency spectrum, as does the “chirp” produced by a bird or cricket. This means, as

a function of time and geometrical beam layout, the red (lower) frequency components of the pulse will arrive sooner than the blue (higher) frequency components. In practice, this is done with a diffraction grating pair with a telescope in between. The grating initially disperses the light, and the telescope sets up a purely geometrical path difference that the extrema of the dispersed frequencies must follow through the expander optics. The eventual exit beam is chirped and ready to be safely amplified.

In our lab, the expander is built with only a single grating, and is a “folded” version of a double grating expander. The injected pulse strikes the grating four times before exiting, expanding it temporally by a factor of ≈ 2000 . A retroreflecting mirror in the system introduces a slight level shift along the optical path of the expanding beam, eventually expelling the expanded beam from the system. Two apertures are provided to align the incoming beam properly into the expander each time the laser is prepared for use.

The diffractive effects of the expander are primarily first order, so they are linear and reversible. After amplification, the pulse is sent through a compressor, which is functionally the inverse of the expander, so it cancels the temporal chirp. In this laser system, the “grating angle” is approximately 54 degrees. For additional pulse shaping, a retro-mirror pair in the compressor is mounted on a translation stage. Translating the retro mirror increases or decreases the effective time the frequency components have to “align” in time as they are compressed. Ideal compression occurs when the compressed pulse has zero temporal chirp, and the dimensions of the compressor exactly match that of the expander. Beam drifts and the fact that such precise alignment is impossible makes translation stage a necessary “fine tuning” control.

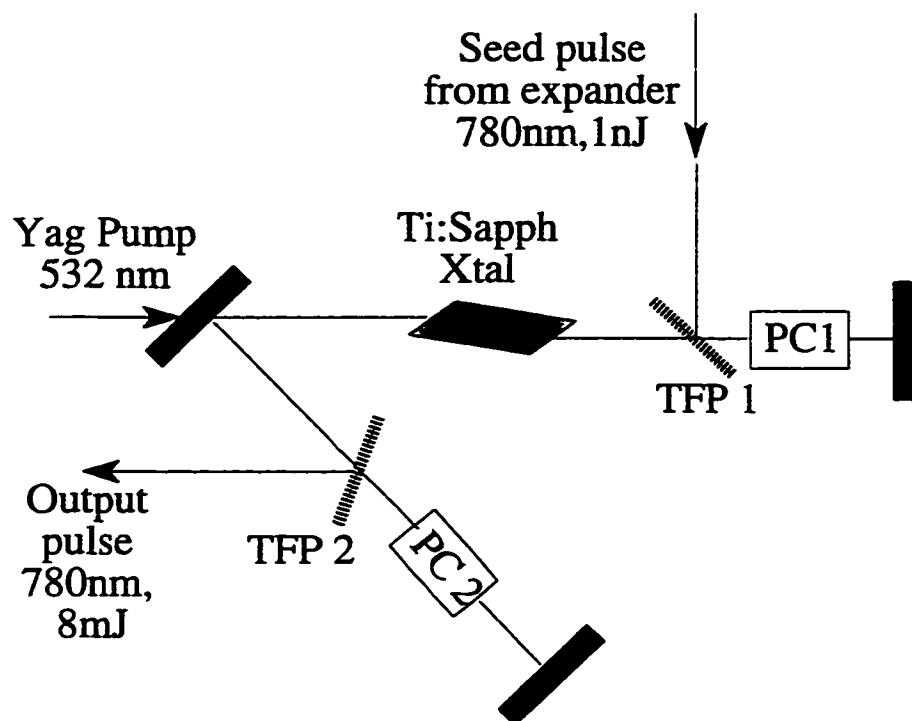


Figure 2.2: A schematic of the regenerative amplifier.

Regenerative Amplifier

Between the expansion and compression stages, the expanded pulse is amplified by the regenerative amplifier (RA). The RA is really just another laser itself. It has two mirrors, a dual Q-switch mechanism, and an active gain medium, which is another Ti:Sapphire crystal. The dual Q-switch mechanism is similar in operation to that inside the YAG cavity. Its operation goes as follows, with the aid of Fig. 2.2.

The second harmonic output from a YAG beam, at 532 nm pumps the RA's Ti:Sapphire crystal. The YAG pump energy is about 40 mJ, not to be exceeded for fear of damaging the crystal during the amplification process. The YAG harmonic at 532 nm is well within the absorption band of the crystal, and a population inversion,

or gain, is created in the crystal. A Pockels cell (PC1) and thin film polarizer (TFP 1) pair sits at the beam input to the RA. In this pair's configuration, if a voltage is applied to the Pockels cell, an injected pulse will pass through the TFP and into the RA cavity. Initially, this is the case, and an expanded pulse is injected into the RA. The "A" time, as set on the Stanford Research Systems (SRS) timing box near the RA tells when the voltage on the input PC will be turned off, blocking any additional pulses from entering the cavity, and locking the current pulse in the cavity.

The injected pulse, or "seed" pulse begins to traverse the carefully aligned RA cavity, sweeping gain out of the Ti:Sapphire crystal with each pass through it. A thin film polarizer TFP 2, and Pockels Cell PC2 at the other end of the RA cavity serve to switch the pulse out of the cavity at the time set by the "D" time on the same SRS timing box. At a typical setting, the A time is set at ≈ 40 ns and the D time at ≈ 220 ns. This traps a pulse in the cavity for ≈ 180 ns, allowing a pulse to make about 20 round trips through the cavity. A photodiode monitors the small amount of radiation that leaks through one of the highly reflecting mirrors that bounds the RA. The gradual pulse amplification can be seen by monitoring the photodiode's output signal on an oscilloscope, which shows a series of pulses, each increasing in amplitude. The amplitudes of the pulses are contained by an envelope approximating the gain curve of the RA. Ideally, the amplified pulse is switched out of the cavity at a time where it has reached the saturation point of the gain curve. This greatly improves the output pulse's stability, making it a function purely of the YAG's input pump power. The optics bench and crystal are temperature controlled, as slight temperature changes during the day greatly effect the precise alignment of the RA.

Setting up the RA typically goes as follows. Be sure the seed pulse is blocked. The YAG pump power is set at about 15 mJ, the approximate lasing threshold of the RA. This power can be read directly off of the GCR power meter which should be nearby.

At this low setting, the D time must be increased by several microseconds, trapping the maximum amount of Ti:Sapphire crystal fluorescence in the RA cavity. Watch the TV monitor, showing the output of a CCD camera that is aimed at the inside face of one of the RA's highly reflecting cavity mirrors. While watching, slowly and carefully turn one of the two alignment knobs on that mirror. Only turn one knob at a time, and don't turn either one too far from where you found it. At some point, you should see a bright spot appear on the TV monitor. When this happens the RA is lasing. The spot is crystal fluorescence traversing the RA cavity. This is a condition where the two RA mirrors, crystal, PCs, and TFPs all precisely interact with radiation such that it all remains along a single line through the cavity. Maximize the brightness of the spot by making small additional adjustments of the mirror's alignment. At this point, remove the additional time from the D setting of the timing box. Next, increase the YAG pump power to about 40 mJ. The RA is now ready for use, and the seed light may be unblocked.

If you are unable to find the bright spot on the TV camera after very slight adjustments to the mirror, try increasing the YAG power by a small amount (0.1 W or so). Also, be sure the D time has been moved out. Getting the RA to lase is like falling off a log. If you are taking too much time, or adjusting things too much, something is wrong and you should get help. Don't just sit there randomly turning knobs, and only turn one knob at a time.

At optimal performance, the RA will have an energy gain of about 10^7 . Ultrashort pulses will be delivered from it at 15 Hz/0.08 Watts. This corresponds to a pulse energy of about 5 mJ/pulse.

Multipass Amplifier

Following amplification by the regenerative amplifier, additional pulse amplification is performed by the multipass amplifier. This amplifier is essentially similar to the RA, except there are no Pockels Cell/Thin Film Polarizer pairs. A pulse passes through still another YAG pumped Ti:Sapphire crystal three times (passes). This amplifier has a gain of ≈ 10 , and brings the total laser power up to ≈ 0.60 W, or a pulse energy up to 40 mJ. The multipass amplifier needs little day to day attention, and can be used or unused in the grand scheme by simply unblocking or blocking the YAG pump beam. The multipass amplifier also adds quite a bit of “tunability” to the final output power of the laser system. A half-wave plate regulates the amount of YAG pump light into the crystal, hence the overall amplifier gain. This is contrasted to the regenerative amplifier that has a fixed gain. Final output powers of the laser can range between 0.08 Watts and 0.6 Watts. The crystal in this amplifier is temperature controlled as well.

2.1.4 Dye Lasers

In exciting Rydberg states, a variety of optical frequencies are needed for any number of transitions that may be required. To excite a pure Rydberg state, a laser whose bandwidth is narrower than the Rydberg resonance separation is desired. For this reason, different harmonics of the YAG laser are used to pump organic dye lasers, which are capable of producing tunable light over practically the entire visible spectrum, depending on what dye is used in the laser. Exact resonance lines required will be discussed in the later chapters.

At the first level, one begins by selecting dye from a list of cataloged dyes offered by a variety of companies. The minimum and maximum wavelengths in the dye's gain profile will be given. Usually, it is not hard to find a dye that can generate

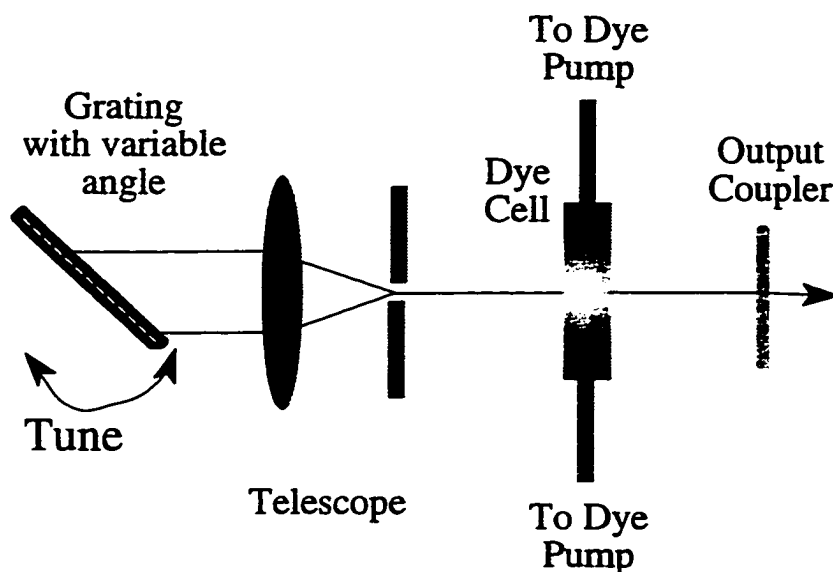


Figure 2.3: The basic design and components of a Hansch-style dye laser.

the wavelength desired. Typically the raw laser dye exists in a powder form, to be dissolved in a suitable solvent, typically methanol or ethylene glycol. Concentrations vary, depending on the dye. Hansch-style dye lasers are used exclusively in this work, and will be discussed. In a Hansch-style dye laser, as illustrated in Fig. 2.3, the organic dye is pumped through a “dye cell,” which is a quartz cuvet with 3/8 inch glass tubes blown onto the top and bottom. This dye cell, with liquid flowing, serves as the active medium for this laser. Tygon tubing is clamped to the tubes, which runs to the dye pump and reservoir.

Depending on the dye itself, a given harmonic of the YAG will be absorbed. This absorption causes the dye to fluoresce at all wavelengths within its gain profile, as cataloged by the manufacturer. The dye cell is pumped from the side, perpendicular to the laser cavity, by a YAG beam sent through a cylindrical lens. The cylindrical lens focuses the pump light to a line, to create a linear lasing source in the cavity. It is important to ensure that the focal point of the pump light is inside the dye cell,

not on the quartz surface itself, where it can cause the cuvet to crack.

Fluorescence from the dye cell travels along the axis of the cavity, enlarged by a telescope before striking a diffraction grating at one end of the cavity. The other side of the cavity is an output coupler, allowing some light to escape as the output laser beam. Beyond this output coupler, another dye cell and pump beam may be used for additional pulse amplification.

The grating serves as the tuning element of the laser, retroreflecting only a portion of incident fluorescence spectrum back into the laser cavity. The rest of the spectrum can be seen reflecting around the room or ceiling, depending on the grating's orientation. Care must be taken to block these unwanted reflections. The retroreflected light serves as the operating frequency of the laser. Typically, the bandwidth of such a laser is $< 1 \text{ cm}^{-1}$.

A few practical notes regarding the use and operation of these lasers might help diagnosing these lasers a bit easier.

- Be sure the dye pump is on and circulating the dye before turning the YAG pump beam on.
- When using the laser, look at the dye cell once in a while (from far above) and examine the penetration length of the pump light going into the dye. If the pump light seems to be penetrating more than 3 mm or so, it might be time to replace the dye. Dyes have a finite lifetime, depending on use and dye type. To increase the lifetime of the dyes (some are rather expensive), you should always block if you aren't going to be using them (e.g. during lunch, etc.).
- Of critical importance, is to ensure the dye laser is working at all. This is most conveniently done by using an appropriately coated etalon (blue for blue dyes, yellow for reddish and yellow dyes). Send the output of the dye laser through a

diverging lens, and then through the etalon. If the dye laser is working properly, it should be easy to observe a circular interference pattern on a white card or paper behind the etalon. Slight adjustments to any and all dye laser optics should allow one to improve this interference pattern. If the thickness of the etalon is known, the bandwidth of the dye laser can be estimated from the interference maxima and minima spacing, given that the free-spectral range of an etalon is given by $1/2nd$, where n is the index of refraction of the etalon material, typically 1.5, and d is the thickness of the etalon. A test like this should be repeated periodically, and helps to prevent your dye laser from acting like a “flashlight.” Tuning the laser while observing the etalon fringes (by turning the diffraction grating), should cause the interference pattern to smoothly move through itself—light to dark, and dark to light, etc.

- Intensity fluctuations in the dye laser output may be due to the YAG pump beam. Perhaps the YAG flashlamps need to be replaced. More commonly, air bubbles in the dye cell have the same effect. Try slowing the dye pump speed and checking your Tygon tubing for leaks and drips (e.g. see if there is a puddle of dye all over the floor). And remember to check the pump beam’s penetration depth into the dye itself.
- Laser dye is toxic and hazardous. Always wear latex gloves when handling it, and be careful not to splash/spill it.

It is very important that dye lasers are tuned and performing as well as possible, as they provide the critical atomic excitation step in most experiments. Keep an etalon around, or always know where you can get one.

2.2 Rydberg Atom Production

Having working, properly aligned, tunable dye lasers available, one is ready to produce Rydberg atoms. Aligning an atomic beam and dye laser beams such that they intersect, creates an “atom/radiation” mix at the interaction volume. If the dye laser frequencies are appropriately tuned, the atoms will absorb photons from the laser beams, becoming excited species. Rydberg atom production is typically a multi-step process, from the ground state to an intermediate state, then to the final Rydberg state. Each step in the process is a single photon transition. This means each dye laser will typically be responsible for causing a single photon transition. There is a nice lesson in this:

the relative intensities, construction, optics, and operating principles associated with our homemade dye lasers give us some feeling for what type of device is needed to stimulate a controlled, coherent, and predictable single photon transition in nature.

Since a photon carries 1 unit of angular momentum, each step in such an excitation process will take the atom to an angular momentum state differing from its current one by ± 1 . Further, the excitation sequence typically involves one or more intermediate states, which have a very short lifetime, perhaps only a few nanoseconds. For this reason, dye laser beams must be carefully positioned so that the next (2nd, 3rd, etc.) excitation step can occur before the intermediate state has de-excited. Typically, this means the different dye laser pulses must arrive at the atomic beam within 1 nanosecond of each other. This careful timing can be accomplished using a fast photodiode (≈ 0.9 ns rise time), oscilloscope, and the rule of thumb that light travels about 1 foot every nanosecond.

The Thor-lab photodiodes in our lab are very sensitive and can pick up the presence of laser beams reflecting off of nearby optics (e.g. so don't place the photodiode directly in the dye laser beam). Position the photodiode so it "looks at" an optic that all dye laser beams visit (usually reflections off of the entrance window to the vacuum chamber are best for this). By monitoring the photodiode's response with an oscilloscope, it is possible to observe a voltage peak from each dye laser pulse on a single oscilloscope trace, yielding precise timing intervals between the pulses. For a timing check like this, be sure the oscilloscope channel used does not have a bandwidth limit set on it. If there is a bandwidth limit, Fourier components of the input signal will be truncated, and it will be impossible to resolve two separate laser pulses separated by only a couple of nanoseconds.

Once each dye laser pulse can be independently observed on an oscilloscope trace, the beam-routing optics, or even the lasers themselves, should be moved until each pulse arrives within one pulse width or so of the preceding one. The "foot per nanosecond" rule helps in initial optics layout. Precise timing is done later by making small changes to beam paths. On the oscilloscope trace, the pulses should look like one large pulse, with small time-lags between the individual pulse peaks.

Consider exciting Na to a Rydberg state. In this excitation scheme, the 3s ground state is excited to the $3p_{1/2}$ state by the absorption of a single 590 nm photon, from a dye laser using Rhodamine-610. Note the s to p transition with the absorption of a single photon. Within 1 ns of this initial excitation, a second, blue photon, at approximately 410 nm arrives from a dye laser using Stibene-1. From the $3p_{1/2}$ state, a transition to an s or d state are possible (both s and d are 1 unit of angular momentum away from the intermediate p state). In practice, s and d states are distinctly observable in a Na spectroscopic study. After the 2nd dye laser pulse, the Na-atom is left in a nd Rydberg state, for $n \geq 15$ or so, depending on the tuning

(grating angle) of the Rydberg laser.

The existence of a Rydberg state can be verified. Within $1\mu s$ after the dye laser pulses have passed, a positive high voltage pulsed field can be applied to the bottom plate of the interaction region. Using a $\times 100$ transformer, pulsed fields up to 6000 V/cm are possible. A field of this magnitude can ionize a Rydberg state with $n \geq 15$, sending a stream of charged ions into our detector, which can be picked off directly by an oscilloscope. The classical limit for ionization occurs at $1/16n^4$ (a.u). If there is no signal with the application of such a pulsed field, then there must not be any Rydberg population present. Problems of this nature can be hard to figure out, but are most likely solved by checking the timing of the dye laser pulse arrivals, and the tuned frequencies of the dye lasers themselves.

Initial Rydberg atom production can be difficult the very first time in an experiment is set up. Typically, in a two step excitation process, the “Rydberg laser” (2nd laser) is set to the highest possible frequency for the current diffracted order, and within the dye laser gain (e.g. be sure the laser is still lasing—the grating angle can’t just be turned as far as it will go). This high frequency is found by tuning the grating angle of the laser such that higher frequencies are diffracted back into the laser cavity (e.g. recall the diffraction grating equation, from section 2.1.4). Smaller wavelengths diffract off at smaller angles with respect to the normal. In this “maximum frequency” configuration, the 2nd laser will typically be capable of exciting a very high n -state (40 or higher). If this state is created, a large static field applied to the field plates will certainly be able to ionize the Rydberg state, giving a detectable signal level. The initial set up process is now reduced to “scanning” the frequency (grating angle) of the 1st laser through its gain profile until a signal is generated. The whole process is like “falling off of a log.” If it doesn’t all happen after a little time, something major must be wrong. It is quite exciting when a signal suddenly pops up

on the oscilloscope. When this happens, congratulations: you're producing Rydberg atoms.

2.3 Half Cycle Pulse (HCP) Generation

Designing switches for high voltages, even like those for the 120 VAC in a house, is a tricky business. When the switch is in the process of being closed, the two contacts, one a high potential, the other at ground, are brought into close proximity, then forced together, closing the switch. At the close proximity point, there is undoubtedly a spark or electrical breakdown, when the field between the two contacts, exceeds the breakdown constant of air. Radiation is even emitted, as there are, after all, accelerated charges in such a breakdown. This is why rapidly turning off and on a wall switch can cause interference on nearby televisions (at least on my old television). Relays are even clumsier versions of switches. The author knows firsthand how relay contacts breakdown when switching 120 VAC. Large, blue sparks can be seen. It is precisely this breakdown, or transient effect, at the onset of a switch closure, that is the principle behind the generation of half cycle pulses of radiation.

Gallium Arsenide (GaAs) has a bandgap of about 1.4 eV, or the energy of photon with a wavelength of 880 nm photon[10]. This means, an energy gap of about 1.4 eV separates electrons in the valence band from being in the conduction band. A material with electrons in the valence band does not conduct very well (it has a very large resistance, $\approx 10^9 \Omega/cm$ [8]). But a material with electrons in the conduction band conducts, or its resistance can become orders of magnitude lower than the previous case. The band in between is called the "forbidden band." [11], and in the case of GaAs, the relatively small gap size means GaAs is a semiconductor, and an input energy input of 1.4 eV will cause it to conduct. In our optics-based lab, this

makes GaAs an ideal candidate for an optical or photoconductive switch. The central frequency of our ultrafast laser system is about 780 nm. This means a pulse of light from our laser can effectively “turn on” a piece of GaAs, transforming it from an insulating state to a conducting state, or more correctly, cause its effective resistance to drop by several orders of magnitude.

In generating HCPs, the GaAs is biased with a high voltage source. Afterwards, it is bathed in 780 nm light from the ultrafast laser system. The laser pulse is fast, on and off in 150 fs. While the pulse is on, the resistance of the GaAs drops several orders of magnitude, and the high voltage bias forces a current through the GaAs. As the charges in this current accelerate, they radiate. The radiation field is in the form of a large half-cycle, THz (submillimeter band) unipolar lobe, during the first 1 ps of the total field. This process is illustrated in Fig. 2.4. The ultrafast pulse is gone long before the GaAs turns off again, returning to its semiconducting state. As the wafer begins to turn off, the electrons decelerate. This deceleration causes a long tail to follow the main HCP lobe, with opposite field polarity (see Fig. 1.3). Imperfect transmission of the THz field through the wafer causes a large “reflection” peak to appear in the total field about 11 ps after the main lobe. An index of refraction of about 3.6 can be calculated given this 11 ps arrival of a field traveling through 0.5 mm of GaAs. Generating these subpicosecond (0.5 ps FWHM) HCPs in practice requires the following:

GaAs Wafers. GaAs wafers are purchased from American Xtals Corp. in 2 inch diameter circular form for about \$90 each. From this, four quadrants are cut, then sized to be $\approx 2 \text{ cm} \times 2 \text{ cm}$ rectangles, about 0.5 mm thick. Conductive silver paint is used to paint electrodes on the top and bottom of the wafer. A thin line is painted along the top and bottom edges of the wafer. The two

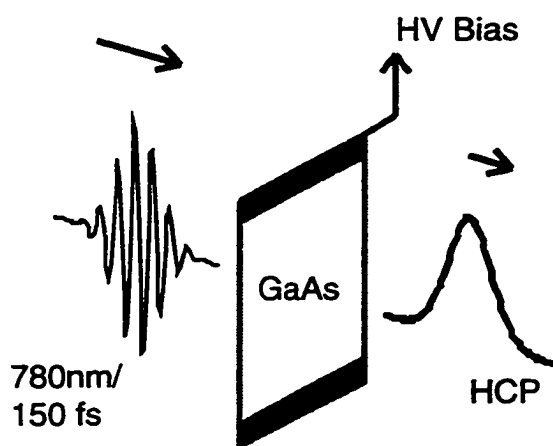


Figure 2.4: Generating a THz HCP of radiation.

conducting lines are separated by approximately 2.0 cm and are painted on opposite sides of the wafer. The wafers are mounted in a variety of ways, most commonly by using the adhesive properties of wet silver paint to “glue” them to a thin aluminum mount. Stripped ends of high voltage wire are then painted to the top and bottom stripes for external connection. This whole process is somewhat messy and unrefined, but it works.

High Voltage Bias. A high voltage bias source is needed. Our bias method charges up a capacitor with 0 - 60 V. Upon electronic trigger, the capacitor’s charge is dumped by an SCR, through an automobile transformer, producing an approximately $\times 100$ output pulse, lasting about $10\mu s$ at peak. This pulse is effectively DC as far as the GaAs photoconducting process is concerned. The peak in the high voltage pulse is timed to coincide with the 780 nm light striking the wafer.

Switch Light. As mentioned, the wafers are about $2\text{ cm} \times 2\text{ cm}$. The pulses from the ultrafast laser (red light) have a beam diameter of $\approx 1\text{ cm}$. It is important

for the preservation of the wafer itself to illuminate it wholly and as uniformly as possible. This means, the red light must be greatly expanded to bathe the entire wafer. A simple telescope, made up of a diverging then converging lens is commonly used for this purpose. The final expanded beam diameter of the red light should be approximately twice that of the wafer itself. The beam is aligned such that the wafer sits at the center of the expanded beam. This can be verified by observing the unimpeded red light on a white piece of paper at some position after the wafer assembly. The input power of the red light is of importance as well, and the total amount of THz generated does not increase in proportion to the power of the red light, past a certain point. The amount of atomic signal generated by a HCP should be optimized as a function of 780 nm light power in any experiment. Recall the power of the red light can be controlled at the multipass amplifier stage (see Section 2.1.3). The wavefront curvature of the THz field produced will mimic that of the switch light.

Collimating Optics. Very near to the mounted GaAs wafer is a large 2" gold parabolic mirror, with a focal point of about 20 cm. This mirror collects the generated radiation before it travels too far from the generating wafer, and lightly focuses it into the interaction region.

2.4 Vacuum System, etc.

Our experiments take place in a vacuum chamber, with a background pressure of about 10^{-6} torr. There are several subsystems involved in the vacuum system to be discussed below. When the vacuum is set up and working, several standard components that drive the experiment are assembled inside of it, which are also discussed below. Fig. 2.5 is included to illustrate how these components all come together.

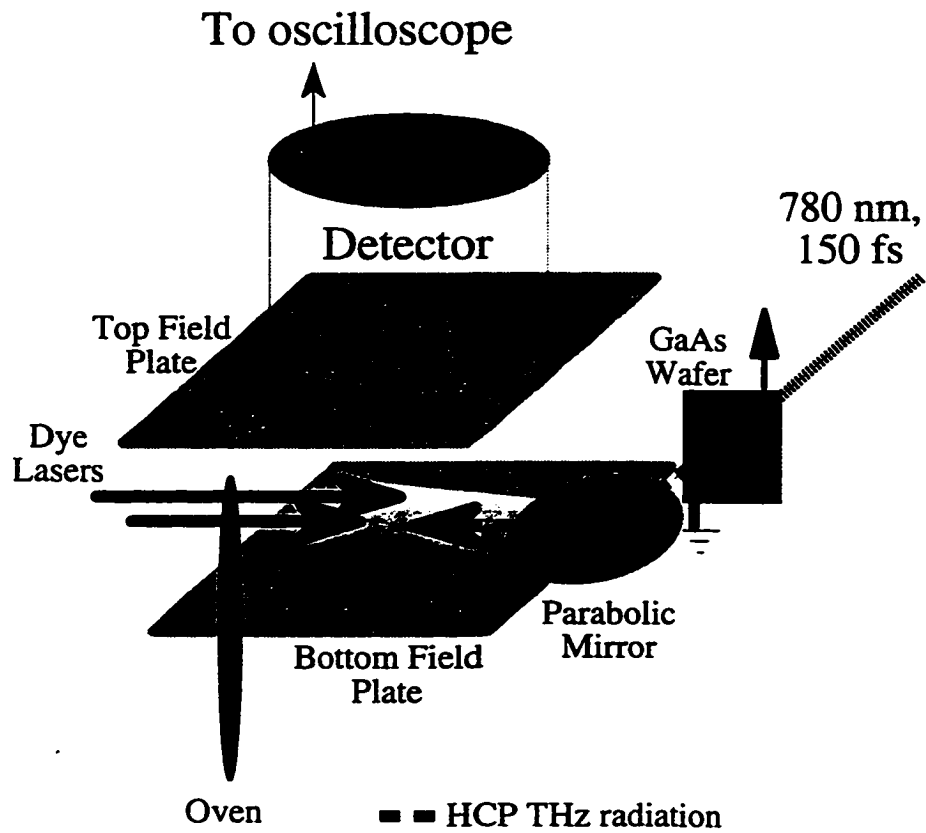


Figure 2.5: Experimental components, as assembled inside of the vacuum system.

Vacuum Chamber. This is a large cylindrical aluminum tank about 1'10" in diameter by 1' high. It has many ports on it for laser beam windows, electrical and mechanical feedthroughs, and a ionization gauge controller. All seals between the inner vacuum and atmosphere are made with Buna-type o-rings for easy installation and removal.

Diffusion Pump. This is a 1200 Watt, oil based diffusion pump, connected directly to the bottom of the vacuum chamber. A heater at the bottom of the pump heats a reservoir of oil poured directly into the pump enclosure. The heat creates an oil vapor above the reservoir, filling the remaining volume of the pump. Residual gas in the vacuum chamber is caught in the oil vapor, and exhausted by the mechanical roughing pump through the diffusion pump's foreline. The top of the diffusion pump is at the lowest pressure in the entire vacuum, typically $< 10^{-6}$ torr. In other words, all residual background particles in the vacuum are forced towards this low pressure region. Between the diffusion pump and chamber are a cold trap and gate valve. The cold trap prevents oil vapor from the diffusion pump from entering the vacuum system. The gate valve allows for total isolation between the chamber and diffusion pump, and is kept open during normal vacuum operation.

Ionization Gauge. This is the device that glows like a lightbulb on the side of the chamber, and is responsible for reporting the pressure inside the vacuum chamber. Inside the glass housing, electrons emitted by the hot filament are accelerated to the grid which is at positive potential with respect to the filament. These electrons collide with any gas molecules present. These collisions produce positive ions which are attracted by the collector and recorded as an "ion current." This current is related to the pressure in the chamber.

Vacuum Interlock. There are certain fire dangers associated with the 1200 W constantly being dumped into heating the diffusion pump oil. For this reason, a vacuum interlock system is a part of the total vacuum system. The heart of such an interlock system is a large, high current relay which can turn the diffusion pump heater on or off. The coils of the relay can be de-energized, turning off the diffusion pump, if certain conditions exist:

- Loss of cooling water. If the water in the building goes out, the water cooled diffusion pump can start to get very hot. A temperature switch physically touching the pump will de-energize the relay coils if the temperature of the pump exceeds 150 degrees C.
- Overpressure. If there is some air leak in the chamber, the diffusion pump's capacity can be overloaded. A thermocouple located on the pump's fore-line. If the pressure here exceed 150 mTorr, the relay that provides power to the heater will de-energize, shutting off the pump. This set point value is electronically set on the Varian ionization gauge controller unit.
- Loss of lab power. If the power is lost in the lab, obviously everything else will be off too, however should the power come back on, perhaps the diffusion pump heater should not automatically turn itself back on. The lab and vacuum system should be checked for problems *more* than just a power outage. For this reason, the vacuum interlock also prevents the diffusion pump heater from restarting unless manually restarted.

Interaction Region. This defines the region where the atomic beam, lasers, and any other fields will interact. Typically, two 7.5 cm × 7.5 cm × 0.5 cm thick aluminum plates, separated by non-conducting Teflon stand offs, define the

interaction region. The atomic beam and laser beams are aimed at the center of these plates. Electrical contacts are made independently from each plate to an electrical feedthrough to the outside. This allows for the application of any type of field or voltage pulse to each plate independently. A small hole or slit in the top plate allows for the passage of charged particles out of the interaction region into the detector.

Ion Detector. The only types of particles our lab is capable of detecting are charged particles. There is no mechanism in place for the direct observation of neutral atoms. An atomic physics lab still works though, because charged particles are created in a variety of ways as a result of atom/field interactions. The physics behind the interaction can typically be extrapolated back to the neutral, based solely on its break-up (e.g. charged particle creation). However, the raw ions or electrons created in such an interaction are far too few to produce any measurable signal; amplification is needed.

The ion detector used here is a cylindrical unit that sits on top of the upper interaction region plate. Any ions created in the interaction region can be forced through the hole or slit in the top plate by the application of a positive pulsed field on the bottom plate. As the ions travel through the top plate, they enter the detector. The first component they encounter is a microchannel plate. This is a circular "glassy" plate 25 mm in diameter by 0.31 mm thick. It is composed of 10 μm pores onto which incident charged particles may scatter, producing 10,000 more electrons; microchannel plates are electron amplifiers. Typically, they are mounted on stainless-steel rings, which are biased with 1900 volts to maintain an upwards flow of charge through the detector, and to ensure adequate charge amplification. There is another microchannel plate immediately

following the first, for addition amplification. Ions or electrons may be incident on the detector and first microchannel plate, but only electrons exist thereafter in the detector. Following the 2nd microchannel plate is a stainless steel collection plate that is capacitively coupled to the oscilloscope for voltage pickoff and subsequent signal display.

In a new type of detector (See Appendix C), the stainless steel collection plate is replaced with a phosphor screen, which is imaged by a CCD camera. Since microchannel plates preserve the spatial distribution of the incident charge, the phosphor not only captures the charge amount, but spatial distribution as well. This new "imaging" detector is a truly powerful tool in detecting charged particles, allowing us to effectively capture multidimensional data at once, and is just beginning to show its potential at the time of this writing.

Atomic Beam Source . The source of atoms in experiments is a thermal beam of atoms of the experimenter's choice. In practice, the atoms are filled in the lower half of a 1/4" or 3/8" diameter stainless steel tube, with walls that are 0.006" thick. The tube has a 0.5 mm hole drilled in the center of it. A metal of choice is then filled into the tube, to a level just below the hole. The metal can be ordered in stock form from a chemical supply house. The author has easily filled ovens with Na, Ca, K, and Ba during this thesis work. Depending on the metal, the distribution method may vary. For example, Na is very reactive and is shipped under mineral oil, which must be rinsed off with Toluene before use. Ca is very easy and comes in very dry, small, gray pellets.

After filling the tube, both ends of it are clamped firm and connected to a high-current power supply. The stainless steel tube conducts and is resistively heated by the current. This heating melts the metal sample, causing it to vaporize; for

this reason, an atomic source like this is often called an “oven.” As atomic-gas pressure builds in the tube, the only escape is through the small 0.5 mm hole. Different heating currents are required for different atoms. Na and K require around 15 - 30 Amperes. Ca and Ba can requires as much as 90 Amperes. Generally, the current must be increased with oven age and use.

The oven is mounted in the vacuum chamber such that the hole is horizontally and vertically centered between the field plates, although it is usually placed several inches away. The entire oven assembly is enclosed in a water-cooled “cold shield” to shield the interaction region from the hot tube that is a strong source of blackbody radiation. In the case of a Ca oven at 100 amps, the oven tube even glows bright orange. Copper or Teflon strips with holes drilled in them, can serve as collimating elements for the atomic beam as it travels from the oven hole to the interaction region.

The high current power supply is typically a series of transformers that steps down common 120 VAC to a very low level, near 6.3 V, while conserving the total input power ($P = IV$). In conserving power, the lowered voltage is compensated for by a high current through the oven, which typically has $< 1\Omega$ of resistance. The high currents needed, especially in older Ba and Ca ovens, have been known to melt ovens, causing them to break in half, melt the solder on various electrical connection along the way (on transformer terminals or oven feedthroughs), and generally cause a “smoke smell” in the lab. Keep your eye on the oven when in use.

2.5 Data Acquisition

All data acquired thus far in this lab is by way of a digital oscilloscope, either a Lecroy 9350A or Tektronix 2440. In either case, the signal line from the detector is coupled at 50Ω into a channel on the oscilloscope, which performs all analog to digital conversion. What typically results on the oscilloscope display are a variety of peaks, or just a single peak, depending on what is being studied. The area under a peak is proportional to the total number of charged particles striking the detector.

Since the oscilloscope is digital, it “talks” (interfaces) very easily to a PC-type computer via Hewlett-Packard’s GPIB interface protocol. Simple English like commands allow, for instance, for an entire oscilloscope trace to be transferred from the scope to the PC’s memory for later processing or storage.

The author has written software to perform such processing. For instance, for monitoring the area under a peak, computer software was written to “gate” a peak, then integrate under it for each shot of the laser system. This returns a single number: the area under the peak. Each such number can then be averaged together any number of future triggers, and is eventually written to a disk file. Typically this integrating and averaging is done while some control variable is being slowly changed, like a voltage, laser frequency, beam delay, etc. This process is called “taking data.” The saved data then represents the number of charged particles produced as a function of some physical parameter. It is saved in a format for convenient loading and analysis at a later time.

Bibliography

- [1] Spectra Physics, *Pulsed Nd:Yag Laser User's Manual*, Spectra-Physics, Mountain View, Ca. 1994.
- [2] J. Wilson and J. Hawkes, *Optoelectronics: An Introduction*, Prentice Hall, Englewood Cliffs, New Jersey, 1983, pgs. 92 - 105.
- [3] J. Hecht, *The Laser Guidebook*, McGraw Hill Inc., New York, 1986, pps. 103 - 106.
- [4] Spectra-Physics, *3900S Owner's Manual*, Spectra Physics, 1992.
- [5] C. Davis, *Lasers and Electro-optics: Fundamentals and Engineering*, Cambridge University Press, 1996, p. 132.
- [6] J.C. Diels and W. Rudolph, *Ultrashort Laser Pulse Phenomena*, Academic Press 1996.
- [7] *ibid.*, p. 209.
- [8] American Xtals, Inc., GaAs Data Sheet.
- [9] G. Mourou, et. al., *Physics Today*, January 1998, ppg. 22 - 28.
- [10] J.C. Brice, *Properties of Gallium Arsenide*, INSPEC, 1986, Chapter 7.

- [11] D. Halliday and R. Resnick, *Physics, Part 2, Extended Edition*, John Wiley and Sons, 1986, p. 1243.

Chapter 3

The interaction between a Half-cycle pulse and a Rydberg electron

The interaction between a subpicosecond half-cycle pulse (HCP) of radiation and a free or nearly free electronic charge distribution is the basic atom/field interaction used throughout this thesis. It is thought appropriate then, to dedicate an entire chapter just to this interaction, so it can be discussed in detail here, then used more freely with less detail in subsequent chapters.

HCP/Rydberg atom interactions were just beginning to develop at the time the author started working in this lab, and are very attractive fields in studying Rydberg atoms because of their unique field properties, including their:

Half Cycle Nature. The field envelope of a HCP executes only 1/2 of an optical cycle. This contrasts sharply to more conventional forms of radiation which execute many, if not an “infinite” number of oscillations.

Short Relative Duration. Compared to orbital periods of classical Rydberg electrons, the duration of HCP fields can be very short. HCPs can be used to impulsively probe Rydberg states with good resolution.

Strong Relative Field Strengths. The amplitude of a HCP can be varied, from very small to very large, relative to the binding field of a Rydberg electron. A very small field can be set that hardly perturbs the electron at all, or a very large field can be set that literally “kicks” the electron right out of the atom.

Unique Interaction Mechanism. The interaction between a HCP and Rydberg electron can be characterized as a significant transfer of momentum and energy from the field to the electron. This contrasts to the interaction with other static or slowly varying fields that interact with the electron by altering its binding potential.

In this chapter, detailed discussion of these properties and their effects on a Rydberg electron will be discussed.

3.1 Introduction

As mentioned in Chapter 1, half-cycle pulses (HCPs) are most uniquely characterized by their non-zero time integrated field. This allows them to impart momentum to free, or nearly free electrons. They are particularly novel fields when used in conjunction with Rydberg atoms, because the electron in a Rydberg atom has an average radius that is rather far from the nucleus. This is evident by the fact that $\langle r \rangle$ for a Rydberg electron is[1]

$$\langle r \rangle = \frac{1}{2Z} [3n^2 - l(l+1)] \quad (3.1)$$

where n is the principal quantum number of the Rydberg state, l is the angular momentum of the state, and Z is the effective atomic number. Typically for Rydberg states in the laboratory, $n \gg l$, and $Z = 1$, in which case Equ. 3.1 can be approximated by

$$\langle r \rangle = \frac{3}{2}n^2, \quad (3.2)$$

proportional to the square of the principal quantum number, n . This means the electron is expected to be found at positions further and further from the core, as a function of n . Also, the further from the core the electron is, the smaller is the field that binds the electron to the atom. Even though still a bound system, Rydberg electrons can in some cases be treated as if they are free, or very nearly free. HCPs are well suited for Rydberg atom studies in that their field amplitudes can be set to fully span and exceed the range of Rydberg electron binding fields. This affords the opportunity to study atom/field interactions that are not always dominated by the natural binding fields of the atom.

3.2 The HCP/Rydberg Atom Interaction

HCP/Rydberg atom interactions can take place in the impulsive or non-impulsive regime. Which regime applies depends on how the time scale of the HCP field ($\tau_{HCP} \approx 0.5$ ps) compares to time scales associated with electron motion of the given Rydberg state, typically given by $\tau_K = 2\pi n^3$. If $\tau_{HCP} < \tau_K$ the interaction is impulsive, and the HCP behaves like a quick, fast-acting field. If not, the interaction is non-impulsive, and the HCP behaves like a more conventional, slowly varying field. The interaction, in each regime, will be discussed below.

3.2.1 The Interaction in the Impulsive Regime

To begin this discussion, we will consider the HCP/Rydberg electron interaction as impulsive, much like the interaction of a baseball with a bat. The HCP (bat) exerts a large force over a very small time period (this is the impulse approximation)[4]. "Very

small time period” means a time interval small compared to time periods associated with the motion of the electron (ball) during the interaction.

A classical impulse, denoted here by the symbol \vec{A} is defined as

$$\vec{A} = - \int \vec{F}(t)dt, \quad (3.3)$$

where \vec{F} is the time-dependent impulsive force under consideration, be it the HCP field, or the force on a baseball due to a bat. Note that Equ. 3.3 is simply interpreted as the area under the force curve, and has physical units of momentum. If $\vec{F}(t) = F_0 \cos \omega t$, a continually oscillating force, like that from a continuous wave laser acting on an electron, \vec{A} integrates to zero; the field imparts no net impulse to the electron. To a good approximation in Rydberg atom studies, a HCP field function might resemble a single lobe of a sine wave, or a Gaussian, defined as $\vec{F}(t) = F_0 e^{-t^2/2\sigma^2}$, in which case \vec{A} evaluates to some *non-zero* value; this is the HCP’s unique property as an electromagnetic field. It *can* impart a net impulse to an free or nearly free electron[5]. So in using a HCP and Rydberg atom as our system of study, we have a field which we can use to impulsively alter the momentum of an electron.

In experiments though, we will not directly attempt to measure electron momentum shifts, as all we can directly detect in the lab are charged particles. But whenever there is a change in the momentum of a particle, there must also be a change in the particle’s energy, since its total energy, E_0 is

$$E_0 = \frac{1}{2}p_0^2 + V, \quad (3.4)$$

where p_0 is the particle’s momentum, and V is the binding potential. This change in energy can drive a bound electron towards the ionization limit and possible create an ion, which can be detected. So there is a somewhat direct path between a HCP

interaction and observed data.

If a particle has momentum \vec{p}_0 before the HCP interaction, it will have momentum $\vec{p}_0 + \vec{A}$ after the interaction. This interaction has been modeled classically, and the abrupt momentum shift is illustrated in Fig. 3.1. In this figure, an $n = 25d$ Rydberg electron is irradiated with a Gaussian HCP polarized along the x-axis, incident at $t = 1$ ps. Clearly, the momentum distribution is seen to shift over, by the amount \vec{A} along the x-axis. This abrupt shift is normally called the HCP “kick.”

Substituting $\vec{p}_0 \rightarrow \vec{p}_0 + \vec{A}$ into Equ. 3.4 gives[6]

$$E = \frac{1}{2}p_0^2 + V + \vec{p}_0 \cdot \vec{A} + \frac{1}{2}A^2. \quad (3.5)$$

E_0 , the electron’s initial energy before interacting with the HCP, is immediately recognized as the first two terms. The remaining terms must be the shift in the electron’s energy, ΔE , as a result of the HCP interaction. It can be written as,

$$\Delta E = \vec{p} \cdot \vec{A} + \frac{1}{2}A^2. \quad (3.6)$$

This shift in the electron’s energy has lead to a newly observed ionization mechanism not seen prior to the first HCP/Rydberg atom experiments that were performed [2]. This ionization process can best be described with the aid of Fig. 3.2

In this figure, a one dimensional representation of the Coulomb potential, $V = -1/r$, is plotted, along with the energy level of a highly excited $n = 25$ Rydberg electron, at energy level E_{25} . The system is irradiated with a HCP, of impulse \vec{A} , and the energy of the electron changes by the amount ΔE . Each arrow represents a different possibility of ΔE , depending on what dynamical conditions (\vec{p}_0) existed at the onset of the HCP, as given by Equ. 3.6.

Leftmost Arrow. After the interaction, $E_{25} + \Delta E > 0$, and the electron is ionized.

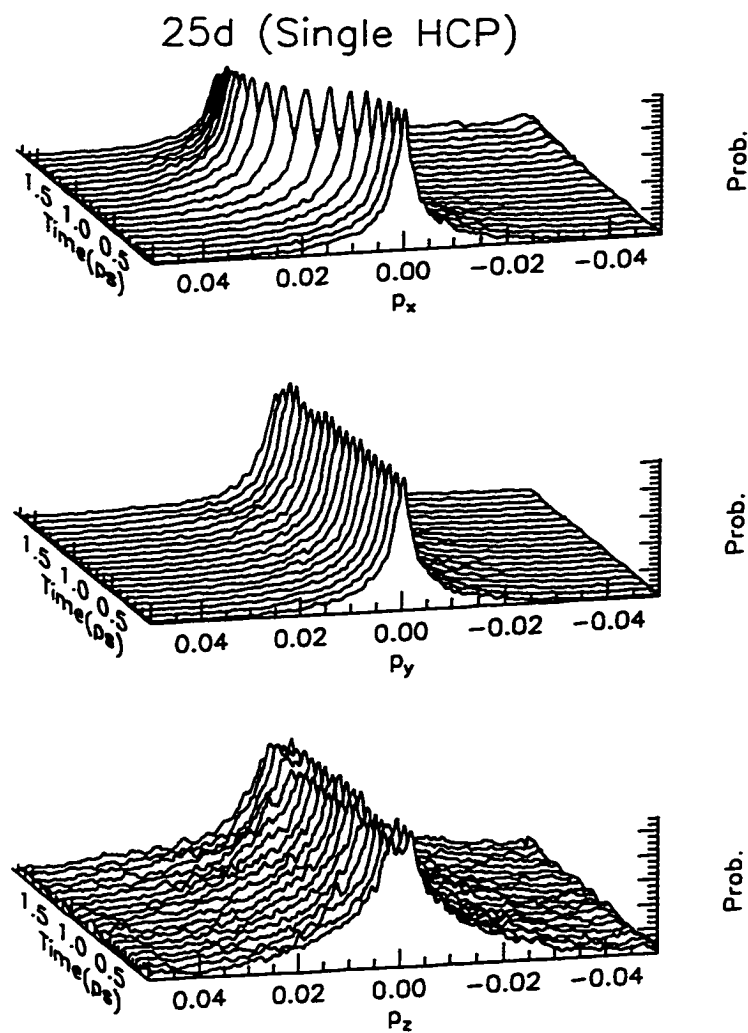


Figure 3.1: The shift in a classical $n = 25d$ electron's momentum distribution due to a HCP polarized along the x-axis, incident at $t = 1$ ps. The HCP impulse \vec{A} was set to 0.015 (a.u.)

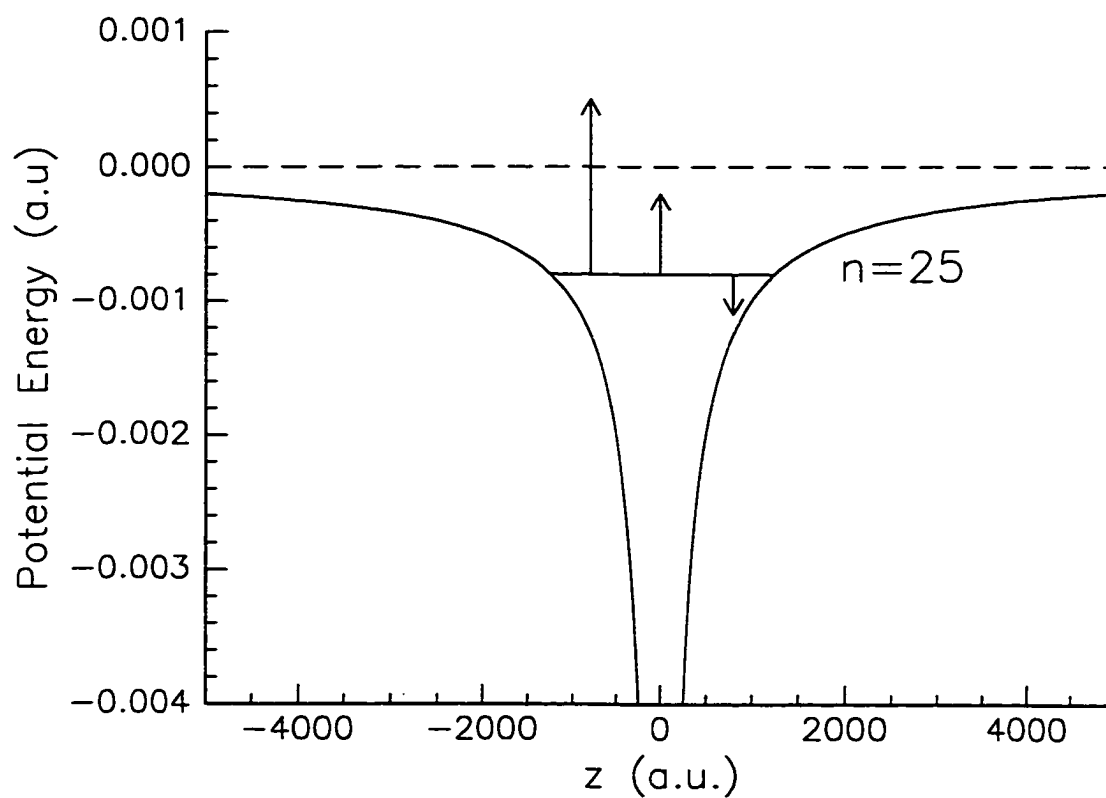


Figure 3.2: A $-1/r$ attractive Coulomb potential. The arrows represent different ways in which energy can be imparted to a Rydberg electron by a HCP.

Middle Arrow. ΔE is positive, but $E_{25} + \Delta E$ is still less than zero. The Rydberg state is still bound, but has been promoted to a higher lying bound state.

Rightmost Arrow. ΔE is negative, and $E_{25} + \Delta E < 0$. The Rydberg state becomes more deeply bound after interacting with the HCP.

In the impulsive regime, this simple momentum/energy exchange is a remarkably accurate description of the HCP/Rydberg electron interaction.

The ionization probability is not solely dependent on the magnitude of \vec{A} , but also on the momentum, \vec{p}_0 (both magnitude and direction) of the classical electron at the time of the interaction. Although \vec{A} is a controlled quantity, details of the ionization process are complicated by the fact that the Rydberg electron has a *distribution* of momenta, not a single, well defined momentum. This, in combination with \vec{A} contribute to the three outcomes illustrated in Fig. 3.2. The details of this ionization process are described in reference[2].

As a fundamental experimental observation, consider the ionization probability of a Rydberg electron due to a HCP, as a function of the HCP's amplitude. Intuitively, the larger the HCP amplitude, the more ionization we might expect. To a large extent, this is true, but what is the functional form of "ionization vs. HCP field?" Stated another way, what amount of ions do we expect to detect as a function of HCP amplitude? A sample of such experimental data is shown in Fig. 3.3

The ionization is seen to have a highly non-linear dependence on the HCP's amplitude. Of great experimental delight here, when the results were first analyzed is the fact that 100% ionization is possible for a field like this. After 25 kV/cm in Fig. 3.3, the HCP amplitude continues to increase, but the ion signal just doesn't get any larger. This complete ionization is not possible with more conventional, multi-cycle optical fields [3].

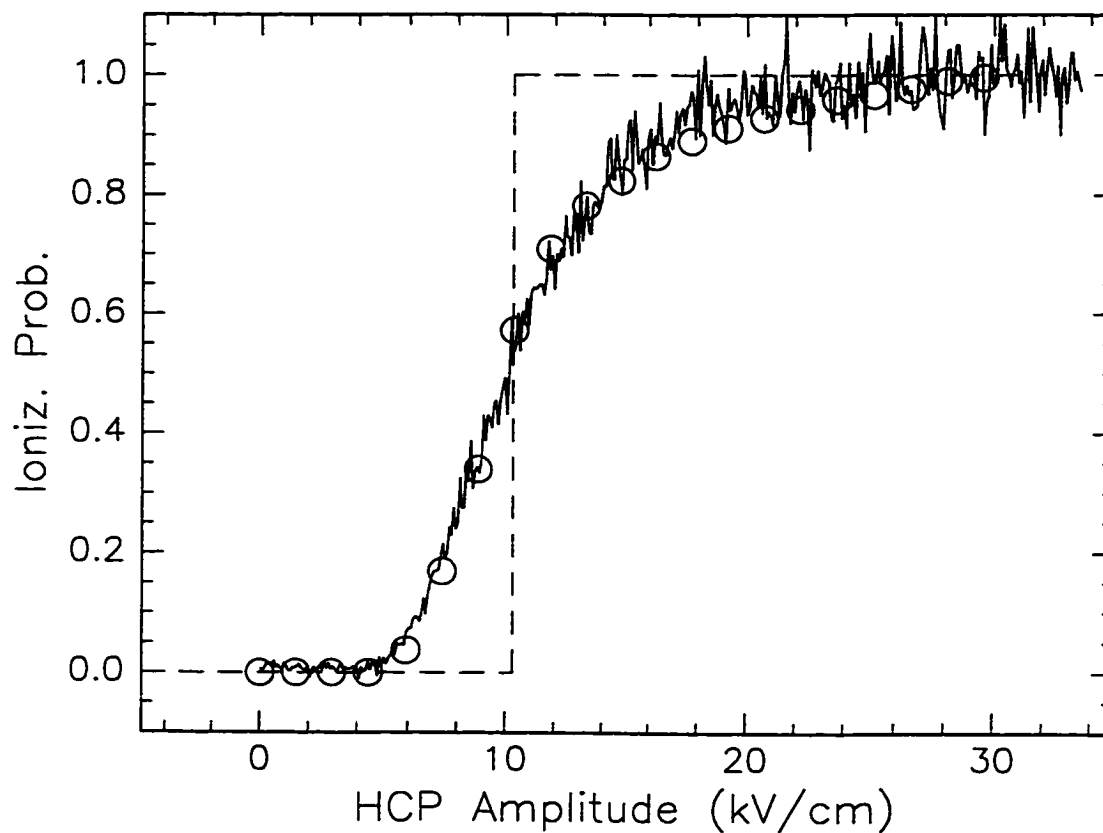


Figure 3.3: Experimental data of the ion signal collected from an $n = 25d$ Rydberg electron as a function of incident HCP amplitude. The circles are predicted by a classical mechanics based analysis. Note the dashed step function passes through the 50% ionization level. There is an experimental uncertainty in the actual HCP amplitude by a factor of ~ 2.5 .

A manifestation of the fact that a Rydberg electron is only *nearly* free, can also be seen in Fig. 3.3 as well, by comparing the data with the dotted line step-function. Consider the hypothetical case of a Rydberg electron, at rest at its outer turning point. Incident is a HCP kick polarized away from the core. We begin ramping the HCP amplitude from 0 V/cm on up. We see no ionization; the HCP kick is not large enough to produce a ΔE that will ionize the electron. Suddenly, we reach the point where ΔE imparted by the HCP exceeds the binding energy of the Rydberg electron; the electron is ionized with 100% certainty. This is the nature of the step function: a perfect system in which we impart momentum to a bound electron with zero momentum. The actual ionization data resembles a “smeared” or “rounded” version of this step. The smearing is a consequence of the *distribution* in momenta (\vec{p} in Equ. 3.6) of the bound state at the onset of the HCP interaction.

3.2.2 The Interaction in the Non-Impulsive Regime

Up to this point, we have been discussing HCP/Rydberg atoms in the impulsive regime. But the interaction can also take place in a non-impulsive manner as well. The regime in which the interaction takes place depends on the time scales of the systems involved (the HCP and the Rydberg state).

The FWHM of the HCP generated with a biased GaAs wafer is approximately 0.5 ps. The Kepler-orbital period of a classical Rydberg electron, τ_K is related to the principal quantum number of the electron via $\tau_K = 2\pi n^3$. Setting $2\pi n_c^3 = 0.5ps$ and solving for n_c (n-critical) gives $n_c = 15$. This means the time scale of the Rydberg electron (dominated by its orbital period) equals the time scale of the HCP field, $\tau_{HCP} = 0.5ps$ at around $n = 15$. For n -states below 15 (and even for a few above 15), HCP/Rydberg interaction are non-impulsive, and ionization mechanism proceeds quite differently than the impulsive model described in the last section. The

non-impulsive regime arises precisely because the Rydberg electron moves during its interaction with the field.

The non-impulsive ionization model is the more conventional model for field ionization, seen long before HCP experiments were performed, and is a model for ionization due to slowly varying fields, even static fields. In this case, the field \vec{F} is seen as a perturbation to the Coulomb potential, instead of an energy/momentum exchange mechanism. If $\vec{F} = F_0\hat{z}$, the Coulomb potential, $V = -1/r$ becomes $V = -1/r + F_0z$, given that V , potential energy, is given by $V = \int \vec{F} \cdot d\vec{r}$.

A combined Coulomb/static field potential is plotted in Fig. 3.4. In this figure, the deformation of the Coulomb potential due to a HCP with a peak field of 10 kV/cm is shown. Several curves are plotted, each at a different percentage of peak field along the HCP field envelope. A pure $-1/r$ potential and bound $n = 25$ Rydberg state is plotted as well for comparison.

Note how the potential “bends over” on one side of the core in response to the field. As the HCP passes through, the potential “animates” between the zero field case (dashed line), and peak field case (bold line), on the rising side of the field, then back again, on the falling side of the field. Clearly, if the radially oscillating electron visits the outer turning point, or saddle point, while the potential is bent over, it can escape the atom, or become ionized. This is an adiabatic, non-impulsive, ionization process, whereby the electron is ionized due to an alteration in the binding potential; it contrasts sharply to the impulsive case described above, where there is a significant exchange of energy and momentum from the field to the particle.

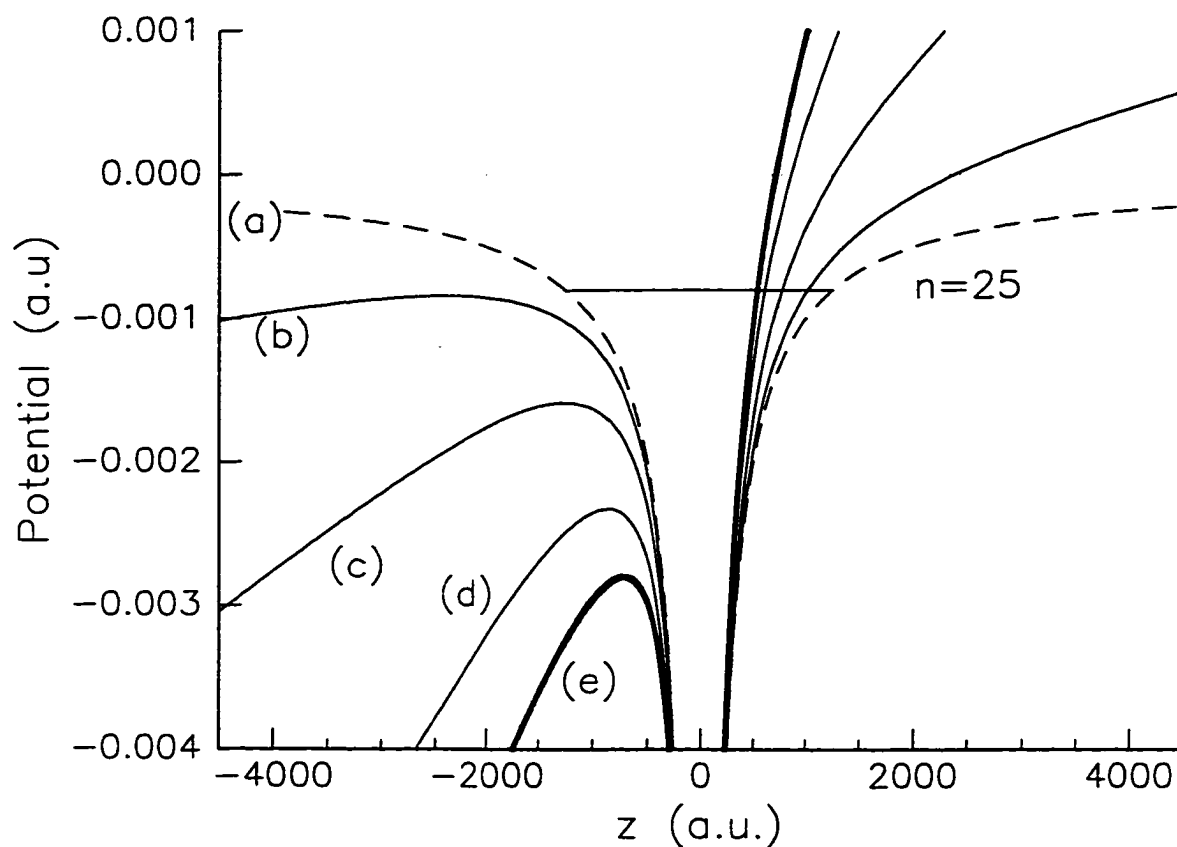


Figure 3.4: The alteration of the Coulomb binding potential due to a HCP electric field, $\vec{F} = F_0(t)\hat{z}$. The dashed line is the unperturbed Coulomb potential. Various levels along a HCP envelope with a peak field of 10 kV/cm are plotted. Curve (A) 0%, (B) 10% (C) 30%, (D) 70%, (E) 100% of maximum HCP amplitude. A bound $n = 25$ Rydberg electron is shown by the horizontal line inside of the potential well.

3.3 Conclusions

In HCP/Rydberg atom studies, the impulsive and non-impulsive regimes can be visited by merely changing the n -state of the Rydberg atom excited. In the impulsive regime, there is a significant exchange of momentum and energy between the HCP field and the electron, which can lead to ionization. The interaction in this regime depends strongly on the full vectorial momentum of the electron, at the onset of the HCP. This regime will play an important role in the experiments presented in chapters 4 and 5. In the non-impulsive regime, the interaction is an alteration in the binding potential of the electron itself. Evidence of this regime will be seen in the experiment discussed in Chapter 4.

Bibliography

- [1] H.A. Bethe and E.E. Salpeter, *Quantum Mechanics of One- and Two-Electron Atoms*, Plenum Publishing Corp, New York, 1977, pp. 17.
- [2] R.R. Jones, D. You, P.H. Bucksbaum, *Phys. Rev. Lett.*, **70**, 1236 (1993).
- [3] G. Mainfray and C. Manus, *Rep. Prog. Phys.* **54**, 1333 (1991); P. Pillet, et. al., *Phys. Rev. Lett.*, **50**, 1042 (1983); C.R. Mahon, et. al., *Phys. Rev. A* **44**, 1859 (1991); R.F. Stebbings, et. al., *Phys. Rev. A* **12**, 1453 (1975); T.F. Gallagher, et. al., *Phys. Rev. Lett.* **37**, 1465 (1976); M.G. Littman, et. al., *Phys. Rev. Lett.* **41**, 103 (1978).
- [4] P.A. Tipler, *Physics for Scientists and Engineers*, Worth Publishers, New York, 1991, p. 210.
- [5] In actuality, any freely propagating field must have a zero time integrated. The *total* time integrated THz field produced by the GaAs wafer is zero if integrated over about 10 ns from the time it is created. However in this total field about 85% of the radiation is contained in a single unipolar lobe present during the 1.5 or so of the field. For our uses here, in studying Rydberg atom interactions, a HCP field *behaves* as if has a non-zero time integrated field.
- [6] E. Merzbacher, *Quantum Mechanics*, John Wiley & Sons, Inc., 1961, p. 157. H. Goldstein, *Classical Mechanics, 2nd ed.*, Addison-Wesley, 1980, p. 331.

- [7] B.I. Greene, et. al., Appl. Phys. Lett. **59**, 893 (1991); D.You, et. al., Opt. Lett **18**, 290 (1993).

Chapter 4

The Interaction of a Rydberg Atom with Two Time Separated Half-Cycle Pulses

The experiments and techniques discussed in this chapter investigate the ionization of Rydberg atoms irradiated by two, time separated half-cycle pulses of radiation. The primary variables of investigation here are

- the amplitudes of the HCPs,
- the time delay between the HCPs,
- the HCP duration vs. atomic time scales,
- and the polarization of one HCP with respect to the other.

The chapter begins with a general discussion of the interaction of Rydberg atoms with two time separated HCPs of radiation. This discussion serves as a prerequisite to main experiment discussed in this chapter, in which Rydberg atoms are irradiated with a pair of HCPs mutually polarized at 90 degrees with respect to one another. This experiment is somewhat unique in that for the first time, it thrusts the study of HCP/Rydberg interactions into three Cartesian dimensions.

4.1 Introduction

4.1.1 Interactions with two parallel time separated HCPs

Extending single HCP experiments to involve two time separated HCPs has opened up a whole new area for experimental study. “Two time separated HCPs” means just what it says. An initial HCP is incident on an atomic system, followed by a brief (picosecond) time delay, then a second HCP. These dual HCP experiments provide very useful information, in particular:

Pump Probe Experiments. As discussed in Chapter 3, in the impulsive regime, HCPs can significantly alter the momentum distribution of Rydberg electrons. Consider the first HCP, irradiating a system of momentum \vec{p}_0 . The system’s momentum is now altered to $\vec{p}_1 = \vec{p}_0 + \vec{A}$. There is now a time delay, between 0 and typically 10’s of picoseconds. The second HCP now irradiates the system, interacting and altering the momentum of the system, no longer \vec{p}_0 , but now \vec{p}_1 . The second HCP interacts with the system, *as altered by the first HCP*. The signal, or information collected by the second HCP will effectively probe the interaction of the first. This is the nature of a “Pump-Probe” experiments (field→time delay→field). Pump-Probe experiments are useful because they can provide the time dynamics of an atom/field interaction.

HCP Autocorrelation. How do we know that a HCP is really a “half cycle pulse?” The field profile of a HCP can be ascertained using a device called a bolometer, capable of converting the nano-Joules of energy delivered by a HCP onto its active area, into a measurable and stable voltage level. In this case, the bolometer acts as a HCP detector, and the half cycle nature has been inferred from such a device [1].

In our lab, however, some of the most valuable information about HCPs has been obtained using Rydberg atoms themselves as HCP-autocorrelators. In this configuration, two HCPs are polarized parallel to each other. One of the HCPs always

irradiates the system at time $t = 0$. All of the laser beams and GaAs bias timings for this HCP are fixed. The other HCP is created at variable times, δ with respect to the first. Typically, δ has extrema on the order of a HCP's total lifetime, about 1.5 ps, from turn on, to turn off. By slowly changing δ between positive and negative extremes, the two HCPs effectively sweep through each other in the interaction region, creating a net linear superposition field.

When $\delta = 0$, for example, the two HCP fields arrive at the interaction region simultaneously, creating a single superposition HCP whose amplitude is the exactly the sum of both component HCPs. The interaction and ionization process proceed as described in Chapter 3, in response to this total HCP field. Values of δ different from zero will produce ionization levels accordingly, depending on the total field amplitude. In fact, the ionization response will be a function of δ , and will produce levels of ionization that closely follow the total HCP field envelope. Sweeping two HCPs past each other in this way is completely analogous to autocorrelators for ultrafast laser system[3]. A sample of such an autocorrelation scan is shown in Fig. 4.1. A clear HCP-like envelope is seen, with FWHM of approximately 0.5 ps. Note slight deviations from zero in the “wings” of the figure. This is a long negative tail due to decelerating charges in the GaAs wafer, as it returns to its insulating state.

Strictly speaking, this not a true autocorrelation function because it includes the time-dynamics of the atom's response to the field. This tends to smear the results, leading to exaggerated time-features in such scans. However these results can be minimized by tuning the initial Rydberg state to the lowest possible accessible n -state, typically around $n = 14$, where the time dynamics of the field exceeds that of the atom. This means the ionization response is due primarily to the HCP field (quantity of interest), not the atom (measurement device).

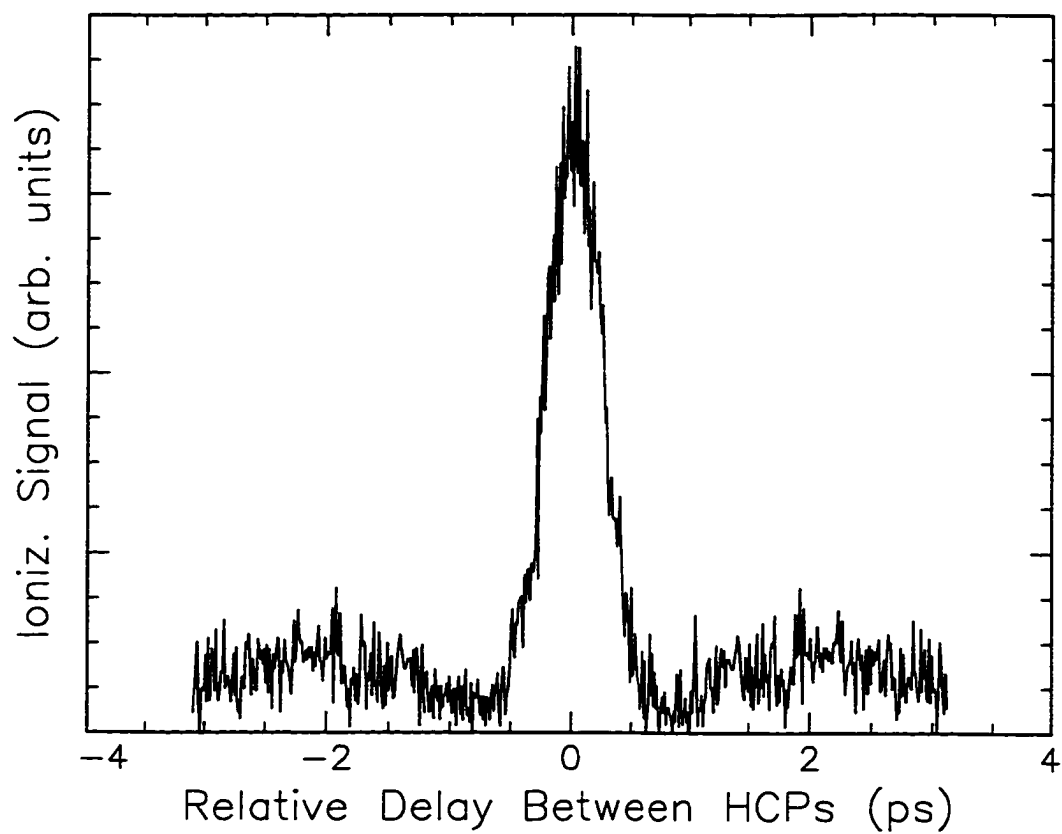


Figure 4.1: Ionization versus δ , the time delay between two HCPs with parallel orientations, for the $n = 18$ Rydberg state of Na. Note the increased in ionization near $t=0$, where the two HCP fields are overlapped. Time delays different from $t=0$ map out the overall HCP envelope seen.

4.1.2 Interactions with two cross polarized time separated HCPs

Studying Rydberg atom interactions due to two cross polarized half-cycle pulses is important for two primary reasons. The first is related to the advent and use of new types of fields in atomic physics, and the other is fundamentally important based on the full three dimensional structure of an atom. These points are elaborated upon below.

New Field Sources. The search and discovery of new and unique fields is largely responsible for past progress in atomic physics, and will undoubtedly dictate future progress. Ultrafast lasers and their use in atomic physics are a good example of this. As it happens, two time separated HCPs can create quite a unique radiation field if one considers the resultant produced by relative time separations and polarizations.

Consider then, two identical HCPs counterpropagating along the \hat{z} -axis, with time delay δ between them. The first, $F_1(t)$ is polarized along the \hat{x} -axis, and the second, $F_2(t)$, is polarized along the \hat{y} -axis. The atom/field interaction region located at $z = 0$. Each HCP has a amplitude of F_0 , and a time dependent “half-cycle” field envelope is defined by $f(t)$. The two HCPs are defined to be identical in structure as

$$F_1(t) = F_2(t) = F_0 f(t). \quad (4.1)$$

The total field, or resultant field produced by these two “component” and time delayed HCPs is

$$\vec{G}(t, \delta) = F_1(t)\hat{x} + F_2(t - \delta)\hat{y}, \quad (4.2)$$

or

$$\vec{G}(t, \delta) = F_0 [f(t)\hat{x} + f(t - \delta)\hat{y}], \quad (4.3)$$

If δ is zero, the two HCPs arrive at the interaction region simultaneously. The resultant field, $\vec{G}(t, 0)$, will be another linearly polarized HCP field, polarized in the xy -plane at an angle 45 degrees with respect to the \hat{x} -axis, with a net amplitude of $\sqrt{2}F_0$. This is somewhat of a useful field, in that it allows us to create a HCP field $\sqrt{2}$ times larger than we could safely do without destroying the HCP generating apparatus.

Now, imagine setting δ to approximately 1 full-width of a HCP, about 0.5 ps. With this delay, F_1 arrives into the interaction region slightly earlier than F_2 , and $\vec{G}(t)$ has an initial component along the \hat{x} -axis only, as F_1 is the only field present. As the leading edge of the second HCP, F_2 enters the interaction region, it begins to add a small field component along the \hat{y} -axis. The angle a vector makes in the xy -plane with respect to the \hat{x} -axis is given by

$$\alpha = \tan^{-1} \frac{G_y}{G_x}. \quad (4.4)$$

When the G_y is initially zero, $\alpha = 0$, and the resultant field vector lies solely along the \hat{x} -axis. As a field component begins to develop along the \hat{y} -axis, with the arrival of the 2nd HCP, α begins to increase from zero, meaning that the polarization direction of the net field begins to change as a function of time. As the 1st HCP moves through and begins to leave the interaction region, the 2nd HCP, is now the dominant field. The resultant field now has its strongest components along the \hat{y} -axis, meaning α begins to approach 90 degrees. The net field vanishes as the 2nd HCP exits.

But what has happened? *THE POLARIZATION OF THE TOTAL FIELD HAS*

SWEPT THROUGH A CIRCULAR 1/4-CYCLE OF ROTATION. The resultant field described here only rotates through a 1/4 of a cycle then abruptly vanishes, due to the half-cycle nature of the component HCPs. This total 1/4-cycle circularly polarized field is possible only by using two *half-cycle* pulses as components. This contrasts sharply to conventional circularly polarized light that continually rotates along its propagation direction.

So a mechanism exists to produce a very unique rotating field, but it is not entirely clear what the precise definition of a 1/4-cycle circularly polarized field is. We do know that it exists only for values of δ no larger than 1 ps or so for HCPs with a full-width of 0.5 ps. To investigate this a little further, and illustrate this concept, the net fields produced due to two cross-polarized HCP fields with varying values of δ are shown in Fig. 4.2

This is truly a new and unique field source. In the experiment discussed below, we will address the question: how will the ionization process of Na Rydberg atoms proceed as a result of this unique field?

Fully investigating quantum mechanical degrees of freedom. In analyzing an experiment from a quantum mechanical point of view, we must often determine some reference frame for our analysis. Any set of axes imposed on a quantum system is a consequence of an attempted measurement on the system (e.g. atoms don't "float" around with little Cartesian axes on them). By convention, the placement of the \hat{z} -axis is of fundamental importance analytically. Conventionally defined operators (L_z, p_z) and solutions to the Schrödinger equation (Y_l^m) are constructed based on information on this axis. About this \hat{z} -axis, the general solutions to the Schrödinger equation are defined. Experimentally, the \hat{z} -axis is usually defined by the initial perturbation to the atomic system. In the experiments this is the linearly polarized dye lasers used to excite the Rydberg state. The \hat{z} -axis is defined to be along their

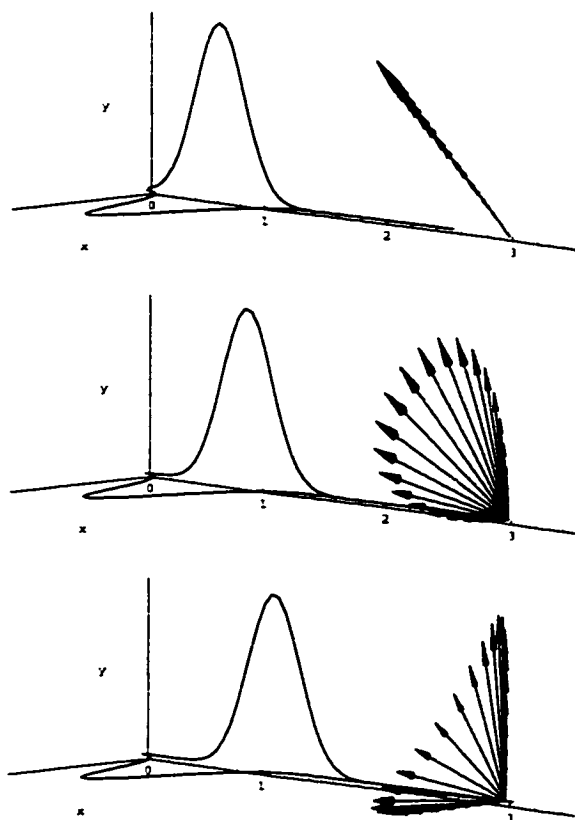


Figure 4.2: The net field produced by two counterpropagating, cross polarized HCP fields. The first HCP is polarized along the \hat{x} -axis, and the second along the \hat{y} -axis. The top inset shows the linear polarized net field produced when $\delta = 0$. The middle inset shows the net field for $\delta = 0.25$ ps. The bottom inset shows the net field for $\delta = 0.5$ ps. Note how in the latter two cases, the net field (the arrows) executes circular motion for only $1/4$ of a cycle.

axis of polarization. To maintain the symmetry of this system, any single or dual (parallel) HCPs, are polarized along the \hat{z} -axis as well.

In the experiment involving two cross polarized HCPs, we wish to preserve the symmetry as well. To so do, the cross polarized HCPs are configured so that their axis of propagation is set along the \hat{z} -axis. This makes the symmetry axis of the total field correspond to the symmetry axis of the atom. However, note in this case, the *fields* are no longer polarized along the \hat{z} -axis, as in previous studies involving single or dual HCPs. Perhaps there is new and interesting physics involved in the interactions involving “off axis” fields, in two dimensions.

4.2 Experiment

To begin the main topic of this chapter, Na Rydberg atoms are irradiated with two HCPs, whose polarizations are oriented at 90 degrees with respect to one another. Of particular interest here is the time delay at which one HCP arrives at the interaction region with respect to the other. We will be interested in how Na Rydberg atoms are ionized by the HCP pair with a time delay set such that net 1/4-cycle circularly polarized field is produced, as discussed above.

4.2.1 Rydberg Atom Production

In this experiment, a thermal beam of Na atoms is created and aimed at the center of two conducting plates situated in a parallel capacitor geometry. These two plates define our interaction region. The thermal beam is produced by running ≈ 35 A through a stainless steel tube (the “oven”) packed with stock Na metal. The current resistively heats the tube, producing an effusive gas that escapes through a 0.5 mm hole in the tube. Next, two tunable, pulsed, ns dye lasers are used to prepare Rydberg states in Na atoms. The excitation scheme is shown in Fig. 4.3.

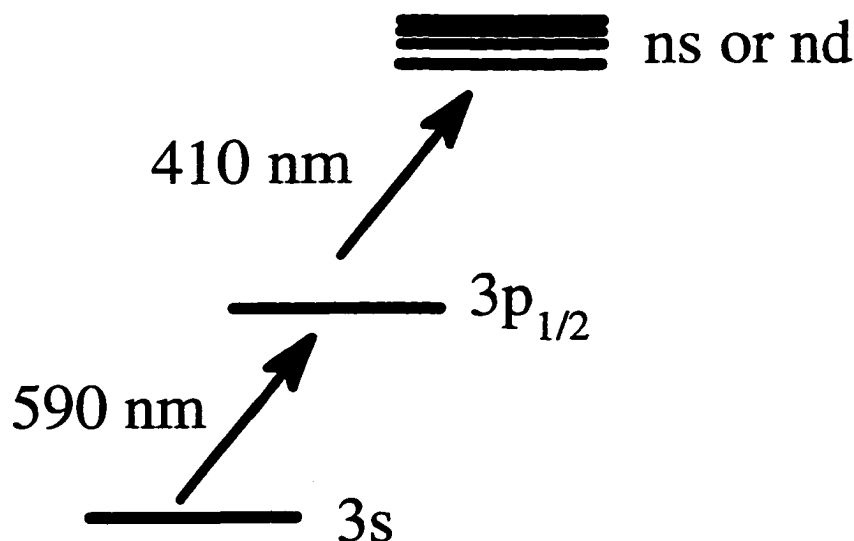


Figure 4.3: The excitation scheme to create Rydberg atoms from ground state Na atoms.

First, an orange 590 nm laser excites the Na 3s ground state atoms to the $3p_{1/2}$ state through the absorption of one photon. Within ≤ 2 ns, a second, blue, 410 nm photon further excites the atoms from the $3p_{1/2}$ state to a highly excited Rydberg state, characterized by nd , where $15 \leq n \leq 50$, by the absorption of a second photon. The orange “resonance-line” laser is always held fixed. The second “Rydberg-laser” is tunable between the ranges of n ’s listed.

To investigate the ranges of n -states it is possible to reach with the 2nd dye laser, spectroscopy of the Na atom was performed prior to the experiment. In this configuration, a strong +6kV pulsed field was applied to the bottom field plate within $1\mu\text{s}$ after the excitation process, which is capable of field ionizing any population with $n \geq 15$. The ions produced are accelerated by the field into an ion detector located above the top plate. The top plate has a slit in the top through which ions may pass. The signal level is monitored with a Lecroy 9350A digital oscilloscope, then integrated

and saved using a PC computer. A slowly turning worm motor is connected to a knob on the Rydberg-laser that changes the angle of its grating, changing the frequency at which it lases. The ion signal is recorded as a function of this knob's position, or the Rydberg-laser frequency. As the knob is scanned through the gain profile of the dye, the ion signal observed rises as Na Rydberg resonances are hit, and falls to zero at off resonance frequencies. A typical spectroscopic scan is shown in Fig. 4.4. Once a scan like this is obtained and calibrated, it can be used as a very convenient tuning guide for the Rydberg laser that tells us what n -state is excited for a given angle of the dye-laser's grating. The resonance peaks can be labeled with n -values, while carefully noting that the quantum defect for s -states in Na is $\delta_s = 1.35$ (see Table 1.2). This effectively places the d resonance peak for state n right next to the s resonance state for $n - 1$.

4.2.2 HCP Generating Apparatus

As discussed in Chapter 2, a HCP is produced by irradiating a biased GaAs wafer with a 150 fs, 790 nm pulse from our ultrafast laser system. The laser pulse effectively "turns on" the wafer. Used this way, the wafer is commonly referred to as a photoconductive switch. Once on, the switch radiates like a dipole antenna because of charges accelerated along a single dimension of the wafer, by the bias voltage. This radiation is in the form of a half-cycle pulse of THz radiation. The polarization of the HCP is a parallel to a straight-line axis between the positive and ground references associated with the bias voltage. In order to produce two HCPs whose polarizations are oriented as 90 degrees with respect to one another, two separate GaAs wafers must be mounted whose bias references are oriented at 90 degrees as well. The experimental setup is illustrated in Fig. 4.5.

In practice, one GaAs wafer is mounted fixed in the vacuum chamber. The sec-

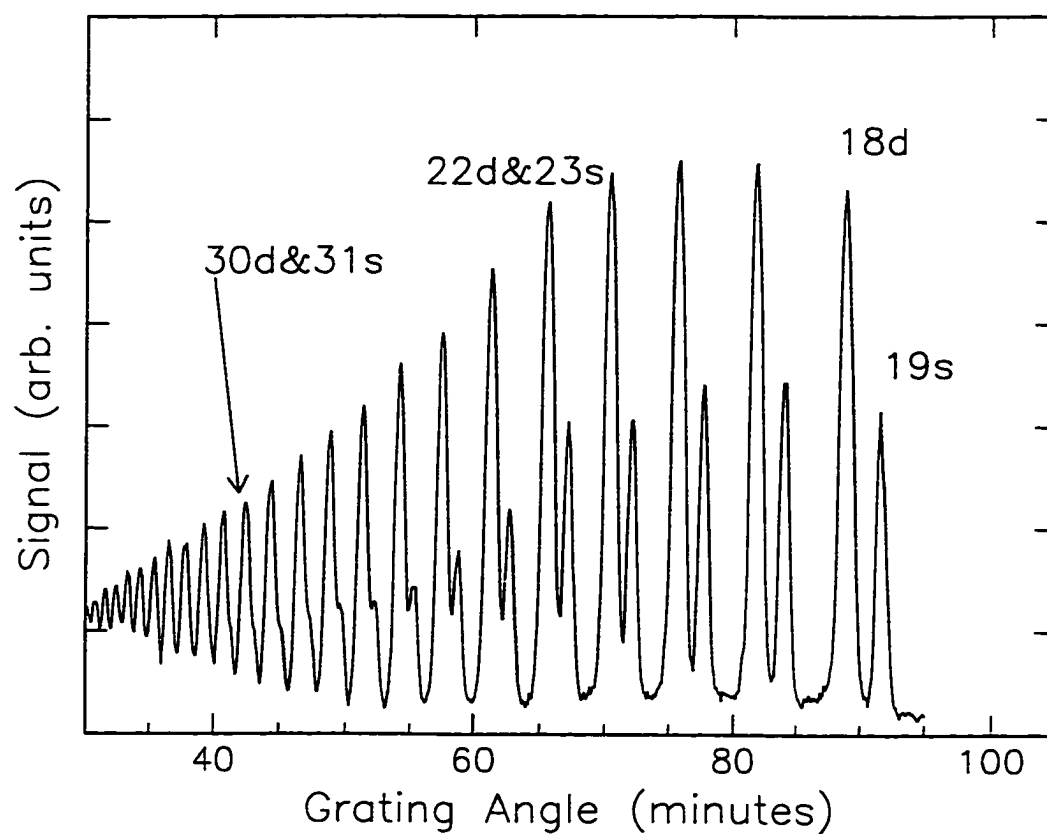


Figure 4.4: The ion signal produced by pulsed field ionization of Na atoms excited via two photon excitation to ns or nd Rydberg states, as a function of the grating angle on the 2nd dye laser (see text).

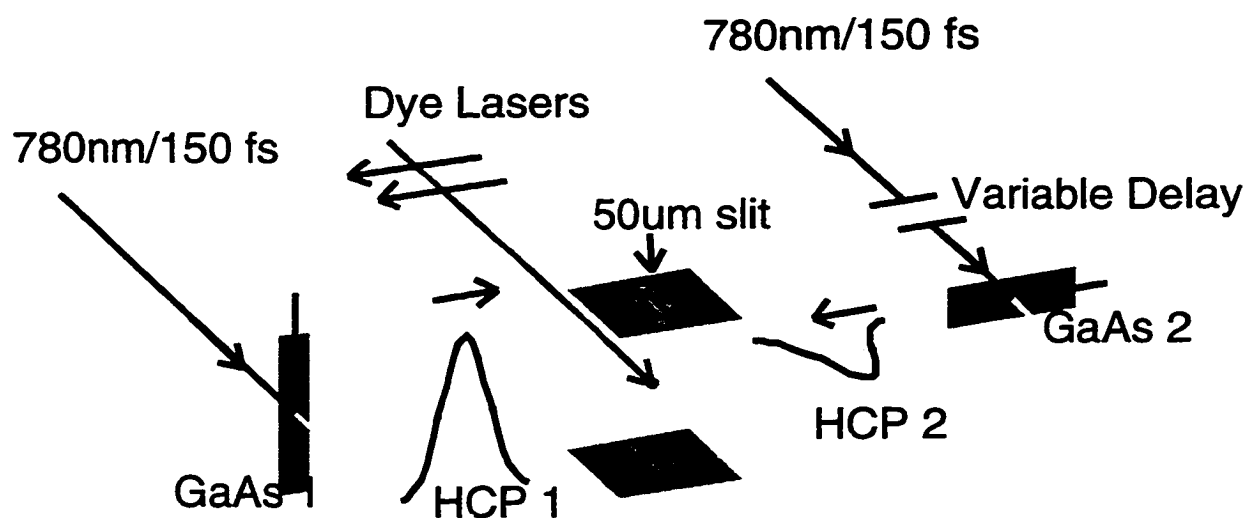


Figure 4.5: The experimental apparatus for irradiating Rydberg atoms with 1/4-cycle circularly polarized THz radiation. Shown in the figure are two GaAs wafers whose bias fields are oriented at 90 degrees with respect to each other. The positions of the atomic beams and dye laser beams are also shown. The dye laser beams are polarized in a direction that maximizes the symmetry of the problem.

ond GaAs wafer is mounted such that it can be rotated between 0 and 180 degrees with respect to the fixed wafer. Having this variability in the polarization between the two HCPs allows for the running of a few important diagnostics before considering the cross polarized case. First, it allows for the running of HCP autocorrelation scans as discussed in Section 4.1.1, to verify that the wafers are properly producing HCPs. Second, the minimum or maximum fields produced in parallel or antiparallel autocorrelation scans allow for the easy determination of “ $t=0$ ” between the two counterpropagating HCPs (see Fig. 4.1). As a definition of a term used hereafter, “ $t=0$ ” corresponds to the experimental conditions where the HCPs arrive at the interaction region at precisely the same instant. The $50\mu m$ slit in the top capacitor plate allows for a temporal resolution of ≈ 166 fs in the counterpropagating HCP geometry. Later, when working with cross polarized HCPs, “ $t=0$ ” will serve as reference point, by which small time delays between the HCPs can be set to create some form of 1/4-cycle circularly polarized light, as shown in Fig. 4.2.

4.2.3 Data Acquisition and Experiment Prerequisites

Timing

There are five fields associated with the working experiment, that must be precisely synchronized before any data acquisition can be performed. The fields are: the Na $3s \rightarrow 3p_{1/2}$ 590 nm dye laser, the $3p_{1/2} \rightarrow nd$ Rydberg dye laser, two HCPs, and a small +50V pulse applied to the bottom field plate, used to force any ions created by the HCP up into the detector. The success of this experiment depends critically on the timing of these fields. Additionally, as discussed in Section 4.1.2, there is a timing parameter between the two cross-polarized HCPs used in creating the desired 1/4-cycle circularly polarized field. The dye lasers are typically arranged to arrive within a few nanoseconds of each other. The dye laser pulses are < 10 ns wide, and

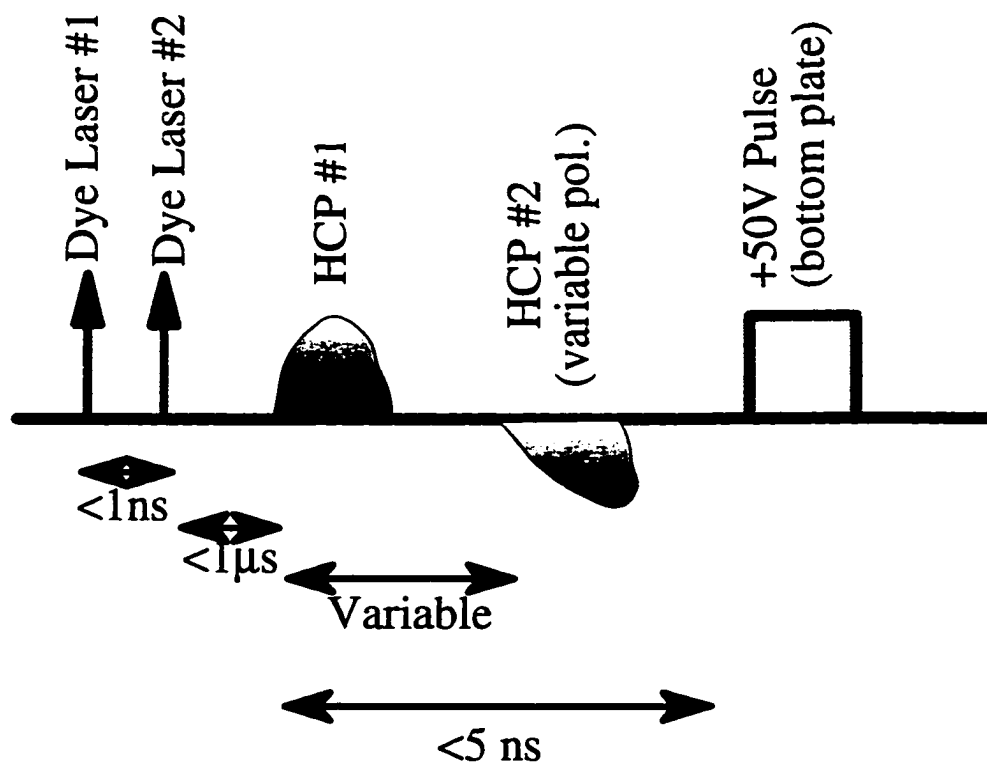


Figure 4.6: The timing of all fields involved in the cross-polarized HCP experiment.

are made to almost completely overlap in their arrival time. Within a microsecond of the second dye laser, the first HCP arrives, followed by a variable delay, then the second HCP. Within 5 ns of the first HCP, the 50V field pulse is applied to the bottom field plate. The complete timing sequence is illustrated in Fig. 4.6.

The creation and arrival times of the HCPs are not controlled by variable GaAs-to-interaction region distances, rather the time at which a ultrafast laser pulse excites a particular wafer into conduction. It is fairly straightforward, experimentally, to mount GaAs wafers in the vacuum system at permanent positions, and create an optical delay in the ultrafast beam arrival on the wafer. The high voltage circuits pulses used to bias the wafers take several hundred nanoseconds to respond to their input triggers, therefore, an output on the YAG lasers called “Q-switch Advance” is

used to trigger the circuits, well in advance of an laser system trigger. This output line on the YAG puts out a TTL pulse just prior to the flash-lamp firing of the YAG. Fine timing control of the circuits is achieved through two dual-oneshot pulse delay circuits based around the 74123 dual monostable multivibrator integrated circuit. So in practice, the YAG “Q-switch Advance” triggers the one-shots. The one shots then trigger the high voltage pulse circuits. These dual-oneshot delay circuits are mounted in a surplus nuclear-physics “NIM-bin” crate near the vacuum system. The fine timing delay is adjusted so that the light arrival on each GaAs wafer corresponds to the peak field in the high voltage bias pulse. This can be confirmed using an alligator clip-to-BNC probe as an antenna placed near the high voltage pulse box. This probe is coupled at $1M\Omega$ into an oscilloscope. When the wafer is turned on by a short laser pulse, its resistance drops several orders of magnitude, and it can no longer hold off the bias voltage. On the oscilloscope, this sudden “short circuit” can be seen as a voltage drop on the antenna pickup channel. The fine timing adjust is performed so this voltage drop will temporally coincide with the peak in the bias field.

Procedure

As mentioned the goal of this experiment is to monitor the ionization yield of Na Rydberg atoms by the 1/4-cycle circularly polarized THz field. To take data, the following procedure was followed, each step was followed generally in the order presented, or on an “as needed” basis. Many of the steps are diagnostics, and necessary prerequisites to actually performing the experiment.

Excite and verify the Rydberg state. Both dye lasers are sent into the interaction region, followed by a +6 kV pulse applied to the bottom field plate. This will ionize any Rydberg states with $n \geq 15$. At this point, the desired n -state of the experiment is set by adjusting the grating angle in the Rydberg (second) dye laser.

This is a good time to perform oven or dye laser optimizations.

Verify the operation of the GaAs wafers. The high voltage pulse is removed, and replaced by a small +50V pulse on the bottom plate. A bias voltage on only one of the two GaAs is applied. An oscilloscope is used to verify that the 50V pulse is arriving after the HCP creation. The bias field on the HCP is increased until a signal appears. This will correspond to the ionization of the set Rydberg state by the HCP itself. At this time, any HCP optimization for this wafer are performed, including:

- The amount of THz field produced depends critically (and nonlinearly) on the power of the incident light from the ultrafast laser. In practice, the amount of THz field increases with irradiation power only until a certain point, at which it begins to *decrease* with irradiation power. While watching the HCP signal of the oscilloscope, the pump knob on the multi-pass amplifier is adjusted until maximum ion signal is achieved. For the combination of optics used in this experiments, an output power of ≈ 0.12 W was found optimal for light immediately exiting the amplifier. Typically, a neutral density filter is also put into the ultrafast beam before it is split off for each wafer. This seems to increase the signal level regardless, perhaps by chopping slowly rising edges on the ultrafast pulse. It also prohibits excessive corona discharge of the wafer at peak bias voltages.
- Large parabolic mirrors are used to collect the THz radiation from each wafer, and direct them into the interaction region. The mirrors are oriented such that the radiation is slightly focused in the interaction region. Horizontal and vertical adjustments on the mirrors are available outside of the vacuum as mechanical feedthroughs. At this point, the two adjustments on the mirror should be optimized to maximize the ion signal. In practice, this optimization works best

for low n -state (near 18 or so) at high bias voltages. This is the region where the ionization signal has a very strong and non-linear dependence on the HCP field. Small changes in HCP field will greatly change the observed ionization signal.

Each optimization is repeated for both wafers. Afterwards, ionization versus bias voltage is collected for both wafers independently. The ion signal on the oscilloscope is gated and integrated using software the author has written. The bias voltage across each wafer is slowly ramped while integrating the signal. Typically, 15 integrations are averaged together and saved as a single data point. Since the two wafers are typically cut from the same or similar GaAs crystals, the excitation pulse and power are the same, and the bias fields are the same, the ionization scans should be identical for both wafers. This means before proceeding with the experiment, the two scans acquired for each wafer should be loaded into some data plotting/analysis software and overlaid on the same set of axes. The ionization as a function of bias field for both wafers should be within 10% (in field) of each other. If not, something must be wrong (HCPs, wafers, oven, alignment, etc.) and the experiment should not continue until better than 10% agreement is achieved.

Verify two-HCP performance. With both HCP generating wafers behaving the same, or very similar, general two-HCP diagnostics are now performed. At this point, both HCP bias voltages should be turned on, creating two (nearly) identical counterpropagating HCPs. The bias input voltages are supplied by splitting the output of the lab power supply across both wafers. This allows for identical wafer biasing using one power supply and one convenient knob.

Two-HCP autocorrelation scan. With both bias fields on, two counter propagating HCPs are now entering the interaction region. Assuming “ $t=0$ ” has already

been found for this experimental setup, the arrival time of one HCP is now scanned versus the arrival time of the other HCP. This scanning is accomplished by attaching a worm motor to the ultrafast beam delay line in exciting one of the two GaAs wafers into conduction. Typically, this delay line is in the form of one or two gold mirrors attached to a micrometer-resolution delay stage. Turning the stage's knob changes the optical path length of light in that particular leg of the experiment. Depending on the polarization of the two HCPs (e.g. the sign of the bias voltages), the scan in Fig. 4.1 should be reproduced. Once such a scan is taken, the data should be loaded and plotted for inspection. The plot should be nearly symmetrical about $t=0$, and the full width at half maximum of the pulse envelope about $t=0$ should be characteristic of either the HCP field (0.5 ps), or the Kepler period of the excited Rydberg state, $\tau_K = 2\pi n^3$, whichever is larger. The reflection peaks near ± 11 ps may or may not appear depending on the experimental setup.

The micrometer position giving "t=0" is of fundamental importance in this experiment and is also determined by this scan. In principal it should remain the same, but does vary somewhat from day to day.

Two-HCP overlap. The micrometer position is now set at the "t=0" position just identified, and bias fields with opposite polarity is applied to both wafers. The signal level should be almost zero, because the HCP fields are canceling each other in the interaction region. The horizontal and vertical adjustments on the spherical mirrors for each HCP are now optimized. Steering one HCP away from maximum overlap with the other HCP will result in an obvious ion signal increase on the oscilloscope (less than optimal overlap will cause less cancellation between the two fields). Both HCPs should be steered until the ion signal is at an absolute minimum. This ensures good spatial overlap between the two HCP fields.

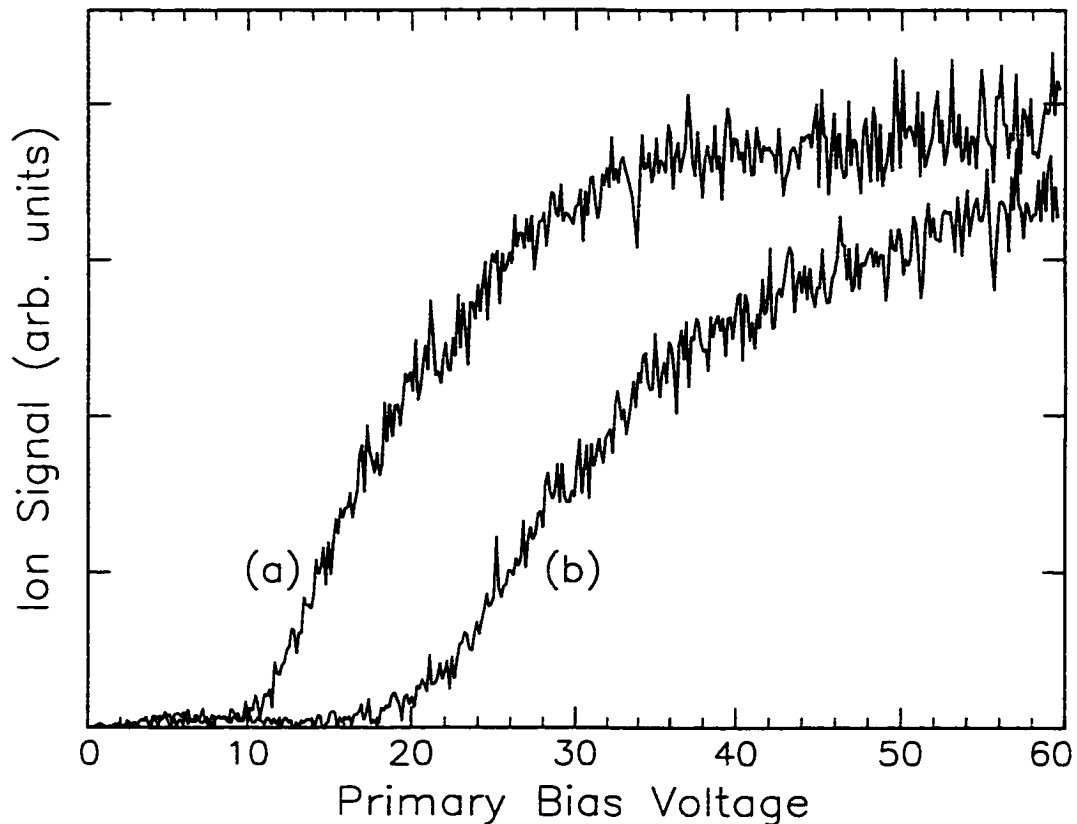


Figure 4.7: Scan (a) is the ion signal level versus bias field for two parallel, simultaneous HCPs at the “ $t=0$ ” position. Scan (b) is the same signal for a single HCP. There is a factor of 1.8 in field between the two scans.

Two-HCP ionization at $t=0$. With the micrometer position still at “ $t=0$,” the bias voltage on each wafer is now set to be the same polarity. The ionization due to both HCPs at “ $t=0$ ” versus bias voltage is now acquired. This dual HCP ionization scan is then compared to that for a single HCP. The scan produced by a single HCP should yield a given percentage of ionization at a bias voltage of twice that for the the dual HCP case. In practice, this has proven a bit hard to achieve (for unknown reasons), but factors of 1.6 - 1.8 are possible. A sample of such data is shown in Fig. 4.7.

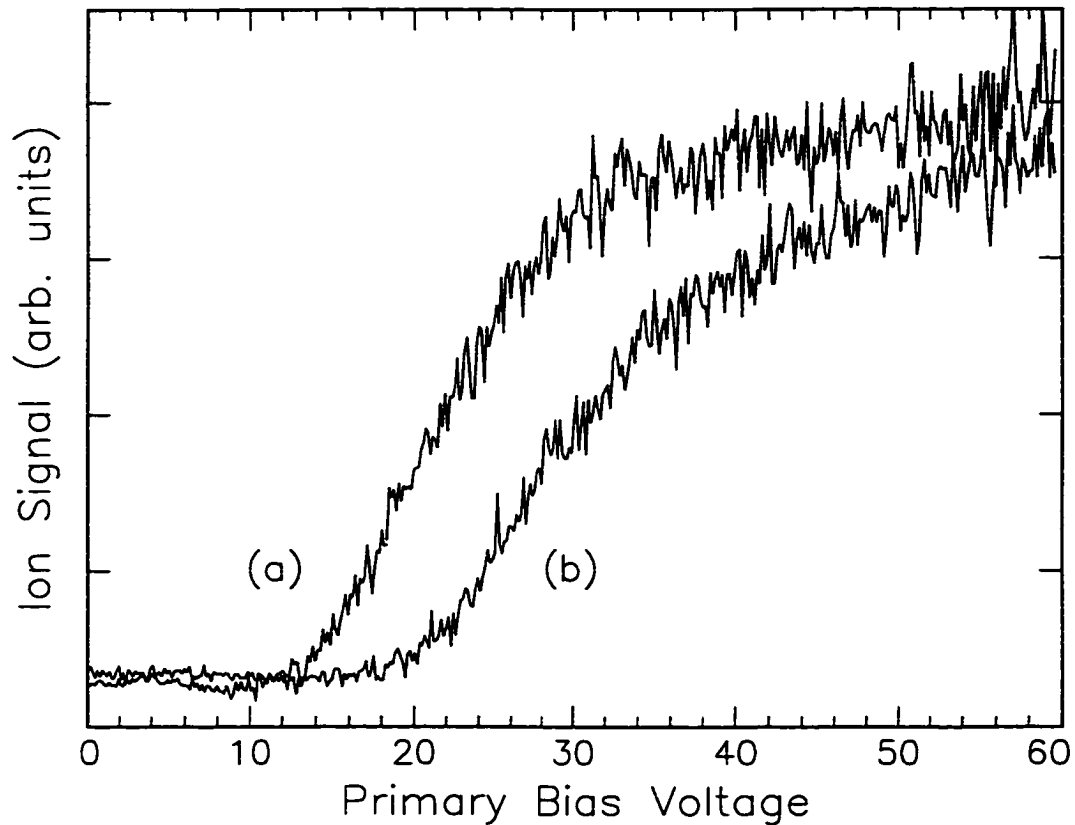


Figure 4.8: Scan (a) is the ion signal level versus bias field for two perpendicular, simultaneous HCPs at the “ $t=0$ ” position. Scan (b) is the same signal for a single HCP. There is a factor of $\approx \sqrt{2}$ in bias fields between the two scans.

Under the same conditions, this scan is repeated with the variable wafer rotated by 90 degrees with respect to the other. This produces a net-linearly polarized HCP with an amplitude of $\sqrt{2}$ times that of a single HCP (see Fig. 4.2). A given ionization percentage for a single HCP should appear at a bias voltage $\sqrt{2}$ times larger than that for this dual cross-polarized case. Factors negligibly different from $\sqrt{2}$ are routinely possible. A sample of such data is shown in Fig. 4.8.

The data acquired up to this point has largely been necessary system diagnostics. At this point, we may begin studying the effects of a 1/4-cycle circularly polarized

THz field.

4.3 Ionization due to a 1/4-cycle circularly polarized field¹

4.3.1 Results and Discussion: Impulsive Regime

At this point, the many diagnostics have been performed and the system is ready for data acquisition on the primary experiment of interest. In this section, results and discussion will be presented in the impulsive regime. This is a set of experimental conditions where any time scales associated with atomic motion (orbital motion of the electron, with period $2\pi n^3$) are slow compared to that of the HCP field (time scale of ≈ 0.5 ps), e.g. the HCP field acts as an impulsive force (see Ref. [2]). Although the impulsive regime for HCP experiments is generally considered to be for $n \geq 20$, for a 0.5 ps HCP, this experiment will clearly serve as an indication of just where the impulse/nonimpulse boundary occurs, as will be demonstrated at the end of this chapter. The following discussion then, will assume the impulsive regime. The non-impulsive regime of this experiment will be considered in the next section.

Using Fig. 4.2 as a guide, it is apparent that relative time delays between the HCPs of 0.25 and 0.5 ps will be of interest here, as they form plausible versions of 1/4-cycle, circularly polarized THz radiation. These time delays are easily set, as we currently have knowledge of the “t=0” position. By simply changing the translation stage position referred to above by a suitable amount, we can achieve any desired time delay. Due to the nature of the delay line created by the stage, the required micrometer setting off of t=0 can be calculated from

¹T.J. Bensity, et. al., Phys. Rev. Lett. **79**, 2018 (1997)

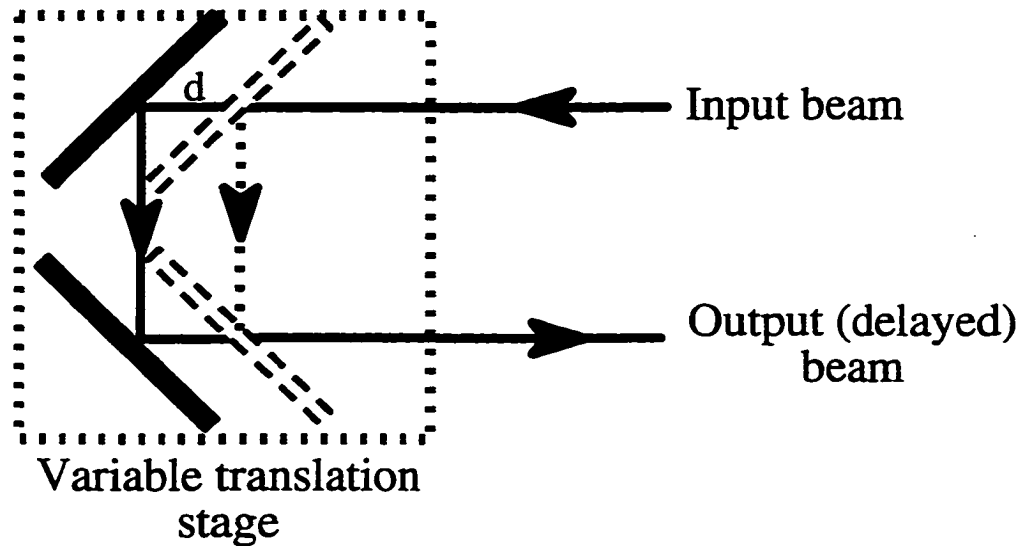


Figure 4.9: The mechanism behind the time delay for light that irradiates one of the two GaAs wafers used in this experiment. Two mirrors mutually oriented at 90 degrees are mounted on a movable translation stage. Note that changing the stage position by an amount d changes the optical path of the light by an amount $2d$. This time delay leg is what is represented by the broken line labeled “Variable Delay” in Fig. 4.5.

$$\Delta d = \frac{ct_d}{2}, \quad (4.5)$$

where Δd is the amount the micrometer must be moved away from the “ $t=0$ ” position, c is the speed of light, and t_d is the desired time delay between the two HCPs. The factor of two arises from the nature of the time delay leg, illustrated in Fig. 4.9.

In acquiring data for this experiment, a time delay $t_d = 0.25$ ps is chosen first, and the micrometer is appropriately set. Both bias voltages are turned on. The bias voltages are slowly ramped from 0 to about 60 V while the ion signal produced is gated and monitored by the digital oscilloscope. A PC interfaced to the oscilloscope via GPIB integrates the signal to a single number (the area under the ion signal) and

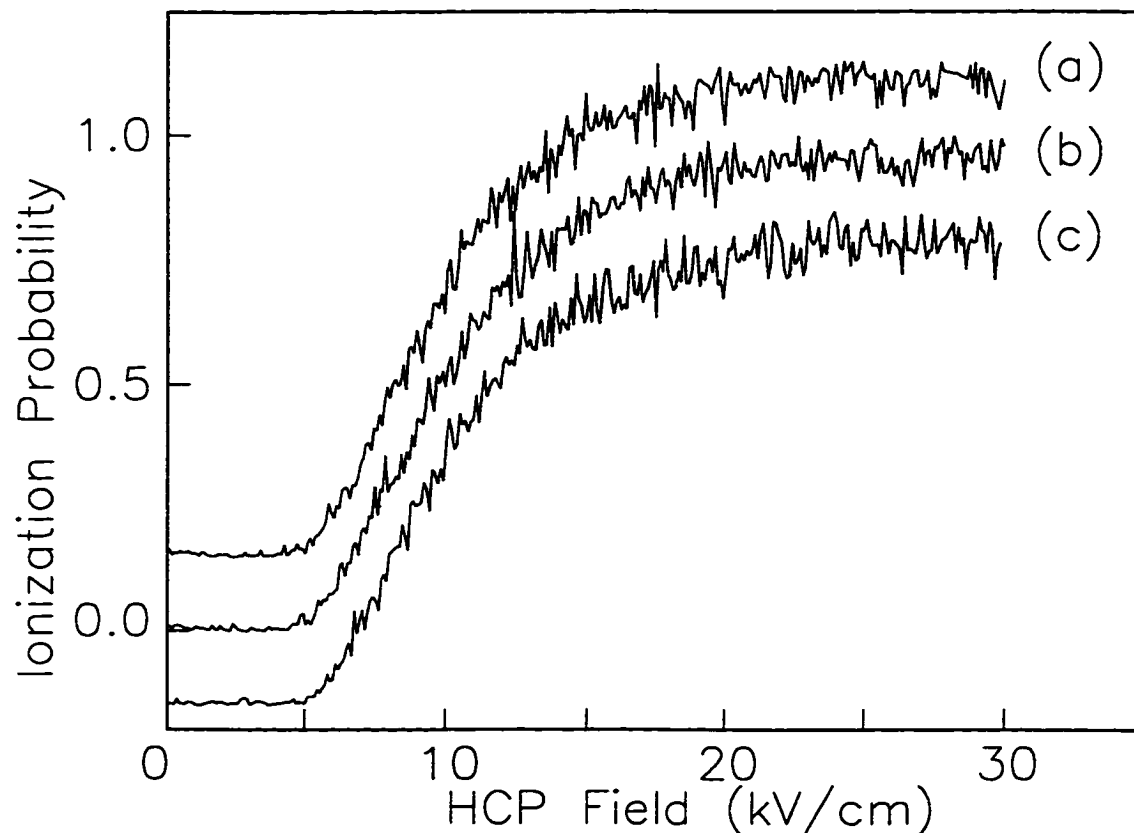


Figure 4.10: The ionization of the $n = 23d$ state in Na as a function of field amplitude in each of two cross polarized HCPs with a relative time delay of (a) 0 ps, (b) 0.25 ps, and (c) 0.5 ps. The scans are identical, and artificially offset for illustration. The HCP amplitude determination was aided by the classical calculation.

saves it to disk for later analysis. In practice, about 15 such “areas” are averaged together to form “a data point.” The micrometer is then set for a time delay of $t_d = 0.5$ ps and the data acquisition is repeated. Finally, the micrometer position is set to $t_d = 0$, and the acquisition is repeated for a third time. The results for the $n = 23d$ state in Na is shown in Fig. 4.10.

This figure captures the remarkable result of this experiment. Moving the micrometer position away from $t=0$ by 0.25 and 0.5 ps produces *the same* ion yield vs.

bias voltage response as the linear $t_d = 0$ case. This indicates, at least in this impulsive regime, that *the ionization of Rydberg atoms by 1/4-cycle circularly polarized THz fields is independent of the time-varying polarization of the field*. This contrasts sharply to the dramatic differences in the ionization of atoms using conventional optical or microwave fields that are linearly and circularly polarized [5]. Intuitively this may be surprising as well.

How can a 2D rotating field (force), to which a charged electron directly responds, via $\vec{F} = q\vec{E}$, eject Rydberg electrons from an atom in exactly the same manner as a 1D field with a fixed direction of polarization?

Clearly some analysis is needed.

The $t_d = 0$ case is very important to this experiment, even though the resultant field is still just a linearly polarized HCP field. Previously formed ideas and conclusions about the HCP ionization process, discussed in Chapter 3, explain the ionization mechanism due to a single, linearly polarized HCP. In other words, “we understand” how a single HCP interacts with a Rydberg electron. So although just another linearly polarized HCP, the $t_d = 0$ case is created from two cross polarized HCPs. Its composition is identical to the more interesting 1/4-cycle cases we desire to study, yet it still retains a link back to the results of previously scrutinized research. For comparison sake later, this $t_d = 0$ case will serve as our new linearly polarized HCP. No work, other than the previously mentioned diagnostics, will be done here with a linearly polarized HCP generated from a single GaAs wafer. However, to test our belief that the $t_d = 0$ case is truly a linear field and behaves as such, we have done a systematic comparison between this field and a single HCP generated by only one GaAs wafer. This study proceeded as follows:

1. Tune to a given n -state, between 15 and 30.

2. Determine the “t=0” position by scanning the relative delay between the two HCPs with parallel (or antiparallel) polarization.
3. Set the relative delay to this “t=0” position.
4. Rotate the variable GaAs wafer so it is oriented at 90 degrees with respect to the other wafer.
5. Slowly ramp the same bias voltage across both wafers simultaneously, from 0 to 60 V, and monitor the ionization yield as a function of this voltage.
6. Turn off the bias voltage on one of the wafers so only a single HCP is now incident.
7. Slowly ramp the wafer’s bias voltage from 0 to 60 V, and monitor the ionization yield as a function of this voltage.
8. Define F_k^p to be the field required to produce a level p of ionization for k (1 or 2) HCPs.
9. Define α as

$$\alpha = \frac{F_1^{10\%}}{F_2^{10\%}} \quad (4.6)$$

10. Plot α versus n , as shown in Fig. 4.11.

In this figure, α is scattered about $\sqrt{2}$. This is consistent with the fact that the peak field amplitude of the linear field produced by two simultaneous cross polarized HCPs is $\sqrt{2}$ larger than that of a single HCP (this is just the Pythagorean theorem). This confirms the linear nature and behavior of the net field produced by the simultaneous cross polarized HCPs. We have defined α at other percentages as well (20%, 50%, and 70%), only to get the same results.

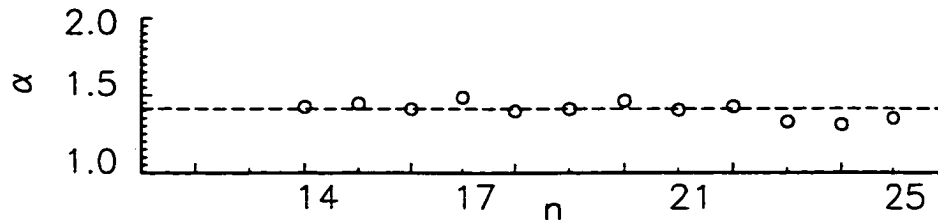


Figure 4.11: The ratio of the field required to produce a certain percentage of ionization between the linear case produced by two simultaneous cross polarized HCPs and a single HCP as a function of n , the principal quantum number.

4.3.2 Results and Discussion: Non-Impulsive Regime

The non-impulsive regime is defined once again by comparing the atomic time scales to those of the HCP field. In this regime, the time scales of the HCP field ($\approx 0.5ps$ FWHM) are slow compared to that of the atom, in particular, the electron's classical motion, with period $2\pi n^3$. This means, for example, that there is significant motion of the electron during the time that the HCP field is present. In this regime, the momentum kick description and accompanying energy shift, that does such a fine job describing the ionization process in the impulsive regime must be modified.

Half-cycle pulses came onto the scene about 10 years ago and were embraced as a tool in Rydberg atom studies because of the short impulsive fields they are, relative to the atoms themselves. But atomic physics is certainly more than 10 years old, and much work has been done on the ionization of atoms due to external fields [10]. In general, the Coulomb potential, $V = -1/r$ is modified by the presence of an external field, $\vec{F} = F_e \hat{z}$ to

$$V = -\frac{1}{r} + F_e z, \quad (4.7)$$

using the relation between field (force) and potential energy that $V_e = \int \vec{F}_e \cdot d\vec{r}$. As

an example of this external perturbation, we again refer to Fig. 3.4, and the discussion in Section 3.2.2.

The figure shows a 1D version of the Coulomb and a combined Coulomb/external field potentials. The additional term in the potential is due to the external field, and adds a linear form to the $-1/r$ term as a function of z , with slope F_e . This causes the potential to “bend down” along the $-\hat{z}$ or “downhill” side, and “bend up” along the $+\hat{z}$, or “uphill” side, as shown. The downhill bending of the potential effectively “opens the door” for electrons to leave the atom, and is the ionization mechanism we seek. In a classical sense, imagine a Rydberg electron oscillating with period $2\pi n^3$ inside of a Coulomb potential so modified by an external HCP field. As it approaches the point along the z -axis where the outer turning point would be in the absence of the static field, it now sees a saddle point, over which it may pass, becoming ionized.

Up until now, nothing has been said about the form of the external field, F_e . This classical ionization picture can proceed as discussed for any type of external field, including a static electric field, oscillating electric field, HCP, or even a strange rotating THz field, but there are a couple of conditions.

The first is that the field amplitude is strong enough to “bend” the potential down enough so some bound state of interest can ionize[11]. This field limit is given by $1/16n^4$.

The second is that the potential is actually bent over at the time the electron travels near the saddle point position.

In a static electric field, the potential is always bent over, but this is not the case for a time dependent field, like the THz fields of interest here. But we are discussing the non-impulsive regime now, where the THz field acts like a slowly evolving, nearly static field, relative to the motion of the electron oscillating inside of the potential, so

when the field is present, the potential bends over, and there is plenty of opportunity for the electron to visit the saddle point and escape.

In the non-impulsive regime, the ionization yield due to the 1/4-cycle circularly polarized THz field versus the field amplitude begins to depend critically on the relative time delay between the two component HCPs. In other words, the ionization yields as a function of field amplitude is no longer identical between the 0, 0.25 and 0.5 ps relative delay cases. This is shown in a different way by the data presented in Fig. 4.12.

In this figure, the $n = 18$ Rydberg state was used. The field amplitude of two HCPs is held fixed, while ionization yield was monitored as a function of the relative time delay between them. In the bold scan, or cross polarized case, notice the small change in the signal level during the delay intervals near $t=0$, where the HCPs begin to overlap, forming some version of the 1/4-cycle circularly polarized light. This signal level change is contrasted to that at the same time interval for the normal pitch scan, in which the same procedure was followed, only for the HCPs polarized parallel to each other (this scan is similar to Fig. 4.1).

The small signal level change in the bold scan is evidence of the non-impulsive regime. For now, it is explained with the aid of Fig. 4.2, and will be further addressed in Section 4.4.3. Notice that in each of the three particular cases shown in Fig 4.2, there are variations in the peak field amplitude. This is simply a matter of how two cross polarized fields, each with a half-cycle structure, combine according to the Pythagorean Theorem. As discussed above, the ionization process depends critically on the external field's amplitude in the non-impulsive regime. If the barrier is not bent down enough for instance, the electron cannot classically escape. The difference in the net field amplitudes between the 0, 0.25 and 0.5 ps delays is in part what causes differing amount of ionization between these cases; each case bends the potential over

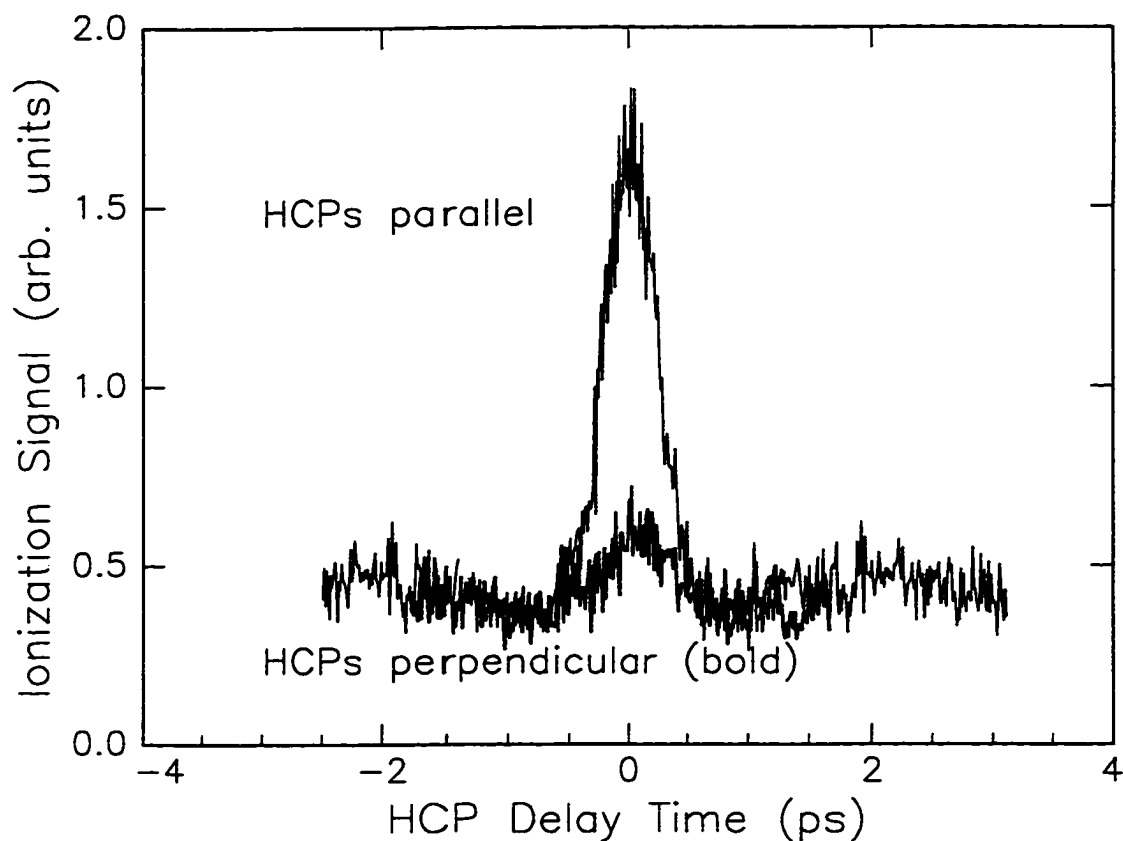


Figure 4.12: The ionization of an $n = 18d$, $m = 0$ Rydberg state as a function of the delay time between two cross-polarized HCPs. The amplitude of each HCP is held fixed during the scan. The normal pitch curve is data for two HCPs polarized parallel to each other. The bold pitch curve is for two cross polarized HCPs. The bias voltage on the HCP pair used each scan is identical.

by slightly different amounts. For other nearby time delays, the amplitude differences give rise to the overall signal variation see near $t = 0$ in Fig. 4.12.

In this section, the ionization mechanism in the non-impulsive regime was discussed. Significant alteration of the Coulomb potential contributes to the ionization here, in addition to momentum and energy transfer effect in the impulsive regime.

4.4 Classical Numerical Analysis

4.4.1 Numerical Integration of the Equations of Motion

HCP/Rydberg atom experiment are strongly linked to the classical ideas of the electron's motion and the forces or "kicks" due to the HCP. In the first HCP/Rydberg atom experiment, a classical numerical analysis successfully predicted much of the observed phenomena and gave ample insight into the single HCP/Rydberg electron interaction [15]. Additionally, classical calculations have been used with success in the past for studying ionization processes due to microwave fields [14]. With this in mind, a classical numerical analysis is performed here as well, to try to explain the surprising result.

A classical numerical analysis involves treating the electron as a classical point particle, with -1 unit of charge, and examining the forces on it. A differential equation of motion (in atomic units) for a classical electron in an attractive coulomb potential due to an arbitrary external force can be written as

$$\frac{d^2\vec{r}}{dt^2} = -\frac{1}{r^2}\hat{r} + \vec{F}(t)_{HCP}, \quad (4.8)$$

where \vec{r} is the electron's position vector relative to the nucleus at $\vec{r} = 0$, $\vec{F}(t)_{HCP}$ is the time dependent force due to the externally applied (HCP) field, and t is time. For two identical, cross polarized HCPs modeled as Gaussians, the external field is

defined as

$$\vec{F}(t)_{HCP} = F_0 \left[e^{-t^2/2\sigma^2} \hat{x} + e^{-(t-\delta)^2/2\sigma^2} \hat{y} \right], \quad (4.9)$$

where F_0 is the field amplitude of either HCP, δ is the time separation between the two HCPs, t is time, and σ is usual width parameter.

Since we want to model a bound particle, its classical total energy will be negative, and in correspondence with the (quantum) experiment, it will have $\sqrt{6}$ units of angular momentum ($\sqrt{l(l+1)}$, for $l = 2$). In the absence of $\vec{F}(t)_{HCP}$, Equ. 4.8 reduces to the Kepler problem, and the equation is exactly solvable [16]. The solution is a highly elongated elliptical trajectory, nearly linear in appearance, due to the low value of angular momentum. The core resides at one focal point. In order to use this differential equation of motion to aid in explaining out two HCP ionization problem, we must numerically integrate this equation to obtain $\vec{r}(t)$ and $\vec{v}(t)$, in particular, to the time t_a , just after the classical electron has interacted with a $\vec{F}(t)_{HCP}$ (note $F(t \geq t_a)_{HCP} = 0$). If we know $\vec{r}(t_a)$ and $\vec{v}(t_a)$, we can calculate the electron's energy via

$$E_a = \frac{1}{2} \vec{v}(t_a)^2 - \frac{1}{r(t_a)}. \quad (4.10)$$

In attempting to reproduce the experimental results, we

1. Choose an initial value of F_0 ,
2. set initial conditions on \vec{r} and \vec{v} such that \bar{r} and \bar{v} for an ensemble of orbits match the quantum mechanical values of $\langle r \rangle$, $\langle r^2 \rangle$, $\langle 1/r \rangle$ to within 1%, and $\langle 1/r^2 \rangle$ to within 5%,
3. numerically integrate the equation of motion through the full duration of the

total HCP field using a 5th order Runge-Kutta algorithm with adaptive stepsize control[6],

4. check if $E_a > 0$ and if so, then $\vec{F}(t)_{HCP}$ has created an ion, and the event is logged,
5. then increment the value of F_0 as in a ramping sequence, and repeat the whole process for a new ensemble.

In actual simulation, this integration then “energy check” is performed for an ensemble of many thousand of classical orbits to build a suitable distribution that mimics a “classical-atom.” All such classical orbits are launched such that the projection of angular momentum, \vec{L} , along the quantization axis of the problem is zero, or $m = 0$ in correspondence to the actual experiment. The quantization axis of the problem is the propagation axis of the two HCPs, or the \hat{z} -axis. There are many interesting details of implementing this classical simulation saved for Chapter 6, which explicitly discusses using classical numerical analysis in HCP/Rydberg atom experiments. Simulation results analogous to the experimental results presented in Fig. 4.10 are shown in Fig. 4.13.

To our delight, the experimental results are reproduced in full. The 0 ps delay case is identical to the 0.25 and 0.5 ps delay cases. These results however, are only the results of many thousands of numerical integrations. Very little practical insight or answers into the overall 1/4-cycle pulse interaction has been gained. Nevertheless, the results are encouraging. The fact that the classical calculation has reproduced our data means some insightful information is buried somewhere in the classical equations of motion.

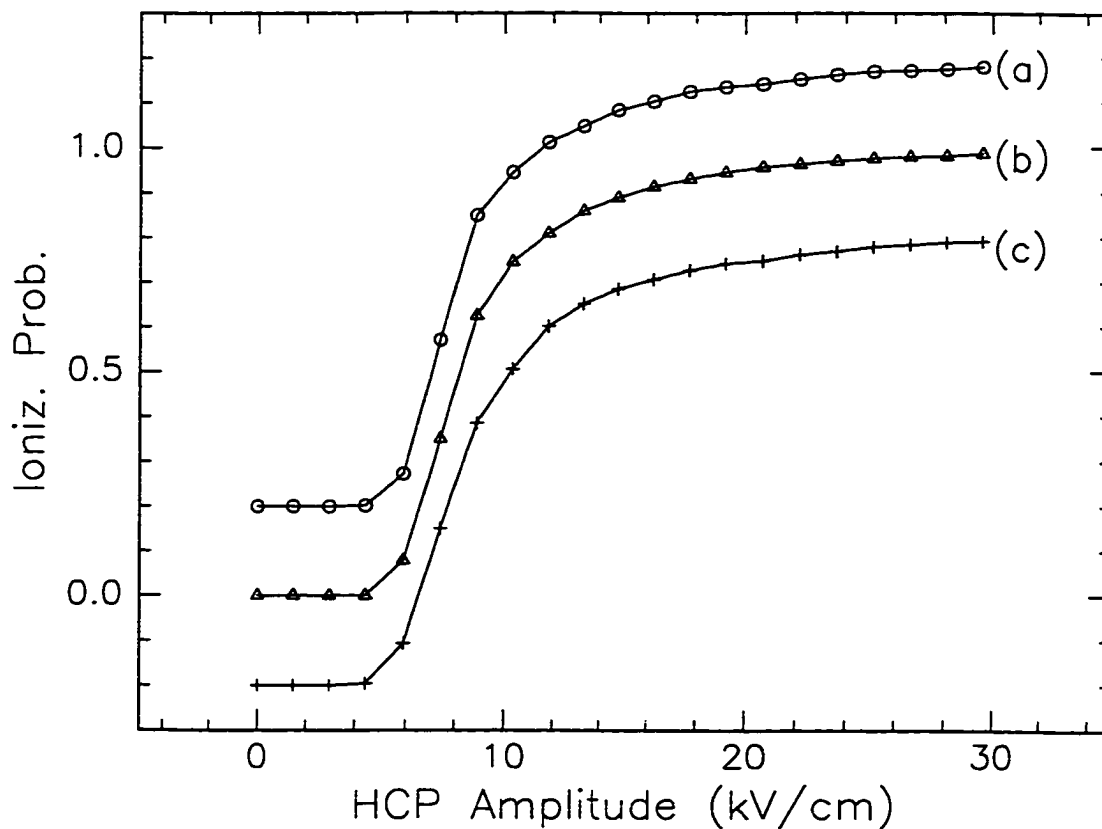


Figure 4.13: Classical numerical predictions of the ionization of the $n = 23d$ state in Na as a function of HCP field, F_0 (see text) for two cross polarized HCPs with a relative time delay of (a) 0 ps, (b) 0.25 ps, and (c) 0.5 ps between them. The scans are identical, and artificially offset for illustration. This figure is the calculated analogy of Fig. 4.10.

4.4.2 Classical Insight: Impulsive Regime

To begin extracting some more insightful information, we return to the most fundamental description of a HCP/Rydberg atom interaction:

1. A HCP changes the momentum distribution of an electron.
2. Since energy and momentum are related, the shift in momentum shifts the electron's energy as well.
3. If the shift in energy causes the electron's energy to become positive, the electron has become unbound, or ionized by the HCP.

With the impulse carried by a HCP having units of momentum, it appears as if examining the momentum distributions might be of use here. In this light, the momentum distribution of a classical ensemble along the numerical integration loop, from time $t = 0$ to after the net field has passed, is examined. For the first look here, a classical $n = 25d$, $m = 0$, ensemble is irradiated with a single HCP polarized along the \hat{x} -axis. The integration process constantly updates six variables of integration as it goes: three components of \vec{r} , (r_x, r_y, r_z), and three components of \vec{v} , (v_x, v_y, v_z). At any fixed time during the integration running histograms of v_x , v_y , and v_z are created (recall $\vec{p} = m_e \vec{v}$, but $m_e(\text{mass})=1$ in atomic units). The results are shown in Fig. 4.14.

In this figure, the compiled momentum histograms are plotted for each of the three Cartesian directions. The HCP interaction is apparent. The momentum distribution along the \hat{x} -axis is clearly shifted by the amount equal to $|\vec{A}|$, the time integral of the HCP field. For a 0.5 ps FWHM Gaussian HCP field with an amplitude of 3.5 kV/cm, $|\vec{A}| = 0.015$ (a.u.). This shift is the HCP "kick." Note that the momentum along the other two orthogonal Cartesian axes are left unchanged.

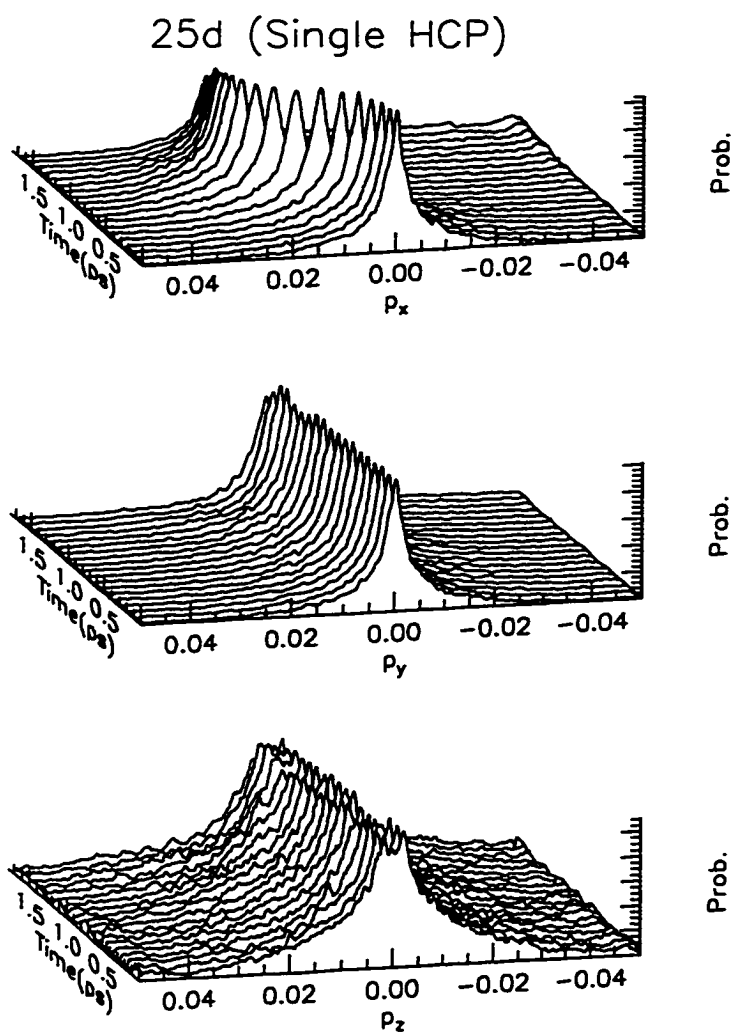


Figure 4.14: Classical momentum distributions of an $n = 25d$, $m = 0$ electron ensemble irradiated with a Gaussian HCP, polarized along the \hat{x} -axis. Note the abrupt shift in the p_x momentum distribution. p_y and p_z remain unchanged.

Next, we compile the same momentum histograms for two cross polarized HCP fields with a 0.25 and 0.5 ps delay between them. The first HCP is polarized along the \hat{x} -axis, and the second along the \hat{y} -axis. The results for the 0.5 ps case are shown in Fig. 4.15. The calculation used to produce these histograms is the same that produced scans (b) and (c) in Fig. 4.13.

Note the abrupt shift in the p_x distribution while p_y and p_z remain unchanged, followed by an abrupt shift in the p_y distribution while p_x and p_z remain unchanged. Energy shifts lead to ionization, so we also consider the energy shift through this process. First only p_x changes. This means any energy shifts towards or away from the ionization limit ($E = 0$) are caused only by changes in p_x . Later, when the 2nd HCP arrives, only p_y changes. Again any energy shift towards or away from ionization are now due solely to changes in p_y . This is the intuitive description we seek. In the impulsive regime,

- shifts in an electron's momentum along orthogonal Cartesian axes do not couple, and
- shifts in an electron's energy towards or away from the ionization limit are independently induced by HCPs polarized along orthogonal Cartesian axes.

Each HCP along an orthogonal axes acts on the Rydberg electron totally independently of any other mutually orthogonal HCP. So the analysis of the 1/4-cycle circularly polarized field data is easier if it is examined in terms of the *component* HCPs creating the net circular field, not the strange, rotating net field itself. The lack of dependence of the ionization yield on the relative time delay between the HCPs simply means orthogonal HCP kicks applied to a Rydberg electron can come at any time, simultaneously or many picoseconds apart[7], but the resulting momentum shifts still do not couple.

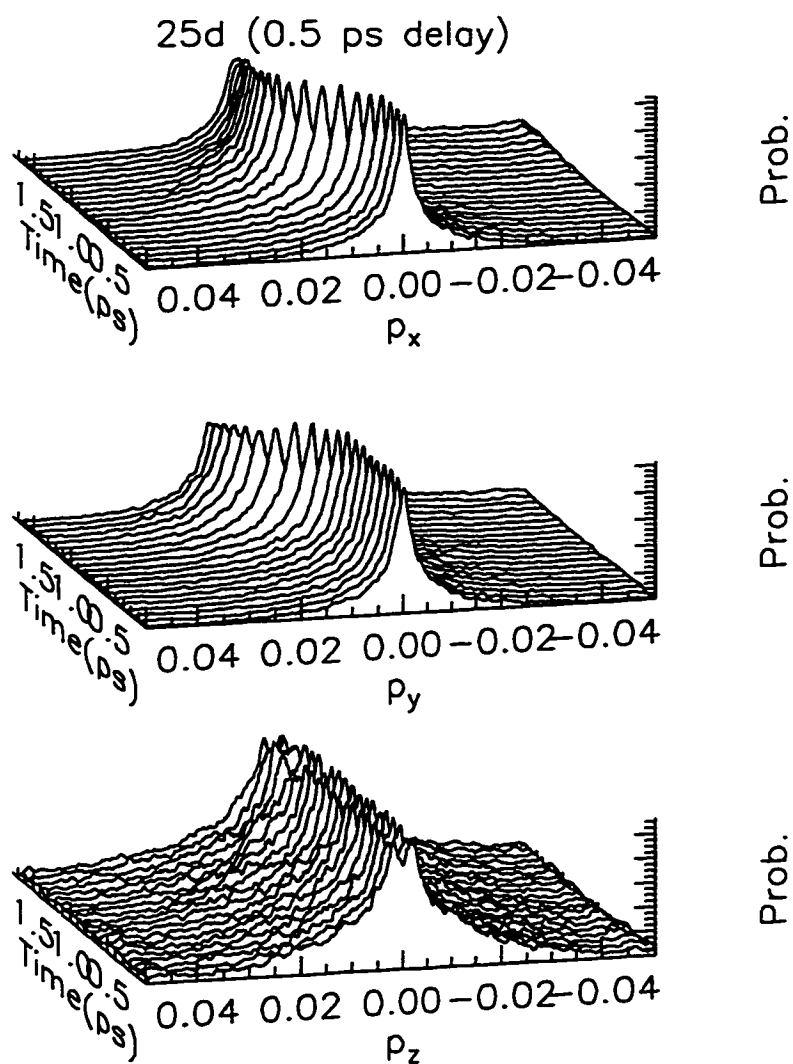


Figure 4.15: Classical momentum distributions of an $n = 25d$, $m = 0$ electron ensemble irradiated with two cross polarized, Gaussian HCPs with a 0.5 ps relative delay. The first HCP is polarized along the \hat{x} -axis, and the second along the \hat{y} -axis.

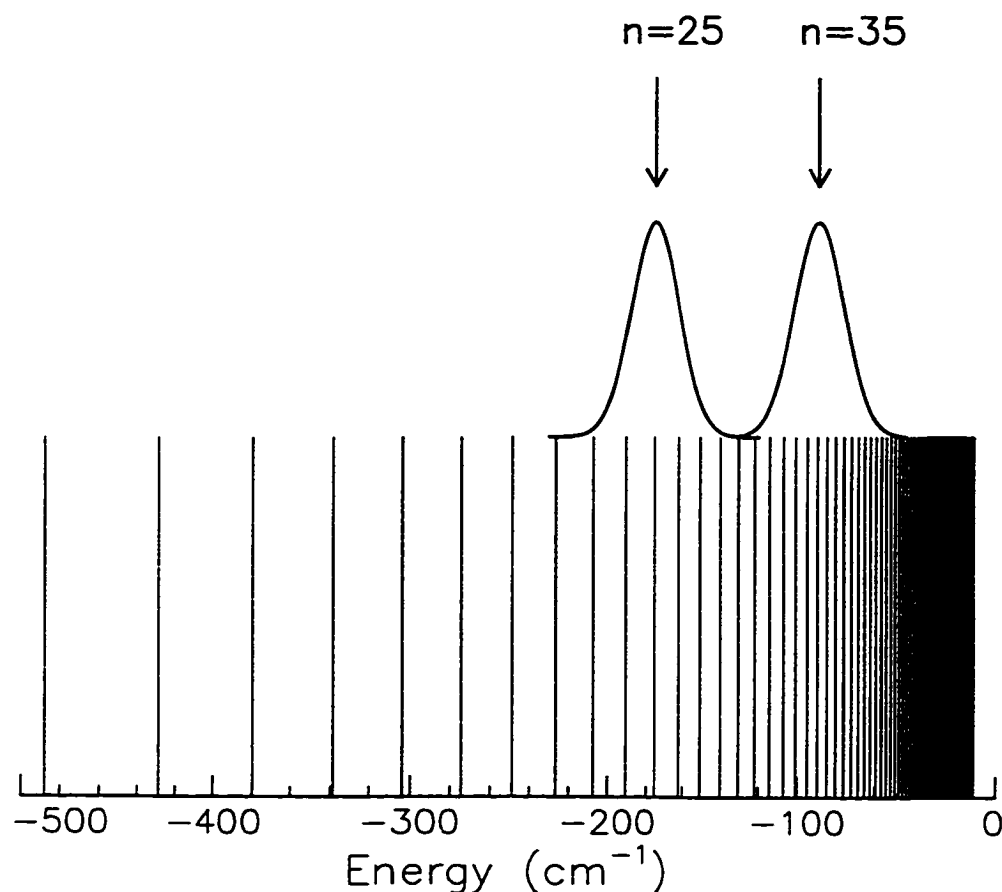


Figure 4.16: A HCP with ≈ 1.0 THz (30 cm^{-1}) of bandwidth plotted against an atomic Rydberg series. The HCP is frequency centered at the $n = 25$ and $n = 35$ resonance energies for comparison. Note how many states lie under the HCP envelope.

There is something quite remarkable in all of this, if the problem is viewed in the frequency domain. A HCP, as generated in this experiment, has a central frequency and bandwidth of about 0.5 THz[15][8]. For an $n = 25d$ Rydberg energy level, there are enough frequencies in such a pulse to couple the the electron population to many nearby states. This is depicted in Fig. 4.16, which shows a HCP plotted in comparison to a Rydberg series, frequency centered at the energy an $n = 25$ and $n = 35$ state for comparison.

In a Rydberg series, the state spacing becomes $2 \cdot 109737/n^3 \text{ cm}^{-1}$. For example, the energy spacing between the $n = 25$ and $n = 26$ Rydberg levels is 13 cm^{-1} . The frequency spectrum of a HCP contains significant power in frequency components between 0 and nearly 30 cm^{-1} [13]. Through dipole couplings, hundreds of states can be coupled together at $n = 25$, and even more at $n = 35$. This means the HCP can spread population all over a local Rydberg spectrum.

Despite this, consider the remarkable order in the momentum distributions shown in Figs. 4.14 and 4.15. A HCP polarized along the j^{th} Cartesian axis simply and independently shifts p_j . Two HCPs polarized along orthogonal axes each shift the electron's momentum components along their respective axes. It's really a very clean interaction, *if viewed in the momentum space picture*. This is a recurring theme in Physics: choose the right perspective, and your answer might be remarkably clear and simple. Trying to model and understand this interaction in terms of quantum state couplings is difficult, but has been done[9][8]. In some of these papers, in particular Bugacov's work, the authors note how the calculations simply become intractable, and had to be stopped when *too many* states become coupled together. These quantum calculation are a more realistic view of the problem, but are not without their difficulties.

4.4.3 Classical Insight: Non-Impulsive Regime

As n is lowered, the interaction begins to have non-impulsive characteristics, as demonstrated by the bold trace of Fig. 4.12. A figure analogous to this is produced by the classical numerical analysis, and is shown in Fig. 4.17. This figure shows the ionization of a classical $n = 14d$, $m = 0$ Rydberg state as a function of time delay between two parallel (normal pitch line) and two cross-polarized (bold line) HCPs.

As mentioned in Section 3.2.2, the ionization process in the non-impulsive regime

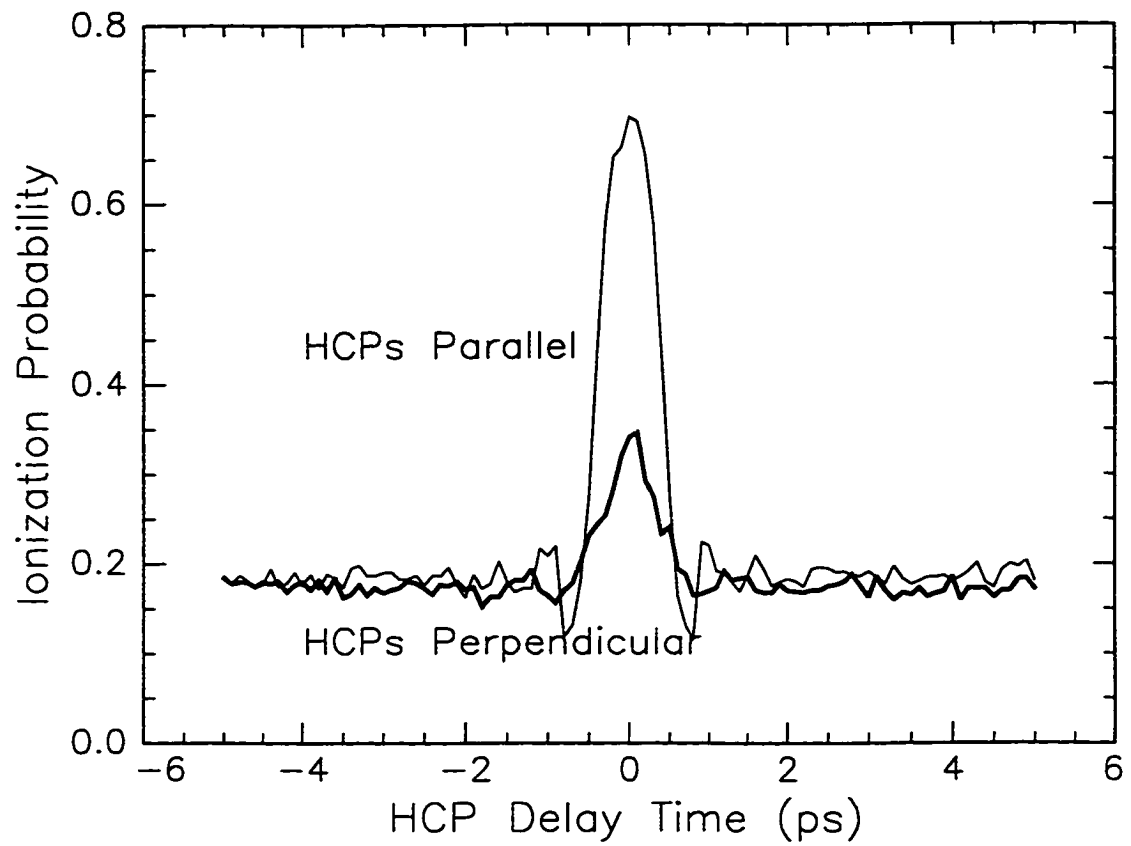


Figure 4.17: Calculated ionization of an $n = 14d, m = 0$ Rydberg state as a function of the delay time between two parallel (normal pitch curve) and cross-polarized (bold pitch curve) HCPs. The field amplitude of each HCP is 20kV/cm

begins to involve an alteration of the binding potential of the electron itself. But this is not the only effect. The electron is now in a time dependent external field. Since there is now significant motion of the electron *during* the HCP field, momentum gained in one Cartesian dimension may very well couple into other dimensions. This is contrasted to the distinct lack of momenta coupling demonstrated in Fig. 4.15. These two non-impulsive effects cause an ionization dependence on the peak amplitude and overall temporal profile of the total HCP field. This is clearly evident in bold traces of Figs. 4.12 and 4.17, near $t = 0$. In the experiment, this non-impulsive behavior is observable at $n = 18$. In the classical model, it is not apparent at $n = 18$, and the calculation had to be run at a lower state, $n = 14$, to demonstrate the effect. This discrepancy is due to uncertainties in the actual HCP duration, set to FWHM=0.5 ps in the calculation. The experimental HCP duration is apparently longer.

4.5 A Systemic Investigation

As a final presentation of the experimental work done, and to bring the two regime problem together, a thorough and concluding systematic investigation, exploring the non-impulsive through impulsive regime is now presented. In this investigation, many n -states of the Na atom, from $15 \leq n \leq 30$ are irradiated by the THz field. The systematic study is done was as follows:

1. Tune to a given n -state, between 15 and 30.
2. Determine the “ $t=0$ ” position by scanning the relative delay between the two HCPs with parallel (or antiparallel) polarization.
3. Set the relative delay to this “ $t=0$ ” position.

4. Rotate the variable GaAs wafer so it is oriented at 90 degrees with respect to the other wafer.
5. Slowly ramp the bias voltage on the two wafers from 0 to 60 V, and monitor the ionization yield as a function of this voltage.
6. Change the relative delay between the HCPs to 0.25 (or 0.5) ps, to begin producing the 1/4-cycle circularly polarized field.
7. Slowly ramp the bias voltage on the two wafers from 0 to 60 V, and monitor the ionization yield as a function of this voltage.
8. Define $F_{t_d}^p$ to be the field required to produce a level p of ionization at a relative HCP delay of t_d between the two HCPs.
9. Define α as the ratio of HCP field amplitudes required to produce equivalent amounts of ionization for two different time delay cases. For example, for an ionization level of 10% for the 0.25 ps delay case,

$$\alpha = \frac{F_0^{10\%}}{F_{0.25}^{10\%}}. \quad (4.11)$$

10. Plot α versus n , as shown in Fig. 4.18, which shows n versus α for the 0.25 (inset A) and 0.5 (inset B) ps delay cases.

Note for $n > 19$, α is scattered about 1.0, indicating that the problem is in the impulsive regime and there is no difference in the ionization yield due to the linear or 1/4-cycle circularly polarized fields. Below $n = 19$, α begins systematically shifting away from 1.0, indicating that there is now a difference in ionization between the linear and 1/4-cycle circularly polarized fields, consistent with the onset of the non-impulsive regime, for this value of n . Data acquired for $n \leq 18$ appears to follow

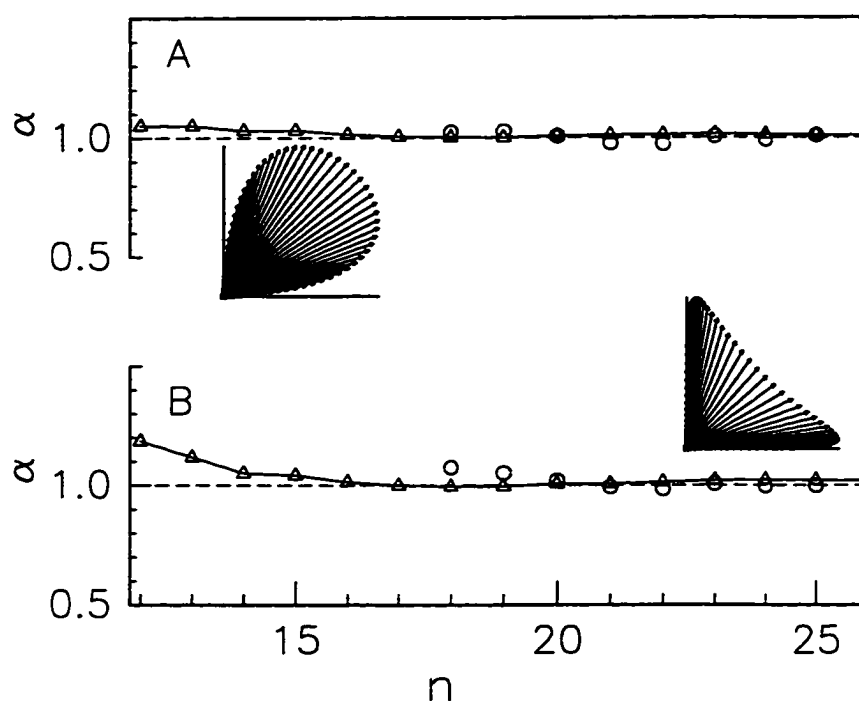


Figure 4.18: The ratio of the field required to produce any percentage of ionization between the 1/4-cycle circularly polarized case and the linear case created by two simultaneous cross-polarized HCPs versus n , the principal quantum number. The triangles are predicted by the classical calculation, the circles are data, and the solid line helps to guide the eye. The insets serve as reminders to the net 1/4 cycle field produced, as viewing it along the propagation axis. Inset A is for the 0.25 ps delay case, and inset B is for the 0.5 ps delay case.

the systematic trend away from 1.0 as well, but is somewhat suspect. The current HCP apparatus cannot produce fields large enough to completely ionize these lower Rydberg states, allowing for proper normalization of the data. The ratio, α , as defined above was also calculated at several other ionization levels, including 25%, 30%, 50%, and 80%. The results are the same as shown in Fig. 4.18.

In a “backup” analysis, the two ionization versus bias voltage scans were taken, both involving two cross polarized HCPs. One scan had a relative time delay of 0 ps (linearly polarized net field), and the other had a relative time delay of 0.25 ps (1/4-cycle circularly polarized). For these two scans, a multiplicative factor in field (a more inclusive definition of α) was applied to the field axes of one scan, in an iterative manner, until χ^2 between the two ionization yields was minimized. A Golden Search algorithm was employed to perform this minimization[6]. This is a linear fit, which appears to be justified based on the equivalent results seen by the individual (10% - 80%) ratios discussed above.

4.6 Conclusions

We have shown in this chapter how ionization of Na Rydberg atoms proceeds for 1/4-cycle circularly polarized THz radiation. Comparisons are made with the more familiar linear polarized field, and the problem is addressed in both the impulsive and non-impulsive regimes. In the impulsive regime, the ionization process is shown to be independent of the time varying polarization of the THz field. This is not the case in the non-impulsive regime. Classical numerical calculation have provided invaluable insight into the ionization process.

Bibliography

- [1] B.I. Green, et. al., *Appl. Phys. Lett.* **59**, 893 (1991); D. You, et. al., *Opt. Lett.*, **18**, 290 (1993).
- [2] P.A. Tipler, *Physics for Scientists and Engineers*, Worth Publishers, New York, 1991, p. 210.
- [3] J.A. Armstrong, *Appl. Phys. Lett.* **10**, 16 (1967); F. Salin, et. al, *Applied Optics* **26**, 4528 (1987); J. Diels, et. al., *Ultrashort Laser Pulse Phenomena*, Academic Press, 1996, p. 377, Fig. 8.6.
- [4] Through a measurement just like this, the index of refraction of GaAs can be calculated to be about 3.6, consistent with cataloged data on GaAs. See J.C. Brice, *Properties of Gallium Arsenide*, INSPEC, 1986, Section 8.7.
- [5] H.R. Reiss, *Phys. Rev. Lett.* **29**, 1129 (1972); R.A. Fox, et. al., *Phys. Rev. Lett.* **26**, 1416 (1971); P. Kappertz, et. al., *Phys. Rev. A* **47**, 4749 (1993); J. Zakrzewski, et. al., *Phys. Rev. A* **47**, R2468, 1993; P. Fu, et. al., *Phys. Rev. Lett.* **64**, 511 (1990).
- [6] W.H. Press, et. al., *Numerical Recipes in C, 2nd ed.*, Cambridge University Press, 1992.
- [7] Experimental data was also acquired for relative HCP time delays as long as 10 ps. The same “no coupling” effect was observed.

- [8] N.E. Tielking and R.R. Jones, *Phys. Rev. A* **52**, 1371 (1995), Fig. 1.
- [9] F. Robicheaux, *Phys. Rev. A*, 1998; K.J. LaGattuta and P.B. Lerner, *Phys. Rev. A* **49**, R1547 (1994); A. Bugacov, et. al., *Phys. Rev. A* **51**, 1490 (1995); C.O. Reinhold, et. al., *J. Phys. B* **26**, L659 (1993).
- [10] T.F. Gallagher, *Rydberg Atoms*, Cambridge University Press, 1992, Chapter XX. M.H. Nayfeh and C.W. Clark, *Atomic Excitation and Recombination in External Fields*, Gordon Breach Science Publishers, 1985. R.F. Stebbings and F.B. Dunning, *Rydberg States of Atoms and Molecules*, Cambridge University Press, 1983.
- [11] In a Quantum picture, there is no such thing as a bound state in the presence of an external electric field, since the population may tunnel through the saddle-point in the potential into the continuum. Classically however, there are.
- [12] N.E. Tielking and R.R. Jones, *Phys. Rev. A*, **52**, 1371 (1995).
- [13] D. You, R.R. Jones, and P.H. Bucksbaum, *Opt. Lett.*, **18**, 290 (1993).
- [14] J.G. Leopold and I.C. Percival, *J. Phys. B*, **12**, 709 (1979); *ibid.*, *J. Phys. B*, **13**, 31 (1980); D. Banks and J.G. Leopold, *J. Phys. B* **11**, 37 (1978).
- [15] R.R. Jones, D. You, P.H. Bucksbaum, *Phys. Rev. Lett.*, **70**, 1236 (1993).
- [16] H. Goldstein, *Classical Mechanics*, 2nd ed., Addison-Wesley, 1980.

Chapter 5

Electron-Ion Recombination Using Half-Cycle Pulses

Chapters 3 and 4 have shown that half-cycle pulses (HCPs) can be used to impulsively alter the momentum and energy of a Rydberg electron. Suppose here, an electron has been forced to leave its host ion. That is, by some external means, it has been given proper energy and momentum to escape the atom, and is shooting off in some direction, leaving its parent ion behind. The atom is breaking apart. The question this experiment will attempt to answer is:

- is it possible to alter the energy and momentum of this escaping electron, using a HCP, such that the electron “recombines” with its parent ion. In effect, can the atom be “put back together” with a HCP?

5.1 Introduction

The prospect of recombining ions and electrons is not new [1]. This process is found in the literature under a variety of names, the most popular are apparently “dielectronic recombination,” “radiative recombination,” or “three-body recombination.” The general scenario for recombination is as follows.

- I. An ion and free electron are created, and prepared (e.g. energy, angular momentum, etc.) such that they are capable of pairing with each other, forming a neutral species.
- II. The ion and electron are brought into close proximity, which encourages them to pair via “electron capture.” This is done, for example, by irradiating an ion target with a free electron beam.
- III. The ion and electron become paired, a neutral is formed.

In the literature, a variety of situations that form a potential recombination environment are used. A common theme they share is that the electron capture mechanism extracts energy and momentum from the free electron, forcing it back onto the ion, into a bound state. Typically this mechanism is a third body to which energy and momentum may be transferred. Recombination is an area rich with past work in many branches of science, including chemistry, atmospheric science, interstellar space, combustion, and fusion; anywhere electrons and ions might be found[4]

In this experiment, recombination occurs in an experimental setup very different from those cited above. There are no ion targets or electron beams. In their place, neutral atoms are purposely excited into an electron/ion pair using laser beams. This charged pair is then irradiated with a HCP, which serves as the recombination agent. It appears as if the recombination we propose here is radiatively assisted, but the HCP makes the process appear more like three-body recombination. This is due to the similarity between the unipolar HCP field and the transverse component of the force felt by a charged particle passing by.

5.2 HCP Assisted Electron-Ion Recombination

To introduce the proposed concepts, consider the one-dimensional Coulomb potential plotted in Fig. 5.1. In this figure, ground state population, which is bound, with negative energy, E_1 is excited to the continuum, and is free to escape the atom at position (a). It has positive (unbound) energy E_2 in the continuum. Since this continuum population has energy and angular momentum, it begins to expand outwards along the \hat{z} -axis with momentum p_0 , as shown by the two small portions of charge and the arrows at positions labeled (b). In the continuum, the charge is unbound, without an outer turning point, and continues to expand away from the core. Clearly, for recombination to occur, the energy of the continuum population must be lowered. In Fig. 5.1, this means the energy of the continuum population must be lowered below $E = 0$, in order to become bound again. Some external means must be provided to lower the energy back to a negative, bound level.

Our proposal here is to extract linear momentum from the outgoing charge distribution using a HCP. As mentioned in Chapter 3, HCPs are best characterized by a parameter \vec{A} , defined as $\vec{A} = -\int \vec{F}(t)_{HCP} dt$, the negative of the time integrated HCP field, $\vec{F}(t)_{HCP}$. This parameter \vec{A} has units of momentum, and is simply the impulse carried by the HCP field that it may impart to a free, or nearly free electronic charge distribution[5]. The idea of extracting linear momentum from a continuum charge distribution is illustrated in Fig. 5.2.

This figure is identical to Fig. 5.1 except that it shows the direction of an impulse, \vec{A} , as delivered by an incident HCP, and the proposed effects it will have. The effect of the applied impulse on the outgoing charge distribution is summarized by the arrows connecting each initial and final charge state. It is straightforward to predict whether or not recombination will occur for a given portion of the charge distribution,

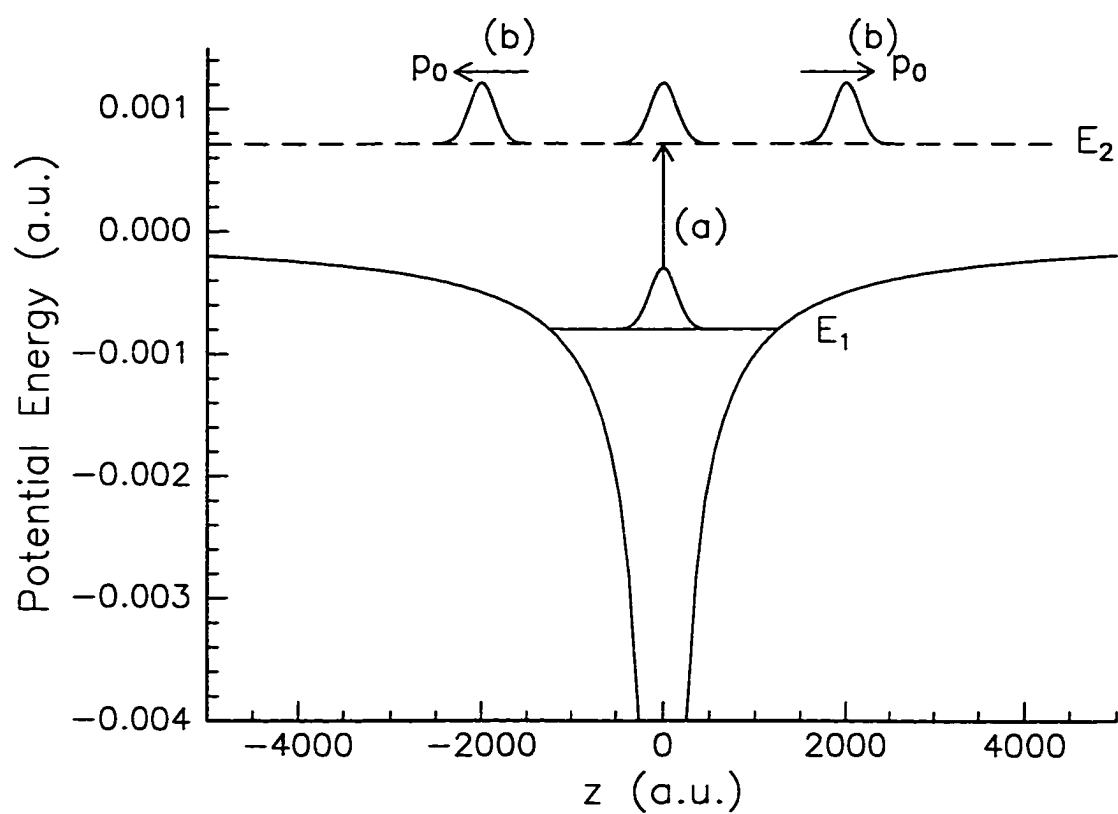


Figure 5.1: A one dimensional Coulomb potential. Bound, state population with energy E_1 is excited into the continuum, at (a), with positive energy E_2 , and begins to expand outwards, at (b). The charge expands with momentum p_0 .

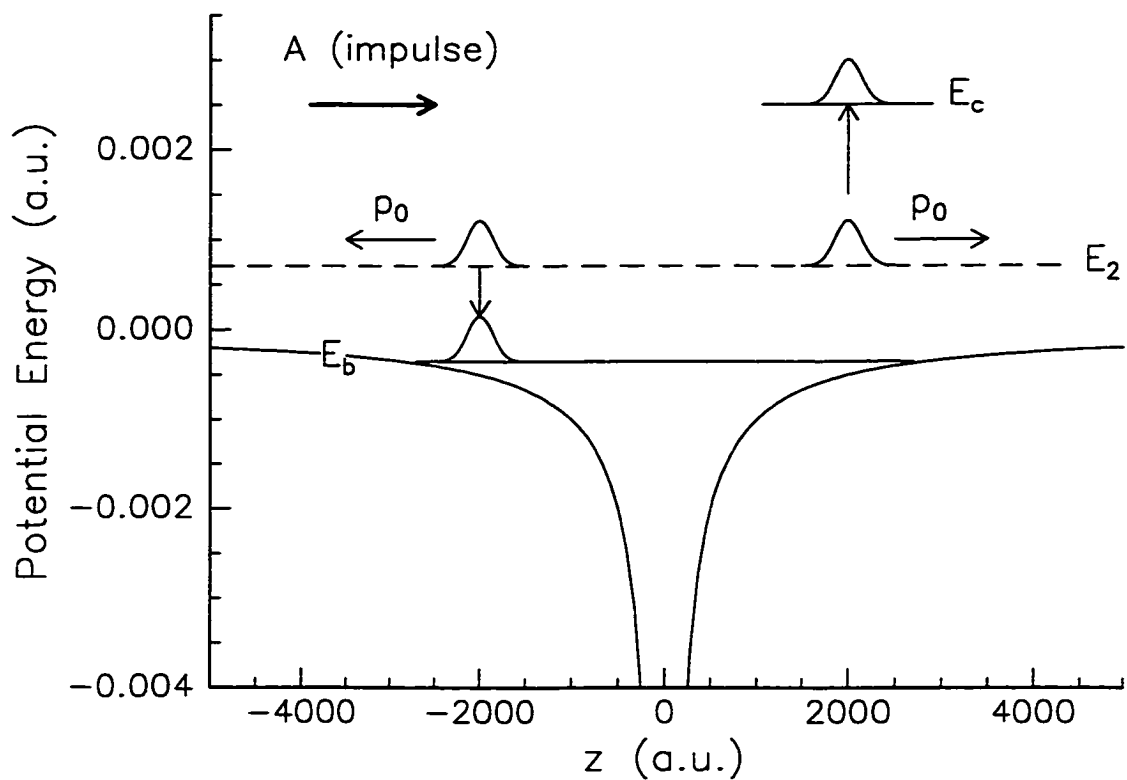


Figure 5.2: A one dimensional potential with an unbound, outgoing charge. The momentum, p_0 , of the outgoing charge is shown. The direction of the impulse, \vec{A} , delivered by the HCP is shown by the large arrow. Initially, the charge portions are all at energy E_2 . After interacting with the HCP, the charges are placed at energy E_b and E_c .

by simply exhausting the possibilities of how the impulse and charge may interact. In fact, there are only three scenarios by which these charge portions will or will not become recombined by the applied impulse. Given that the impulse is oriented towards the right, as shown, possible scenarios include:

I. The charge initially moving towards the left. Its momentum is *opposite* to that of the applied impulse. A vectorial addition of the charge's momentum and the applied impulse will result in a net *extraction* of momentum, relative to the initial momentum of the charge. The charge can be recombined with the ion if the *right amount* of momentum is extracted. Just what the right amount is creates some more possibilities itself:

1. **The impulse is within range.** The charge/impulse orientation is correct. Momentum is extracted from the charge, and its energy is lowered to some bound level, E_b , as shown.
2. **The impulse is too large.** The charge/impulse orientation is correct, but too much momentum is extracted from the charge, reversing its direction, sending it "flying" past the ion with energy $\geq E_2$. The charge remains unbound, in the continuum.
3. **The impulse is too small.** The charge/impulse orientation is correct, but too little momentum is extracted from the charge. Its energy is lowered, and is now less than E_2 , but still positive, and recombination does not occur.

II. The charge initially moving towards the right. Its momentum is *parallel* to that of the applied impulse. A vectorial addition of the impulse and momentum will always result in a net *addition* of momentum, relative to the initial

momentum of the charge. It is impossible to lower the energy of this portion of the charge, and it cannot be recombined. There is still an exchange of energy to the charge, however, and it is further placed in at continuum energy level E_c , as shown in Fig. 5.2. Clearly then, this recombination process will have a strong directional dependence.

III. Three-dimensional consideration. The charge is initially moving perpendicular to the HCP impulse. This case is similar to II above in that there can be no extraction of linear momentum or energy from the electron. In this case, the transfer of energy will always be a positive quantity, and an additional component of momentum will be given to the particle in the direction of the impulse. However, *unlike II*, recombination is possible due to the new orientation the classical orbit may obtain. The trajectory may be reoriented such that it never visits the saddle point spatially, remaining bound to the atom.

These conditions, resulting or not resulting in recombination, can be quantified somewhat, using some simple analysis. Consider the energy transfer to an electron by a HCP, given by

$$\Delta E = \vec{p} \cdot \vec{A} + \frac{1}{2} \vec{A}^2, \quad (5.1)$$

where \vec{p} is the momentum of the electron at the onset of the HCP, and \vec{A} is the impulse carried by the HCP. In order for recombination to occur, for an electron with positive energy E_0 , the condition must hold that

$$E_0 + \Delta E \leq 0. \quad (5.2)$$

In other words, the energy imparted to an electron by the HCP field must lower the initial energy below zero, back to a bound state. For this to happen, ΔE in Equ. 5.1

must be less than zero. If \vec{A} and \vec{p} are antiparallel, momentum can be extracted from the electron, and the dot product in Equ. 5.1 gives some negative value. In this case, ΔE can become negative and recombination can occur (scenario I.1 above). But recombination can only occur up to a certain value of $|\vec{A}|$. If it becomes too large, then the \vec{A}^2 term will dominate Equ. 5.1 and ΔE is a positive number. In this case, the relative orientation between \vec{p} and \vec{A} is correct, but too much momentum is extracted, reversing the direction of the electron, but leaving it in the continuum (scenario I.2 above). Also, if \vec{A} is too small, ΔE will not be negative enough to cause $E_0 < 0$ (scenario II.3 above). Finally, if \vec{A} and \vec{p} are parallel, ΔE will never be negative, and recombination cannot occur; no momentum is extracted and the electron's momentum and energy are merely increased (scenario II above).

This model, of a positive energy charge distribution being recombined by a HCP via momentum extraction is a helpful model for introducing the concepts of HCP assisted recombination, that will be used throughout this chapter. However, experimentally, this system does not prove to be a particularly interesting or rich in dynamics. The experiment has been performed[6] in Ca, in which an electronic wavepacket is photoexcited directly into the continuum. The wavepacket is allowed to evolve for some time t_0 , before being irradiated by a HCP. Initially, a large recombination fraction is observed, which tapers off to zero as a function of t_0 , which confirms the scenarios presented above. Initially, the momentum distribution of the charge is fairly wide, and a significant fraction of the wavepacket's momentum distribution is available to be recombined with a "usual" lab HCP field amplitude ($\sim 5\text{kV/cm}$). As the wavepacket evolves in time, the momentum distribution begins to narrow. A smaller and smaller portion of the wavepacket has momentum that can be recombined; most of it is now moving too slowly, as the momentum distribution narrows and "pinches in" towards the $\langle p \rangle = 0$. Too much momentum is extracted by the impulse (sce-

nario II.3 above). This process is captured by a classical simulation of the process, summarized in Fig. 5.3.

This figure shows three snapshots of a classical continuum $E > 0$ wavepacket evolving in time (left column), and their associated momentum distribution (right column). The dotted line in the figure represents the equivalent condition from Equ. 5.2, which can be found by solving this equation for p_z given that $\vec{A} = A\hat{z}$, giving

$$p_z > \frac{E_0 + \frac{1}{2}A^2}{-A}. \quad (5.3)$$

As the wavepacket evolves, its momentum distribution narrows, while the “momentum cut” line remains fixed, which is a function of the currently set (constant) experimental parameters A and E_0 . A smaller and smaller portion of the wavepacket can be recombined. The experiment was fairly simple to perform and was completed in a matter of days.

5.3 HCP Assisted Recombination with a Static Field Induced Continuum

In the last section, which served to introduce the relevant concepts, the continuum into which electrons were excited was the common sense “sea” of continuum states with positive energy. But a continuum, as it applies to atomic physics, only refers to a state of an electron which has the character of being free, or unbound from the parent ion. In the recombination experiment presented here, a continuum state was induced in an atomic system by the use of a static field. Consider Fig. 5.4, which shows a Coulomb potential immersed in a static field of strength 212 V/cm.

This figure illustrates the significant distortion of the Coulomb potential due to the presence of the static field. The potential is modified from $V = -1/r$ to $V =$

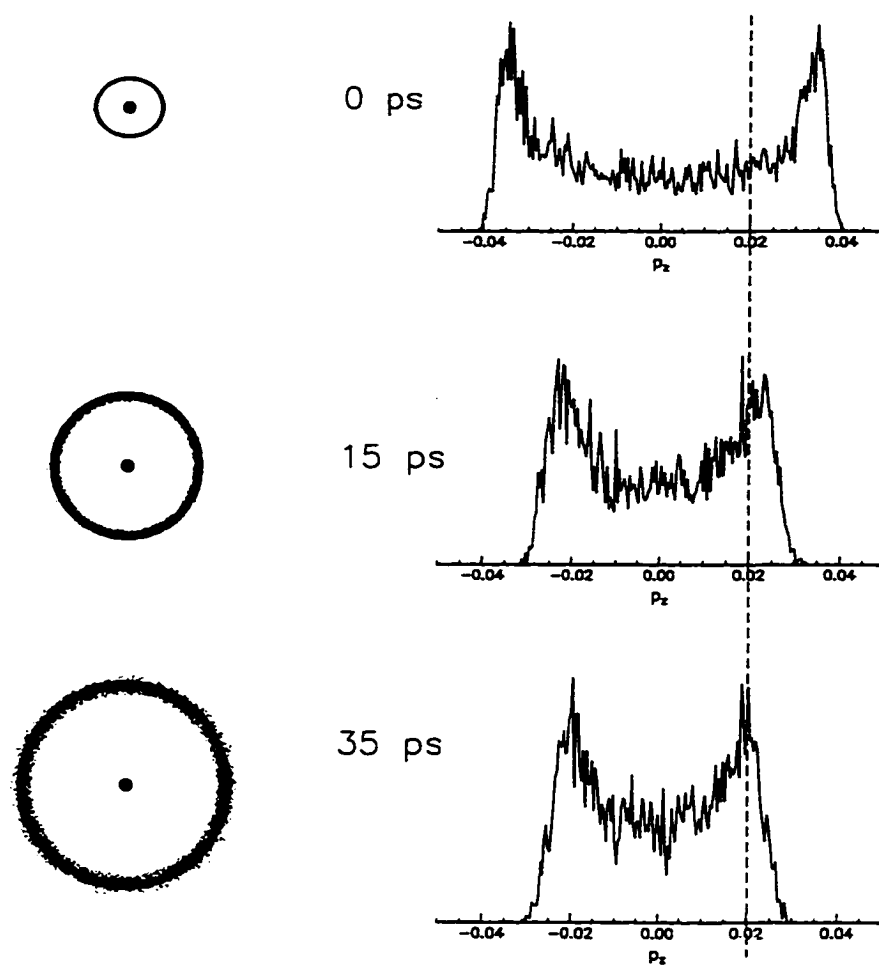


Figure 5.3: Three snapshots of a classical continuum wavepacket evolving in time (left column), and their associated momentum distributions (right column). Note the gradual narrowing of the momentum distribution as a function of time. The dotted line represents a boundary in the momentum distribution, below which population cannot be recombined.

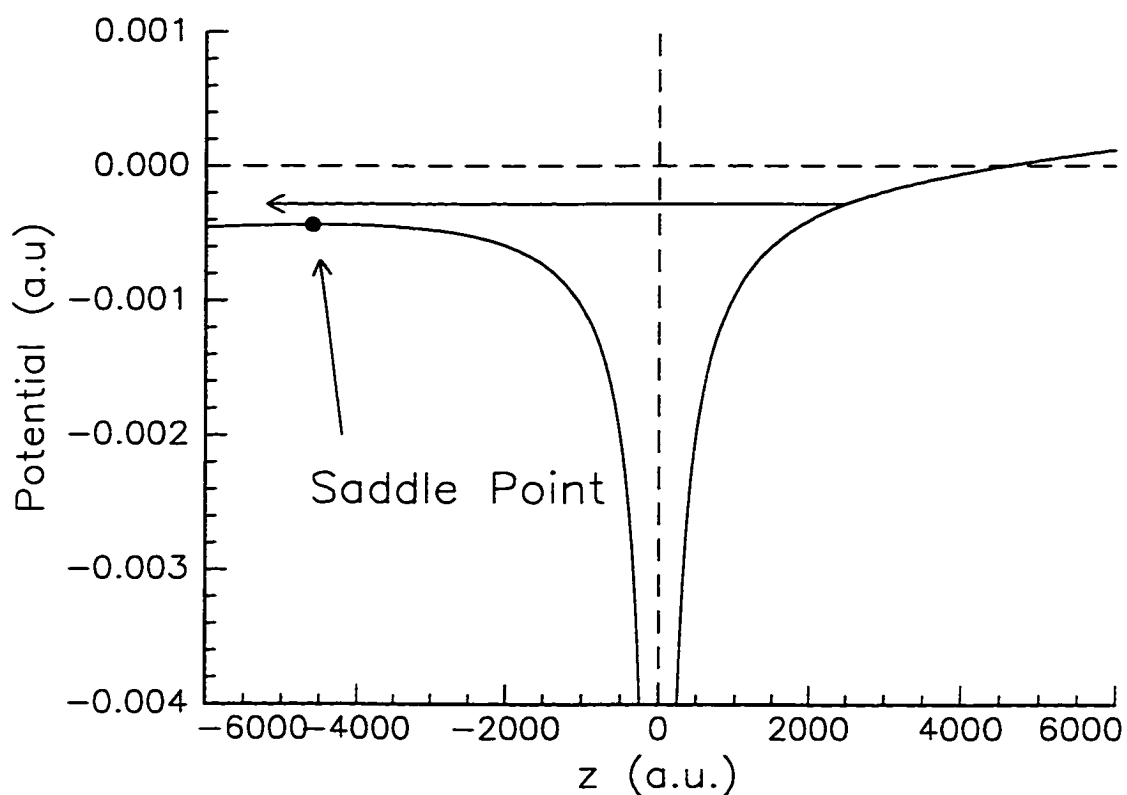


Figure 5.4: Potential energy vs. z . A one-dimensional Coulomb potential immersed in a static field of strength $F_s = 212$ V/cm along the $+\hat{z}$ -axis. The energy level shown (the arrow) is the energy level of a bound $n = 42$ Rydberg state. The $z > 0$ side of the potential is called the “uphill” side, while the $z < 0$ side is called the “downhill” side, for obvious reasons.

$-1/r + F_s z$, for a static field F_s , oriented along the $+\hat{z}$ -axis. The potential bends “up” for $z > 0$, and is called the “uphill” side of the potential. It bends “down” for $z < 0$ and is called the “downhill” side. Additionally, a saddle point is created on the downhill side at position $z_{saddle} = -1/\sqrt{F_s}$ and energy $E_{saddle} = -2\sqrt{F_s}$ (see Ref. [3], p. 83).

Notice the energy level (the long arrow), which is the bound energy level of an $n = 42$ Rydberg state. In the absence of the static field, the state is bound. Its classical motion is periodic between two turning points, one near the core and the other at an outer turning point, defined by the potential function itself. The period of its motion is $2\pi n^3$ (a.u.). The classical ionization limit for this state is given by $1/16n^4$ [3], or 106 V/cm. Clearly, immersing this state in a static field of strength 212 V/cm will ionize the bound state. This is illustrated in Fig. 5.4 as well. As the electron moves along the $-\hat{z}$ -axis, towards its outer turning point, it no longer sees the potential barrier, but instead, passes over the saddle point, becoming free. In other words, immersing this state in a static field of 212 V/cm gives the normally bound state *continuum character*. This continuum character will serve as our test-bed for HCP assisted recombination. Immersing the atom in such an electric field and performing $n = 42$ photoexcitation immediately produces the electron-ion pair, much as in the system presented in the Section 5.2.

This “Stark potential” does not form a purely continuum state however. Referring once again to Fig. 5.4, we now examine the potential for $z > 0$. The classically allowed motion of an electron here is bound between two turning points, one near the core, and the other near an outer turning point defined by the potential itself. In a pure Hydrogenic potential, population on the uphill side of the core in a static field does not have any continuum character; it has no path out of the atom.

This system, with its static field induced continuum, is hinting at some very

interesting properties. In creating the excited state, we see that it will have both continuum character *and* bound character. The continuum character gives provides the electron-ion pair, needed to test HCP assisted recombination. Just how the bound character will affect the system is at this point unclear.

5.4 Experiment

The experimental setup used in shown in Fig. 5.5. The interaction region is defined by two 7.5×7.5 cm conducting plates oriented in a parallel plate capacitor geometry, separated by 1.5 cm. These plates are also referred to as “field plates.” A thermal atomic beam of Ca atoms is aimed at the center of this region.

The only signal we can detect is that from charged particles. Ions are, of course, charged, and very easy to detect in the lab using various electric fields to accelerate these ions into a detector/collection plate. Any voltage that appears on the collection plate due to incident charges can be picked off using an oscilloscope, capacitively coupled to the collection plate. This detection process was described in Chapter 2.1

During this experiment, a rather unique detector is used that is still being developed in our lab (as of this writing), which shows much promise. This detector has been described elsewhere (see Ref. [7] and Appendix C), but briefly, a phosphor area is preceded by a dual microchannel plate assembly, and is configured so that different regions of its active area will fluoresce in proportion to the local number of impacting electrons. This active area is viewed with a CCD camera and monitored with a digital oscilloscope. With each laser shot, any ion creation in the interaction region is directly projected onto the phosphor screen. What is so unique about this detector is that it essentially maps temporal information into the active spatial area of the phosphor, which is about 2” wide. If a “pump” and a “probe” pulse are coun-

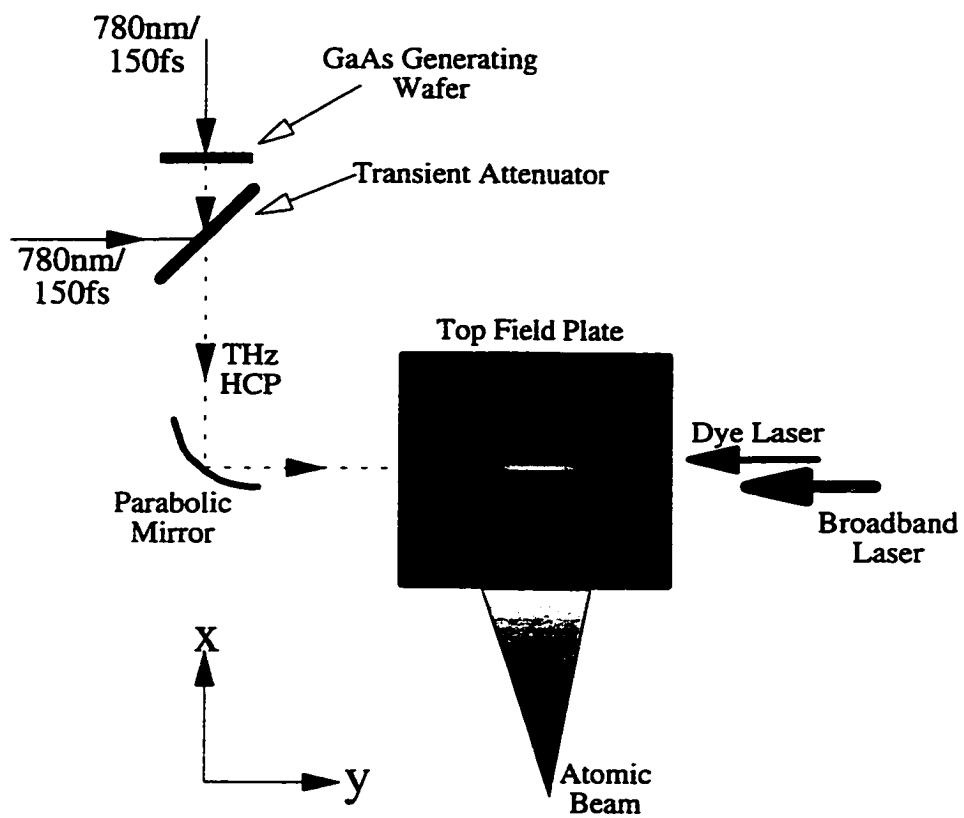


Figure 5.5: The experimental setup used in the HCP assisted recombination experiment.

terpropagating under this active area, atomic time evolution between the pump and probe pulses can be captured and imaged by the detector, in a single laser shot. This detector is mounted on top of the top field plate. There is a small slit in the top plate through which ions may be accelerated, out of the interaction region, and into the detector.

To create the electronic wavepacket, one of the outer $4s^2$ electrons on Ca is excited from the $4s4s^1S_0$ ground state to an intermediate $4s4p^1P_1$ state using a 423 nm pulse from a 5 ns dye laser. Within 1 ns of this pulse, the atoms are further excited to a linear superposition state of $4snd^1D_2$ Rydberg states using a 1.5 ps, 392 nm laser pulse. This 392 nm laser pulse is frequency doubled light from the 786 nm ultrafast laser system. To create this light, the 786 nm beam is passed through a 2 cm long KDP crystal, and phased matched such that a maximum amount of 392 nm light is created. The phase matching conditions and length of the crystal restrict the bandwidth of the doubled light to about 10 cm^{-1} . This is a broadband laser pulse, capable of coherently exciting approximately 5 n -states, frequency centered about $n = 42$. The laser beams are incident on the system as shown in Fig. 5.5.

Two steps are taken to confirm the creation and structure of the wavepacket:

Broadband, short pulse laser excitation. A time of ionization signal (TOI), is used to probe the component structure of the wavepacket. Approximately $1 \mu\text{s}$ after the 10 cm^{-1} , laser pulse has passed, a high voltage pulse is applied to the bottom field plate with a magnitude of $\approx 6 \text{ kV/cm}$, and rise time of $\approx 6 \mu\text{s}$. As the field rises from 0 V/cm to its peak value, higher lying Rydberg states will be ionized sooner than lower lying states, since the ionization limits of higher lying Rydberg states will be reached earlier during the rise time of the pulse. Examining this signal directly on the oscilloscope yields the bold curve shown

in Fig. 5.6.

Narrow band dye laser laser excitation. If the broadband laser used above is substituted with a narrow band, tunable dye laser, individual components of the wavepacket can be probed and determined. A dye laser has a bandwidth of $\approx 1 \text{ cm}^{-1}$, which is less than the state spacing at or near $n = 42$. If we scan the frequency of this dye laser near the $n = 42$ resonance, while monitoring the TOI signal on the oscilloscope, we can observe the individual resonances that are component states of the wavepacket. These are illustrated in Fig. 5.6 as the peaks plotted with regular pitch lines.

We now proceed to create the continuum wavepacket, and to perform HCP assisted electron/ion recombination. The crucial elements of the experiment are all oriented as follows, as shown in Fig. 5.5:

- the atomic beam defines the \hat{x} -axis,
- the resonance line dye laser, and broadband laser pulse propagate in along $-\hat{y}$ -axis, with a $\approx 1 \text{ ns}$ time delay between them,
- the HCP, which will serve as the recombination agent, counterpropagates with the optical laser beams, in the \hat{y} direction,
- non-unipolar components are “cleaned” from the HCP using the transient attenuator shown in the figure (see Appendix B or Ref. [20]),
- the \hat{z} -axis is an imaginary line perpendicular to both field plates, passing though the volumetric center of the interaction region,
- the static field is oriented along the \hat{z} -axis, and

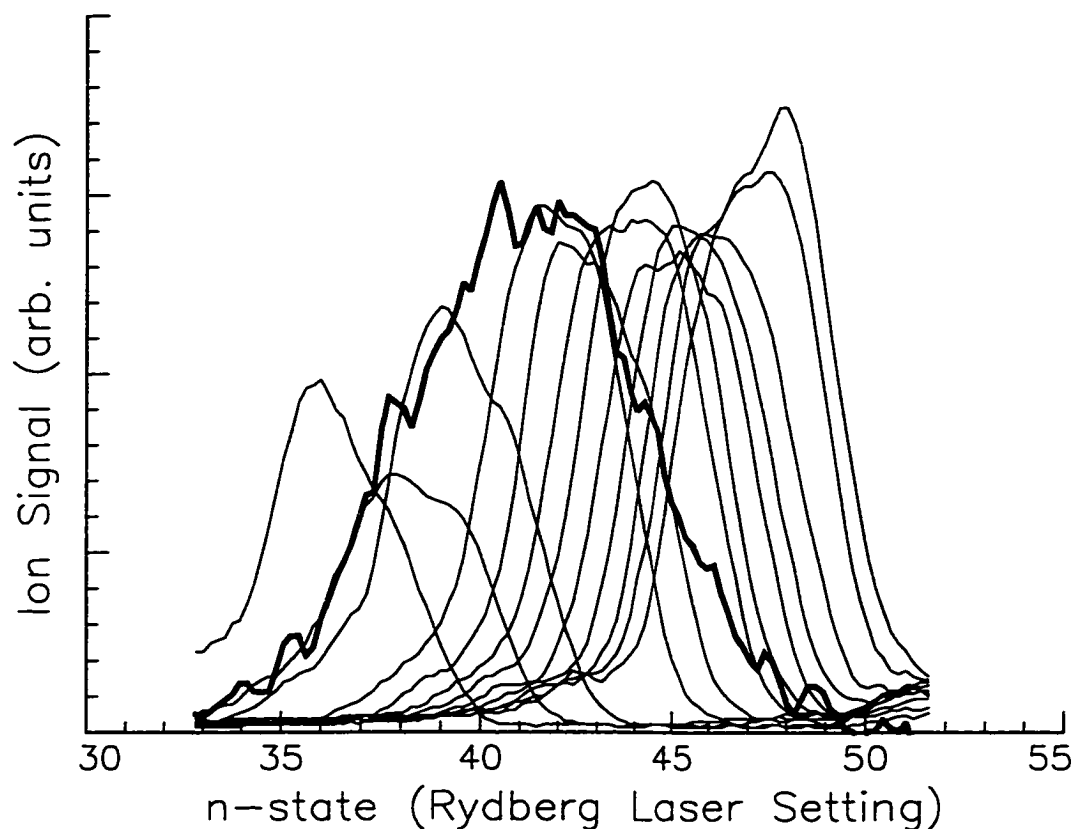


Figure 5.6: Time of ionization scans for different excitation methods near $n = 42$. The bold line is coherent excitation of the wavepacket by a 10 cm^{-1} wide laser pulse centered on $n = 42$. The normal pitch lines are the wavepacket's component states found by scanning a narrow band (1 cm^{-1}) dye laser through the same frequency range covered by the broadband laser. Both the laser bandwidth and wavepacket composition can be inferred from this scan using a Rydberg series as a backdrop.

- the slit in the upper plate has its long dimension along the \hat{y} -axis, oriented as $0.15\hat{x} \times 2.5\hat{y}$ cm.

With the 1.5 ps laser frequency held constant, a voltage of 318 V is now applied to the bottom field plate. The static field produced across the 1.5 cm gap between the field plates is 212 V/cm, twice the classical ionization limit of an $n = 42$ Rydberg state. This means that the potential barrier is bent down far enough so that the excited state can escape over the saddle point, and leave the atom (it is ionized). The static field is oriented in this manner so that any ions created by the static field will be accelerated away from the detector, into the bottom field plate. Under these conditions, no signal will be observed on the detector. Any ions created are accelerated into the bottom plate and lost.

After allowing time for this static field ionized population to reach the bottom plate, a strong, high voltage +6kV/cm pulse is now applied to the bottom plate $\approx 1 \mu s$ after excitation. A pulse of this magnitude will field ionize any bound states with $n > 15$. In principle, the application of this pulsed field at this point should not produce any signal, since it should have all been accelerated into the bottom field plate. Nevertheless a small background signal always appears on the detector, perhaps due to:

1. Residual lower lying Rydberg states, with energies below the static field induced saddle point, ionized into the detector by the pulsed field, or
2. static field created ions that have not yet been accelerated and lost onto the bottom field plate; these are reversed by the pulsed field and accelerated back into the detector.

A background signal is observed for pulsed field timing delays as large as $8\mu s$.

This small signal level is considered our “zero” or “minimum” signal level. In contrast, removing the static field completely yields a very strong signal, $\approx 100\times$ greater than this background signal. This is the “maximum” signal level, as it is generated by pulse field ionizing all Rydberg states excited by the photoexcitation lasers.

With the combined static and pulsed fields applied, the minimum signal level confirms the excitation of a continuum wavepacket. The $1\mu s$ delay was carefully chosen to provide a measurable signal while ensuring that most of the continuum population has been accelerated into the bottom plate and will not reach the detector. With the absence of any recombination mechanism (e.g. a HCP), there is only a minimum background of bound species for the strong pulsed field to ionize and/or accelerate into the detector. In this scheme, the strong pulsed field effectively acts as a “neutral species monitor.” Any neutral species with $n > 15$ created by the HCP between the photoexcitation and pulsed field events can be detected.

To perform the recombination experiment, a HCP is now injected. Portions of the signal level on the oscilloscope are seen to rise above the zero signal level, confirming that the HCP is creating bound (neutral) species that are ionized by the strong pulsed field. The higher signal levels are seen to shift as a function of the HCP polarization. This bound signal created by the pulsed field is our signal; it is the raw data we will collect.

During the actual experiment, a CCD camera monitors the active area of the phosphor detector, which has local regions that glow in proportion to the amount of locally impacting electrons (electrons: recall the phosphor detector is preceded by a microchannel pair). Before the HCP is turned on, the minimum signal level is seen as a faint greenish glow, registering no more than a few millivolts (< 10 mV) on the oscilloscope monitoring the CCD camera output. When the HCP is turned on, an

array of “bright” spots appear glowing bright green along the excitation and probe axis (\hat{y} -axis). The peaks on the oscilloscope now approach ≈ 100 mV in height. The entire signal collected across the phosphor surface instantaneously represents ≈ 80 ps data between the pump/probe pair formed by the excitation lasers and the HCP. This “single shot” acquisition of signal level in parallel with time evolution is the true power of this new detector.

5.5 Data Analysis and Discussion

At this point, the wavepacket has been excited, a static field level has been set, a HCP has been injected into the system, and recombination is occurring. In this section data will be presented and discussed.

5.5.1 Data Presentation and Discussion

With the experiment up and running, a central frequency has been set for the wavepacket excitation, as has a static field magnitude. The only free parameters left deal directly with the HCP, namely the amplitude, and the polarization relative to the static field. In this experiment, a very weak dependence on the HCP amplitude is observed. There was little or no signal at small HCP amplitudes, a maximum overall signal level found at moderate HCP strengths (≈ 10 kV/cm), followed by a gradual drop off in signal as the HCP amplitude was further increased. This situation is quite analogous to the zero field recombination scenario described in the introduction. There is a very strong dependence, however, on the polarization of the HCP relative to the static field, and this will serve as the most critical free HCP parameter. The HCP field amplitude is conveniently set from day to day to maximize the signal level, and the ideal amplitude was found to vary within 10% from day to day.

The excitation frequency of the wavepacket is, of course, a free parameter as well.

Although a wavepacket centered about $n = 42$ serves as the basis for the discussion here, $n = 30$ and $n = 35$ wavepackets were studied as well. Trends in this data are discussed at the end of this section.

A wavepacket whose central state is $n = 42$ is excited in a static field of magnitude 212 V/cm. Two data scans were acquired as described above. One was taken with the HCP field polarized parallel to the static field and other with the HCP field polarized antiparallel to the static field. A more convenient convention will now be set that will make the discussion on the data later a bit easier. The polarization of the HCP will henceforth be referred to by the direction of the impulse carried by the HCP, \vec{A} , which is *opposite* to the field direction. With this convention, two data scans are presented in Fig. 5.7. In the top plot, the HCP impulse is oriented antiparallel to the static field, and in the bottom plot, the HCP impulse is oriented parallel to the static field.

A quick inspection of the two plots shows a few important time dependent features:

Strongly modulated spectrum. There are strong modulations in the both sets of data, some appearing periodic and others not periodic. The modulations appear very different between the two scans, indicating that the recombination has a strong dependence on the polarization of the HCP relative to the static field.

Fast modulations. These are modulations seen with period of ≈ 11 ps. This period corresponds with the classical Kepler period of a bound Rydberg state of principal quantum number n , given by $\tau_K = 2\pi n^3$. For $n = 42$, $\tau_K = 11.3$ ps, in good agreement with the observed modulations.

Slow modulations. These are the slow modulations dominating the overall structure of the plots, with a period of approximately 28 ps. This corresponds to the period of precession of the angular momentum quantum number, l . Since the

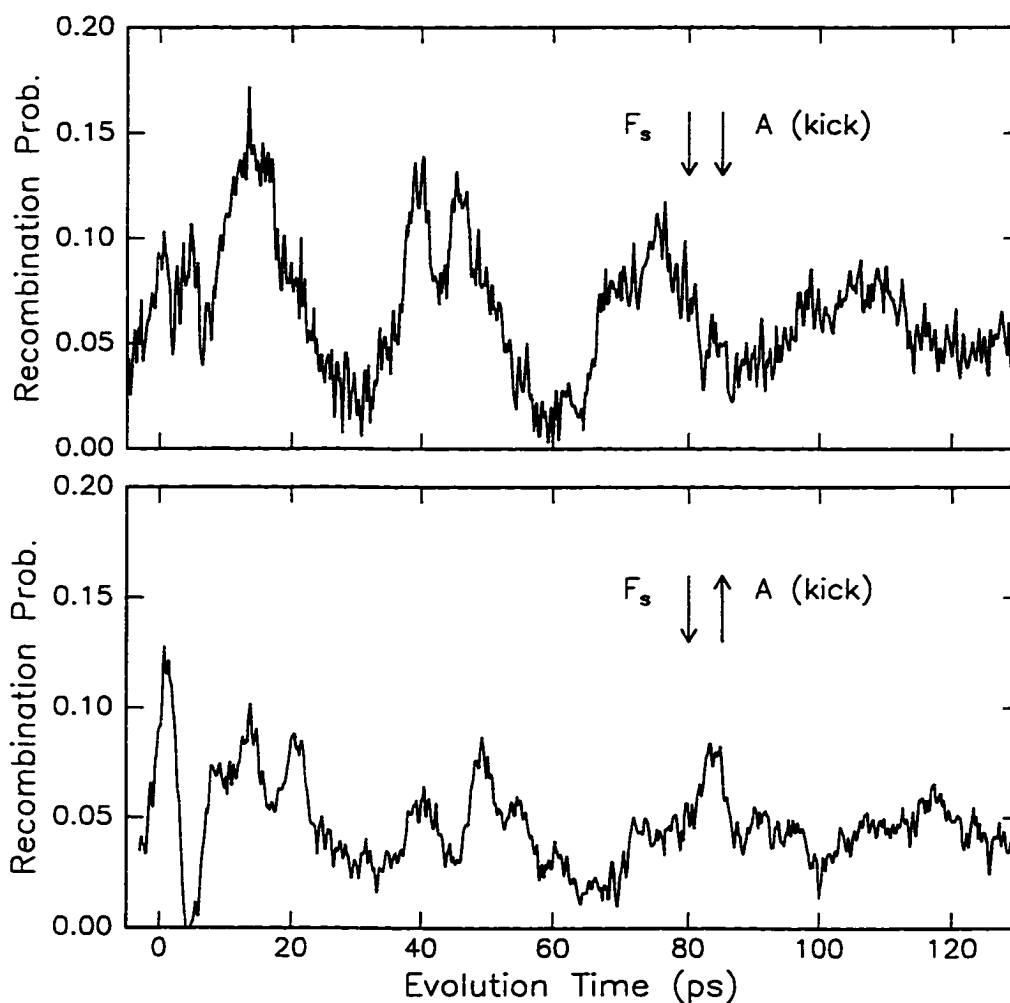


Figure 5.7: A sample data set for an $n = 42$ wavepacket in a static field with strength 212 V/cm. Top: the HCP field is polarized antiparallel to the static field, meaning the HCP's impulse, \vec{A} , is parallel to the static field. Bottom: the HCP field is polarized parallel to the static field, meaning the HCP's impulse, \vec{A} , is oriented antiparallel to the static field. The plots illustrate the absolute bound fraction versus wavepacket evolution time before interacting with the HCP.

atom is immersed in a static field, l is no longer a conserved quantity, but now oscillates between 0 and $n - 1$. Throughout this discussion, it is referred to as the “angular momentum precession period,” given by $\tau_l = 2\pi/3nF$, where n is the principal quantum number, and F is the static field strength. For $n = 42$ and $F = 212$ V/cm this is $\tau_l = 29$ ps, in good agreement with the observed value.

Irregular modulations. In Fig. 5.7 (top), the signal for times less than 10 ps shows two strong “quick” peaks spaced *less than* one Kepler period (τ_K) apart.

As mentioned, wavepackets frequency centered around $n = 30$ and $n = 35$ were studied as well. It is found that the data acquired at these n -states strongly resembles that taken at $n = 42$. Observed values of τ_K and τ_l change accordingly, and the structure for times ≤ 20 ps remains virtually identical to that shown in Fig. 5.13. For illustration then, $n = 42$ is considered representative here, and is the only data discussed and analyzed in the remainder of this chapter.

These are just empirical observations of the data. The Kepler period, τ_K , is a very common parameter in Rydberg atom studies [3]. The angular momentum precessional time, τ_l is a little less common, but has been observed before in studies involving wavepacket in static fields [8]. Some further analysis is needed.

5.5.2 Data Calibration

A short discussion is in order on preliminary processing of the raw data. Scans taken directly from the oscilloscope are very raw in nature; both axes are uncalibrated to any physical parameter. The horizontal axis is related to the arbitrary “time/div” set on the oscilloscope, and the vertical by the “volts/div” knob. The axes must be calibrated to something related to the recombined fraction on the vertical axis, and wavepacket evolution time on the horizontal axis, consistent with the pump/probe

nature of the lasers directly under the phosphor detector. This was done as follows.

Horizontal axis. This axis represents the wavepacket evolution time before irradiation with the HCP. At the time of data acquisition, there is no correspondence between the “time/div” set on the acquiring oscilloscope, and “wavepacket evolution time.” This calibration is done as follows.

1. The HCP is turned on, and the phosphor detector glows with recombination signal, that is composed of many distinguishable, static features along the laser beam axis (the \hat{y} -axis).
2. A single such feature is visually isolated.
3. The time at which the HCP is created relative to the excitation lasers, is altered, by moving a translation stage containing mirrors that route the ultrafast beam towards the GaAs wafer. This changes the overall spatial overlap between the excitation lasers and HCP under the phosphor detector, along the \hat{y} -axis.
4. As the translation stage is moved, the position of the isolated feature is tracked along the phosphor surface, or more precisely, on an oscilloscope trace.
5. A correspondence between the amount the translation stage is moved (mm) and the amount the feature moves is developed. This correspondence is a factor, typically with units of “ps/data point,” where a 1 data point is one digitized value off of the oscilloscope trace. This is the calibration.

Vertical axis. This axis to represent the absolute bound fraction recombined by the HCP. What is important in this calibration is to determine what represents the zero, or minimum signal level, and what represents maximum signal level. The

intermediate recombination signal can then be scaled accordingly between these two extremes, to some number between zero and one, representing the absolute bound fraction. The most problematic factor in determining this calibration is background radiation from the bias GaAs wafer. This calibration is done as follows.

Determine the minimum background level

1. Determine and set the desired GaAs bias voltage, and apply it to the wafer. The HCP field is on at some field amplitude and is present in the system.
2. Determine and set the desired voltage across the field plates. For recombination, this value is set above the classical ionization limit of the n -state excited ($> 1/16n^4$).
3. A typical recombination signal is observed on the phosphor and oscilloscope.
4. The transient attenuator is now timed to fully attenuate the entire HCP field. This blocks the HCP field from entering the interaction region, but allows any stray background from the GaAs generating wafer to remain present, as it will be during data acquisition.
5. The recombination signal is gone, and a flat background signal is observed. In principle, the phosphor should appear black for static fields $> 1/16n^4$, but in practice, there is always some background signal to due residually bound Rydberg states, or static field ionized population that has not reached the bottom field plate. Perhaps even stray radiation causes some recombination or ionization. All features in the recombination signal, however, are observed to be greater than or equal to this signal level.

6. A time-trace is recorded from this signal level and is called y_{min} .

Determine the maximum background level

1. Determine and set the desired GaAs bias voltage, and time the transient attenuator to fully attenuate the entire HCP field, as described above.
2. Turn the static field off. No static field ionization takes place, and the strong pulsed field ionizes any excited Rydberg states with $n \geq 15$, and a flat signal level is observed. This signal level represents the maximum amount of Rydberg population excited and available for use in the recombination process.
3. Slowly ramp the static field level and approach, but do not exceed the classical ionization limit for the n -state excited, $1/16n^4$. The flat signal level is not observed to change while ramping the field, nor is any difference observed to the level obtained in the previous step. Recall that the strong pulsed field is ≈ 6 kV/cm, which is much greater than any static field setting, which never exceeds ≈ 700 V/cm.
4. A trace is recorded from this signal level and is called y_{max} .
5. In principle, this signal level could serve as a global maximum level for any data acquired at this n -state setting. In practice however, this level is repeatedly acquired immediately before any data acquisition, and is used in the normalization process of that particular data only.

Determine the absolute zero signal level

1. All optical laser beams are blocked, including the excitation beams and HCP generating beam.

2. The phosphor is observed to be dark, and the oscilloscope trace is near 0 mV. This signal level takes into account any background light in the laboratory itself, that might be picked up by the CCD camera. During all stages of this experiment, the CCD camera and vacuum chamber were enclosed in an black plastic sheet.
3. A trace is recorded from this signal level, and is called y_{dark} .

With the three quantities y_{dark} , y_{max} , and y_{min} , a raw oscilloscope trace, y_{raw} , can be properly normalized to units of “absolute bound fraction” by calculating a normalized trace, y_{norm} from the following:

$$y(t)_{norm} = \frac{(y_{raw} - y_{dark}) - (y_{min} - y_{dark})}{(y_{max} - y_{dark})}. \quad (5.4)$$

With these calibrations, our data is now conveniently and physically calibrated to “bound fraction” versus “wavepacket evolution time.” This is how the data in Fig. 5.7 were calibrated. Furthermore, the normalization removes any spatial non-uniformities in the phosphor response. The calibration is crucially based upon the physical determination of the minimum and maximum signal levels. It is important to determine these values for any experiment performed using a detector such as this.

5.5.3 Systematic Study

The two most dominant parameters in the data are the Kepler period, τ_K , and the angular momentum precessional period, τ_l . τ_K is a function only of n , while τ_l is a function of both n and F , the static field strength. To fully investigate these parameters, data were acquired for a ramped range of static field strengths, at a several different n states, for both polarizations of the HCP, relative to the static field. The static field F was ramped beginning at a level below the classical ionization

limit for the n state selected, $1/16n^4$, to as high as 2.5 times this limit. No unusual transition was observed as the static field value passed through the ionization limit. The observed angular momentum period in data taken at each static field value very closely follows the predicted value, according to the definition of τ_l .

For $n = 42$ a series of such scans are shown in Fig. 5.8 for a HCP impulse antiparallel to the static field, and in Fig. 5.9 for a HCP impulse parallel to the static field. Note in each figure, as the static field is increased (from back to front), the period of the angular momentum period smoothly and monotonically decreases (faster oscillation), as required by the definition of $\tau_l = 2\pi/3nF$. Radial modulations are also apparent.

To further quantify τ_K and τ_l , a Fourier transform was taken of the time domain data. As an example, a single time domain trace from Fig. 5.8, acquired at a static field of 110 V/cm, was isolated and Fourier transformed into the frequency domain. The Fourier transform is shown in Fig. 5.10. The Fourier transform represents the results of a rigorous numerical search for any periodic motion we casually view in the time domain scan, that results in power or "strength" found at a given frequency.

This analysis captures the radial and angular dynamics discussed in the time domain above. Referring to Fig. 5.10, the large peak near 0.7cm^{-1} is the power of the angular, or slow oscillation, τ_l , that dominates the time domain. The smaller numerous peaks to the right of this large peak represents the radial, or fast oscillation, τ_K of the wavepacket, a bit less evident in the time domain. The fact that there are several peaks centered around the $n = 42$ radial frequency ($\tau_K = 2.9\text{cm}^{-1}$) confirm the superposition structure of the wavepacket: there are several adjacent n -states in the wavepacket, each executing radial motion, clearly illustrated by this group of peaks.

The Fourier transform was taken for all scans shown in Figs. 5.8 and 5.9. The

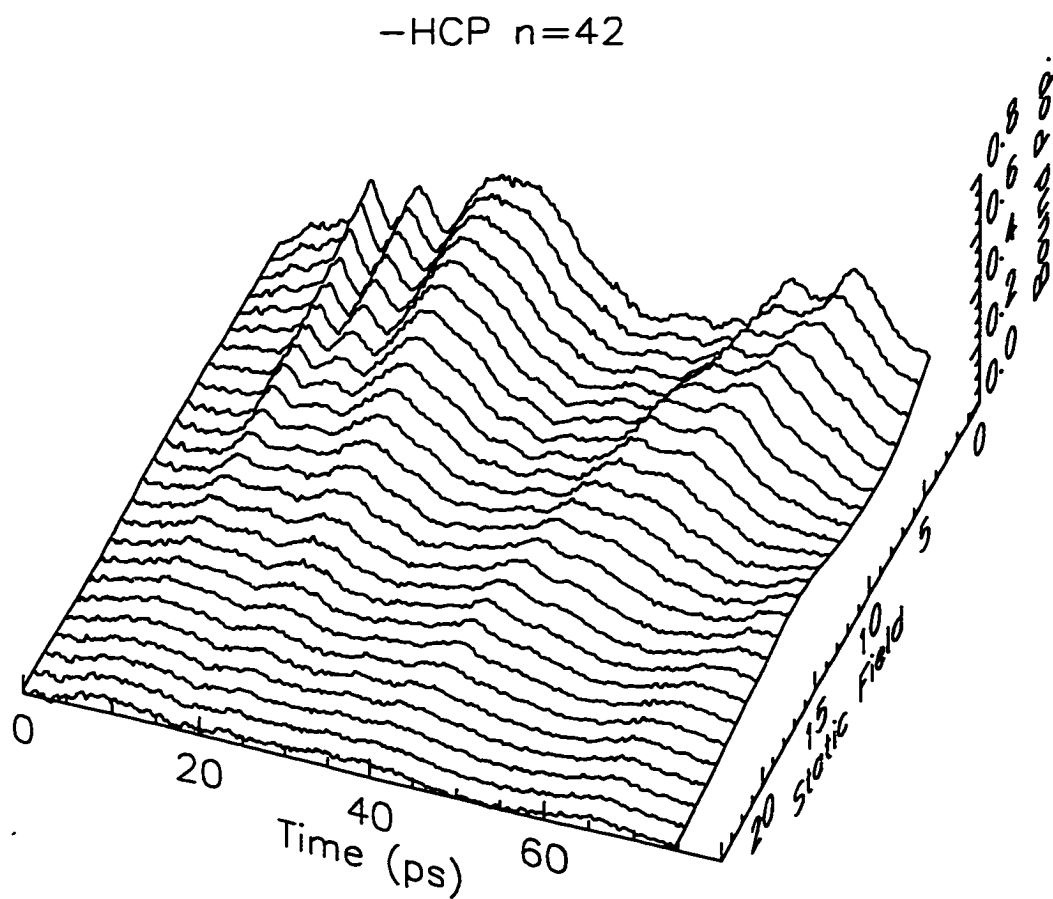


Figure 5.8: Bound fraction versus time at 25 different static field values, for $n = 42$. The static field was ramped between 90 V/cm (static field count 0) to 340 V/cm (static field count 25) in steps of 10 V/cm. The HCP impulse is antiparallel to the static field.

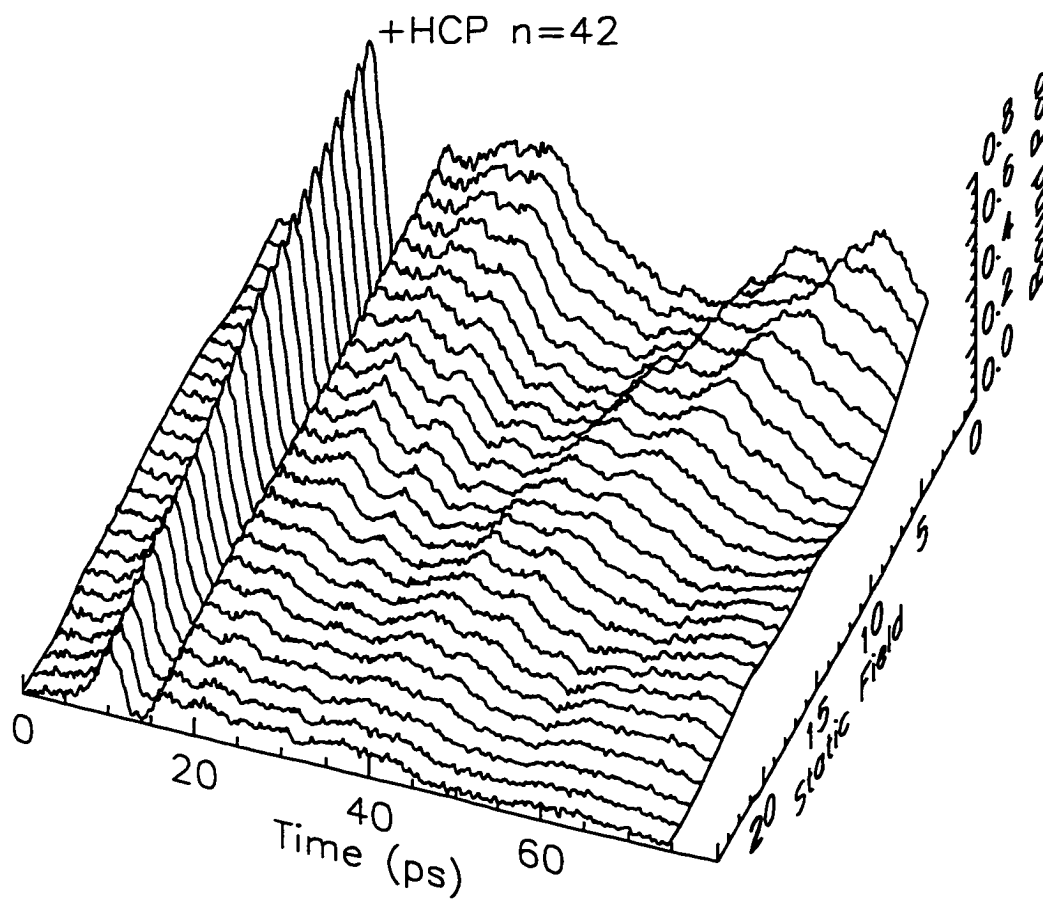


Figure 5.9: Bound fraction versus time at 25 different static field values, for $n = 42$. The static field was ramped between 90 V/cm (static field count 0) to 340 V/cm (static field count 25) in steps of 10 V/cm. The HCP impulse is parallel to the static field.

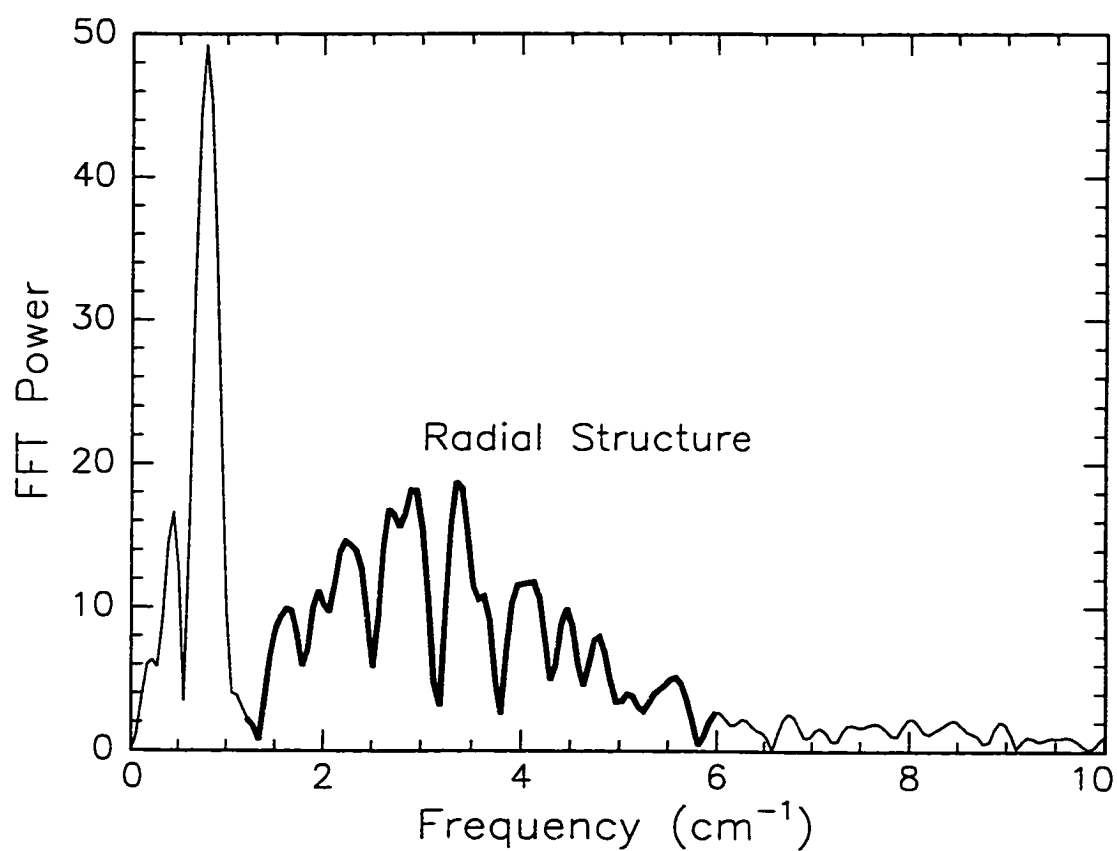


Figure 5.10: Frequency domain representations of the acquired recombination data at 110 V/cm. The Stark structure is evident by the large peak towards the left. The radial structure is evident by the bold group of peaks.

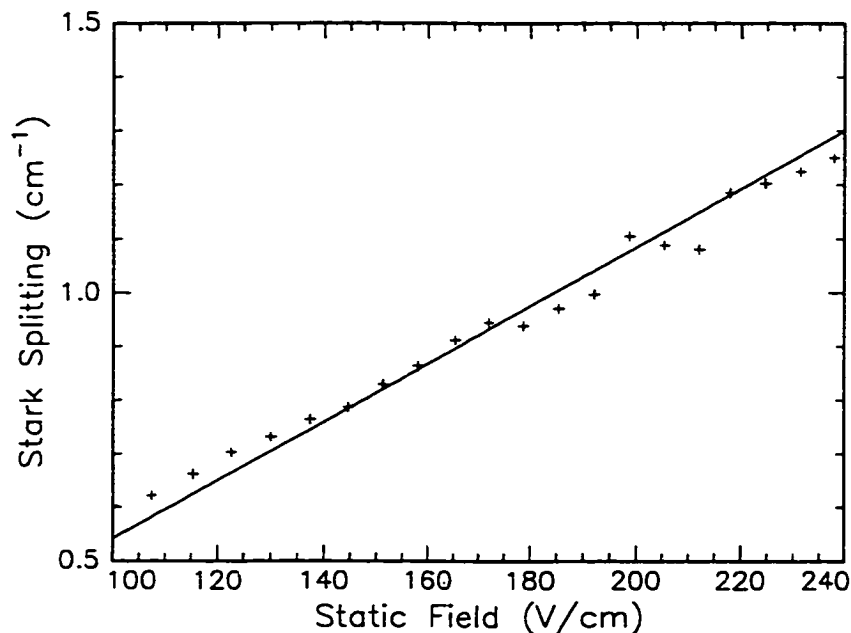


Figure 5.11: Stark splitting versus static field strength for recombination when the HCP impulse oriented antiparallel to the static field. Bottom: The line is the Stark energy splitting, $3nF$, and the points (+) are data.

central frequency of each angular frequency peak in the Fourier spectrums was found and plotted versus static field in Fig. 5.11 (the + symbols).

The frequency domain is very much like an energy space, and we are no longer looking at the angular oscillation, rather its inverse, or the Stark energy splitting, given by $2\pi/\tau_l$, or $\Delta E_{stark} = 3nF$. If plotted as a function of static field, F , this represents a line with slope $3n$ (a.u.) with zero y-intercept. This is the linear Stark splitting of the $l = 2$ (d-character) of the wavepacket as a function of field. This line is shown plotted in Fig. 5.11 as well. With the absence of any fitting parameters, the agreement is quite good.

The period of field free radial oscillation, $\tau_K = 2\pi n^3$, depends only on n , with no explicit dependence on any external field. However, in the data, the dependence of τ_K

on the static field strength is debatable. As the static field strength is increased, the outer turning point on the uphill side of the potential moves inward, towards the core, as shown in Fig. 5.12. This has the effect of *decreasing* τ_K as a function of increased static field magnitude. In the data, this effect is seen in the upper plot of Fig. 5.7. The “quick” peak pair that appear within the first 10 ps are separated by *less than* one Kepler period, τ_K , indicating this seemingly only n dependent quantity has been modified. Other attempts were made to view this effect in the data, as a function of static field strength. Within the experimental noise, it was simply not possible to see this effect firsthand in the time domain data. In the frequency domain, accurately isolating the center of the radial peaks or the entire envelope in the frequency domain is error prone and somewhat arbitrary at best. More will be discussed on this effect in Section 5.9.

5.6 Classical Numerical Analysis

5.6.1 Introduction

The discussion of the data up to this point has been largely empirical. We have been able to isolate two periodic motions in the recombination data, τ_K and τ_l , and trace them to known properties of Rydberg states and atoms in static fields. Further analysis of this is still needed to understand the dynamics of this continuum wavepacket and how it contributes to the oscillations in the recombination spectra.

To this end, a full classical mechanics based numerical study has been performed for this system. The study is based around the differential equation of motion for a particle with unit charge in combined Coulomb and static fields, subject to a HCP:

$$\frac{d^2\vec{r}}{dt^2} = -\frac{1}{r^2}\hat{r} + F_s\hat{z} + F(t - t_0)_{HCP}\hat{z}, \quad (5.5)$$

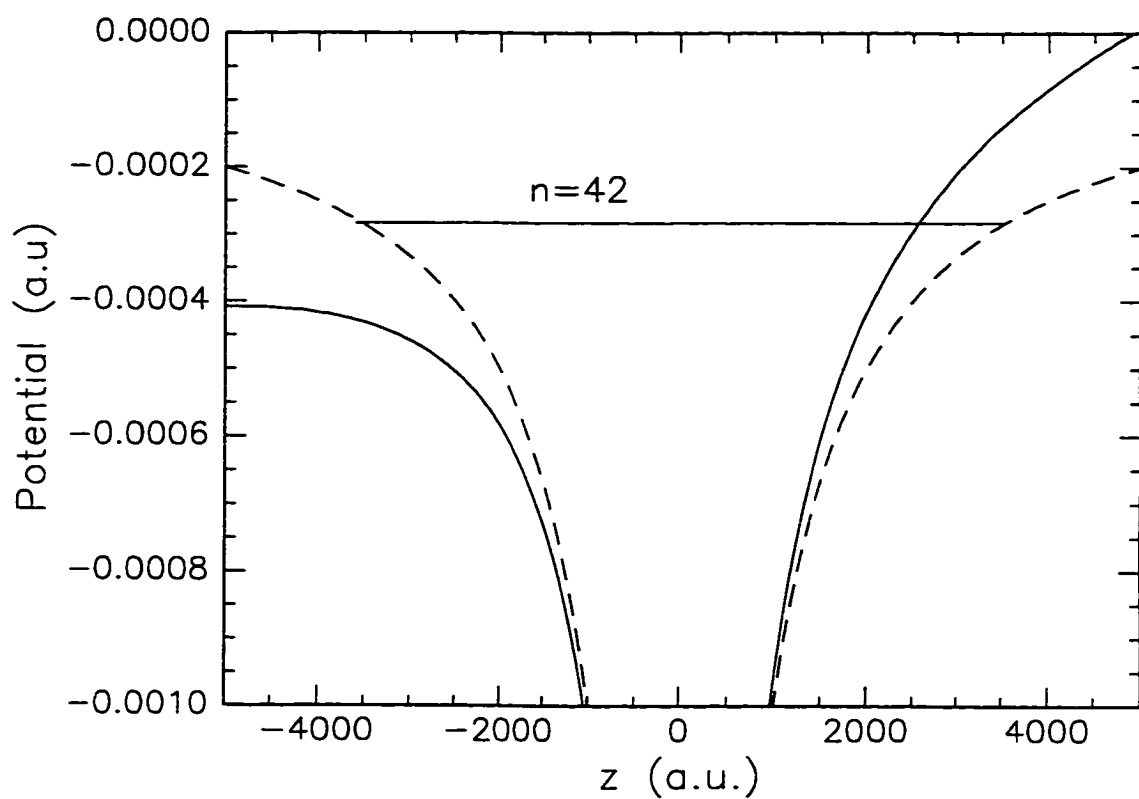


Figure 5.12: Dotted line: Pure Coulomb potential. Solid line: Combined Coulomb and static field potential. The static field magnitude is 212 V/cm. The horizontal line is the bound energy level for $n = 42$. Note the inwards shift of the outer turning point on the uphill ($z > 0$) side.

where F_s is the magnitude of the static field, F_{HCP} is the half-cycle pulse field, and t_0 is the arrival time of the HCP with respect to the wavepacket launch time.

To simulate the recombination experiment, a computer program was written that numerically integrates Equ. 5.5 using a 5th-order Runge-Kutta algorithm with an adaptive time-step size algorithm[10]. The procedure goes as follows:

1. **Initial conditions are set.** To begin the numerical integration process, initial conditions in both the position and velocity of the classical particle must be set, \vec{r}_0 and \vec{v}_0 . A convenient correspondence to the actual experiment is to supply the initial conditions in terms of n and l , the principal quantum number and angular momentum of the excited atom. Classically, l is set to $\sqrt{6}$ which is $\sqrt{l(l+1)}$ for $l = 2$ quantum mechanical (d-states). From n , the initial energy, E , can be calculated from the Rydberg formula $E = -1/2n^2$.

Since photoexcitation of the wavepacket occurs near the core, the initial conditions from E and l are found for a classical particle at the *inner* turning point of a Kepler orbit[11]. The classical orbits are all oriented with respect to the field axis (\hat{z} -axis) such that the component of l along the \hat{z} -axis is zero (l_z or $m = 0$).

2. **Initialize other parameters.** The magnitude of the static field, F_s , amplitude of the HCP field, F_{HCP} , and arrival time of the HCP, t_0 are determined and set. In practice, F_{HCP} is usually set to some constant, while F_s and t_0 take on nested and ramped values.
3. **Begin the integration.** With all parameters set, the integration begins from time $t = 0$ to just after the HCP field has passed, which is a function of the variable t_0 . In practice, the differential equation presented above is split into

six differential equation of motion, three for each component of \vec{r} and three for each component of \vec{v} . At any step through the integration loop, all variables of integration are available for examination, including $r_x, r_y, r_z, v_x, v_y,$ and v_z . From these, many other classical quantities can be derived and examined as well (angular momentum, Runge-Lenz vector, etc.)

4. **Check post-HCP variables of integration.** The post-HCP variables of integration contain information on:

a free (continuum) particle that has been allowed to evolve in a combined Coulomb and static field for a time t_0 , at which time it was irradiated with a HCP field. What happened?

The variables of integration tell “what happened.” We wish to ask the question now, is the particle bound (recombined) after interacting with the HCP?

As mentioned above, the static field creates a saddle point in the potential characterized in energy and position by: $z_{saddle} = -1/\sqrt{F_s}$ and $E_{saddle} = -2\sqrt{F_s}$. To determine if the particle is bound after the HCP, we ask the question is:

$$|r_z| < |z_{saddle}| \quad (5.6)$$

AND

$$E < E_{saddle}? \quad (5.7)$$

This is our “recombination condition.” If both conditions are met after the integration, the particle is bound, and we log this event as a function of t_0 .

5. **Build an ensemble.** To accurately simulate “an atom” classically, an entire ensemble of classical orbits is launched, oriented in all possible directions in 4π space, relative to the static field (\hat{z} -axis) such that $l_z = 0$.

5.6.2 Results

Using the classical calculation mentioned, recombination spectra (“bound fraction” versus “time”) can be computed, analogous to the experimental results. In order to emulate a wavepacket as closely as possible, the calculation was run for all integer n such that $40 \leq n \leq 44$. The recombination spectra produced for each run are then averaged together, with the contribution from each n -state being weighted with a Gaussian excitation envelope, 10 cm^{-1} wide, frequency centered on $n = 42$.

The calculation was run for the $n = 42$ wavepacket in a static field $F_s = 212 \text{ V/cm}$. The arrival time of the HCP was set such that $0 \leq t_0 \leq 150 \text{ ps}$. The results are shown by the bold line in Figs. 5.13 (F_s and HCP impulse antiparallel) and 5.14 (F_s and HCP impulse parallel). The normal pitch line is the same data shown in Fig. 5.7. The results are very pleasing. There is good qualitative agreement between the classical theory and inherently quantum data, at least for delays of $< 30 \text{ ps}$. The angular oscillations match very well in Fig. 5.14 and for unknown reasons, only moderately well in Fig. 5.13.

We can gain a better understanding of the modulations in the recombination spectra by examining the evolution of the classical ensemble shown at various times above and below the data and calculation plots in these figures. The small insets are snapshots of the classical ensemble in coordinate space (z versus x) at particular instants in time during the integration. Note that these insets are *not* individual electron orbits. They show an *ensemble* of classical electrons, and are created by including the instantaneous $x - z$ coordinates of 5,000 individual electrons, each

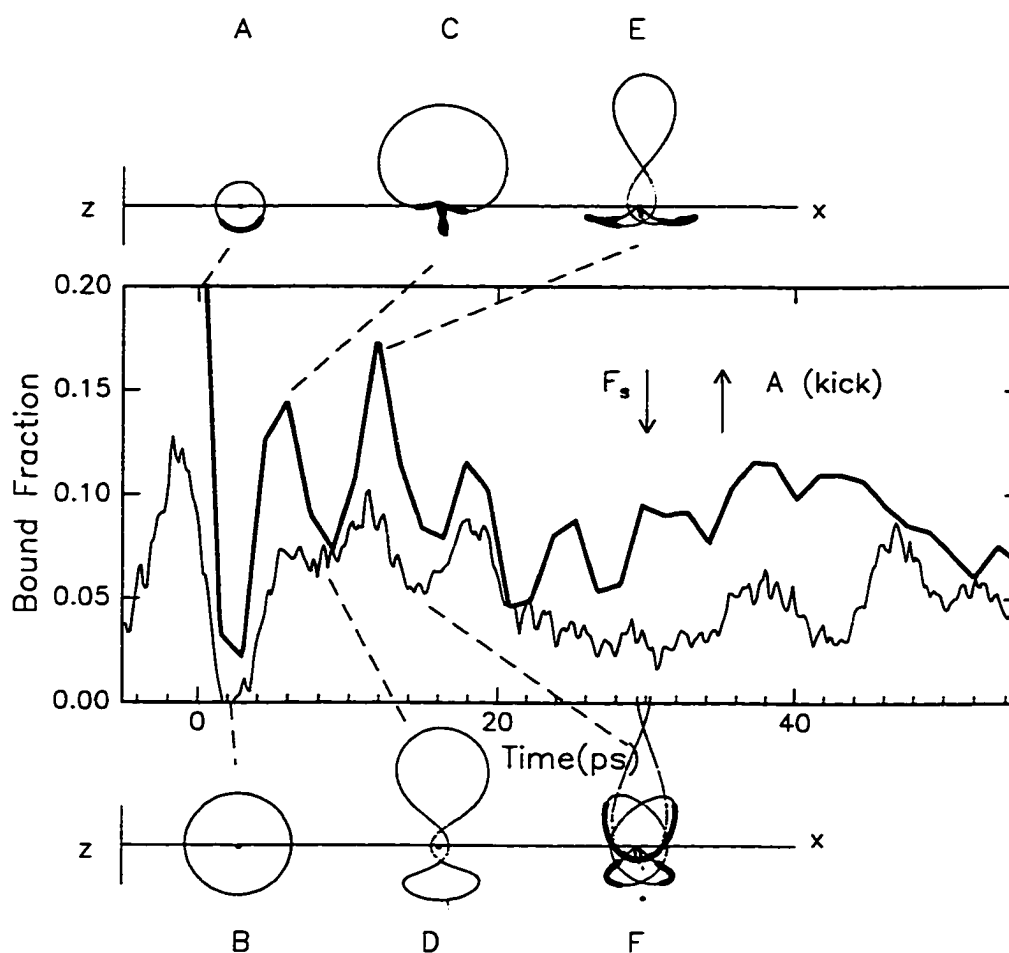


Figure 5.13: Absolute bound fraction versus time for classical calculation (bold line) and data (normal line). This plot is for an $n = 42$ wavepacket involving approximately 5 n -states. The static field and HCP impulse are oriented antiparallel to each other. The figures at the top and bottom of the plot are the $z-x$ coordinates of the classical electron ensemble launched by the calculation. The bold curve is artificially offset by 0.05.

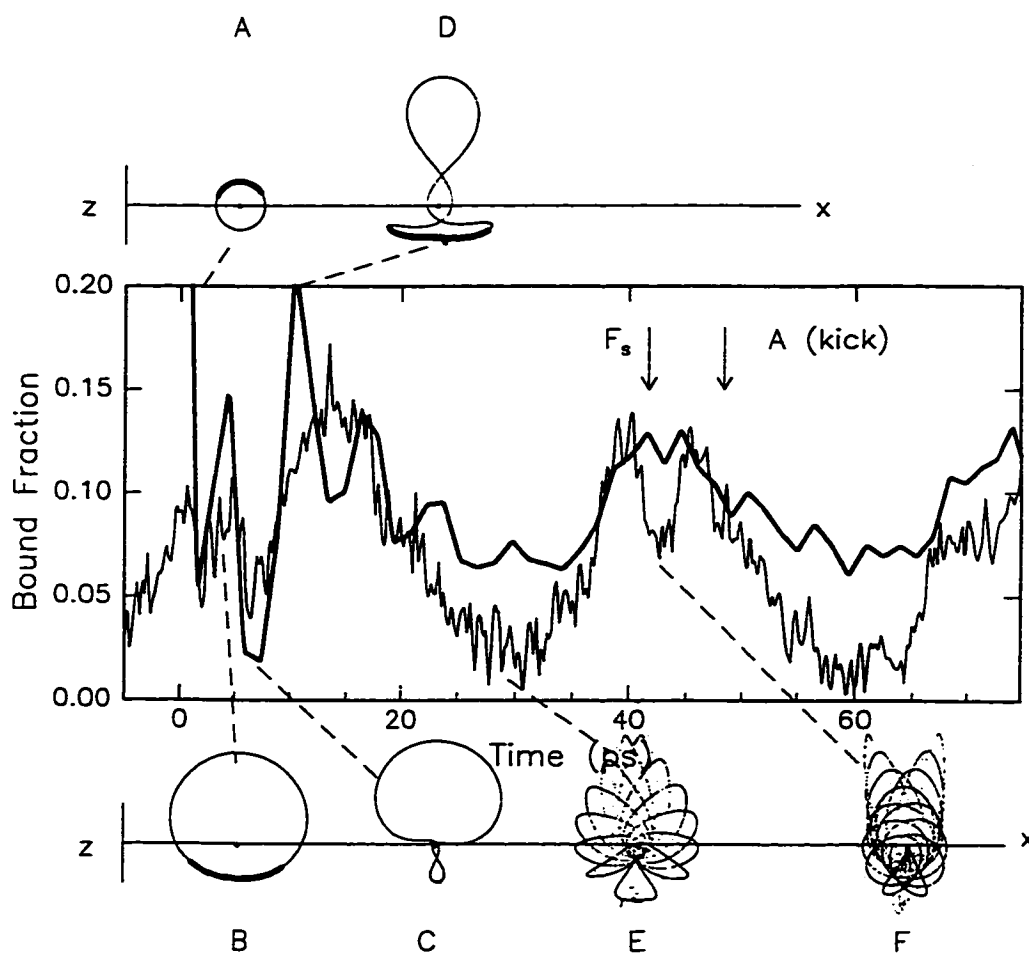


Figure 5.14: Absolute bound fraction versus time for classical calculation (bold line) and data (normal line). The static field and HCP impulse are oriented parallel to each other. This plot is for an $n = 42$ wavepacket involving approximately 5 n -states. The figures at the top and bottom of the plot are the $z - x$ coordinates of the classical electron ensemble launched by the calculation. The bold curve is artificially offset by 0.05.

individually launched into the combined Coulomb and static fields. Each inset is integrated over the angular distribution in ϕ , and are for a single n -state only. The plotting convention is as follows:

Bold pitch represents portions of the ensemble that *would have been recombined* by a HCP whose impulse is oriented as noted. In other words, the bold pitch represents ensemble portions that after the integration, meet the reattachment condition stated above.

Normal pitch represents portions of the ensemble that would *not* have been recombined by a HCP whose impulse is oriented as noted; these ensemble points *do not* meet the reattachment condition and remain in the continuum.

Choosing to show the classical ensemble in this manner allows us to simultaneously gain insight into the ensemble's evolution as well as into the dynamics of the recombination. The next two subsections will step through both figures in time, with the aid of these insets, examining the entire process. Recall that in general, momentum can be *extracted* from a charged particle by a HCP only when it is moving *opposite* to the HCP impulse. This extracted momenta can result in a lowering of energy and recombination. So what do we learn?

Figure 5.14

In this figure, the static field is oriented down and the HCP impulse is oriented down as well.

Inset A: $t \approx 0$ ps. The ensemble has just begun its initial expansion, just after being excited. It is expanding uniformly in a radial direction away from the core. A large fraction of the ensemble is moving up, opposite to the impulse which is

directed down. Adequate momentum and energy are extracted from this portion of the ensemble and recombination occurs (bold points). This recombined portion gives rise to the first peak in the spectra.

Inset B: $t = 4$ ps. The initial and uniformly spherical expansion has been interrupted: the uphill ($z < 0$) population has encountered its outer turning point, and has reversed its direction. Classically, it has run into the potential wall, has reversed its direction, and it is now moving towards the core. The bold fraction of the ensemble is moving opposite to the HCP impulse and is recombined. This gives rise to the second “quick” peak in the recombination spectra. The irregular spacing between these first two peaks ($< \tau_K$) is explained by the wavepacket encountering its outer turning point and reversing its motion on the uphill side, after $\approx 1/2$ of a full Kepler period. No recombination is possible for the downhill population since it is now moving too slow. The impulse extracts too much momentum for recombination to occur.

Inset C: $t = 7$ ps. The recombination signal drops to a local minimum value. The downhill ensemble is moving too slow and no recombination occurs. The uphill population has now encountered its inner turning point near the core and has reversed its direction. It is moving parallel to the HCP impulse and cannot be recombined.

Inset D: $t = 10$ ps. A sharp rise in the recombination signal. The downhill ensemble portion continues its expansion away from the core and no recombination occurs. The uphill population has once again encountered its outer turning point, has reversed its direction, and it moving back towards the core, opposite in direction to the HCP impulse. A substantial fraction of the uphill ensemble is recombined as shown by the bold points.

Inset E: $t = 29$ ps. The recombination spectra reaches a local minima in the slow or angular period. For clarity, no bold point have been plotted in this inset. The motion of the wavepacket has grown increasingly complex at this time, as evident by this inset. In general, the “petals” seen on the downhill side of the ensemble symmetrically oscillate towards and away from the \hat{z} -axis much like windshield wipers on a bus about the center of the front window. The period of this oscillation is the angular period, τ_l . This oscillation “moves” ensemble portions into and out of an orientation that periodically allows and does not allow recombination to occur. This is the classical nature of the slow modulation in the recombination spectra. This particular ensemble snapshot (inset E) is a configuration such that the angular oscillations do not fully contribute to the recombination signal. The uphill portion of the ensemble continues to oscillate between its inner and out turning points with period τ_K .

Inset F: $t = 43$ ps. Much the same as Inset E, only the petals have oscillated to a configuration that allows for maximum recombination in the angular period τ_l . The uphill portion continues to oscillate with period τ_K .

Figure 5.13

In this figure, the static field is oriented down and the HCP impulse is oriented up, opposite to the static field.

Inset A: $t \approx 0$ ps. The ensemble has just begun its initial expansion after excitation, similar to Inset A above. It is expanding circularly and uniformly in all radial directions away from the core. A large fraction of the ensemble is moving down, opposite to the HCP impulse which is up. Adequate momentum and energy are extracted from this portion of the ensemble and recombination occurs (bold

points). This recombined portion gives rise to the first peak in the spectra. Note that due to the opposite orientation of the impulse, relative to Fig. 5.14, the bold (recombined) ensemble portions at this early time are on the opposite side of the core, as in inset A, Fig. 5.14.

Inset B: $t = 3$ ps. The ensemble continues its free, radial expansion. Currently, all ensemble portions are moving such that no recombination is possible. This leads to a hard zero in the recombination spectra.

Inset C: $t = 5$ ps. The uphill ($z < 0$) side of the ensemble has reached its outer turning point returned to the core, and is just beginning to move towards the outer turning point once more. As it does so, its motion is opposite to the HCP impulse and recombination is possible for the bold points.

Inset D: $t = 9$ ps. The uphill ensemble has just completed its 2nd outer turning point return, and is now moving towards the core. The downhill ensemble continues its outwards expansion.

Inset E: $t = 11$ ps. This situation is analogous to Inset C, only the uphill ensemble has just executed its 2nd core return, and is once again beginning to move towards the outer turning point. Some recombination is possible. The downhill ensemble continues to expand.

Inset F: $t = 16$ ps. The evolution of the classical ensemble become increasing complex. The uphill ensemble has made its 3rd outer turning point return and is once again moving towards the core.

5.7 Electron-ion recombination or Wavepacket Dynamics?

The data analysis discussion presented above was strongly centered around two periodic motions in the wavepacket, that dominate each recombination spectrum acquired. So what does all of this “motional” analysis have to do with electron-ion recombination?

Consider the general recipe for probing the dynamics of a bound wavepacket:

1. **The wavepacket is created.** This is the photoexcitation step, typically involving some form of broadband light.
2. **The wavepacket is allowed to evolve.** A wavepacket is, by nature, a non-stationary object, so it is allowed to evolve for some time t . This evolution typically exposes the behavior and many dynamical properties of the wavepacket.
4. **The wavepacket is probed.** This is a crucial step, that interrupts the free evolution of the wavepacket, so we may “see” what it was doing.
5. **The wavepacket is detected.** Immediately after step 4, information probed about the wavepacket must be frozen and sent to the detector; in effect, a “snapshot” of the probed dynamics must be taken. This is most commonly done by creating ions from the probed wavepacket, since ions are so straightforward to detect experimentally.

In this experiment, however, we are creating a continuum wavepacket. The charge separation normally done in the *detection* step (step 5 above), is now a part of the *initial excitation*. So the detection step outlined above will not work. This is why a strong pulsed static field is applied after the HCP field: to monitor the recombined

population. The pulsed field creates a charge separation *for detection*, based on the wavepacket dynamics that the HCP field probes. So electron-ion recombination is still relevant here. It's just that we are really monitoring the dynamics of a portion of a wavepacket: the portion that got recombined.

As shown in Figs. 5.13 and 5.14, the recombination process has very unusual symmetry characteristics. In the data, this is apparent by the different spectra obtained for HCP polarizations parallel and antiparallel to the static field. In the classical ensembles (insets), this is apparent by the direction the **bold**, or recombined fraction, when recombination occurs. To further illustrate this point, the momentum distribution of the bold, or recombined *fractions* of the classical ensemble, at various time, are illustrated in Fig. 5.15.

The left column are the momenta of the ensemble fraction that are recombined by a HCP impulse polarized antiparallel to the static field, and the right column by a HCP polarized antiparallel to the static field. Notice the deep asymmetry between the two columns at any given time instant. To explore these symmetry considerations in the data, plots are shown in Fig. 5.16 that captures the dynamics of this wavepacket.

The plots shown in this figure are derived from the data sets shown in Figs. 5.8 and 5.9. Recall these figures were taken with identical experimental parameters, only with opposite HCP polarities. The upper plot in Fig. 5.16 shows the sum of these two data sets, and the lower plot, the difference between the two.

Subtracting the two data sets removes common features, and leaves differing features behind. Differing features include those probed by a HCP with one polarity, but not with the other, at some instant during the wavepacket evolution. Note the multitude of fast, or Kepler period features (the "islands") in the lower (difference) plot, and the general lack thereof in the upper plot. These correspond to antisymmetric motion of the wavepacket, or asymmetric portions of its momentum distribution,

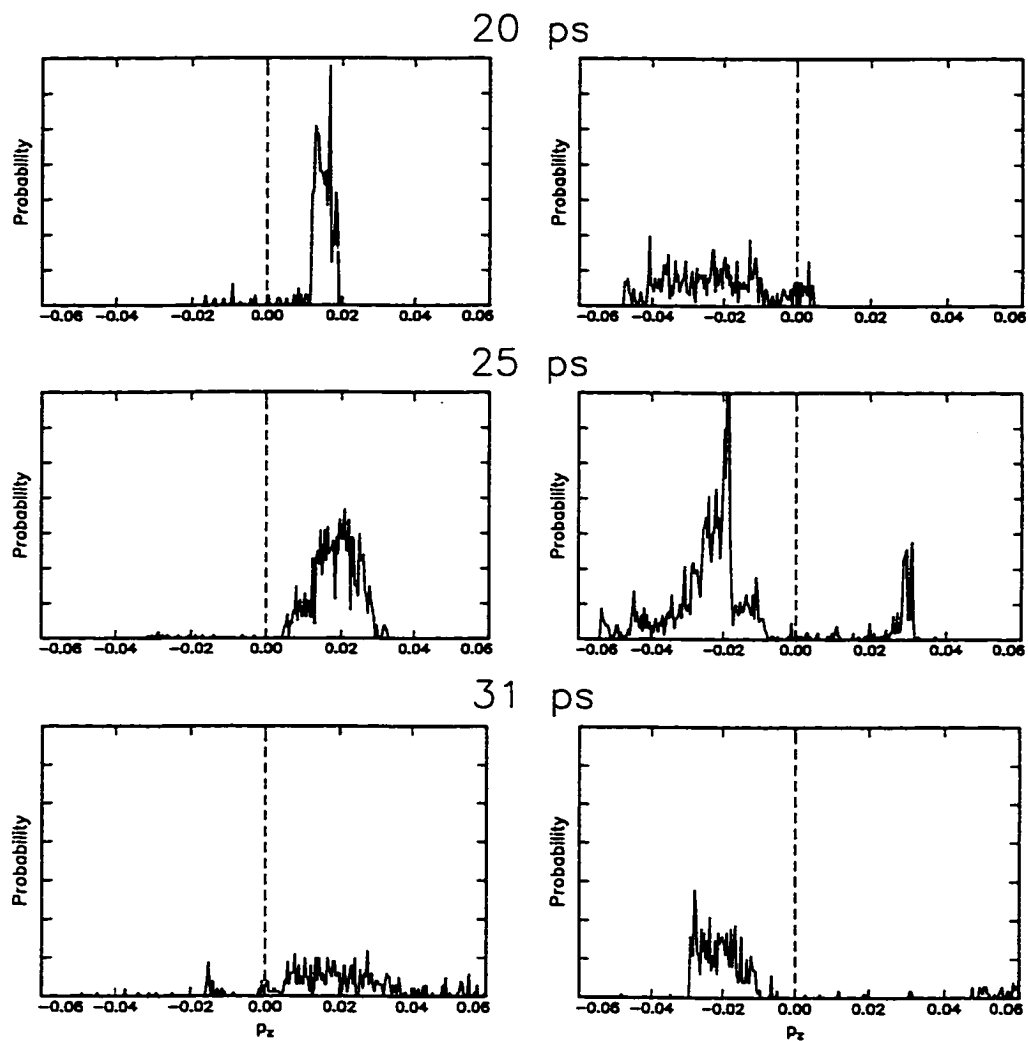


Figure 5.15: Various time snapshots of the calculated momentum fraction that are recombined. Left Column: HCP impulse polarized antiparallel to the static field. Right Column: HCP impulse polarized parallel to the static field.

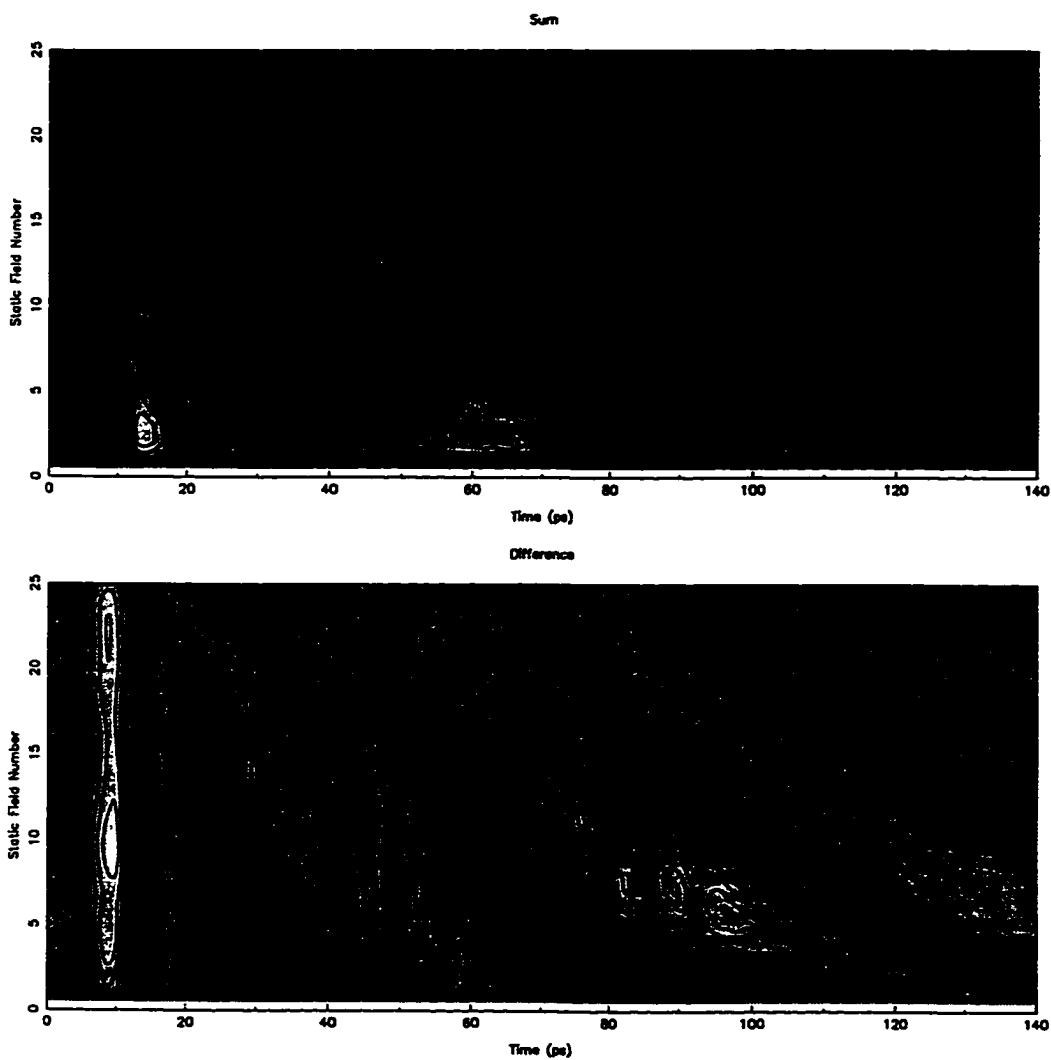


Figure 5.16: Upper: Sum of $n = 42$, $F = 212$ V/cm between recombination spectra obtained for the HCP impulse oriented parallel and antiparallel to the static field. Lower: Difference between the same recombination spectra.

as shown in Fig. 5.15. The time scales observed identify this motion as the bound, radial motion, which we hypothesize at the start to be confined asymmetrically to the uphill side of the core.

The symmetry in the angular oscillations are somewhat harder to classify, as they are present in both plots in Fig. 5.16. It is also difficult to ascertain information on this from the classical ensemble, due to the complexity in its evolution over the long angular period.

5.8 Wrap-Up

With the classical analysis, we have gained some insight into the nature of the modulations in the recombination signal. The fast radial oscillations with a period of approximately τ_K are due to the bound uphill character of the wavepacket, persistently oscillating between the core and outer turning points. The observed radial oscillation period is somewhat shorter than the predicted period of $2\pi n^3$, due to deformation in the potential on the uphill side caused by the static field. For lower lying n -states, this would not cause a significant difference, but for $n = 42$, there is a significant shift in the outer turning point for $z < 0$. A state as high as $n = 42$ was selected for data acquisition because relatively large radial oscillation period (11 ps), which was readily observable in the data scans. Radial oscillations for lower central n wavepackets were not as obvious in the data, due to their increased period, and resolution of our detector. This radial beating is the contribution of the bound portion of the wavepacket.

The slow, or angular oscillation appears in the recombination spectra due to a rather complex evolution in the classical ensemble. A more inclusive computer generated movie of the evolution shows the “petals” referred to above, oscillate into and

out of the “recombination condition” alternately contributing and not contributing to the overall recombination signal, with periods τ_l . The evolution of these petals is evident in the longer time ensembles of Figs. 5.13 and 5.14. This evolution is perhaps one that preserves the z -component of dipole moment as a function of time [12], as required. The conservation of this component of the dipole moment is confirmed for this calculation.

5.9 Quantum Numerical Analysis

Relying solely on Classical Mechanics to explain an inherently quantum system might leave this analysis somewhat incomplete. Several aspects of classical versus quantum mechanics, as well as apparent weaknesses in the classical model will be addressed here.

Why not a quantum numerical analysis? In order to understand the dynamics of the wavepacket evolution at a quantum mechanical level, the classical prescription presented in Section 5.6.1 would still be followed, only the time dependent Schrödinger equation (TDSE) would replace the classical equations of motion. The general solution to the non-relativistic TDSE is known exactly for any system. It's simply Ψ such that

$$\Psi = \sum_n^{\infty} c_n(t) \psi_n e^{-i\omega_n t}, \quad (5.8)$$

where $c_n(t)$ are time dependent expansion coefficients, ω_n is the energy of the n^{th} eigenstate, ψ_n . It is implied that the sum includes integration over the continuum as well. The problem then is reduced to finding the expansion coefficients c_n for each basis state ψ_n [15].

In the strong field in which this study takes place, a good basis set is hard to define. The static field mixes a myriad of states together, each contributing to Ψ . This mixing occurs where the Stark effect causes levels to shift in energy and mix at avoided crossings, due to the finite sized core in Ca [16] [3]. Many, many states, including continuum states, would have to be included in a quantum calculation to even to begin to accurately represent the excited wavepacket at a numerical level. In addition, the static field is so strong ($> 1/16n^4$) in this study that the wavepacket can escape the atom. This means Ψ must also contain *continuum* character as well, which adds an additional *infinite* number of states to the system. Determining just what ψ 's to include in the the series expansion of Equ. 5.8 and how much character of each (the c_n 's), is difficult.

In practice, however, the basis set used is simply a truncated version of the total available. Just where to truncate the basis set is largely up to the operator, computational resources, and required accuracy. The problem is interesting, and an attempt to implement such a numerical system would be worthwhile, but for now, is simply out of the scope of this work.

Since this experiment involves such a highly dynamical system, another approach would be to numerically integrate the non-relativistic TDSE including all fields directly, to obtain a numerical version of $\psi(t)$. Once obtained, examining $\psi(t)$ might provide clues to the evolution of the system, in much the same manner as was done with the classical model.

Phase. One of the two most important distinctions between quantum and classical mechanics is phase (see **Energy Quantization** below for the second). Phase is responsible for quantum interference effects, so prominent and important in atomic and quantum studies. For non-stationary states, like a wavepacket,

phase is the $-i\omega t$ term in the exponent of Equ. 5.8. It is a time dependent phase giving rise to constructive and destructive interference, in much the same way that optical or mechanical waves interfere. Interference is a crucial phenomena in wavepacket experiments.

The classical simulation used here does not take any phase into consideration whatsoever. The radial and angular oscillations in the data are likely due to some quantum mechanical phase interference with periods τ_K and τ_l . But in this case, a classical analog is obviously present as evident by the relatively good qualitative agreement between the data and calculated results, at least over short (≤ 30 ps) time periods. The power of the classical analysis lies in the insight it provides into the interaction with a familiar kinematic-based picture.

Energy Quantization. The next equally important distinction between classical and quantum mechanics is energy quantization. Classically, all energies are allowed, quantum mechanically, they're not. In simulating the wavepacket, the classical model includes the effects of energy quantization by compiling the final recombination spectra as a linear combination of that from the individual n -states in the wavepacket itself. As an example, consider the $n = 42$ wavepacket. In producing the recombination spectra shown in Figs. 5.13 and 5.14, individual spectra were first computed for the states with $n = 40, 41, 42, 43,$ and 44 . The results were then subsequently averaged together, weighting each n -state according to the excitation laser pulse used in the experiment. This is classical energy quantization.

The effects of energy quantization have more of an effect at longer times, for instance $> 50ps$, where effects of dispersion and revivals in the real quantum wavepacket might become important. Perhaps this is a strong contributing

factor to the disagreement between the classical theory and data for times longer than $\sim \tau_l$.

Core Effects. The classical model is a Hydrogen-atom model, with no core effects (polarization, precession, etc.) included. Core effects cause state mixing at avoided level crossings, meaning uphill stark states can be mixed with downhill states, and vice versa.

A zeroth order test of the effects of the classical model's lack of any state mixing, or core effects can be obtained by comparing the excitation spectra of Hydrogen and Calcium. In the calculation we wish to monitor the d -character of the wavepacket as a function of static field. A quantum mechanical calculation is performed, in which a Hamiltonian is set up with ground state energies as diagonal matrix elements, including the quantum defect factors. Off diagonal dipole-coupling matrix elements are represented by

$$\langle n'l'|rcos\theta|nl \rangle \quad (5.9)$$

which can be separated into the radial and angular parts like

$$\langle n'|r|n \rangle \langle l'|cos\theta|l \rangle . \quad (5.10)$$

The radial matrix elements are calculated numerically using the Numerov method [18], and the angular matrix elements are calculated analytically (all are zero, unless $l' - l = \pm 1$). Once constructed, the matrix is diagonalized [19], and from this, the wavefunctions in the static field can be found, as linear superpositions of the zero field wavefunctions.

As mentioned we are particularly interested in what happens to the d -character of wavefunctions in the static field. The results are shown in Fig. 5.17 and Fig. 5.18 for H and Ca. These figures show plots of energy versus d -character as a function of static electric field strength. The small peaks plotted at a given (energy,field) coordinate represent the “amount” of d -character present in a wavefunction at that point. The important result here is the coarse structure of the “Stark maps” for H and Ca *look similar*. At least at a qualitative level, this tells us that the core effects do not play a particularly prominent role in the short time dynamics in the experiment, and our Hydrogen model is justified at this level.

To close this section, one more remark is made about the dependence of the radial period, τ_K on the static field. As shown in Figs. 5.17 and 5.18 at larger static field values (“up” on the vertical axis), the d -character of the wavepacket begins to originate from *lower* n -states. This can be seen by choosing some n -state, such as $n = 35$, and placing one’s finger at the coordinate $n = 35, F = 0$ V/cm on one of these two figures. Now follow straight up from this point to $n = 35, F = 200$ V/cm (a relatively large static field). This point intersects a density pattern of d -character that appears to originate at $n = 33, F = 0$ V/cm. The lower n -state is Stark shifted into contributing to the the $n = 35$ character. An $n = 35$ wavepacket with $n = 33$ character would tend to *decrease* the Kepler period, in analogy to the classical reasoning of the same effect shown in Fig. 5.12.

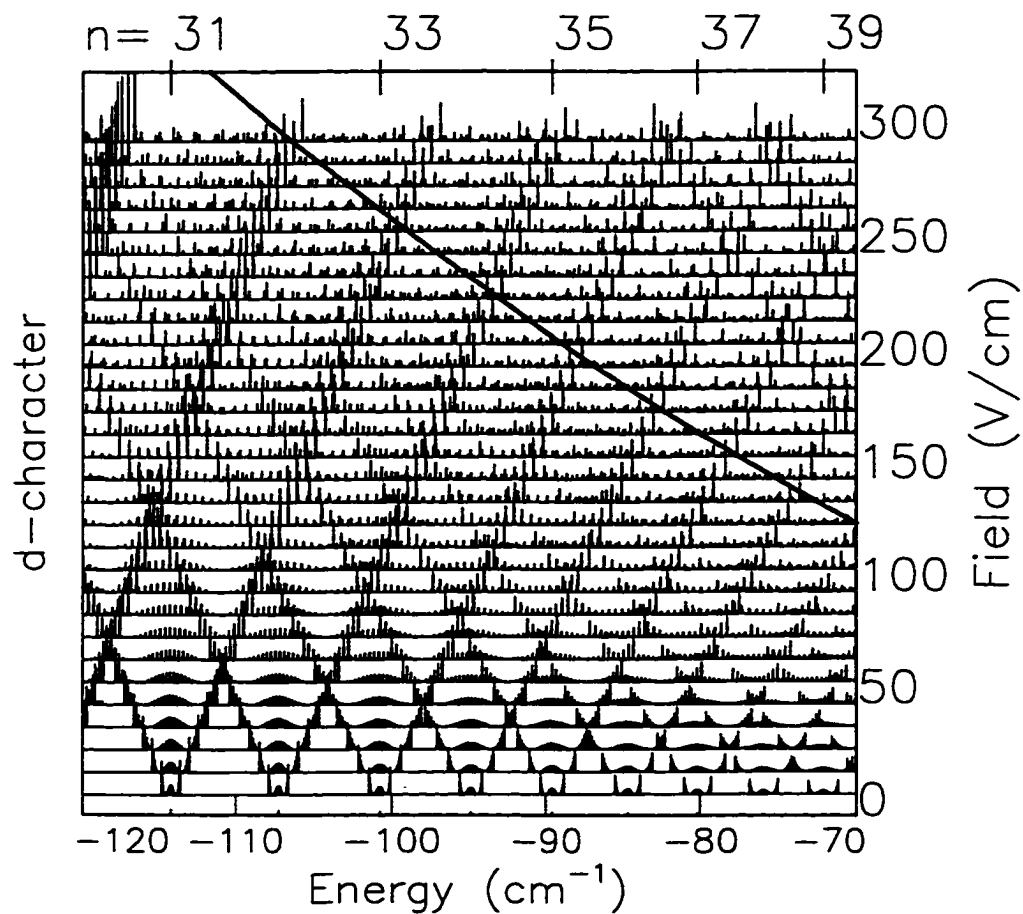


Figure 5.17: Quantum mechanical stark map of d -character for H. The difference in field between each horizontal trace is 10 V/cm. The solid line is the classical field ionization limit, $1/16n^4$.

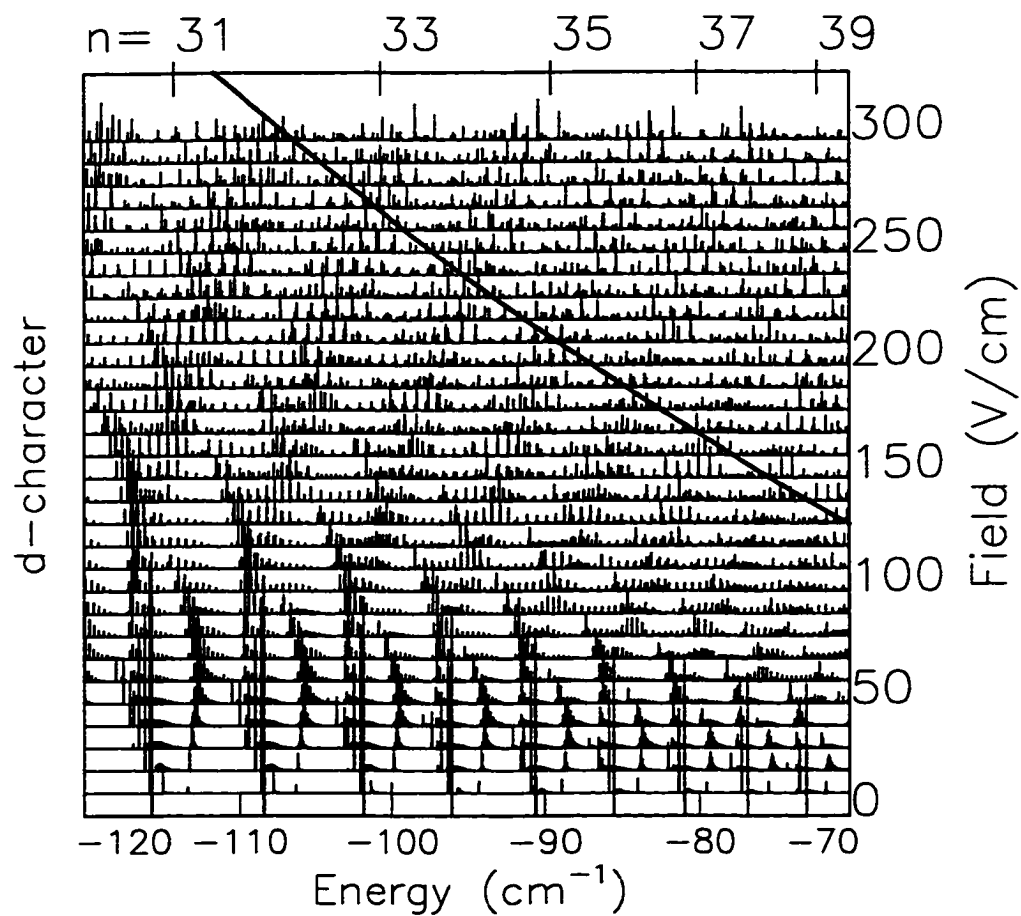


Figure 5.18: Quantum mechanical stark map of d -character for Ca, which includes quantum defects (core effects). The difference in field between each horizontal trace is 10 V/cm. The solid line is the classical ionization limit, $1/16n^4$.

5.10 Orienting the HCP perpendicular to the static field

As a final experimental probe into this wavepacket, the HCP is also polarized at *90 degrees* with respect to the static field. Additional data was acquired following the identical experimental steps and data acquisition presented above. Although not a systematic part of this study, this polarization case is discussed here for sake of completeness.

1. **Absence of radial oscillations.** There is a distinct absence of any radial oscillations the recombination spectra. This lends support to our classical model above, which shows radial oscillations only along the static field axis. In the impulse approximation, a HCP polarized perpendicular to the static field axis will not “see” motion along a perpendicular axis. This is the primary conclusion of the experiment presented in Chapter 4 and reference [13].
2. **Phase difference in the angular oscillations.** There is a phase difference in the angular oscillations, relative to the parallel and antiparallel cases. Experimentally, this phase difference has some functional dependence on the static field strength.

The language in this section is somewhat vague, presenting only empirical experimental observations, that were not fully investigated in the laboratory. The primary focus of this experiment was for the parallel and antiparallel HCP polarizations presented above. Attempts to model this perpendicular polarization case classically have failed to reproduce what is seen experimentally. Since the HCP field is no longer polarized along the quantization axis of the system (the static field axis), the m quantum number can now be changed by the HCP. The saddle point of a potential in an ex-

ternal field is known to have a dependence on m [14]. Strong oscillations in m are seen in the classical model, in response to the HCP, in phase with the observed data. However, modifying the recombination condition presented in Section 5.6.1 to depend on m , does not cause the simulation to reproduce the experimental data. The simulation merely produces a flat recombination fraction as a function of time, at some level above zero.

5.11 Conclusions

In this chapter, HCP assisted recombination of a wavepacket in a static field induced continuum has been presented. Classical numerical analysis has shown a remarkable qualitative agreement to the data acquired. Using a static field induced continuum has provided a highly dynamical, and interesting system in which to study this recombination effect.

Explaining the data has revolved strongly around a kinematic analysis and a high degree of localization of the wavepacket. Strong radial and angular oscillation in the wavepacket are observed in the recombination signal and are explained in terms of a strong time dependence of the momentum distribution of the wavepacket, as illustrated by the classical ensemble.

Bibliography

- [1] V.L. Jacobs, et. al., *Phys. Rev. Lett.* **37**, 1390 (1976); S.M. Jaffe, et. al., *Phys. Rev. A* **30**, 1828 (1984). Also see [2, 4].
- [2] D.S Belic, et. al., *Phys. Rev. Lett.*, **50**, 339 (1983).
- [3] T.F. Gallagher, *Rydberg Atoms*, Cambridge University Press, 1994, Chapter 19.
- [4] F. Brouillard and J.W. McGowan, *Physics of Ion-Ion and Electron-Ion Collisions*, Plenum Press, New York, 1983, p. 279.
- [5] For a very direct example of momentum transfer between a Rydberg electron and a HCP, see R.R. Jones, *Phys. Rev. Lett.* **76**, 3927 (1996). Further, a classical numerical calculation demonstrating the momentum shift is presented in Fig. 3.1.
- [6] M.B. Campbell, *private communication*.
- [7] M.B. Campbell, T.J. Binsky, and R.R. Jones, *Opt. Express* **1** 197 (1997).
- [8] E. Luc-Koenig and A. Bachelier, *J. Phys. B.* **13** 1743 (1980); T.P. Hezel, et. al., *Am. J. Phys.* **60** 324 (1992); F. Robicheaux, *Phys. Rev. A* **56** 4032 (1997); G.M. Lankhuijzen, et. al., *Phys. Rev. Lett.* **79** 2427 (1997); B. Broers, et. al., *Phys. Rev. A*, **49** 2498 (1994).

- [9] B. Bederson and H. Walther, *Advances in ATOMIC, MOLECULAR, and OPTICAL PHYSICS*, Academic Press, Vol. 38, 1998. In particular, see p. 16 Fig. 4, and the discussion of “Radial Wavepackets” on p. 12.
- [10] W.H. Press, et. al., *Numerical Recipes in C, 2nd ed.*, Cambridge University Press, 1988.
- [11] H. Goldstein, *Classical Mechanics*, Addison Wesley, 1980.
- [12] See the definition of \vec{M} in E. Luc-Koenig (above); Classically, the dipole moment is directly related to the z component of the Runge-Lenz vector, which is a little discussed constant of the motion in the unperturbed Kepler problem. See Goldstein, p. 102.
- [13] T.J. Benschky, G. Haefliger, and R.R. Jones, *Phys. Rev. Lett.*, **79**, 2018 (1997).
- [14] W.E. Cooke and T.F. Gallagher, *Phys. Rev. A*, **17**, 1226 (1978).
- [15] C. Cohen-Tannoudji, B. Diu, and F. Laloë, *Quantum Mechanics, Volume Two*, John Wiley and Sons, 1997, p. 1286.
- [16] M.L. Zimmerman, et. al, *Phys. Rev. A*, **20**, 2251 (1979).
- [17] R.L. Liboff, *Quantum Mechanics, 1st ed.*, Addison-Wesley, 1988, p. 568.
- [18] S. Koonin, *Computational Physics*, Benjamin/Cummings Publishing Company, Inc., Menlo Park, CA, 1986; J. Blatt, *J. Comp. Phys* **1**, 378 (1967).
- [19] The matrix to be diagonalized is a real, symmetric matrix. See W.H. Press, *ibid.*, p. 456.
- [20] N.E. Tielking and R.R. Jones, *Phys. Rev. A* **51**, 3370 (1995).

Chapter 6

Conclusions

This thesis has described two HCP/Rydberg atom interactions from a classical perspective. The first involved the ionization of Na atoms due to a unique THz field that executed circular polarization for only 1/4 of a field cycle. The second involved ion-electron recombination using a HCP and a continuum state of Ca. The following discussion highlights the major points of each interaction, and closes with some speculative suggestions for possible future studies.

6.1 Ionization due to 1/4 Cycle Circularly Polarized Radiation

The unique radiation field used in this experiment was created using two counter-propagating, cross-polarized HCPs. Depending on the initial Na Rydberg state excited, the interaction could be studied in one of two regimes.

The impulsive regime, where the duration of the total HCP field is small compared to any motion of the Rydberg electron. In this regime, the field acts like a quick, impulsive force, and the Rydberg electron is virtually at rest during the interaction.

The non-impulsive regime, where the duration of the total HCP field meets or

exceeds that of the motion of the Rydberg electron. There is significant motion of the electron during its interaction with the field.

In the impulsive regime, the ionization of Na atoms was found to be remarkably insensitive to the rapidly varying polarization of the HCP field. This was shown classically to be a result of independent shifts or “kicks” in the momentum distribution along each Cartesian direction containing a component HCP. Further, a momentum kick along one Cartesian coordinate was not found to couple into the momentum distribution of an orthogonal coordinate. This result has not been seen before, and is the first experiment to push HCP/Rydberg atom experiments into three full Cartesian dimensions. As for the ionization process, these momentum kicks produced energy shifts on the Rydberg state, independently driving it towards or away from the ionization limit.

In the non-impulsive regime, the ionization mechanism was found to depend on the precise structure of the total HCP field, including its peak field, and total duration. The momentum kicks are no longer independent along orthogonal Cartesian dimensions, but are found to couple into one another. Further, an alteration of the electron’s binding potential by the HCP field now plays a role in this regime’s ionization process.

6.2 HCP Assisted Electron-Ion Recombination

In this experiment a HCP was used to extract momentum and energy from a free electron, forcing it to pair with a nearby ion. To create the ion-electron system, a static field was used to induce a continuum state in Ca. The static field created a highly dynamical system, that depended on the initial Rydberg state and static field strength. Classically, the recombination mechanism was described in terms of a

vectorial extraction of linear momentum from the continuum state, by the HCP. If the accompanying energy shift resulted in sufficient energy extraction, the continuum state could become rebound to the ion. This classical model had good qualitative agreement with the data over a short time duration after excitation, and aided greatly in our description of the recombination process. It provided enough information to interpolate the explanation to longer times, and to find deficiencies in the classical model in describing an inherently quantum system.

6.3 Future Directions

6.3.1 1/4 Cycle Circularly Polarized Fields

This unique field might be used to create novel Rydberg states. Although not observed in the lab, near the end of the study, the classical model indicated that the 1/4 cycle field leaves the atom with a wide distribution in the m quantum number. Further, the spread in m is either over negative or positive values, depending on the helicity of the 1/4-cycle pulse, and the width of the distribution becomes larger and larger as a function of the field amplitude. If m is some large value, then l must be high as well. If the final state distribution in m and l can be narrowed, it might be possible to create high- l , high- m Rydberg states using this field. These states are potentially interesting because high- l states execute near circular orbits, with very little core interaction. An atomic state with little or no core interaction would provide an interesting system for future study. In particular, electron scattering with a second, core electron, leading to autoionization would become less probable, meaning external control of this atomic process might be possible. Also, for high- l states, the quantum defect parameter would be near zero, meaning the state would be virtually purely Hydrogenic, even though the actual atom is an alkali metal. Also, as a contribution to atomic physics

itself, creating high- l Rydberg atoms on a picosecond time scale, seems somewhat elusive at this time.

It might prove difficult to practically perform this experiment, however, because another HCP would be needed to directly probe the high- l state, meaning *three* biased GaAs wafers would be needed. Also, the method of generating the 1/4 cycle field is not very applicable as a tool. Currently, it is not very portable or convenient, and remains an entire experiment in itself. Perhaps there is some other method of generating circularly polarized THz fields. For example, does some material exist that would behave like a 1/4-wave plate for THz fields?

6.3.2 HCP Assisted Recombination

In the introductory sections of Chapter 5, a version of the recombination experiment was mentioned that did not involve a static field. However, it did not prove very interesting, and was performed in a matter of days, requiring little analysis. However, the classical model has shown a rather interesting prospect unfold in this relatively dull experiment. If the continuum population that becomes rebound to the atom is tracked in its bound state for many tens of picoseconds after becoming recombined, something very interesting happens, as shown in Fig. 6.1.

This figure shows the evolution of a wavepacket photoexcited directly into the continuum, with no static field present. Initially, the charge distribution is expanding radially outwards (inset A). At 10 ps, the HCP recombines a small portion of the wavepacket (inset B). Monitoring the recombined population for ≈ 70 ps (inset D) reveals the formation of a highly localized charge distribution on one side of the core, that persists for nearly 20 ps. An atomic state with this high degree of localization is very unusual, with many possibilities, such as:

Three dimensional, oriented wavepacket. The charge distribution can be placed

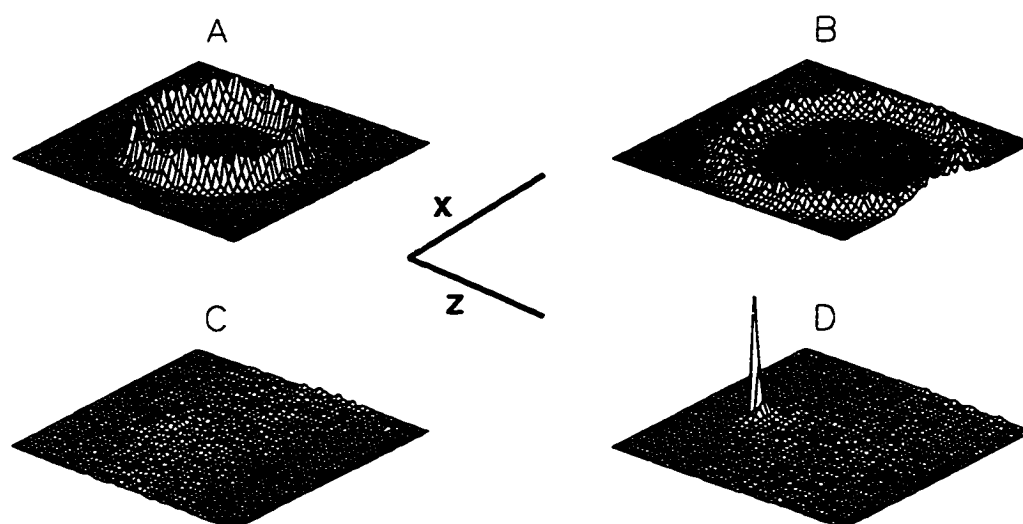


Figure 6.1: A two dimensional plot of the charge distribution of a continuum wavepacket recombined to its parent ion by a HCP 10 ps after excitation. Its spatial distribution is shown after A) 10 ps, B) 15 ps, C) 47 ps, and D) 72 ps. The HCP is polarized along the $+\hat{z}$ -axis. There is no static field present in this problem. Note the highly localized charge distribution that develops in inset D. All plots are identically scaled, with the x and z axes running between ± 20000 a.u.

anywhere about the core in three dimensional space, depending on the orientation of the recombining HCP.

Classical/Quantum Correspondence. What exactly is this localized charge distribution? A singly localized classical electron? What are its values of $\langle n \rangle$ and $\langle l \rangle$? Can it be used to study a transition from quantum to classical behavior?

A Second HCP kick. Suppose the localized charge is further kicked by a second HCP field,

- in a direction perpendicular to a radial vector from the core. Can it be made to execute a purely circular, high- l , planetary orbit?
- in a direction directly towards the core. Would a radiation field be produced when the charge scatters from the core?

Recombine Multiple Portions of the Continuum Wavepacket. Suppose more than one HCP was used to create multiple localized charge spikes, like the one shown in Fig. 6.1D. Could the resultant spikes be used to encode or store information on the atom? Perhaps a charge spike could represent a logical “1” and the absence thereof a logical “0,” forming “qbits” (quantum bits). As a first “computation,” how could bitwise operations such as not, xor, or, and and be performed and detected?

Appendix A

$\vec{F} = m\vec{a}$: Classical Numerical Analysis of Rydberg Atom/HCP Interactions

A.1 Introduction

In this appendix, a computer based, classical mechanics approach to modeling the interaction between a Rydberg electron and external field is presented. Since classical mechanics is based on familiar kinematic or “motional” ideas, a great amount of physical insight is gained about the interaction. However, classical mechanics is not the final word in atomic physics. Atoms are inherently quantum mechanical objects, strongly coupled to the ideas of energy quantization and phase, two items most definitely not a part of classical mechanics. Nevertheless, classical mechanics is a surprisingly useful tool in answering questions it might not be expected to answer. The insight gained is invaluable, and the methods used are not so difficult that they become research projects themselves.

In principle, performing a classical analysis for HCP/Rydberg experiments is fairly straightforward; in fact, it involves only one concept, which is to

integrate the classical equations of motion for an electron bound by the

Coulomb force and subjected to the required external fields.

In practice, however, there is some degree of sophistication that goes into implementing such an analysis. The integration process cannot just be carried out on paper using analytical techniques. Instead, numerical integrations must be performed on a computer. So, this is a programming project, with many required support routines and implementation details, all of which *will not* be discussed in this appendix. Only the most critical facets of implementing this classical model are discussed, that are at the heart of it all. These are the items I recall not understanding at all at first, and being very frustrated over, but then appreciating the most when they were all worked out.

Since a computer serves at the active ingredient here, the topics covered in this appendix are written presented almost like a computer manual, in a very “step by step” approach, with the hope of helping anyone to understand or even implement such classical analysis themselves. The order of presentation of this appendix will be from the “ground up,” in much the same way the code itself was written and improved upon over time.

While reading this appendix, it will be helpful to have two textbooks nearby:

1. H. Goldstein, *Classical Mechanics, 2nd Ed.*, Addison-Wesley, 1980.
2. W.H. Press, et. al., *Numerical Recipes in C, 2nd Ed.*, Cambridge University Press, 1992.

When needed, instead of constantly referring to references at the back of this appendix, the books will be referred to as “in Goldstein...” or “in Numerical Recipes” throughout.

A.2 Numerical Integration

The power of classical mechanics is to be able to predict the trajectory of a particle based on the forces acting upon it. The particle of interest here will be an electron, and the forces of interest will be the Coulomb force, and some external force, like that from a HCP. At the onset of the problem, the only information we can state is the differential equation of motion of the electron, resembling something with a $d^2\vec{r}/dt^2$ on the left hand side, and the functional form of forces on the right hand side, with an equal sign in between. This is the force law of the problem, where all of the analysis begins.

However, there is not all that much immediate information in this force law. There would be more information in $\vec{r}(t)$, or $\vec{v}(t)$, as these would represent the familiar position and velocity of the electron, as a function of time, subject to the forces of interest. These can be plotted, analyzed, and actually *used* for something. But these quantities are, of course, *integrals* of the force law, which must be found. For an arbitrary force (a HCP, static field, etc.), the force law is not integrable to any analytic form (at least in the familiar $x - y - z$ coordinate space[1]). In other words it will not be possible to write down nice, neat functions for $\vec{r}(t) = \dots$ and $\vec{v}(t) = \dots$ for subsequent use.

This is where numerical integration enters. In a nutshell, knowing $\vec{r}(t_0)$ and $\vec{v}(t_0)$, the position and velocity of the the electron at some start time t_0 , the numerical integration will find what $\vec{r}(t_1)$ and $\vec{v}(t_1)$ are at a time $t_1 = t_0 + dt$ later. In other words, it takes the dynamical quantities one step forward in time, by the amount dt . Once known, another time-step forward can be taken from t_1 , then another, and another. These “time steps” are the process of numerical integration. Each one of them takes into account all of the relevant forces on the system, finding \vec{v} from $d^2\vec{r}/dt^2$

and \vec{r} from \vec{v} , at each infinitesimal step through the desired integration period.

It is also a recursive process, where a given step depends on the previous one. A starting point must be supplied for this sequence, so we must provide the *initial conditions*, or $\vec{r}(t_0)$ and $\vec{v}(t_0)$, upon which the recursive process may begin. In effect, the numerical integration tracks how the electron's motion evolves as a function of time.

There is even more information to be had at each time step, other than just the position and velocity of the particle. These are other physical quantities related to the classical object, including momentum, energy, and angular momentum, to name a few. From \vec{v} and \vec{r} , we can calculate the following variables, but why are these variables important?

Energy. $E = 1/2v^2 - 1/r + V_{ext}$ (if any). This variable is of critical importance for a very fundamental reason: the energy allows one to determine if the electron is bound or not. In the absence of an external field, a classically bound particle will forever remain bound. But an external field can change this, much as a HCP can ionize a bound Rydberg state, or a static field can create a continuum electron state.

Momentum. $\vec{p} = m\vec{v}$. HCPs are known to affect the momentum of electrons. Watching this variable has proven invaluable in the Chapter 4 experiment, and is readily available along the integration process.

Angular Momentum. $\vec{L} = \vec{r} \times \vec{p}$. This is a conserved quantity in the Kepler problem, but is no longer conserved in the presence of an external field. Watching this variable might provide clues into the angular evolution of Rydberg states, especially in the Chapter 5 experiment, which involves the presence of a static field.

All of these “physical” quantities about the system, and more, can be found at any time using the variables of integration, thanks to the stepwise numerical integration process.

So the numerical integration process takes time steps through the evolution of a system, according to the “rules of the game,” or the system’s differential equation of motion. At any point along the way, the variables of integration may be examined and applied against physical ideas we may have concerning the system. It’s all really very powerful, and once a basic system has been implemented, there is great flexibility in potentially finding answers to questions one might wish to ask.

A.3 A Classical Rydberg State

In the experiments themselves, studies are performed on Rydberg states of atoms. To begin then, a numerical model of a Rydberg state must be created. A classical Rydberg state of an atom is most accurately described in the planetary sense: a pointlike electron orbiting a pointlike nucleus, bound by the Coulomb force. In the context of an actual experiment, usually, the first picture that comes to mind of a classical orbit is often wrong, thanks to pictures presented in modern physics books about “Bohr orbits.” In the experiments done in this thesis, Rydberg states with very low values of angular momentum are typically excited, usually $l = 2$. This appears as anything but a circular “Bohr” orbit, as shown in Fig. A.1.

The low- l orbit is highly elongated due to its low value of angular momentum. Recall, a particle in straight line motion has no angular momentum, or $l = 0$. This orbit is only 2 units away from that. Nevertheless, this is the nature of the classical orbit we must model, in light of the experimental conditions. They appear much different from the high- l circular “Bohr orbits” that were used to introduce us to

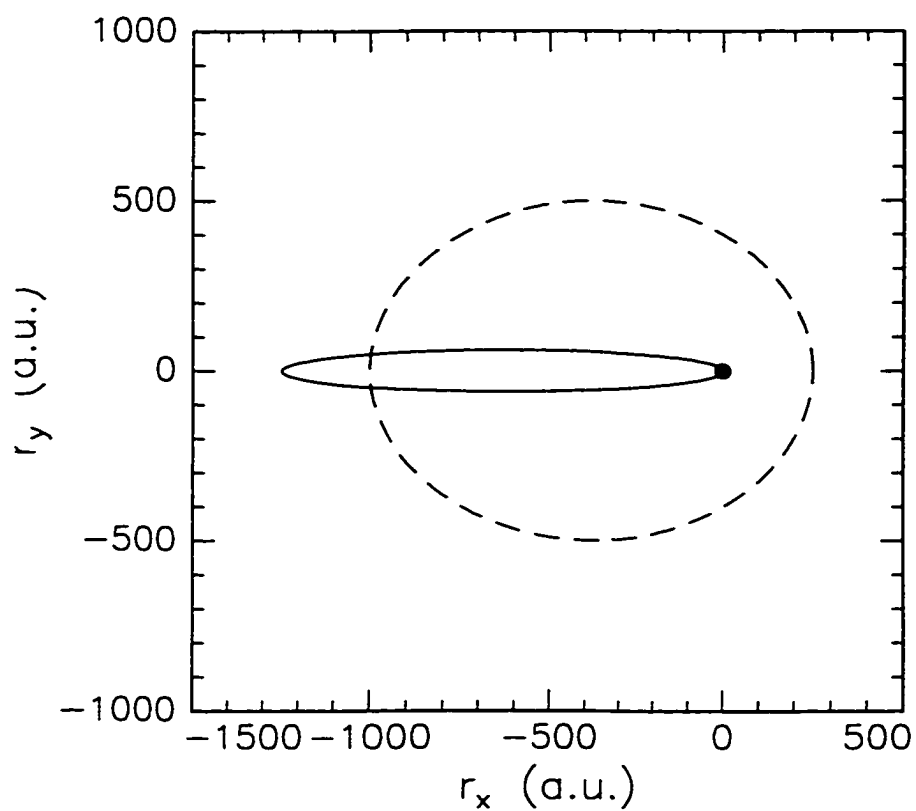


Figure A.1: An $n = 25$, $l = 2$ classical orbit (solid line). The x and y axes have the same scale. Note how highly elongated the low- l orbit appears (solid line) compared to the high- l , more circular orbit (dashed line). The nucleus is the dark dot at the focus near $(0, 0)$.

atomic physics in Modern Physics texts.

A.3.1 The Differential Equation of Motion

Goldstein discusses the Kepler problem in some detail, on p. 94, Section 3-7, but not in the form that will be of help here. In this section, the Kepler problem is solved exactly for $\vec{r}(\theta)$, where \vec{r} and θ are the radial and angular positions of the electron in the closed orbit, with $\theta = 0$ being the inner turning point. Why is this form of no use to us?

Recall the most important parameter in the last two experimental chapters: **time**. The critical field throughout this whole thesis is the the HCP field, which is a time-dependent field. In fact, this time dependence divided the entire experiment in Chapter 4 into two parts: the impulsive and non-impulsive regime. In Chapter 5, the classical ensemble produced was found to be a highly time-dependent entity whose time evolution both before and after the HCP interaction was of interest, and greatly helped to explain the experimental data. In other words, we don't have any θ , or position dependent fields we wish to study; our critical field is not one with some strange gradient that affects one side of the atom more than the other, for example. This makes the discussion in Section 3-7 instructive, but limited. We must instead turn to Section 3-8, which discusses finding $\vec{r}(t)$.

Finding $\vec{r}(t)$ is not as easy as finding $\vec{r}(\theta)$, however. In fact, the second sentence of Section 3.8 in Goldstein reads:

“To describe the motion of the particle in time as it traverses the orbit is, however, a much more involved manner.”

If *this* pure Coulomb case is “involved,” then it goes without saying that there is simply no analytic solution for $\vec{r}(t)$ of an electron in a combined Coulomb/HCP

field. This is of little concern to us here, and will not add excessive hardship. The numerical integration technique is very much a “turn the crank” approach. As long as everything we “throw” at the algorithm is relatively smooth and well behaved, the numerical integration will happily integrate along, and provide us with stepwise solutions in time for as long as we like.

For such a planetary system then, the differential equation (DE) of motion *in time* is

$$\frac{d^2\vec{r}}{dt^2} = -\frac{1}{r^2}\hat{r}, \quad (\text{A.1})$$

where r is the radial coordinate of the electron, and t is time. So we proceed then, to numerically integrate Equ. A.1.

A.3.2 Preparing it for the Computer

In preparing to actually implement the numerical integration process on a computer, we refer to Numerical Recipes, Chapter 16 as a guide. As outlined on page 707, a second order differential equation such as Equ. A.1 can be always be broken up into two first order equations. In this case, the two first order DEs of motion are

$$\frac{d\vec{r}}{dt} = \vec{v} \quad (\text{A.2})$$

and

$$\frac{d\vec{v}}{dt} = -\frac{1}{r^2}\hat{r}. \quad (\text{A.3})$$

At first look, writing down these equations is of little use; they are so blatantly obvious, and contain no new information. Nevertheless, they are first order equations,

and are much easier to deal with at a numerical level than second order equations.

For the integration process, these first order equations are broken down into their scalar component forms, namely

$$\frac{dr_x}{dt} = v_x, \quad (\text{A.4})$$

$$\frac{dr_y}{dt} = v_y, \quad (\text{A.5})$$

$$\frac{dr_z}{dt} = v_z, \quad (\text{A.6})$$

in position, and

$$\frac{dv_x}{dt} = -\frac{r_x}{r^3}, \quad (\text{A.7})$$

$$\frac{dv_y}{dt} = -\frac{r_y}{r^3}, \quad (\text{A.8})$$

$$\frac{dv_z}{dt} = -\frac{r_z}{r^3}, \quad (\text{A.9})$$

in velocity. Note that the Cartesian components of the Coulomb force have been found and included in right hand sides of Equations A.7 - A.9. Integrating these six differential equations of motion will give us the full position and velocity of the electron as a function of time.

A.3.3 Initial Conditions

The numerical integration process needs a “send off.” In other words, assuming that we want to start integrating at some time t_0 , we need to supply the integration

algorithm $\vec{r}(t_0)$ and $\vec{v}(t_0)$, from which all successive values in time can be found. Just what initial conditions to supply is based very strongly on the physics of the system.

A Rydberg Orbit

In the planetary model, a bound Rydberg orbit is a point-like electron orbiting a point-like nucleus. Some information about its motion can be inferred from the potential in which it moves, as shown in Goldstein, ppgs. 77 - 78, Figs. 3-3 and 3-4. The motion is bound and periodic, moving between two turning points, the inner turning point, near the core, and the outer turning point, far from the core. Given that the kinetic energy of the electron is $E - V$, where E is its energy and V is the value of its potential energy, its motion near the turning points can be studied (recall E is constant):

Inner Turning Point. V is very large and negative, and r is small ($V = -1/r$).

This makes the kinetic energy of the electron very large; the electron moves very rapidly as it turns around near the core.

Outer Turning Point. V is very small since r is large. This makes the kinetic energy of the electron very small; the electron is practically at rest near the outer turning point.

So the electron doesn't move at a uniform speed throughout its orbit; fast near the core, and slow near the outer turning point, accelerating and deaccelerating at points between. This has drastic consequences on what initial conditions will make the model physically correct. Why?

In a classical sense, the amount of time an object spends at a particular position is inversely proportional to its velocity at that point. An object moving very rapidly through a particular point in space spends a small amount of time there; one moving

very slowly through the same point spends much more time there. In the case of the motion of a Rydberg electron, this means it spends little time near the core and a lot of time near the outer turning point. So in selecting the initial conditions for the integration, choosing points uniformly distributed about the orbit, for example, (the easiest thing to do), will not accurately reproduce the physics of a Rydberg state.

The time the electron spends at a particular point around an orbit is somewhat vague. A related quantity is a “classical probability” which is instead the fraction of the total orbital time spent in some small volume. Recall the classical Kepler period of a Rydberg orbit is $\tau_K = 2\pi n^3$. When thought of in this way, a plot of the classical probability density versus orbital position can be made, as shown in Fig. A.2.

This figure clearly demonstrates the peaked probability density near the outer turning point, where the electron is most likely to be found, and near zero probability near the core. So in selecting initial conditions for the Rydberg orbit, the initial points must be weighted against a probability density such as this one.

The classical probability begins with the basic assumption that the “probability of being there” and “time spent there” are related, as in

$$dP = \frac{dt}{\tau_K} \quad (\text{A.10})$$

where dP is the differential probability of a particle to spend a time dt somewhere along the orbit, and τ_K is the familiar Kepler period. The differential time, dt can be written in terms of a small unit of radial length as

$$dt = \frac{dr}{\dot{r}}, \quad (\text{A.11})$$

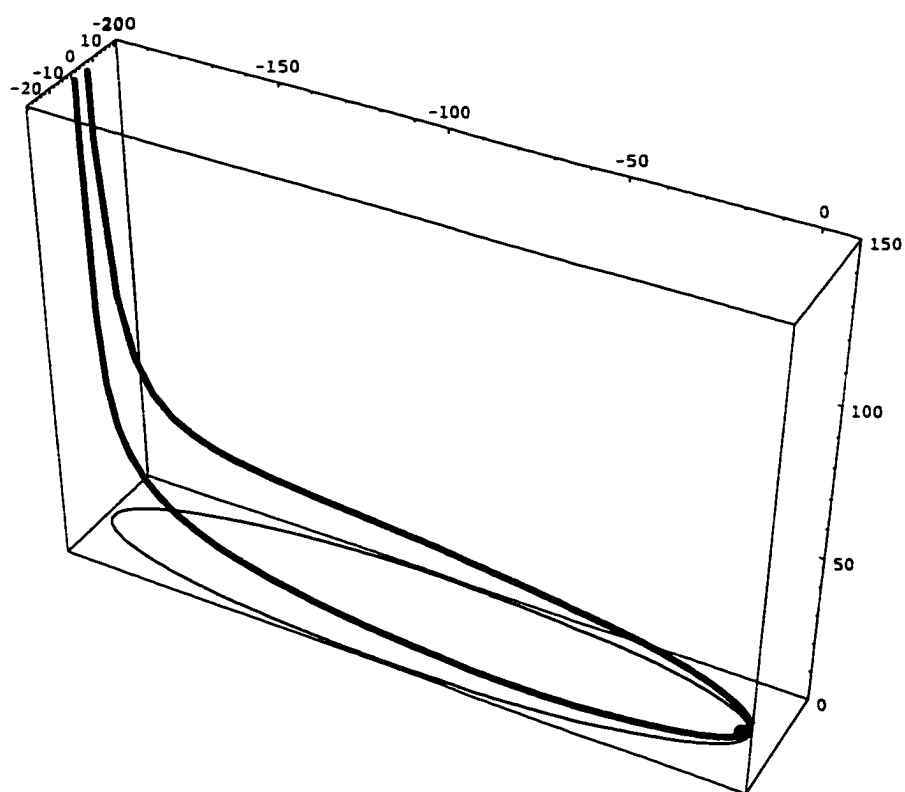


Figure A.2: The classical probability density of finding an electron at any given point along a Rydberg orbit (bold curve). The nucleus is the point on the right part of the plot. The classical trajectory is the shown in the bottom plane of the plot (normal pitch line). Notice the highly peaked density towards the left, at the outer turning point. The height scale is chosen so that the peak at the outer turning point does not completely dominate the plot, at the expense of “cropping” it as shown.

where dr is a small unit of length, and \dot{r} is the velocity of the electron. An expression for \dot{r} can be found by taking one time derivative of Goldstein, p. 96, Equ. 3-55. Combining Eqs. A.11 and A.10 gives the expression for dP as

$$dP = \frac{dr}{2\pi n^3 \left[\frac{2}{r} - \frac{1}{n^2} - \frac{l^2}{r^2} \right]^{\frac{1}{2}}}, \quad (\text{A.12})$$

which is the differential classical probability of finding an classical Rydberg electron with a radius between r and $r + dr$. This is what is plotted in Fig. A.2.

A Classical Atom

A real atom, however, is not a single orbit. This is confirmed by the concept of expectation values, which are found by finding moments of a *distribution* of charge around a core. As guide in this regard, a classical atom can be created by considering an ensemble of initial conditions and comparing the classical averages of \bar{r} against the quantum mechanical values of $\langle r \rangle$ [3]. If they agree, then the classical model is exhibiting the physically correct behavior.

In practice, selecting initial conditions weighted against the classical probability function, of Equ. A.12 can be accomplished in a variety of ways. Monte Carlo selection techniques [4] were attempted here, but proved to be very inefficient, and required an enormous number of trials before reproducing the expectation values of $\langle r^n \rangle$.

Instead, Kepler's equation (Goldstein, p. 101, Equ. 3-76)

$$\omega t = \Psi - e \sin \Psi, \quad (\text{A.13})$$

was solved numerically for Ψ , the eccentric anomaly, for t (time) uniformly and randomly distributed between 0 and $2\pi n^3$. In this equation, ω is the frequency of revolution, defined in Goldstein, p. 101, Equ. 3-75, and e is the eccentricity of the

orbit, defined by Goldstein, p. 96, Equ. 3-57. Once Ψ is found, it can be related back to the orbital angle θ , using Goldstein, p. 102, Equ. 3-77 or 3-76. The θ 's found in this manner are properly distributed according to the physical motion of an electron in a Rydberg orbit. This is the same θ found in the orbit equation in Goldstein, p. 94, Equ. 3-51.

The Actual Initial Conditions

Now that we have a variable that reflects the proper distribution of initial points around a Rydberg orbit, we are ready to calculate the initial conditions on \vec{r} and \vec{v} that can be used to start the integration process. The initial orbital angle will be called θ_0 .

As shown by Equ. A.4 - A.9, we need six initial conditions, one for each equation. Two are simple to find. The Kepler problem is confined to a plane (call it the x-y plane), so r_{z0} and v_{z0} will both be zero. The others are found as follows, given that we have the properly distributed orbital angle, θ_0 :

Position. From the orbital equation, Goldstein, p. 94, Equ. 3-51, we can obtain

$r_{x0}(\theta_0)$ and $r_{y0}(\theta_0)$ from:

$$r_{x0} = r(\theta_0)\cos\theta_0 \quad (\text{A.14})$$

and

$$r_{y0} = r(\theta_0)\sin\theta_0 \quad (\text{A.15})$$

where

$$r(\theta) = \frac{l^2}{1 + \sqrt{1 + El^2 \cos\theta}}. \quad (\text{A.16})$$

E is the electron's energy, derivable from the principal quantum number n via $E = -1/2n^2$, and l is the angular momentum of the electron, which is 2 quantum mechanically. Classically, this value is set to $\sqrt{l(l+1)}$, or $\sqrt{6}$.

Velocity. From r_{x0} and r_{y0} above, the v_{x0} and v_{y0} can be found using the fact that $v_x = \dot{r}_x$ and $v_y = \dot{r}_y$. From these we get that:

$$v_{x0} = \dot{r}(\theta_0)\cos\theta_0 - \frac{l}{r(\theta_0)\sin(\theta)} \quad (\text{A.17})$$

and

$$v_{y0} = \dot{r}(\theta_0)\sin\theta_0 + \frac{l}{r(\theta_0)\cos\theta}, \quad (\text{A.18})$$

where $r(\theta)$ is defined in Equ. A.16, and $\dot{r}(\theta)$ is its time derivative, given by

$$\dot{r} = \sqrt{\frac{2}{r(\theta_0)} - \frac{1}{n^2} - \frac{l^2}{r^2(\theta_0)}}. \quad (\text{A.19})$$

In practice, the positive root of \dot{r} is chosen for $0 \leq \theta_0 \leq \pi$ (outward motion of the electron, away from the core), and the negative root for $\pi \leq \theta_0 \leq 2\pi$ (inward motion of the electron, past its outer turning point, back in towards the core).

So we have the physically correct initial conditions for all three components of \vec{r} and all three components of \vec{v} . This is sufficient to begin the actual integration process.

A.3.4 Performing the Integration

There are many ways to numerically integrate a differential equation. None of the conceptual “whys and hows” of these methods will be discussed here, except one, which was a very valuable lesson learned during the course of this work. This is the concept of *stepsize*.

Stepsize

To illustrate this case, consider integrating the simple differential equation

$$\frac{dx}{dt} = v_x(t), \quad (\text{A.20})$$

where we wish to find $x(t)$ from $v_x(t)$. From a purely dimensional analysis, if we multiply both sides of this equation by Δt , then the left hand side, dx/dt will become $(dx/dt)\Delta t$, which has units of position; it has been integrated to $x(t)$. This is the familiar freshman mechanics approach, where one finds the next position of a particle via

$$x_{new} = x_{old} + \frac{dx}{dt} \Delta t. \quad (\text{A.21})$$

But this method assumes that over the time interval, Δt , the force acting on the particle is constant. So there is immediately a question here. How large or small should Δt be? Well, there are some tradeoffs:

Δt too large. If Δt is too large, important features of the force law as a function of time might be missed. In extreme example of this, say Δt was chosen to be about 2 ps or so. In a case like this, the integration process could potentially completely “over step” a 0.5 ps HCP field, excluding its effect entirely!

In the case of integrating a Coulomb force, having Δt too large would not work well near the core either, where the electron is moving very fast. Near the core (small r), the force function has a very large changes over small distances, as it diverges towards $-\infty$. In a situation like this, large errors can accumulate very quickly from step to step, even causing the orbit not to close back on itself after only one period.

Δt too small. Most of these problems can be circumvented by just making Δt smaller and smaller. But this is accomplished with great computational expense, in other words, your integration program will run very slowly [5].

A great lesson learned during the course of this work is that it is best in a case like this not to fix Δt to any particular value, rather let it *adapt* to the current integration needs. In the Rydberg electron case, Δt can be large near the outer turning point, where the Coulomb force is relatively flat and constant. Near the inner turning point, Δt should decrease to handle the rapidly changing force. The essence of this is most eloquently captured in a quote from Numerical Recipes, p. 714:

“Many small steps should tiptoe through treacherous terrain, while few great strides should speed through the uninteresting countryside.”

In this light, the numerical integration algorithm most most suitable for this job is a Runge-Kutta algorithm with “adaptive stepsize control.” Runge-Kutta is, in general, a very robust, workhorse method of integrating differential equations of all types. It has been modified to have an adaptive stepsize, in Numerical Recipes, p. 714, Section 16.2, “making the old workhorse more nimble with new shoes.” This is the algorithm of choice here, and the routines `rkqs` and `rkck` were keyed in, verbatim, from the book, and used in this calculation.

A.3.5 Programming Examples

The numerical integration routines `rkqs` and `rkck` are at the heart of the numerical analysis here. For this reason, small samples of the C code used in this thesis, that set up and call these routines are presented here.

The following names are used for commonly referred to variables:

n3 The principal quantum number n to the 3rd power (n^3).

rnd() A uniform random number between 0 and 1.

M_PI The constant $\pi=3.1415926535$.

t_start The desired integration start time.

t_end The desired integration end time.

h_start A proposed initial integration step.

h Stepsize in actual use.

e Eccentricity of the classical orbit, defined as $\sqrt{1 + 2El^2}$, where E is the energy of the Rydberg state ($-1/2n^2$) and l is angular momentum.

EPS Desired accuracy of the numerical integration (typically 1.0×10^{-7})

Now, the implementation begins.

Select the initial orbital position, θ_0

1. Choose some time, t , uniformly in $0..2\pi n^3$, one Kepler period.

```
t=2.0*M_PI*n3*rnd();
```

2. Numerically solve the Kepler equation for Ψ , given t .

```
psi=SolveKeplerEqu(t);
```

In this case, function `SolveKeplerEqu(t)`; takes in a single parameter, t (time), solves the Kepler equation numerically for Ψ using a bisection method (see Numerical Recipes, p. 350), and returns the solution.

3. Compute the initial orbital angle, θ_0 (θ_0).

```
theta0=2.0*atan((1+e)/(1-e)*tan(psi/2.0));
```

where e is the eccentricity of the orbit.

Set up the Numerical Integration

1. Declare a real array to hold the six variables of integration.

```
double y[6]
```

Each element is defined as follows: $y[0] = r_x$, $y[1] = r_y$, $y[2] = r_z$, $y[3] = v_x$, $y[4] = v_y$, $y[5] = v_z$.

2. Declare a real array to hold the derivatives of the six variables of integration

```
double dydt[6]
```

3. Set up the initial conditions.

```

y[0] = r_func(theta0) * cos(theta0);
y[1] = r_func(theta0) * sin(theta0);
y[2] = 0.0;

y[3] = vx_func(theta0);
y[4] = vy_func(theta0);
y[5] = 0.0;

```

where `r_func` is a function that returns the radius of a Kepler orbit at a given θ (computed from the exact orbit equation from Goldstein, p. 96, Equ. 3-55), and `vx_func` and `vy_func` return the x and y components of the velocity of a particle bound in a Kepler orbit, as a function of θ , as shown in Eqs. A.17 and A.18.

4. Prime the integration loop

```

// choose an initial stepsize
// this formula is strange and empirical, but it works
h_start=r_func(theta0) / 200.0;
h = SIGN(h_start,t_end - t_start);

//choose the integration limits
t_start=0.0;
t_end = whatever_you_want;

```

5. Write a function that finds the derivatives of array `y` (defined above) at time `t`, and puts them into array `dydt`


```

void Derivatives(double t,double *y,double *dydt)
{
    // t is not used, yet
    r=sqrt(y[0]*y[0]+y[1]*y[1]+y[2]*y[2]);
    // velocities
    dydt[0] = y[3];
    dydt[1] = y[4];
    dydt[2] = y[5];
    // accelerations
    dydt[3] = -y[0]/(r*r*r);
    dydt[4] = -y[1]/(r*r*r);
    dydt[5] = -y[2]/(r*r*r);
}

```

Note this essential code is directly translated from the “obvious” first order Eqs. A.2 and A.3.

Do the Integration

This is the “driver routine” called `odeint` from Numerical Recipes that the book forcefully suggests you use, on p. 721.

```

do
{
    // compute derivates
    Derivatives(t,y,dydt);

    for(i=0;i<6;i++)

```

```

        yscal[i]=fabs(y[i])+fabs(dydt[i]*h)+TINY;
    if ((t+h-t_end)*(t+h-t_start)>0.0)
        h = t_end-t;
    // take a step in time
    rkqs(y,dydt,6,&t,h,EPS,yscal,&hdid,&hnext,Derivatives);
    h = hnext;
}
while((x-t_end)*(t_end-t_start)<0.0);

```

The integration is done

Now the “time-evolved” variables contained in `y[0]..y[5]` can be used, in this case, to calculate the energy of the electron, and test if it has been ionized.

```

//calculate energy
r=sqrt(y[0]*y[0]+y[1]*y[1]+y[2]*y[2]);
v=sqrt(y[3]*y[3]+y[4]*y[4]+y[5]*y[5]);
E=0.5*v*v-1/r;
if (E > 0.0)
    an_ion_has_formed;
else no_ion_was_formed;

```

A lot of initialization and other details have been left out, but in a nutshell, this is the core of the numerical calculation. Note now the `Derivatives` function contains the entire effects of any forces (fields) on the electron. Above, it only contains the Coulomb force. Later, it will be modified to contain an external force, such as a HCP or static field.

A.3.6 After the Integration

We now have the capability to numerically integrate the Kepler problem from time $t = 0$, out to some arbitrary time later. Now what? Well, not much. This problem isn't particularly interesting, as it is a stationary, periodic orbit. With the absence of any numerical roundoff errors or power-outages, this numerical orbit would last forever, continually closing on itself every $2\pi n^3$ time period. After the integration, we have effectively allowed six variables of integration to evolve in time, under the influence of the appropriate forces, and may now examine them. What might be of interest now are the derived variables discussed in Section A.2, such as energy, angular momentum, and linear momentum.

In this simple Kepler problem case, where no external fields are present, energy and angular momentum are always constants as a function of time. Linear momentum, \vec{p} is strongly dependent on time, and the value of it will depend on when we decide to examine it during the integration process. These derived quantities are more interesting in a Kepler system that includes external fields, like HCPs. More on that later.

A.4 Orientation Considerations

The last bit of consideration here concerns how to make the calculations just presented correspond to observed values in the lab. The x-y-z coordinates presented above have no physical meaning. The x, y, and z-components of \vec{r} and \vec{v} discussed were only a convenience, and are a natural way to think of a Kepler orbit: the particle executes orbital motion in the x-y plane, with a constant angular momentum vector oriented along the z-axis. Atoms, however, do not have little coordinate systems built onto them. But an orientation, or coordinate system is fixed onto them as soon as an

external perturbation is applied (e.g. we attempt a measurement).

The motivating reason for writing this section about “orientation considerations” is due to the fact that throughout this thesis, all excited atoms had a value of l_z , or m equal to zero. In other words, there is no projection of the total angular momentum on the z -axis of the excited atoms. In the lab, the z -axis was set by the polarization of the excitation dye lasers; the projection of l along this axis is zero. How do we make this correspondence in our numerical Kepler model, which up until this point has been formed in a fictitious coordinate system? There are no dye-lasers in a numerical model, so the first “axis forming” perturbation the model will see some external field. There is no physical orientation of the pure Kepler state just discussed.

This orientation problem is handled by defining the coordinate system by the externally applied fields themselves. In the lab, a coordinate system such as this is real; we know the polarization of the dye lasers, call this the z - or quantization-axis, and purposely apply external fields along this axis. We can say this axis is “up towards the ceiling” or “parallel to the optics bench” or something real like that. In the model, we are free to set any coordinate system we like, and will always choose the traditional notation, such that the axis named “ z ” will be the axis of symmetry of the system. This will be a *real* coordinate system for our model.

Now the problem remains, just how to orient our numerical Rydberg state into this real coordinate system. The quantities \vec{r} and \vec{v} don’t have any real in-lab analogs. We all hope to someday more directly observe and control these parameters, but for now, scalar expectation values are about as close as one gets to these. It turns out that a helpful orientation quantity is the angular momentum of the classical orbit, or \vec{L} . The motion of a particle in a Kepler orbit is confined to a plane with both the direction and magnitude of \vec{L} , fixed. By orienting \vec{L} properly with respect to the model’s z -, or external field-axis, we can also set $m = 0$ properly. The rest will take

care of itself. This orientation is illustrated somewhat in Fig. A.3.

The easiest way to handle this is to relate the fictitious x-y-z “integration space” coordinates to the “real-lab” x-y-z coordinates with a transformation matrix. Many transformations are available, and the Euler angle transformation discussed on p. 143, Section 4-4 of Goldstein is used here. Following along Goldstein, p. 146, Fig. 4-7, the real z-axis in the lab is set by the z-axis shown. The angular momentum of the numerical Kepler orbit (the fictitious z-axis) is considered the z' -axis shown.

Requiring that $m = 0$, to match the experimental set up, means that the Euler angle $\theta = \pi/2$. This forces the Kepler orbit \vec{L} to be perpendicular to z-axis, onto which the external (HCP) field will later be programmed. The other two Euler angles, ϕ and ψ are free and may take on any angle in $[0..2\pi]$. In Fig. A.3B, these two free angles correspond to arbitrary rotation of the orbit about its angular momentum vector, and about the z-axis. Rotations such as these do not change the projection of \vec{L} along the z-axis, so it will remain equal to zero. That’s it; by taking any quantity from the integration space $(r_x, r_y, r_z, v_x, v_y, v_z)$, and transforming it into “real” space using the Euler transformation matrix (Equ. 4-46, p. 147) we’ll get out *real* lab-observable quantities.

A.4.1 Results

After all of this discussion, the results are finally presented in Fig. A.4. Such a boring plot, but in it, all of the important concepts of numerical integration are brought together, and we finally have a numerical Rydberg state.

Note, in particular, the high concentration of dots near (0, 0) (the core), and the low concentration of dots near the outer turning point. This is the adaptive stepsize algorithm at work; small step sizes near the core, and larger step sizes near the outer turning point. To demonstrate the success of our initial condition selection, the

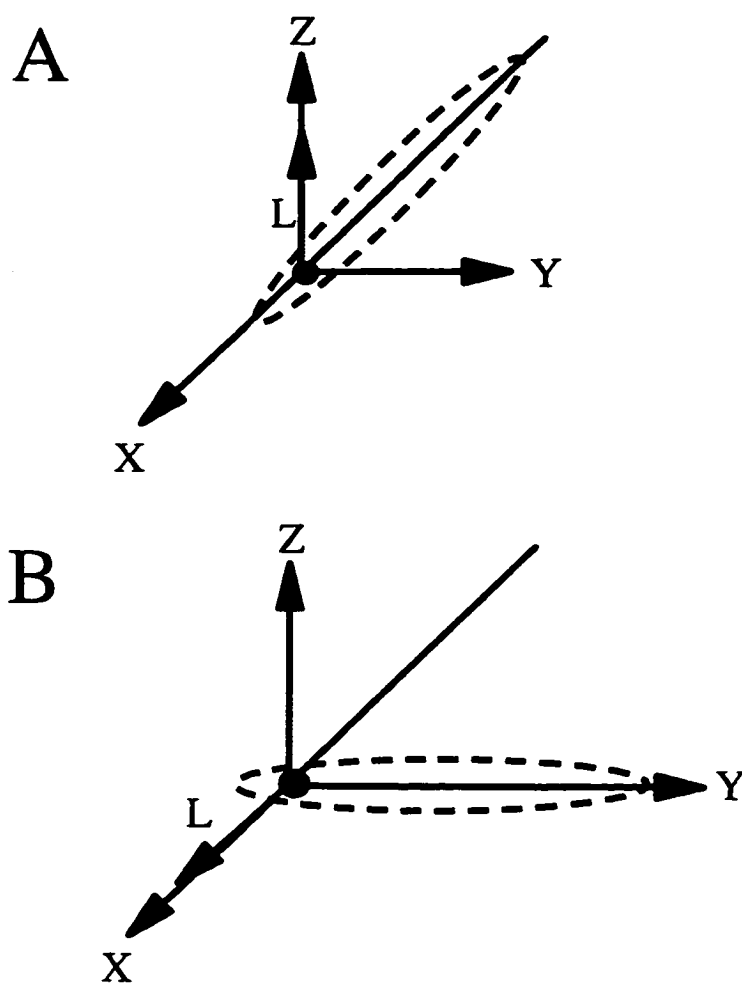


Figure A.3: Inset A: Orbit in a fictitious integration space coordinate system. Inset B: Orbit oriented with respect to a real lab coordinate system such that $m = 0$.

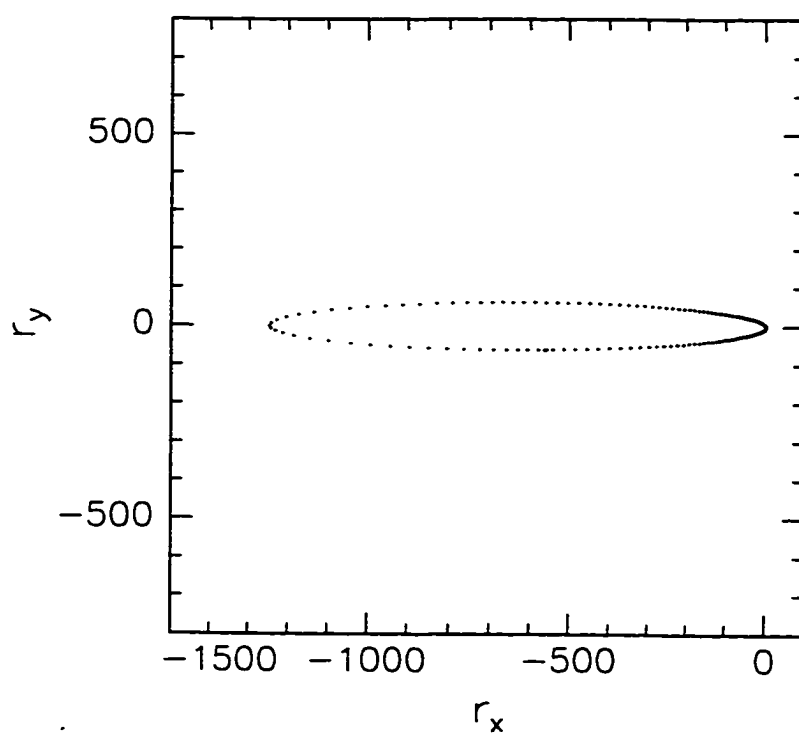


Figure A.4: A numerical Rydberg state. The plot shows the numerically integrated values of r_x vs. r_y for one Kepler period.

computed expectation values of $\langle r^n \rangle$ versus the quantum mechanical values are shown in Table A.1.

Quantity	Calculated	Exact	Error
$\langle r \rangle$	9.29×10^2	9.35×10^2	0.51%
$\langle r^2 \rangle$	9.64×10^5	9.71×10^5	0.71%
$\langle 1/r \rangle$	1.59×10^{-3}	1.60×10^{-3}	0.57%
$\langle 1/r^2 \rangle$	2.45×10^{-5}	2.56×10^{-5}	4.27%

Table A.1: Initial conditions of a numerical $n = 25d$ classical Rydberg state, and how they compare to quantum mechanical expectation values. These values are computed for an ensemble of 10,000 initial orbits.

So after all of this “baggage” we have achieved the following:

Creation of a Classical Atom. Choosing 10,000 initial points for an ensemble of orbits, properly oriented in space, reproduces the quantum mechanical expectation values to within an acceptable error. Spatially then, our classical model “looks” like an atom.

As for the validity of the model, consider an outsider wanting to ask a physical question of the model, such as “What is the value of $\langle r \rangle$?” If we put the classical model into a black box, and right next to it, another black box containing a full-quantum model, the two would be indistinguishable at this level. So there is some justification to proceed with this classical model.

Numerical Integration. Given the initial conditions, an algorithm has been implemented that can successfully integrate a closed orbit for a Coulomb force, which is tricky, since it has a singularity at $r = 0$. For now the fact that $l = 2$ keeps the orbit from passing directly through the origin, avoiding the singularity, but the Coulomb force is nevertheless something to be reckoned with at small values of r . The adaptive stepsize algorithm seems to handle it just fine.

Prior to implementing this adaptive algorithm, simple “Euler” steps, discussed in Section A.3.4 were used; this method *did not work at all*.

A.5 Applying External Fields

The real use of the calculation comes when it is modified to include any external fields relevant to the experiment. With external fields added to the integration, the “if ($E > 0.0$) question” asked after the integration, in Section A.3.5, for example, takes on a whole new, dynamical behavior.

As far as the external fields go, in Chapter 4, this is a time dependent HCP field. In the Chapter 5 experiment, this is a time dependent HCP field *and* a static field. The only change in the calculation is in the force law, which is all contained in the Derivatives function described above.

The fields cannot just be directly inserted into each component of the array `dydt` however, since the fields are oriented in the real lab frame, and the integration takes place in a fictitious frame. Instead, the fields are first, and conveniently set up on their own x-y-z coordinate frame, which corresponds to the real-lab frame (e.g. z means “up” in the the lab, for instance). Next, they are rotated into the fictitious frame, according to the discussion in Section A.4, with careful consideration to what m should be. The field components that have been *rotated* into the fictitious frame can then be directly inserted into the Derivatives function. To handle all of this, a function called `double GetField(int n, double t)` was written that returns the n^{th} component (0..2) of any external field(s) at time t , in the fictitious frame.

A.5.1 Adding an External HCP field

```
double GetField(int n, double t)
{
```

```

// declare temporary field components
// in[0]=x-comps, in[1]=y-comps, in[2]=z-comps
double in[3];

//put the HCP field along the real z-axis
in[0] = 0.0;
in[1] = 0.0;
in[2] = F0*exp(-(t-t0)*(t-t0)/(2*sigma2));

return(Rotate(n,in));
}

```

Here, the HCP field is modeled as a Gaussian, with field amplitude F_0 and a width parameter σ^2 of sigma2 . The function `Rotate(n,in)` rotates the 3-component vector `in` into the fictitious integration frame, and returns the n^{th} component after the rotation. The function just performs a matrix multiplication of the transformation matrix between the lab and fictitious frames, and the input vector `in`, returning the n^{th} component.

Now, the `Derivative` function may be modified to include any external fields, as follows.

```

void Derivatives(double t,double *y,double *dydt)
{
// t is not used, yet
r=sqrt(y[0]*y[0]+y[1]*y[1]+y[2]*y[2]);
dydt[0] = y[3];
dydt[1] = y[4];
}

```

```

dydt[2] = y[5];
dydt[3] = -y[0]/(r*r*r)+GetField(0,t);
dydt[4] = -y[1]/(r*r*r)+GetField(1,t);
dydt[5] = -y[2]/(r*r*r)+GetField(2,t);
}

```

A.5.2 Adding External HCP and Static Fields

For this, only the `GetField` function must be modified, as follows.

```

double GetField(int n,double t)
{
    double in[3];

    //put the static and HCP fields along the real z-axis
    in[0] = 0.0;
    in[1] = 0.0;
    in[2] = Fs + F0*exp(-(t-t0)*(t-t0)/(2*sigma2));

    return(Rotate(n,in));
}

```

Where F_s is the magnitude of the static field, and t_0 is the time at which the HCP arrives in the interaction region.

A.5.3 Adding Two Cross-Polarized HCPs

Once again, only the `GetField` function must be modified, as follows.

```

double GetField(int n,double t)

```

```

{
    // declare temporary field components
    // in[0]=x-comps, in[1]=y-comps, in[2]=z-comps
    double in[3];

    //put the two HCPs along the lab's x and y axis
    //the z-axis is the axis of propagation
    in[0] = F0*exp(-(t-t1)*(t-t1)/(2*sigma2));
    in[1] = F0*exp(-(t-t0)*(t-t0)/(2*sigma2));
    in[2] = 0.0;

    return(Rotate(n, in));
}

```

Where F_s is the magnitude of the static field, and t_0 and t_1 are the arrival times of the two HCPs into the interaction region.

A.6 Conclusions

In this appendix the most critical components of the classical calculation used in this thesis were presented. The real power of the program lies in the few lines after the integration is done, where the user is free to evaluate physical quantities such as the energy after the integration has been completed for the classical particle, subjected to any external fields. Creating momentum distributions either before, after, or even during the integration has also been done, for instance, by logging and histogramming the lab-frame components of \vec{v} as needed. Also, logging *all* variables of integration, say r_x vs r_z , or v_x vs v_z , at evenly spaced time intervals, has allowed for frame-by-

frame computer movies of the entire classical ensemble as a function of time. These logs take up many megabytes of disk space, but the computer movies developed have helped immensely in explaining field/electron interactions, and also provide for nice demonstrations during talks.

For any one setting out to write their own classical calculation: it's very enlightening work and you'll most likely learn a lot.

Bibliography

- [1] R. Rockmore, *Am. J. Phys* **43**, 29 (1975); F.H.J. Cornish, *J. Phys. A* **17**, 323 (1984).
- [2] L. Garner, *Calculus and Analytic Geometry*, Dellen Publishing Company, 1988, p. 732.
- [3] H. Bethe and S. Salpeter, *Quantum Mechanics of One- and Two-electron Atoms*, Plenum Press, 1977, p. 17.
- [4] S. Koonin, *Computational Physics*, Benjamin/Cummings Publishing Company, Inc, 1986, p. 185.
- [5] At the time of this writing, 1998, the fastest computer at my disposal is run by a 266MHz Intel Pentium II processor.

Appendix B

**Publication: Effects of unipolarity
on the ionization of Rydberg atoms
by subpicosecond half-cycle pulses**

Effects of imperfect unipolarity on the ionization of Rydberg atoms by subpicosecond half-cycle pulses

N. E. Tielking, T. J. Bensity, and R. R. Jones

Department of Physics, University of Virginia, Charlottesville, Virginia 22901

(Received 6 September 1994)

Rydberg atoms are ionized by nearly unipolar, subpicosecond electromagnetic pulses. Deviations from a perfectly unidirectional pulse are found to alter substantially the ionization probability as a function of peak field. Quantitative agreement between classical theory and experiment is achieved if the pulse imperfections are significantly attenuated.

PACS numbers: 32.80.Rm

In recent experiments [1,2], Rydberg atoms have been exposed to ultrashort, electric-field pulses. The electric field in these pulses is nearly unipolar, and has a temporal shape which resembles one-half of a cycle of THz-band radiation [3]. In the experiments [1,2], the 0.5-psec duration of these "half-cycle pulses" (HCPs), τ_{HCP} , is shorter than or comparable to the classical Kepler period of the Rydberg states, $\tau_K = 2\pi n^3$. The dynamics of the ionization process in these experiments is distinctly different from that in either a long field pulse ($\tau_{\text{pulse}} > \tau_K$) [4] or a short laser pulse ($\tau_{\text{laser}} < \tau_K$) [5].

In a long electric-field pulse, essentially no energy is transferred to the Rydberg electron. Instead, ionization occurs due to the modification of the electronic binding potential [4]. In a HCP, the electron is unable to respond to the rapid changes in the binding potential, and the electron must gain energy from the field in order to escape the Coulomb attraction of the nucleus. Classically speaking, the electron receives an energy "kick" or impulse from the rapidly changing field [1].

$$\Delta E = - \int_{-\infty}^{\infty} \vec{F}(t) \cdot \vec{v}(t) dt \quad (\text{a.u.}), \quad (1)$$

where $\vec{F}(t)$ is the HCP field and $\vec{v}(t)$ is the velocity of the electron. Therefore the ionization probability is strongly dependent on the velocity or momentum distribution of the initial-state wave function as well as the temporal shape of the electric-field pulse.

The time dependence of the electric field is extremely important in the ionization of Rydberg atoms where $\tau_{\text{pulse}} \ll \tau_K$. In a Rydberg atom, the electron probability distribution is peaked far from the ion core, and the probability for finding the electron near the nucleus during the pulse is $\tau_{\text{pulse}}/\tau_K$. Therefore, in order to have an ionization probability greater than $\tau_{\text{pulse}}/\tau_K$, energy transfer between the electron and the time-dependent field must occur far from the ion core where the electron is essentially free. Equation (1) clearly shows that a free electron can gain energy from a unipolar field pulse. However, this electron cannot gain energy from a pulse whose time-integrated electric field is zero. Indeed, Rydberg atoms may be ionized with 100% efficiency by a HCP, but not by a short laser pulse [1,5].

The results of the ionization experiments [1] are in qualitative agreement with classical simulations [1,6].

The agreement is quantitative if the experimental field values are rescaled by a multiplicative factor of 2.5. A more recent field calibration suggests that the field discrepancy is actually only a factor of 1.6. A description of the differences between the two calibration techniques is given later in the paper. A possible source for the persistent disagreement between experiment and theory is the presence of small, nonunipolar field components in the HCPs used in the experiments.

This report describes an experiment which studies the effects of HCP imperfections on the ionization of Rydberg atoms. Specifically, an optical gating technique is used to substantially attenuate unwanted components in the pulse which appear after the main half-cycle [3,7]. In the following sections we describe the experimental techniques and results. Using these results, quantitative agreement between classical theory and experiment is achieved.

With the exception of the gating device, the experimental apparatus is identical to one described previously [1,2]. Rydberg atoms are produced from a thermal beam of ground-state Na atoms using two, nanosecond pulsed-dye lasers. The Rydberg atoms interact with the HCP between two parallel capacitor plates (see Fig. 1). A ~ 50 -V pulse is applied to the lower plate, pushing any ions which are formed by the HCP through a small hole in the upper field plate toward a microchannel plate detector.

The HCP is generated by illuminating a large-aperture GaAs photoconductive switch with a 120-fsec, 780-nm laser pulse [3,8]. The radiation which is transmitted through the GaAs wafer is collected by a parabolic mirror and directed into the interaction region. The parabolic mirror is used to collimate the radiation, not focus it. The diameter of the HCP beam is approximately 1 cm in the interaction region. The peak field in the HCP is varied by changing the bias voltage across the switch.

Before entering the interaction region, the HCP passes through a second GaAs wafer. We will refer to this wafer as the attenuator. As shown in Fig. 1, a second 120-fsec laser pulse travels through the interaction region antiparallel to the HCP and is absorbed in the attenuator. The frequency of the laser pulse is above the direct band gap in GaAs; therefore on absorption electrons in the crystal are promoted to the conduction band. The pres-

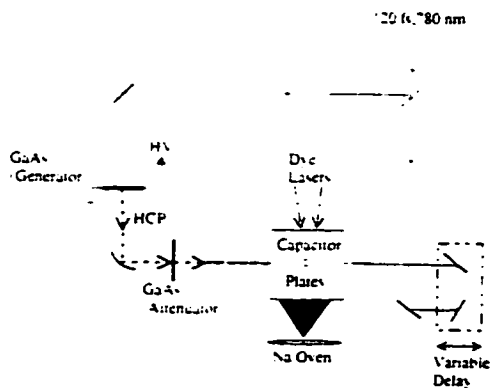


FIG. 1. Schematic of the apparatus showing the GaAs wafer which generates the HCP, the attenuating GaAs wafer, the atomic oven, and relative orientations of the various laser and HCP beam paths. The Rydberg atoms are unaffected by the unfocused 120-fsec laser pulse which travels through the interaction region to the attenuator.

ence of the essentially free electrons on the wafer surface reduces the transmission of the HCP through the wafer by a factor of ~ 10 . The attenuation persists for hundreds of picoseconds. Therefore, to a good approximation, the attenuator "slices off" any parts of the HCP which reach the attenuator surface after the laser pulse [3]. The duration of the HCP which is allowed to reach the Rydberg atoms is selected by varying the time at which the laser pulse strikes the attenuator.

Figure 2 shows the ionization signal for the $25d$ state as a function of the delay of the 120-fsec laser pulse

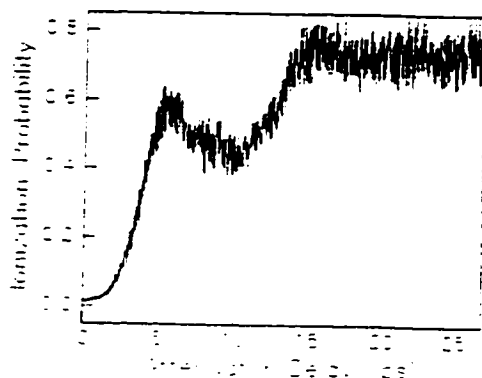


FIG. 2. Ionization signal as a function of the relative delay between the HCP generation and the laser which triggers the transient attenuator. The initial state is $25d$ and the peak HCP field is 12 kV/cm. The ionization signal rises sharply as the attenuator is delayed through the main half-cycle component in the field pulse. The decrease and then increase in the signal at later times are due to the "negative tail" and "reflection" pulse, respectively.

which is used to initiate the transient attenuation. Note that for sufficiently small delays, the entire HCP is attenuated and no ionization is observed. As the delay is increased, the ionization signal rises steadily. At still longer delays, additional signal increases and decreases can be observed. The structure in the ionization signal after the initial large increase is due to nonunipolar components in the pulse (see Fig. 3).

The temporal electric-field profile shown in Fig. 3 is inferred from a measurement of the ionization of a Rydberg atom as a function of delay between two, temporally separated (ungated) pulses. The ionization signal vs delay is similar to a cross correlation of the two pulses. For these measurements, the atom acts as a field detector. Consequently, information on the field that the atoms actually experience is obtained. The pulse shape derived from these two-pulse measurements is consistent with those obtained using conventional pulse-energy detection combined with optical gating or field autocorrelations [3].

The initial sharp increase in the ionization signal in Fig. 2 is due to the main unidirectional peak in the HCP temporal profile. The dominant feature is followed by a *negative* component to the ionization probability. This ionization inhibition is due to the "negative tail" of the field pulse which can be seen in Fig. 3. During this part of the pulse, electrons which had been promoted to the continuum by the half-cycle component of the pulse are recombined with the ion. Approximately 11 psec after the main pulse, a second increase in the ionization signal occurs. This increase is caused by a "reflection" of the main pulse due to imperfect transmission of the pulse through the radiating wafer. Figure 3 clearly shows that the field direction in this part of the pulse is opposite to that of the main pulse. However, unlike the "negative tail," the ionization probability increases due to this reflection.

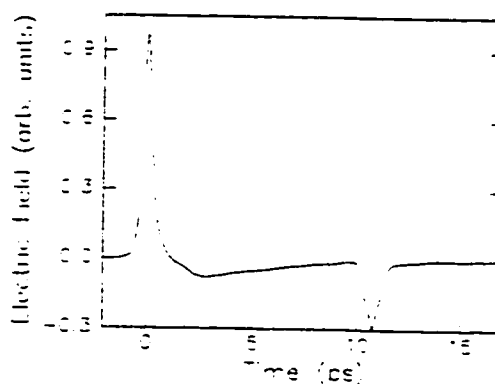


FIG. 3. Temporal shape of the HCP field inferred from measurements of ionization as a function of delay between two identical pulses. The uncertainty in the field at any time is approximately 5% of the peak field. This pulse shape is consistent with previous measurements including electric-field autocorrelations and cross correlations utilizing a transient attenuator as discussed in Ref. [3].

Evidently, the response of the Rydberg atom to the various electric-field components depends on the history of the pulse. This observation can be qualitatively understood through the use of classical mechanics. During the dominant unipolar component of the pulse, the bound electrons get a momentum "kick." This kick is in the same direction for all electrons, regardless of their initial position or momentum. If the energy transfer is large enough, some electrons will be promoted to the continuum. A fraction of these continuum electrons leave the atom directly without passing by the nucleus, while others scatter from the ion core one last time before departing. If the applied field changes direction before any of the ionized electrons scatter from the nucleus, then each of these electrons receives an additional momentum kick which decreases its energy. Therefore the ionization probability drops. However, if the field changes sign long after the initial pulse, the ionized electrons will be far from the atom. Due to ion-core scattering, field inhomogeneities, and stray fields, this field reversal is unlikely to recombine the free electrons with the atom. On the other hand, any electrons which remain bound to the nucleus have a second chance to ionize. Therefore field reversals after long delays will cause ionization enhancement. The degree to which this enhancement occurs depends on the delay, the amplitude of the additional field component, the energy of the initial Rydberg state, and other less well-characterized factors such as stray electric and magnetic fields.

Figure 2 clearly shows that the imperfectly characterized features in the HCP substantially affect the ionization probability for a given peak field. However, the primary concern of this experiment is not the determination of the exact pulse shape. Instead, the purpose of this experiment is to establish quantitatively the effects of the nonunipolar components of the HCP on the measured ionization thresholds. To this end, the ionization probability as a function of peak HCP field has been measured for several nd Rydberg states using (1) as full "unclean" (i.e., unattenuated) HCP and (2) a "clean" HCP with all but the main half-cycle component attenuated.

In Figs. 4(a) and 4(b) we plot the peak electric fields required to ionize 10% and 50% of the Rydberg population with "clean" and "unclean" HCP's. The general shapes of the ionization vs field curves are not affected by the pulse cleaning. However, the threshold fields observed with a "clean" HCP are larger by a factor of 1.3 for both 10% and 50% ionization. As mentioned above, using a different calibration, the measured fields required for ionization using an "unclean" HCP are a factor of 1.6 below those predicted using a Gaussian pulse (Ref. [1] reported a discrepancy of a factor of 2.5).

The field calibration used in Ref. [1] was based on combined measurements using bolometric (Infrared Laboratories) and pyroelectric (Molelectron P1-42cc) detectors [3]. The systematic errors acquired using that technique

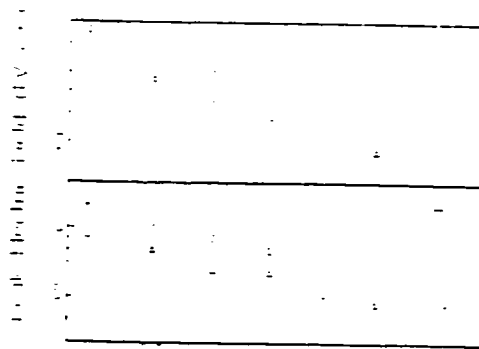


FIG. 4. Peak HCP field required to ionize (A) 10% and (B) 50% of the Rydberg population as a function of n for a (○) "clean" pulse and (△) "unclean" pulse. Significantly attenuating the imperfections in the pulse increases the requisite fields by a factor of 1.3.

[9] include (1) the combined deviations of the spectral response of the two detectors from their accepted values over the bandwidth of the pulse (the manufacturers suggest that this could be as much as a factor of 2 for both devices [10]); (2) geometric factors due to the different angular acceptance of the two devices (the bolometric detector includes a paraboloidal collection cone); (3) errors in the temporal pulse shape used to infer the peak electric-field amplitude from the pulse-energy measurements.

The present calibration involves direct energy measurement with the pyroelectric detector. Using this technique removes any errors due to geometric considerations as well as the response of the bolometric detector. Therefore we believe it to be more reliable. However, the manufacturer's uncertainties in the energy response of the pyroelectric detector result in a systematic error as high as a factor of 1.4. Using the present calibration, the results using the "clean" pulse agree with the classical theory to within 25%. Therefore this error is within the systematic uncertainty of the field calibration.

In conclusion, the dynamics of the ionization of Rydberg atoms by subpicosecond half-cycle pulses are significantly altered by imperfections in these pulses. An optical gating technique has been used to "clean" HCPs so that they more closely resemble pure, unipolar field pulses. Using these "clean" HCP's, the ionization probability vs peak electric field is in quantitative agreement with classical theory.

This work has been supported by the Office of Naval Research.

- [1] R. R. Jones, D. You, and P. H. Bucksbaum, *Phys. Rev. Lett.* **70**, 1236 (1993).
- [2] R. R. Jones, N. E. Tielking, D. You, C. S. Raman, and P. H. Bucksbaum, *Phys. Rev. A* **51**, 2687 (1995).
- [3] D. You, R. R. Jones, D. R. Dykaar, and P. H. Bucksbaum, *Opt. Lett.* **18**, 290 (1993).
- [4] J. A. Bayfield and P. M. Koch, *Phys. Rev. Lett.* **33**, 258 (1974); R. F. Stebbings, C. J. Latimer, W. P. West, F. B. Dunning, and T. B. Cook, *Phys. Rev. A* **12**, 1453 (1975); T. F. Gallagher, L. M. Humphrey, R. M. Hill, and S. A. Edelstein, *Phys. Rev. Lett.* **37**, 1465 (1976); M. G. Littman, M. M. Kash, and D. Kleppner, *ibid.* **41**, 103 (1978).
- [5] R. R. Jones and P. H. Bucksbaum, *Phys. Rev. Lett.* **67**, 3215 (1991); H. Stapelfeldt, D. G. Papaioannou, L. D. Noordam, and T. F. Gallagher, *ibid.* **67**, 3223 (1991); R. R. Jones, D. W. Schumacher, and P. H. Bucksbaum, *Phys. Rev. A* **47**, R49 (1993).
- [6] C. O. Reinhold, M. Melles, H. Shao, and J. Burgdorfer, *J. Phys. B* **26**, L1 (1993).
- [7] B. I. Greene, J. F. Federici, D. R. Dykaar, A. F. J. Levi, and L. Pfeiffer, *Opt. Lett.* **16**, 48 (1991).
- [8] P. R. Smith, D. H. Auston, and M. C. Nuss, *IEEE J. Quantum Electron.* **24**, 255 (1988); Ch. Fattinger and D. Grischkowsky, *Appl. Phys. Lett.* **53**, 1480 (1988); B. B. Hu, J. T. Darrow, X.-C. Zhang, and D. H. Auston, *ibid.* **56**, 886 (1990).
- [9] D. You, R. R. Jones, and P. H. Bucksbaum (unpublished).
- [10] D. You (personal communication).

Appendix C

**Publication: Single-shot detection
of wavepacket evolution**

Single-shot detection of wavepacket evolution

M.B. Campbell, T.J. Benschky, and R.R. Jones

University of Virginia, Charlottesville, VA, USA

mbc5m@virginia.edu

Abstract: We have developed a new instrument for monitoring electronic wavepacket dynamics using a single electromagnetic pulse pair. The operation of the device is analogous to that of single-shot cross-correlators commonly used to monitor the temporal evolution of short laser pulses. We have used the instrument to probe wavepacket evolution over time scales ranging from 100 psec to less than 1 fsec. The device reduces the amount of time required to collect pump-probe time delay data by orders of magnitude, greatly reducing the deleterious effects of experimental drifts. In addition, the single-shot feature provides real-time feedback as to the affect of various experimental parameters on the electron dynamics, allowing us to literally tune-up our equipment to enhance desired behavior at specific times.

©1997 Optical Society of America
 OCIS codes: (020.1670) Coherent optical effects; (020.4180) Multiphoton processes; (020.5780) Rydberg states; (320.7100) Ultrafast nonlinear optics; (320.5300) Picosecond phenomena

References

1. R.R. Jones and L.D. Noordam, "Electronic Wavepackets," in *Adv. At. Mol. Opt. Phys.*, Vol. 38 (in press).
2. L.D. Noordam and R.R. Jones, "Probing Rydberg Electron Dynamics," *J. Mod. Optics* (in press).
3. N.F. Scherer, A.J. Ruggiero, M. Du, and G.R. Fleming, "Time resolved dynamics of isolated molecular systems studied with phase-locked femtosecond pulse pairs," *J. Chem. Phys.* **93**, 856 (1990).
4. N.F. Scherer, R.J. Carlson, R.J. Matro, M. Du, A.J. Ruggiero, V. Romero-Rochin, J.A. Cina, G.R. Fleming, and S.A. Rice, "Fluorescence-detected wave packet interferometry: Time resolved molecular spectroscopy with sequences of femtosecond phase-locked pulses," *J. Chem. Phys.* **95**, 1487 (1991).
5. L.D. Noordam, D.I. Duncan, and T.F. Gallagher, "Ramsey fringes in atomic Rydberg wave packets," *Phys. Rev. A* **45**, 4734 (1992).
6. B. Broers, J.F. Christian, J.H. Hoogenraad, W.J. van der Zande, H.B. van Linden van den Heijvell, and L.D. Noordam, "Time-resolved dynamics of electronic wavepackets above the classical field-ionization threshold," *Phys. Rev. Lett.* **71**, 344 (1993).
7. R.R. Jones, D.W. Schumacher, T.F. Gallagher, and P.H. Bucksbaum, "Bound-state interferometry using incoherent light," *J. Phys. B* **28**, 405 (1995).
8. R.R. Jones, "Creating and Probing Electronic Wave Packets Using Half-Cycle Pulses," *Phys. Rev. Lett.* **76**, 3927-3930 (1996).
9. D. You, R.R. Jones, and P.H. Bucksbaum, "Generation of high-power sub-single-cycle 500 fs electromagnetic pulses," *Opt. Lett.* **18**, 290 (1993).
10. R.R. Jones, D. You, and P.H. Bucksbaum, "Ionization of Rydberg atoms by subpicosecond half-cycle electromagnetic pulses," *Phys. Rev. Lett.* **70**, 1236 (1993).
11. C. Raman, C.W.S. Conover, C.I. Sukenik, and P.H. Bucksbaum, "Ionization of Rydberg Wave Packets by Subpicosecond, Half-Cycle Electromagnetic Pulses," *Phys. Rev. Lett.* **76**, 2436-2439 (1996).

#2271 - \$10.00 US
 (C) 1997 OSA

Received August 7, 1997; Revised September 19, 1997
 29 September 1997 / Vol. 1, No. 7 / OPTICS EXPRESS 197

During the last decade a large number of experiments have focused on the study of a variety of different types of electronic wavepackets in atoms.[1,2] Almost invariably, these experiments employ "pump" and "probe" laser pulses to create and monitor wavepacket evolution. The pump pulse populates a coherent superposition of electronic levels from some initial state. The evolution of this non-stationary state is reflected in the time-dependence of its stimulated photoabsorption and emission cross sections. Therefore, the motion of the wavepacket can be monitored experimentally using the probe pulse to (de)excite the wavepacket to some final state. Depending on the specifics of the experiment, different types of information on the electron dynamics can be obtained by measuring the electronic population in the final state as a function of the relative delay between the pump and probe pulse.[1,2]

Unfortunately, this type of measurement is destructive. The wavepacket that is produced by the pump pulse is destroyed by the probe. Therefore, the time-dependent evolution of the wavepacket can only be obtained from multiple measurements at different relative delays between the pump and probe. All experimental parameters must remain perfectly constant during consecutive measurements as the relative pump-probe delay is varied if an accurate determination of the electron dynamics is to be made. Of course, rapid shot-to-shot variations can be eliminated by averaging the results of multiple measurements at the same pump-probe delay. However, this necessarily increases the amount of time required to obtain a full delay scan and increases the possibilities for long term drifts, particularly in low repetition rate systems. In some situations, maintaining the required stability during hours of data collection makes experiments prohibitively difficult. Moreover, the destructive experimental method lacks real-time feedback. A delay scan must be performed before one can ascertain the affect on the dynamics of changing *any* experimental parameter.

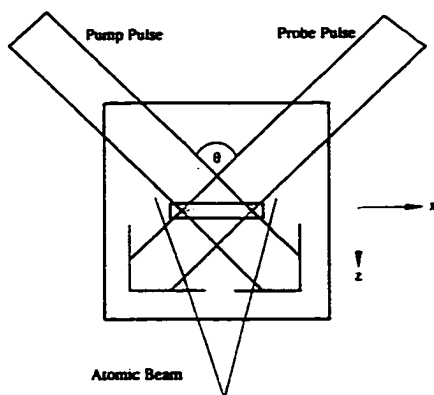


Figure 1. Operation schematic for a single-shot detector.

In an attempt to circumvent these experimental problems, we have constructed a device which is capable of monitoring electron dynamics using a single pump-probe pair. The detector utilizes pump and probe beams which cross at some non-zero angle, θ , through a sample of atoms as shown in Fig. 1. The relative pump-probe delay varies linearly along an axis, \hat{x} , perpendicular to the average propagation direction of the two pulses, \hat{z} . The difference in the relative pulse delay for two atoms separated by a distance, d , along the \hat{x} axis is $\Delta\tau = \frac{2d}{c} \sin(\theta/2)$. Therefore, in a single shot, atoms which experience a range of delays are present in the sample, and the problem of determining the final state population as a function of time-delay becomes one of measuring the number of final state atoms as a function of position along the \hat{x} axis. This measurement is straightforward if the final state is in the continuum or can be selectively coupled to the continuum through subsequent photo-, field-, or auto-ionization.

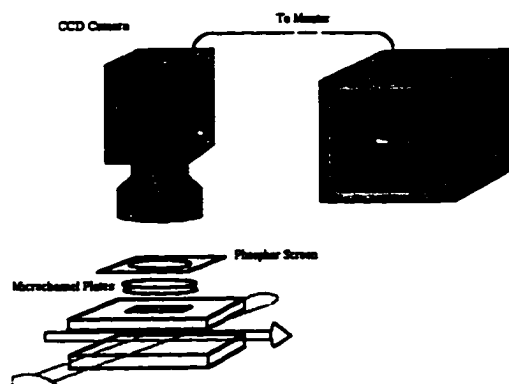


Figure 2. Schematic of the single-shot detector.

We have built an imaging detector capable of recording the spatially dependent ion signal produced by a single pump-probe pair in a crossed beam geometry. A schematic diagram of the detector is shown in Figure 2. A thermal beam of atoms propagates between two field plates that are separated by 1.5 cm. A long slit (2.5 cm x 0.16 cm) in the upper field plate is oriented with its long dimension along the \hat{x} axis. A voltage applied to the lower field plate pushes any ions in the interaction region through the slit in the upper plate. The details of the experiment dictate how the ions are actually produced, either directly by the probe pulse or through subsequent photo-, auto-, or field-ionization of a final state populated by the probe. In any case, ions travel out of the interaction region and strike a microchannel plate detector with their relative positions preserved. Amplified electron current from the microchannel plates is accelerated towards a phosphor screen (Kimball Physics, ZnS:Ag Type 1330), and the fluorescence from the phosphor is imaged with a CCD camera. The ion distribution in the interaction region is reflected in the brightness of the CCD output as viewed on a television monitor. The CCD output is also transferred to a personal computer using a digital oscilloscope.

NOTE TO USERS

Page(s) not included in the original manuscript and are unavailable from the author or university. The manuscript was microfilmed as received.

Pages 237-239

This reproduction is the best copy available.

UMI

Appendix D

**Publication: Probing electronic
radial wave packets using impulsive
momentum retrieval**

Probing electronic radial wave packets using impulsive momentum retrieval

M. B. Campbell, T. J. Benschky, and R. R. Jones

Department of Physics, University of Virginia, Charlottesville, Virginia 22901

(Received 29 January 1998)

Subpicosecond half-cycle pulses and a single-shot imaging detector have been used to monitor the evolution of electronic radial wave packets in calcium. The time-dependent momentum-space probability distribution is obtained using the impulsive momentum retrieval (IMR) method. The measured distributions are compared to the results of quantum and classical simulations allowing a comprehensive evaluation of the benefits and limitations of the IMR method. [S1050-2947/98/060707-9]

PACS numbers: 32.80.Rm, 33.80.Rv

I. INTRODUCTION

During the past decade, rapid technological progress has made it possible to create and probe a variety of different coherent superposition states, or wave packets, in atoms [1]. Understanding the dynamic evolution of these nonstationary states is important to studies of classical-quantum correspondence, the response of atoms to strong static and dynamic electromagnetic fields, and quantum control in atoms and molecules. Experimentally, the problem of how to accurately probe electronic dynamics has proved to be as difficult as, if not more difficult than, producing the wave packet in the first place [2]. The techniques of short pulse pump-probe ionization [3], bound-state interferometry [4], and time-resolved streak camera detection of ionization [5] have all been used to characterize wave packet evolution with varying degrees of success. However, none of these methods are useful for determining the time-dependent electronic probability distribution.

Recently, two methods have been developed that make it possible to measure, approximately, the projection of the probability distribution of an electronic wave packet on one coordinate axis. The first, time-resolved isolated core excitation (ICE) [6], relies on electron correlation in multielectron atoms to determine the position of one electron during the optical excitation of another, tightly bound electron [7]. The second, impulsive momentum retrieval (IMR), utilizes ultrashort, unipolar field pulses (HCPs) to determine one Cartesian component of the momentum space probability distribution of a wave packet [8]. Although these two methods are quite straightforward in concept, they are both extremely difficult to implement in practice. Both require that data be collected to fill a two-dimensional parameter space. For example, the IMR method requires a measurement of wave packet ionization probability versus HCP field amplitude versus delay [8]. The time required to make these measurements is often so great that unavoidable equipment drifts make an accurate determination of the probability distribution impossible.

To circumvent this problem, we have constructed a detector that makes it possible to collect time delay data in real time using a single laser shot [9]. As a result, the time-resolved ICE or IMR procedures can be reduced to a scan over a single parameter. This paper describes the use of this "single-shot detector" and the IMR method in the measure-

ment of the time-dependent momentum distribution of a radial electronic wave packet. In the following sections we describe our experimental method and compare the experimental results to those of theoretical simulations. We conclude with a discussion of the applicability of the method to future experiments.

II. EXPERIMENTAL PROCEDURE

Atoms in the $4s4s\ ^1S_0$ ground state in a thermal Ca beam are pumped to the $4s4p\ ^1P_1$ level using 423-nm radiation from a 5-nsec dye laser pulse. The intermediate state atoms are further excited to a linear superposition of $4snd\ ^1D_2$ Rydberg states using a 0.5-psec, 392-nm laser pulse. The 0.5-psec laser pulse is generated via second-harmonic generation of the 120-fsec, 786-nm output from an amplified Kerr lens mode-locked Ti:sapphire laser. Phase-matching effects in the 1-cm-long potassium dihydrogen phosphate (KDP) doubling crystal restrict the bandwidth of the 392-nm pulse to approximately 30 cm^{-1} , increasing its duration to approximately four times that of the fundamental. Since the lasers are all linearly polarized in the vertical \hat{z} direction, the z projection of the orbital angular momentum of the nd Rydberg electron is restricted to $m = 0$. Using state-selective field ionization [10], we determine that the radial wave packet contains appreciable amplitude from approximately seven $4snd$ states centered about a mean principal quantum number $N = 32.9$.

After its creation, the wave packet is exposed to a unipolar HCP. The HCP is created by gating a GaAs photoconductive switch with a portion of the 120-fsec, 786-nm Ti:sapphire output [11]. The HCP field amplitude is linearly proportional to the bias voltage on the switch and its polarization direction is parallel to the bias field [11]. The switch is mounted on a rotation stage so that the HCP polarization can be rotated continuously about its propagation direction. Before reaching the Rydberg atoms, the HCP propagates through an unbiased GaAs wafer. The reflectivity of this wafer is gated by an additional 120-fsec, 786-nm laser pulse producing a transient mirror that significantly attenuates any nonunipolar components of the HCP from reaching the Rydberg atoms [11,12].

After passing through the transient attenuator, the duration of the "cleaned" HCP is approximately 1-psec. The fundamental oscillation period of the wave packet $\Delta = \pi \hbar^2 a.u.$

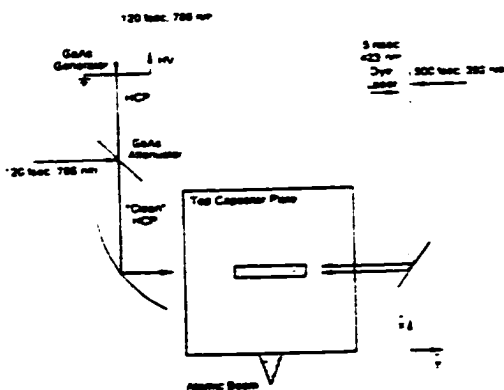


FIG. 1. Schematic of the laser-atom interaction region showing the relative orientation of the laser and atomic beams, the high voltage (HV) based GaAs wafer, and the extraction slit.

≈ 5.4 psec is significantly longer. Therefore, to a first approximation, it is not unreasonable to consider the interaction of the HCP and the Rydberg electron to be impulsive. In this short-pulse approximation, the probability for ionizing the wave packet with a HCP depends only on the impulse delivered by the pulse (proportional to the time-integrated HCP field) and the momentum distribution of the wave packet just before the pulse [13,14]. Following the IMR procedure outlined in Ref. [6], the projection of the wave packet's momentum distribution along the HCP polarization direction can be obtained at any instant by measuring the ionization probability versus HCP field amplitude. The time-dependent momentum distribution is constructed by collecting ionization versus HCP field data at different relative delays between the 392-nm laser pump and HCP probe. The distributions along orthogonal axes are obtained by making identical ionization measurements with the HCP polarized in an orthogonal direction.

Using a different detector, the time dependence of the ionization probability at a fixed HCP field can be obtained with a single shot of the laser system [9]. With this device, the data required to span the two-dimensional parameter space, ionization versus HCP field versus delay, are collected in a single scan of the HCP field amplitude. The principle of operation behind the single-shot detector is similar to that of optical cross correlators that are commonly used to measure the temporal profile of ultrashort laser pulses. As shown in Fig. 1, the laser pump and HCP probe beams counterpropagate along the \hat{y} direction and at right angles to the atomic beam so that all three beams lie in a common horizontal plane. The width of the atomic beam along the \hat{y} axis is approximately 2.5 cm. Because the pump and probe beams counterpropagate, the relative delay between the laser and HCP varies linearly along the \hat{y} axis. The difference in the relative delay between the HCP probe and 392-nm pump as "seen" by two atoms separated by a distance d along the \hat{y} axis is $\Delta\tau = 2dc$, where c is the speed of light. Therefore, atoms that experience a continuous range of pump-probe delays are produced with each laser shot and the number of

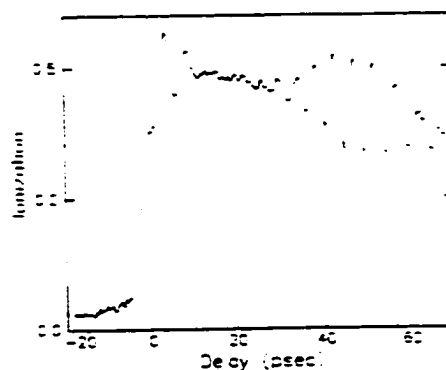


FIG. 2. Probability for ionizing the $4snd$ wave packet as a function of time. The curve is the average of 300 single-line traces from the imaging detector.

ions produced as a function position along the \hat{y} axis reflects the ionization probability as a function of HCP delay.

The laser, HCP, and atomic beams cross between two 7.5×7.5 cm² parallel capacitor plates that are separated by 1.5 cm. The long dimension of a 0.15×2.5 cm² slit is oriented parallel to the \hat{y} axis in the upper capacitor plate. Approximately 20 nsec after the HCP interacts with the atoms, an approximately 50 V pulse applied to the lower field plate pushes any ions formed by the HCP through the slit toward a microchannel plate (MCP) detector. The ions strike the channel plates with their relative positions along the \hat{y} axis preserved. The secondary electrons formed in the channel plates are accelerated onto a phosphor screen mounted to the top of the channel plate assembly. The spatial distribution of ions in the interaction region can be determined after each laser shot by monitoring the phosphor fluorescence level with a charge coupled device (CCD) camera. The spatial resolution of the combined phosphor and MCP is approximately 300 μ m. Therefore, in this geometry, the ionization probability over a 100-psec HCP delay range can literally be seen with 1-psec resolution on a television monitor after a single shot.

Due to the finite width of the ion extraction slit in the upper field plate, approximately 40 lines in the video image contain ionization versus time-delay information. Although integrating the signal from each line enhances the signal-to-noise ratio and reduces the data collection time, it is not possible with our current computer interface to collect all of the useful video image and process it at the 15-Hz laser repetition rate. Therefore, a digital oscilloscope is used to capture a single line of the video signal at the laser repetition rate. This line image is averaged over several hundred laser shots to improve the signal-to-noise ratio. Figure 2 shows the probability for ionizing a $4snd$ wave packet acquired from a single video line averaged over 300 laser shots (20 sec of data collection).

Spatial nonuniformities in the microchannel plate and phosphor efficiency are removed by normalizing the output of each CCD pixel individually. The normalization factor for each pixel is equal to its output voltage when the atoms are exposed to a HCP capable of ionizing the wave packet with

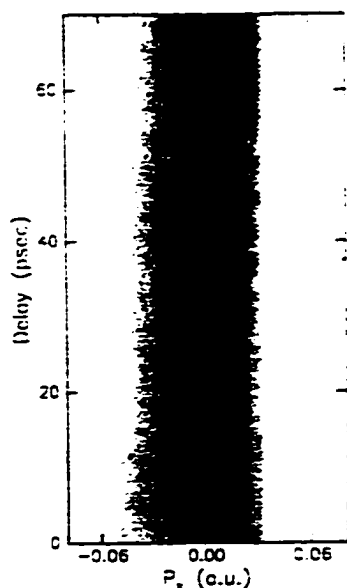


FIG. 3. Density plot of the experimental p_x momentum distribution for a radial wave packet measured using the IMR method. The measured distribution for p_z is similar but not shown due to technical difficulties as discussed in the text. Dark regions indicate high probability. Note the clear oscillations in the width of the distribution as the wave packet oscillates radially.

100% efficiency. In addition, because of slight ion focusing by the extraction slit, the conversion from spatial position to delay is not perfectly linear. Therefore, the delay axis is calibrated using a quadratic function that describes the change in the observed spatial ionization distribution as the optical path length of the 392-nm pump pulse is varied.

Previous measurements [11] indicate that the peak field of the HCP is linearly proportional to the bias voltage on the photoconductive switch while its duration is independent of this voltage. Therefore, the impulse delivered by the HCP (i.e., the time-integrated field) is equal to the measured switch bias multiplied by a constant scaling factor. Taking advantage of the agreement of previous ionization experiments with classical calculations [8,13,15], we assume that the impulse delivered by the HCP at 50% ionization is simply $A = 1/N$ a.u., where A is the impulse or time-integrated HCP field and N is the average principal quantum number of the wave packet.

To measure momentum distributions, ionization probability versus time scans similar to the one in Fig. 2 are collected at 50 different HCP field values. Each time scan is discretized into 300 data points and the data are resorted to give ionization probability versus field curves at 300 different delay times. The time-dependent momentum distribution is obtained by taking the derivative of a spline fit to the ionization versus field (or impulse) data at each time delay. Figure 3 shows the measured distribution of probability along the p_x coordinate for the 3rd radial wave packet. The symmetry

of the atoms ensures that the distribution along p_x is identical to that of p_z . Surface reflections of the HCP from the transient attenuator (prior to its illumination) reduce the HCP amplitude significantly. Therefore, we cannot determine the momentum distribution at large positive momentum where large impulses are required. Nevertheless, the time-dependent distribution clearly reflects the anticipated motion of the wave packet.

At a delay $\tau = 0$, the wave packet is located near the nucleus where there is a high probability that the magnitude of its momentum is very large. The momentum distribution narrows as the wave packet moves away from the nucleus as time evolves. The distribution becomes a narrow peak centered about zero momentum as the wave packet nears the outer turning point of the classical motion. The wave packet returns to the nucleus after a delay equal to the classical Kepler period $\tau_K \approx 5.4$ psec. The return is characterized by a dramatic broadening of the momentum distribution. Due to the anharmonicity of the Coulomb potential, the wave packet spreads and collapses after only two oscillations. Fractional revivals of the wave packet occur, but they cannot be seen due to the limited resolution of the detector. However, a full revival of its momentum oscillation can be seen near 50 psec.

Momentum distributions along p_z are obtained by rotating the GaAs switch by 90°. As anticipated for a pure radial wave packet, these distributions show the same oscillations (period and phase) as those observed in the p_x distributions. Unfortunately, the geometry of the transient attenuator (see Fig. 1) reduces the field amplitude of s polarized HCP radiation (along \hat{z}) by approximately 40% relative to p -polarized (along \hat{x}) pulses. Therefore, there is insufficient field to saturate the ionization probability and no information on the probability distribution for momenta greater than 0.015 a.u. can be obtained. Nevertheless, we have observed the periodic breathing of the wave packet in this dimension as well.

A final test of the symmetry of the wave packet is performed by changing the polarity of the HCP in both the \hat{x} and \hat{z} orientations. Since a pure radial wave packet has no momentum asymmetry along any axis, the observed probability distributions are expected to be independent of the polarity of the HCP. Indeed, the momentum distributions taken along either the \hat{x} or \hat{z} axis are independent of the sign of the HCP field.

III. ANALYSIS

Because the radial wave packet under study is relatively well characterized, the measured probability distributions can be compared to theoretical expectations. The wave packet used in the quantum simulation is numerically prepared in the following manner. First, the magnitude of the probability amplitude for each state in the simulated wave packet is given by the measured Rydberg eigenstate distribution. Second, we assume that the laser pulse that excites the wave packet is transform limited so that the amplitude of each constituent eigenstate is real at the peak of the laser intensity at $t=0$. Next, the radial wave functions for the constituent eigenstates are calculated numerically using a Numerov integration routine. Finally, the momentum space

eigenfunctions are computed [16] and used to propagate the wave packet through time. The projections of the momentum space probability distribution along the \hat{x} and \hat{z} axes are then obtained from the time-dependent momentum space wave function. The calculated evolution of the probability distribution along p_x is shown in Fig. 4. Figure 4(a) gives the distribution calculated with high temporal resolution, while Fig. 4(b) shows the same distribution averaged over the experimental resolution of approximately 1.5 psec.

There is qualitative agreement between the measured and calculated distributions in Figs. 3 and 4(b), respectively. The radial oscillations that are readily observable in both plots occur with the same period and phase. However, there are also clear differences between the measured and simulated results. First, the measured distribution shows a clear asymmetry about zero momentum even though the expectation value $\langle p_x \rangle \approx 0$ at all delays. Second, in the measured distribution, the times at which the wave packet has the largest probability of having a large positive momentum do not coincide precisely with the times at which the wave packet has the largest probability of having a large negative momentum. One would expect that when the wave packet is near the nucleus that it would *simultaneously* have its largest probability of having a large linear momentum in *all* directions.

Neither of these features appears in the simulation nor are they expected from a simple physical picture of the wave-packet motion. Nevertheless, they are robust and persist in the data for all HCP polarization directions and polarities. If for some electron velocity there was an actual difference in the probability for finding the electron moving in the positive rather negative direction, then the features in the momentum distribution would reverse under a change in the HCP polarity. Since no such reversals are observed, it is clear that primary differences in the data and simulation are not due to the properties of the wave packet, but instead are an artifact of the measurement technique.

The fundamental assumption of the IMR method is that the spatial probability distribution of the wave packet does not change during its interaction with the HCP. Clearly, this assumption is not valid at those times when the wave packet is traveling very rapidly near the nucleus. In this experiment, the duration of the HCP is approximately 1/5 of the Kepler orbit period. However, a classical Rydberg electron with low angular momentum requires a time of only 1/10 of the Kepler period to travel from the nucleus (≈ 0 a.u.) to a distance n^2 a.u. away (half the distance to the outer turning point). Therefore, it should not be surprising that the IMR method does not accurately portray the momentum distribution of the wave packet during those times when the wave packet is near the nucleus and its interaction with the HCP is nonimpulsive. In fact, due to the extremely high probability of finding the electron near the nucleus at certain times during its evolution, low angular momentum radial wave packets are probably the least well suited to characterization via IMR. Wave packets involving predominantly higher angular momentum states for which there is little probability of finding the electron near the nucleus are the best candidates for IMR [17]. Interestingly, it is these higher angular momentum wave packets that are the most difficult to probe using the more conventional techniques of ionization by short optical pulses [3] or bound-state interferometry [4].

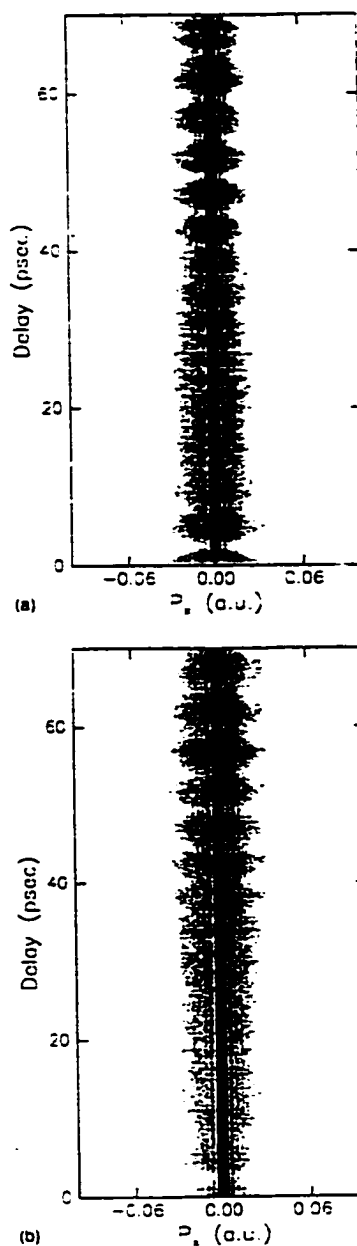


FIG. 4. Density plots analogous to those shown in Fig. 3 obtained from the quantum simulation described in the text. (a) shows the result of the calculation. (b) shows the result in (a) averaged through a 1.5-psec window to simulate the detector resolution of 1.5 psec for a more direct comparison with experiment. Note that the symmetry of the distribution is not reduced by poor temporal resolution.

It is beyond the scope of this work to attempt a full quantum simulation that includes the effects of nonimpulsive ionization of the wave packet. However, since the IMR method is essentially classical in origin, we have simulated the wave-packet ionization classically in an attempt to reproduce the qualitative features of the observed momentum distributions. The simulation begins with an ensemble of electrons with a distribution of energies and well-defined angular momentum in a spherical shell near a hydrogenic nucleus. The discrete energy distribution is weighted according to the eigenstate distribution in the experimental wave packet. A fifth-order, adaptive-step Runge-Kutta algorithm integrates the classical equations of motion for the electron distribution. At some time after the distribution is launched from the nucleus, it is subjected to a Gaussian HCP. After the HCP, the fraction of the ensemble with positive energy gives the ionization probability. The procedure is repeated for another time delay and/or HCP field. The classical simulation produces a set of numerical data, wave-packet ionization probability versus delay versus HCP field, in complete analogy to the experiment. Simulated momentum distributions are derived from the calculated ionization probabilities using a procedure that is identical to the one discussed above for the treatment of the experimental data. The simulated distributions are averaged over a 1.5-psec window to account for the 0.5-psec duration of the actual wave packet and the resolution of the detector.

Figure 5(a) shows the results of the classical simulation using a HCP with a duration of 100-fsec while Fig. 5(b) shows the results obtained from a 1-psec pulse. The results obtained with the 100-fsec pulse show the same symmetric momentum oscillations that are seen in the quantum calculation. However, the 1-psec results have an asymmetry about zero momentum that is very similar to that seen in the experiment. The differences in the distributions produced using 100-fsec and 1-psec pulses are due to two different classical effects. First, since the wave packet spends very little time moving at high velocity near the nucleus, its average rms velocity during the pulse is decreased. Therefore, the amplitudes of the positive and negative momentum wings in the apparent probability distribution are reduced. Since the actual momentum distribution is symmetric, this effect narrows the retrieved distribution symmetrically.

A second effect is responsible for the asymmetry observed in the distributions. When a low angular momentum electron passes the nucleus, its velocity changes sign. So for a certain electron velocity and HCP field strength, the momentum gained (lost) by the electron as it travels toward the nucleus can be exactly canceled by the momentum lost (gained) after reflecting from the nucleus. This impulse cancellation makes it very difficult or impossible to ionize a certain class of electrons in the classical ensemble that scatter from the nucleus during the HCP. However, it is precisely those electrons, moving at high velocity parallel or antiparallel to a true impulse that are the easiest and most difficult to ionize, respectively. Therefore, with a pulse of finite duration, the rising edge of the ionization versus field curve is pushed to higher fields relative to the impulsive ionization result and total saturation of that curve becomes more difficult or impossible. However, the ionization of those electrons in the distribution that are stationary or moving very

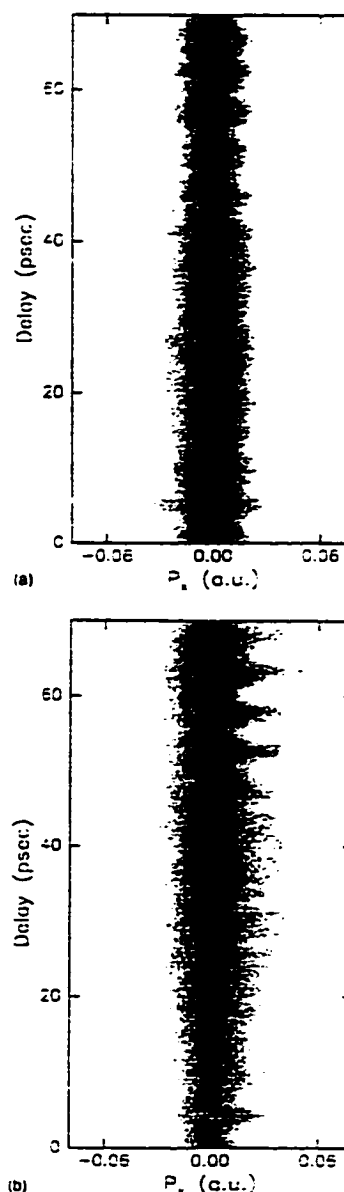


FIG. 5. Density plots of momentum distributions obtained by a classical simulation of the experiment. Ionization of a wave packet is calculated classically and the momentum distribution is obtained from the ionization curves as in the experiment. (a) shows the result of the calculation using a 0.1-psec HCP while (b) shows the distribution obtained from a 1-psec HCP. Both (a) and (b) are temporally averaged with a 1.5-psec window to simulate the detector response. Note that an obvious asymmetry between the negative and positive wings of the distribution appears in (b) but not in (a).

slowly during the pulse is not affected by an increase in the HCP duration, provided the pulse remains significantly shorter than the Kepler period. Therefore, the probability distribution, which is essentially a scaled derivative of the ionization probability curve, rises more sharply and falls less sharply than the true distribution, producing the observed asymmetry.

The source of the temporal shift of the large positive momentum maxima that is observed in the data is not obvious from the simulation. It may be due to nonhydrogenic core scattering or purely quantum effects. More probably, it is due to imperfect characterization of the HCP, which is certainly not Gaussian. Pulse shape effects combined with the nonimpulsive core scattering discussed in the preceding paragraph might produce a similar ionization artifact.

IV. DISCUSSION

In previous work, IMR has been shown to be a potentially powerful measurement method [8,18]. It is particularly useful for monitoring the evolution of nonstationary wave packets far from the nucleus where optical frequency probe techniques fail [1,2]. However, this study clearly shows that care must be taken in interpreting the measured probability distribution if the impulse approximation is not strictly valid at all times during the wave packet's evolution. A breakdown in the impulse approximation does not simply reduce the resolution of the method through temporal blurring. It can also generate artificial asymmetries in the probability distributions. Nevertheless, the general behavior of even radial wave packets is clearly represented in the experimental measurement using 1-psec pulses.

Even considering its limitations, the IMR method provides considerably more information on the dynamic evolution of electron wave packets than either optical pump-probe ionization or bound-state interferometry. However, the IMR method is extremely data intensive. Therefore, without a high repetition rate system or single-shot detector, it is not feasible to implement the IMR technique to study wave-packet dynamics as a function of some external parameter. The single-shot detector allows one to acquire pump-probe data in real time reducing the time required to make the

measurements by one to two orders of magnitude. A full set of ionization versus delay versus HCP field can be obtained in minutes, essentially removing difficulties due to slow equipment drifts. Furthermore, the single-shot capability provides real-time feedback for adjusting equipment, making it possible to tune the wave packet to have specific temporal properties [19].

Measurement of all three Cartesian components of the momentum distribution of hydrogenic wave packets has an interesting benefit that should be noted. In IMR, the probability distribution, and not the momentum space wave function, is measured. Therefore, the spatial probability distribution cannot be recovered. However, this does not imply that no information regarding the position of the wave packet can be obtained. In fact, the time-dependent expectation value $\langle 1/r \rangle$ is easily retrieved if all three Cartesian components of the momentum distribution have been measured. This expectation value gives important information on the proximity of the wave packet to the nucleus. Using the measured distributions, the expectation values $\langle p_x^2, p_y^2, p_z^2 \rangle$ can be computed and inserted into the nonrelativistic hydrogenic Hamiltonian

$$\langle H \rangle = \frac{-1}{2N^2} = \frac{1}{2} (\langle p_x^2 \rangle + \langle p_y^2 \rangle + \langle p_z^2 \rangle) - \langle 1/r \rangle \text{ a.u.} \quad (1)$$

to give the desired result. Unfortunately, this determination is extremely sensitive to the amplitude of the far wings of the momentum distribution, which decreases polynomially and not exponentially. Therefore, computing $\langle p^2 \rangle$ requires a very accurate determination of the HCP ionization probability near 0% and 100% as well as an extremely short pulse to ensure that the impulse approximation is valid at high electron momentum. While neither of these criteria is well satisfied in the current experiment, future experiments might take advantage of the relation in Eq. (1). It is clear that a new source of ultrashort, high-field HCPs would be of great utility for probing electronic wave packets.

ACKNOWLEDGMENTS

We gratefully acknowledge the support of the AFOSR and the Packard Foundation.

-
- [1] R. R. Jones and L. D. Noordam, *Adv. At., Mol., Opt. Phys.* **38**, 1 (1997), and references therein.
- [2] L. D. Noordam and R. R. Jones, *J. Mod. Opt.* **44**, 2515 (1997).
- [3] A. ten Wolde *et al.*, *Phys. Rev. Lett.* **61**, 2099 (1988); J. A. Yeazell, M. Mallalieu, and C. R. Stroud, Jr., *ibid.* **64**, 2007 (1990).
- [4] N. F. Scherer *et al.*, *J. Chem. Phys.* **93**, 856 (1990); L. D. Noordam, D. I. Duncan, and T. F. Gallagher, *Phys. Rev. A* **45**, 4734 (1992); B. Broers *et al.*, *Phys. Rev. Lett.* **71**, 344 (1993); R. R. Jones, C. S. Raman, D. W. Schumacher, and P. H. Bucksbaum, *ibid.* **71**, 2575 (1992); R. R. Jones, D. W. Schumacher, T. F. Gallagher, and P. H. Bucksbaum, *J. Phys. B* **28**, 405 (1995).
- [5] G. M. Lankhuijzen and L. D. Noordam, *Phys. Rev. Lett.* **76**, 1784 (1996).
- [6] J. G. Story, D. I. Duncan, and T. F. Gallagher, *Phys. Rev. Lett.* **71**, 3431 (1993).
- [7] R. R. Jones, *Phys. Rev. A* **57**, 446 (1998).
- [8] R. R. Jones, *Phys. Rev. Lett.* **76**, 3927 (1996).
- [9] M. B. Campbell, T. J. Benschky, and R. R. Jones, *Optics Express* **1**, 197 (1997).
- [10] T. F. Gallagher, *Rydberg Atoms*, 1st ed. (Cambridge University Press, Cambridge, 1994).
- [11] D. You, R. R. Jones, D. R. Dykaar, and P. H. Bucksbaum, *Opt. Lett.* **18**, 290 (1993).
- [12] N. E. Tielking, T. J. Benschky, and R. R. Jones, *Phys. Rev. A* **51**, 3370 (1995).
- [13] R. R. Jones, D. You, and P. H. Bucksbaum, *Phys. Rev. Lett.* **70**, 1256 (1993).
- [14] C. Raman, C. W. S. Conover, C. I. Sukenik, and P. H. Bucks-

- baum, Phys. Rev. Lett. 76, 2436 (1996); M. T. Frey, F. B. Dunning, C. O. Reinhold, and J. Burgdorfer, Phys. Rev. A 55, R865 (1997); C. Raman, T. C. Weinacht, and P. H. Bucksbaum, *ibid.* 55, R3995 (1997).
- [15] C. O. Reinhold, H. Shao, and J. Burgdorfer, J. Phys. B 27, L469 (1994); C. O. Reinhold, M. Melles, H. Shao, and J. Burgdorfer, *ibid.* 26, L659 (1993); M. T. Frey, F. B. Dunning, C. O. Reinhold, and J. Burgdorfer, Phys. Rev. A 53, R2929 (1996); C. O. Reinhold, J. Burgdorfer, M. T. Frey, and F. B. Dunning, *ibid.* 54, R33 (1996).
- [16] B. Podolsky and L. Pauling, Phys. Rev. 34, 109 (1929).
- [17] Examples are Stark wave packets such as those studied by Broers *et al.* (see Ref. [4]) or linear wave packets created with HCPs (see Ref. [8]).
- [18] F. Robicheaux, Phys. Rev. A 56, R3358 (1997).
- [19] The single-shot detector can be used in virtually any type of pump-probe experiment. By increasing the angle between the direction of propagation of the pump and probe beams from near 0 to π , the temporal resolution of the detector can be adjusted from subfemtosecond to picosecond as required for a particular experiment.